THÈSE POUR OBTENIR LE GRADE DE DOCTEUR DE L'UNIVERSITÉ DE MONTPELLIER

En Chimie et Physico-Chimie des Matériaux

École doctorale
Sciences Chimiques Balard

Unité de recherche
Institut Charles Gerhardt Montpellier – UMR 5253

Nanoparticules d'organosilice mésoporeuse pour la thérapie photodynamique à deux-photons et la délivrance d'antibiotique

Présentée par Nicolas BONDON
Le 20 Janvier 2023

Sous la direction de Clarence CHARNAY, Jean-Olivier DURAND et Olivier MONGIN

Devant le jury composé de

Sandrine GERBER, Professeur, EPFL (Lausanne, Switzerland)	Rapporteur
Andreas REISCH, Maître de Conférences, UMR CNRS 7021 (Strasbourg, France)	Rapporteur
Rabah BOUKHERROUB, Directeur de Recherche, IEMN – UMR CNRS 8520 (Lille, France)	Examinateur
Bruno PALPANT, Professeur, LuMIn – UMR CNRS 9024 (Paris, France)	Président du Jury
Clarence CHARNAY, Maître de Conférences, ICGM – UMR CNRS 5253 (Montpellier, France)	Directeur de thèse
Olivier MONGIN, Maître de Conférences, ISCR – UMR CNRS 6226 (Rennes, France)	Co-directeur de thèse
Jean-Olivier DURAND, Directeur de Recherche, ICGM – UMR CNRS 5253 (Montpellier, France)	Co-encadrant de thèse

UNIVERSITÉ DE MONTPELLIER

Cette thèse est dédiée à mon père et à mon grand-père.

Pour votre soutien inconditionnel.

Je vous aime et je sais que vous êtes fiers de moi de là-haut.

PREFACE

Cette thèse a bénéficié d'un financement de l'Agence Nationale de la Recherche (ANR) dans le cadre d'une collaboration internationale (ANR-19-CE09-0034 MSN-2hν) avec des équipes taiwanaises (National Taiwan University, Academia Sinica, Taipei Medical University). Le travail a été réalisé en cotutelle entre l'Institut Charles Gerhardt Montpellier (ICGM, UMR 5253, département D1 *Chimie et Matériaux Moléculaires*) sous la direction des Dr. Clarence Charnay et Jean-Olivier Durand, et l'Institut des Sciences Chimiques de Rennes (ISCR, UMR 6226, équipe COrInt *Chimie Organique et Interfaces*) sous la direction de Dr. Olivier Mongin.

La caractérisation des nanodiamants dans le chapitre 2 et toutes les études bactériologiques décrites dans le chapitre 5 ont été réalisées en étroite collaboration avec Dr. Alexandre Barras et Dr. Rabah Boukherroub de l'équipe NBI (*Nano Bio Interfaces*) de l'Institut d'Electronique, de Microélectronique et de Nanotechnologie (IEMN, UMR 8520) basé à Villeneuve-d'Ascq.

Les études anticancéreuses d'internalisation cellulaire et de thérapie photodynamique à deux-photons présentées dans les chapitres 2 et 5 ont été menées dans le cadre de l'ANR par Dr. Christophe Nguyen, Dr. Lamiaa M.A. Ali, Dr. Denis Durand, Dr. Kamel Hadj-Kaddour, Dr. Nadir Bettache et Dr. Magali Gary-Bobo de l'équipe *Glyco et Nanovecteurs pour le ciblage Thérapeutique* de l'Institut des Biomolécules Max Mousseron (IBMM) situé à Montpellier.

Les études photophysiques des fluorophores et nanoparticules décrites aux chapitres 3 et 4 ont été effectuées en collaboration avec M. Nicolas Richy et Dr. Olivier Mongin qui m'ont accueilli durant six mois à l'ISCR dans le cadre de la cotutelle.

Pour ce qui suit, la langue d'expression sera l'anglais. Un résumé est disponible en français et en anglais à la fin de ce manuscrit.

SUMMARY

ABBREVIATIONS 8

PREAMBLE 9

CHAPTER 1: General introduction 11

1. Organosilica-based nanoparticles as competent vectors for controlled theranostics 11
   - 1.1 Generalities 12
   - 1.2 Non-porous organosilica nanoparticles 12
   - 1.3 Mesoporous organosilica nanoparticles 14
     - 1.3.1 History of porosity 14
     - 1.3.2 Morphology and structure 16
     - 1.3.3 Periodic mesoporous organosilica nanoparticles 19
   - 1.4 Biological applications of PMO-based nanomaterials 24
     - 1.4.1 Anticancer therapy 24
     - 1.4.2 Antibacterial treatments 26
       - i. Context of antimicrobial resistance 26
       - ii. Bacterial infections 28
       - iii. Focus on non-healing wounds 30
2. Two-photon responsive materials applied to theranostics based on two-photon excitation 34
   - 2.1 Introduction to nonlinear optics 34
   - 2.2 Two-photon absorption 34
     - 2.2.1 History 34
     - 2.2.2 Principle and challenges 35
   - 2.3 Two-photon organic fluorophores 36
     - 2.3.1 Photophysical properties 36
     - 2.3.2 Structure-performance relationships 37
     - 2.3.3 Summary of prerequisites for bioapplications 39
   - 2.4 Two-photon excitation photodynamic therapy 40
     - 2.4.1 Generalities about photodynamic therapy 40

2.4.2 Challenges with two-photon excitation therapy 42
2.4.3 FRET-enhanced strategy 44
2.5 Two-photon photosensitizers 48
2.5.1 Generations of photosensitizers 48
2.5.2 Porphyrin derivatives 49
i. Generalities 49
ii. Examples of photodynamic activity 50
2.5.3 The case of nanodiamonds 51
i. Generalities 51
ii. Examples of photodynamic activity 53
2.6 PMO nanoplatforms in PDT-based strategies 53
3. Towards a combinatory therapy against infectious diseases 56
3.1 Delivery of multiple antimicrobial drugs 56
3.2 Synergistic photodynamic/antibiotic therapy 57
3.3 Photodynamic therapy alongside other treatments 58
CHAPTER 2: Photosensitive nanodiamond-PMO core-shell nanoparticles for two-photon excitation PDT 83
1. Introduction 83
2. Results and discussion 84
2.1 Nanodiamonds characterization and TPE-PDT potential against cancer 84
2.1.1 Size and morphology 84
2.1.2 Surface and structural properties 85
2.1.3 Optical properties 87
2.1.4 Photosensitizing ability for anticancer TPE-PDT 88
2.2 Synthesis of ND-silica core-shell nanoparticles and associated grafting strategies 89
2.2.1 Design of ND@PMO nanoparticles 90
i. Impact of sonication time during sol-gel 90
ii. Synthesis and characterization of ND@PMO nanoparticles 91
2.2.2 Design of ND@MSN@ENE nanoparticles 96
2.3 Biological studies of functionalized ND@PMO nanoparticles 98

2.3.1 TPEF imaging of NDs and ND@ENE 98
2.3.2 Phototoxicity studies of ND@ENE 99
2.3.3 Phototoxicity studies of ND@ENE 4S 101
3. Conclusion and perspectives 102
4. Experimental section 103

CHAPTER 3: Synthesis and photophysics of new two-photon responsive octupolar fluorophores 113

1. Introduction 113
2. Results and discussion 114
2.1 Synthesis of new two-photon responsive fluorophores 114
2.2 Photophysical studies 118
2.2.1 Solvatochromic studies 118
2.2.2 Fluorescence lifetime measurements 120
3. Conclusion and perspectives 121
4. Experimental section 122

CHAPTER 4: Fluorophore-porphyrin PMO nanoparticles, FRET evaluation and antibiotic loading studies 131

1. Introduction 131
2. Results and discussion 132
2.1 Design of multifunctional fluorophore-porphyrin biodegradable PMO nanoparticles 132
2.1.1 Preparation of sol-gel precursors 132
2.1.2 Preliminary synthesis of tetrasulfide-based biodegradable PMO nanoparticles 135
2.1.3 Synthesis and characterization of fluorophore-porphyrin biodegradable PMO nanoparticles 139
2.1.4 Functionalization strategy to target cancer cells and bacteria 143
2.2 Vancomycin loading and nanoparticles biodegradability 146
2.2.1 Generalities about vancomycin 146
2.2.2 Antibiotic loading 147
2.2.3 Biodegradability simulation and release kinetics 148
2.3 Photophysical studies 150

2.3.1 Comparison of nanoparticles and silylated chromophores 150
2.3.2 FRET in ethylene-based nanoparticles 151
2.3.3 FRET in ethenylene-based nanoparticles 153
3. Conclusion and perspectives 155
4. Experimental section 156

CHAPTER 5: Biological studies of fluorophore-porphyrin PMO Nanoparticles 169

1. Introduction 169
2. Results and discussion 169
2.1 *In vitro* anticancer studies 169
2.1.1 Fluorophore-based nanoparticles as fluorescence markers 169
2.1.2 Efficiency in two-photon excitation PDT 172
2.2 *In vitro* antibacterial studies 175
2.2.1 Vancomycin-based antibiotherapy 175
i. Bactericidal character of the free drug 175
ii. Antibacterial activity from VAN-loaded NPs 176
2.2.2 Antibacterial photodynamic therapy 178
i. Efficiency in two-photon excitation PDT 178
ii. *In vitro* FRET demonstration 182
3. Conclusion and perspectives 183
4. Experimental section 185

GENERAL CONCLUSIONS AND OUTLOOKS 193

ANNEXES 196

FRENCH RESUME 217

ABSTRACT 243

ABBREVIATIONS

4S: Bis[3-(triethoxysilyl)propyl]tetrasulfide
A: Acceptor
AMR: Antimicrobial Resistance
aPDT: Antimicrobial Photodynamic Therapy
a.u.: Arbitrary unit
AUTES: 11-Aminoundecyltriethoxysilane
BET: Brunauer-Emmett-Teller
BJH: Barrett–Joyner–Halenda
BHI: Brain Heart Infusion broth
BPMO: Biodegradable Periodic Mesoporous Organosilica
CFU: Colony-Forming Unit
CTAB: Cetyltrimethylammonium bromide
D: Donor
DCM: Dichloromethane
DLC: Drug Loading Content
DLS: Dynamic Light Scattering
DMEM: Dulbecco's Modified Eagle's Medium
DMF: Dimethylformamide
DMSO: Dimethylsulfoxide
DND: Detonation Nanodiamond
DRC: Drug Release Content
E: 1,2-Bis(triethoxysilyl)ethane / ethylene-based
E. coli: *Escherichia coli*
ENE: 1,2-Bis(triethoxysilyl)ethylene / ethenylene-based
Et_3N: Triethylamine
EtOH: Absolute ethanol (otherwise 96% ethanol)
F: Tris{4-[(1E)-2-{4-[(3-hydroxypropyl)sulfonyl] phenyl}ethenyl]phenyl}amine
F2: Tris{4-[(1E)-2-(4{(1E)-2[4-(3-hydroxypropylsulfonyl) phenyl]ethenyl}phenyl]ethenyl] phenyl}amine
F-Si: Silylated F
FBS: Fetal Bovine Serum
FDA: Food and Drug Administration
FND: Fluorescent Nanodiamond
FRET: Förster Resonance Energy Transfer
FTIR: Fourier Transform Infrared
GM: Göppert-Mayer
GSH: Glutathione
HpD: Haematoporphyrin Derivative
HPHT: High Pressure and High Temperature
HRMS: High-Resolution Mass Spectrometry
ICPTES: 3-(Isocyanatopropyl)triethoxysilane
ICT: Intramolecular Charge Transfer
ISC: Intersystem Crossing
LB: Luria-Bertani
MAS: Magic Angle Spinning
MBC: Minimum Bactericidal Concentration
MCF-7: Epithelial human breast (cancer) cells
***m*-CPBA**: *m*-chloroperoxybenzoic acid
MDA-MB-231: Epithelial human breast (cancer) cells
ME: Mercaptoethanol
MHB: Mueller-Hinton Broth
MIC: Minimum Inhibitory Concentration
MON: Mesoporous Organosilica Nanoparticle
MRSA: Methicillin-resistant *S. aureus*
MSN: Mesoporous Silica Nanoparticle
MTT: 3-(4,5-Dimethylthiazol-2-yl)-2,5-diphenyl tetrazolium bromide
n.d.: Non-determined
ND: Nanodiamond
NIR: Near-infrared
NLO: Nonlinear Optics
NMR: Nuclear Magnetic Resonance spectroscopy
NP: Nanoparticle
NV: Nitrogen Vacancy
OD: Optical Density
OPE: One-Photon Excitation
P: 5,10,15,20-Tetrakis(4-aminophenyl)porphyrin
P-Si: Silylated P
PBS: Phosphate Buffer Saline
PDI: Polydispersity Index
PDT: Photodynamic Therapy
PEG: Polyethylene Glycol
PEG-Si: (6-{2-[2-(2-Methoxy-ethoxy) ethoxy]ethoxy}hexyl)triethoxysilane
PMO: Periodic Mesoporous Organosilica
PS: Photosensitizer
PTT: Photothermal Therapy
QBS: Quinine Bisulfate
ROS: Reactive Oxygen Species
S. aureus: *Staphylococcus aureus*
sqMAN: Squarate phenyl mannose derivative
STEM-EDX: Scanning Transmission Electron Microscopy-Energy-Dispersive X-ray spectroscopy
TEM: Transmission Electron Microscopy
TEOS: Tetraethyl orthosilicate
THF: Tetrahydrofuran
TPA: Two-Photon Absorption
TPAM: Triphenylamine
TPE: Two-Photon Excitation
TPEF: Two-Photon Excitation Fluorescence
UV: Ultraviolet
VAN: Vancomycin hydrochloride
WH: Wound Healing
XPS: X-ray Photoelectron Spectroscopy
ZPL: Zero-Phonon Line

PREAMBLE

Among silica nanoparticles (NPs), periodic mesoporous organosilica (PMO) are promising materials to take up some of the challenges in the biomedical field. Mesoporous organosilica can serve as multifunctional platforms for the selective delivery of all sorts of biomolecules thanks to their easily tunable porous nanostructure and biocompatible framework, they can serve. PMO can bear switchable functions to control the release of attached and encapsulated drugs, such as biodegradable moieties that are also useful for proper clearance of the NPs from the body. Furthermore, their versatile synthesis offers the possibility to combine them with biomarkers and active elements holding high-potential for theranostics such as magnetic, thermic and photosensitization properties.

Some alternatives or adjuncts to conventional therapies are currently emerging, especially photodynamic therapy (PDT) which is a good candidate for the treatment of some skin and eye conditions, as well as solid tumors. This non-invasive treatment involves light-sensitive medicine and a light source to destroy abnormal cells. Its advantage lies in its three-dimensional resolution and reduced long-term morbidity. Nonetheless, classical one-photon laser excitation cannot penetrate deeply in tissues, and the technique is therefore limited by photobleaching issues. To fully take advantage of the PDT potential, the strategy of simultaneous excitation of two equivalent photons of lower energy allows a sharper control on the irradiated area, thus, reduced collateral damage along the path of the laser. The use of two-photon photosensitizers (PSs) with large absorption cross-section in the near infra-red domain of wavelengths enables laser power reduction and much higher penetration level.

In this manuscript, the potential of new PMO-based nanomaterials is assessed in detail for targeted two-photon excitation photodynamic therapy against cancer or in combination with antibiotic delivery to fight bacterial infections. The strategies behind this, including materials synthesis processes, surface functionalization, physicochemical characterization and biological investigations, will be presented and discussed in the different sections.

CHAPTER 1: General introduction

1. Organosilica-based nanoparticles as competent vectors for controlled theranostics

Current biomedicine research presents a lot of challenges. Translational science and personalized medicine are notably spotlighted to develop the future diagnosis, detection and therapeutic solutions and *in fine* increase treatment efficiency while inducing reduced side effects to the patients.[1]

Nanomedicine has become an important branch in therapy, regrouping biology, physics, chemistry and materials science.[2-3] So-called nanomaterials with at least one dimension between 1 and 100 nm are attractive for their high surface-to-volume ratio and their ability to penetrate cells and cell organelles. For this reason, they are applicable to various diseases, including diabetes, cancer and microbial infections.[4] Nanoparticles (NPs) possess unique optical, mechanical, thermal and electrical properties and can be further modified with biomolecules or functional materials as ligands to build competent systems with increased tolerability and large scopes of action.[5]

NPs can be classified by their chemical composition (**Figure 1**).[6] Inorganic nano-objects include metals such as active gold cores (Au NPs)[7] and antibacterial silver,[8] carbon structures like carbon nanotubes[9] and versatile nanodiamonds,[10] semi-conducting quantum dots[11] and biocompatible silica-based nanoparticles.[12]

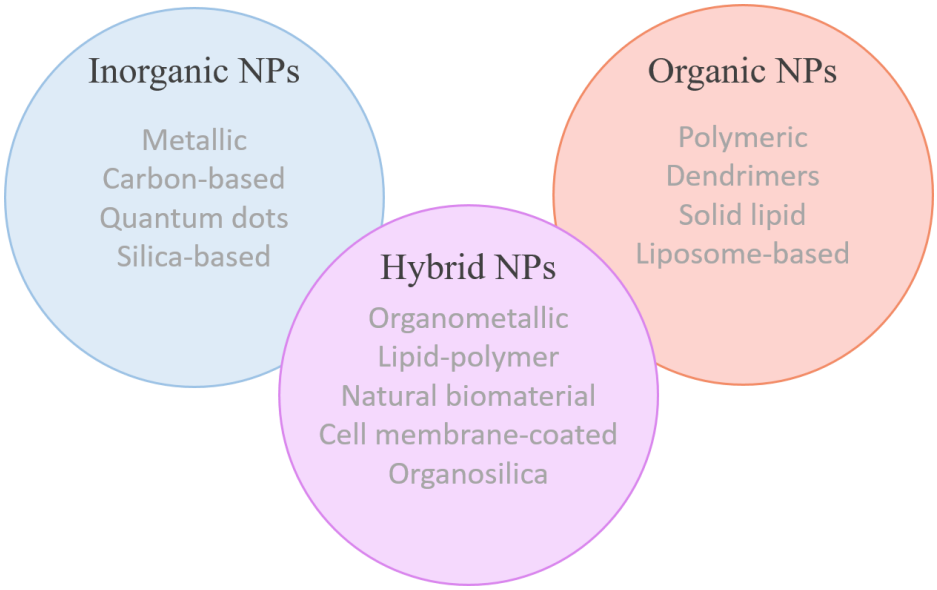

Figure 1: Main types of inorganic, organic and hybrid nanoparticles applied to nanomedicine. Adapted from Yao *et al.* (2020).[6]

Organic NPs are largely employed for the delivery of biomolecules and have taken inspiration from nature. They are mainly constituted of polymers with specific structural arrangements and lipid-based platforms.[13-14]

Among organic-inorganic hybrid nanomaterials, organosilica nanoparticles represent an innovative class combining the advantages of silica and of their intrinsic organic moieties.[15] Next, the different families of organosilica nanoparticles will be introduced, along with their synthesis conditions and their assets for cancer theranostics and the treatment of bacterial infections.

1.1 Generalities

The development of organosilica-based nanomaterials originates from silica nanoparticles history. In 1968, Fink and Stöber upgraded the synthesis of monodispersed amorphous silica spheres early described with lack of characterization in 1956 by Kolbe.[16] This process combines hydrolysis reaction of alkyl silicates and condensation of resulting silicic acid in alcoholic solution, and is nowadays known as the sol-gel Stöber route.[17] Although the first materials were micrometric, the technique was rapidly optimized to control the objects' size down to a couple of nanometers by tuning the ratio between precursors and catalyst.[18] Since this time, ordered silica-based NPs have progressed steadily, finding applications in catalysis,[19] chromatography,[20] opto-electronics[21] and notably nanomedicine.[22]

1.2 Non-porous organosilica nanoparticles

Organic-inorganic hybrid materials cumulate the advantageous properties of their moieties, but they can also display synergistic effects, leading to additional features. This is the case of the versatile organosilica family, especially at the nanoscale for which high surface area and specific surface functionalization enhance the active and passive mechanisms that are allowing NPs to enter diseased cells from blood stream.[23-24]

Among organosilica-based NPs, non-porous ones are interesting for bioapplications since they possess high organic content in addition to silica stability and biocompatibility. With up to 80 weight percent, organic functional groups with intrinsic physicochemical properties can bring superior responsiveness to biodegradation reactions and controlled drug delivery compared to inorganic silica frameworks.[25-26]

Non-porous NPs can be classified by the nature of the precursors used for their synthesis (**Figure 2**). Non-porous organosilica NPs are obtained by the combination of mono or multiple-

bridged organoalkoxysilanes, either directly mixed with a silicate precursor (generally tetraethyl orthosilicate (TEOS) or tetramethyl equivalent) or post-grafted on the surface of hybrid organic-inorganic NPs and SiO_2 NPs, yielding in low to intermediate organic content. In contrast, so-called silsesquioxane (R'-$SiO_{1.5}$) and bridged silsesquioxane ($O_{1.5}$Si-R'-$SiO_{1.5}$) hybrids can attain considerably higher organic content as they are prepared with only organosilica sources with single or multiple silica connectivity. Moreover, surface post-grafting using single organoalkoxysilane can further increase the organic-to-inorganic ratio.

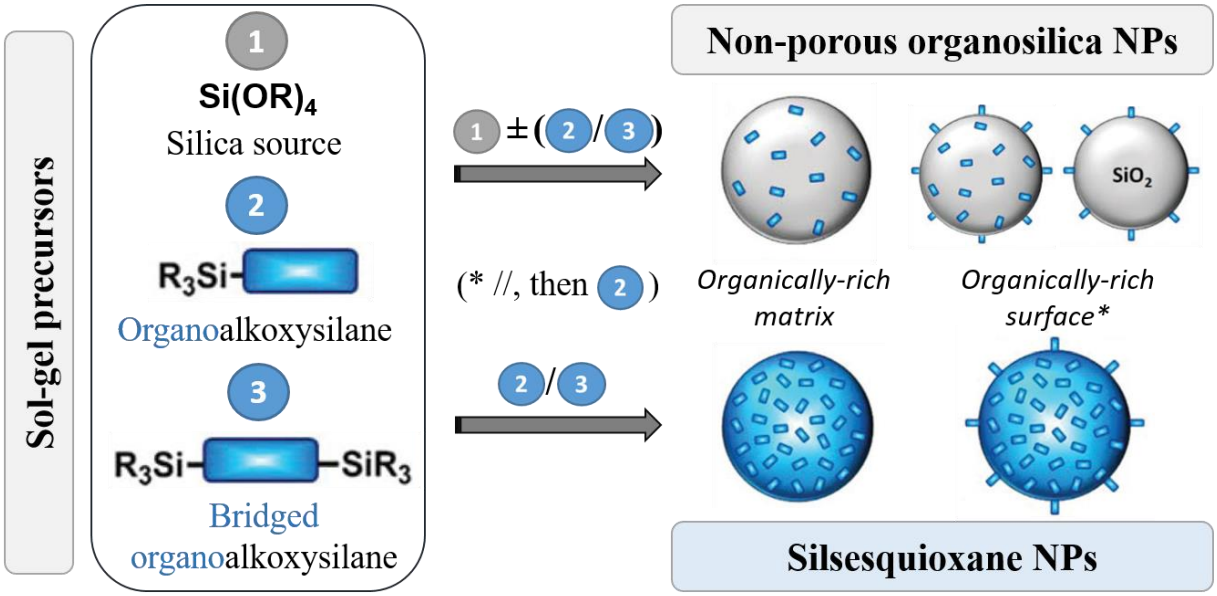

Figure 2: Synthesis conditions and structure specificities of non-porous organosilica and non-porous silsesquioxane nanoparticles. Adapted from Croissant *et al.* (2016).[27]

Aside from conventional sol-gel synthesis, non-hydrolytic sol-gel and emulsion-based syntheses were described more recently. The first one uses organic solvent as a solvent and oxygen donor in the absence of catalyst, but the morphology and size of the final particles are not easy to control.[28] The second process, introduced by Prasad and coworkers, requires a complex water-surfactant-oil micellar emulsion to form organically-modified silsesquioxane NPs, also known as "ORMOSIL", with enhanced mechanical properties.[29]

Silsesquioxane and bridged silsesquioxane NPs are not *sensu stricto* non-porous. They are mostly dense and disorganized with low specific surface area (SSA, < 100 m^2 g^{-1}) and low microporosity (< 2 nm) or mesoporosity (2 to 50 nm).[30] Tens of mono- (R'-$Si(OR)_3$), bis- ($(RO)_3$Si-R'-$Si(OR)_3$) and multi- (R'-$(Si(OR)_3)_n$)) silylated sol-gel reactants have been reported so far for the preparation of organosilica nanoparticles.[27] According to the literature, short alkyl groups (ethyl, propyl, phenyl, etc.) are mostly employed for silsesquioxane NPs. More complex organic moieties (polyaromatic molecules, porphyrins, etc.) can also be integrated, but only low

contents are tolerated to avoid particle aggregation and structure collapse. Switching to bridged silsesquioxane, higher ratio of large organosilane precursors can be afforded with still satisfying stability.

As a result, silsesquioxane NPs may be attractive for biomedical applications. Numerous studies were reported for drug delivery, optical imaging and phototherapy.[31] Fatieiev *et al.* presented hollow nanocomposites with *o*-nitrophenylene ammonium bridges with 50% organic content in weight. The good light-triggered delivery of plasmid DNA in HeLa cells *via* charge reversal was confirmed by kinetic studies of zeta potential and UV-visible absorbance before and after the photoreaction.[32] Kim and coworkers integrated fluorescein isothiocyanate (FITC) fluorophore after its conjugation with aminopropyltrimethoxysilane and subsequent sol-gel reaction with silylated FITC and mercaptopropyltrimethoxysilane precursors. Moreover, different maleimide-PEG with various molecular weight were post-grafted on silsesquioxane NPs with the objective to increase their stealthiness against macrophage uptake. FITC fluorescence allowed comparing the uptake ratio of NPs with various protein corona and PEG decoration using flow cytometry technique.[33]

1.3 Mesoporous organosilica nanoparticles

1.3.1 History of porosity

The question of how to build porosity could be addressed following the classical top-down approach, but drilling uniform nano-sized pores would be extremely difficult. With the bottom-up route, the formation of pore channels is enabled by the use of a soft template, generally using a surfactant or a structure-directing agent that can be categorized by ionic strength. Cationic quaternary ammonium surfactants are the most employed, but there are also sulfonated anionic species and non-ionic copolymers with variable hydrophilicity properties from each block (**Figure 3**). Thus, the creation of interfaces between two phases with low solubility is allowed by either electrostatic interactions for ionic systems or Van der Waals interactions for non-ionic ones, resulting in a mesophase that can be removed after reaction.[34]

In the year 1990, periodic mesoporous silica materials were in the spotlight thanks to Yanagisawa *et al.* and researchers from the Mobile Oil Company.[35-36] From liquid crystal templates, they synthesized this new family of materials possessing periodic mesoporosity with a broad range of particle and pore structures (spheres, rods, lamellar, etc.) obtained from various synthesis compositions.[37] A couple years later, in 2001, the first mesoporous silica nanoparticles (MSNs) were prepared by Cui, Mann and Ostafin's groups.[38]

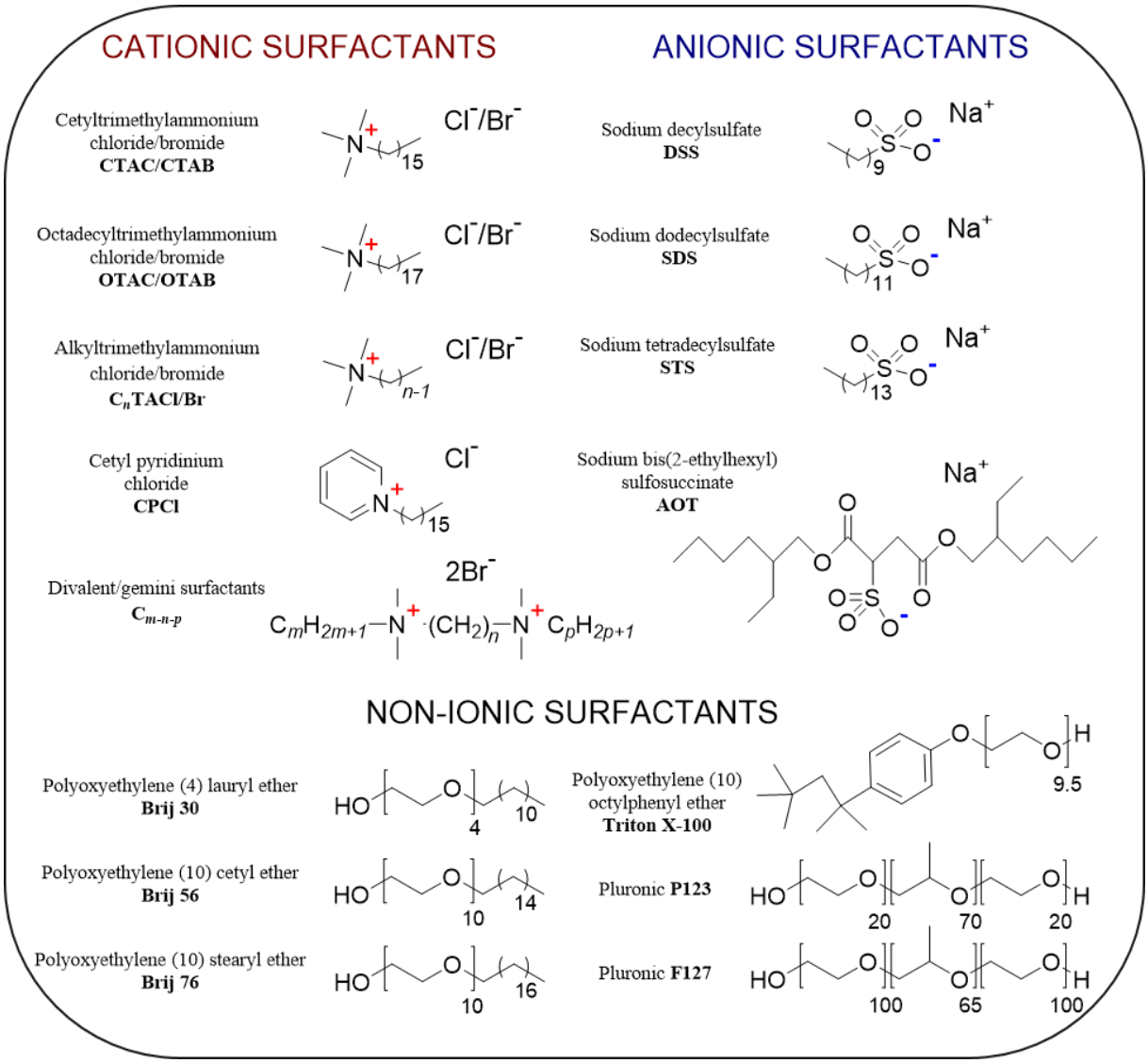

Figure 3: Non-exhaustive list of the most employed surfactants for the synthesis of mesoporous silica-based nanoparticles. Adapted from Nunes *et al.* (2015).[37]

Mesoporous organosilica nanoparticles (MONs) are MSNs derivatives prepared in a surfactant premix containing organized micelles forming a soft template for the co-condensation of a silica source and either a mono or a multiple-bridged organoalkoxysilane. Surfactant-free synthesis of MONs is also possible by using a hard porous solid template.[39] The synthesized hybrid materials contain organic moieties homogeneously distributed in the pore walls, in the pore cavities or both of them (**Figure 4**). Alternatively, periodic mesoporous organosilica (PMO) NPs with dense and uniform distribution of organic groups can also be formed by using only bridged organosilane precursors.

Compared to their MSNs inorganic counterparts, MONs bring novel properties such as hydrophobicity, biocompatibility and biodegradability for bionanotechnology applications.

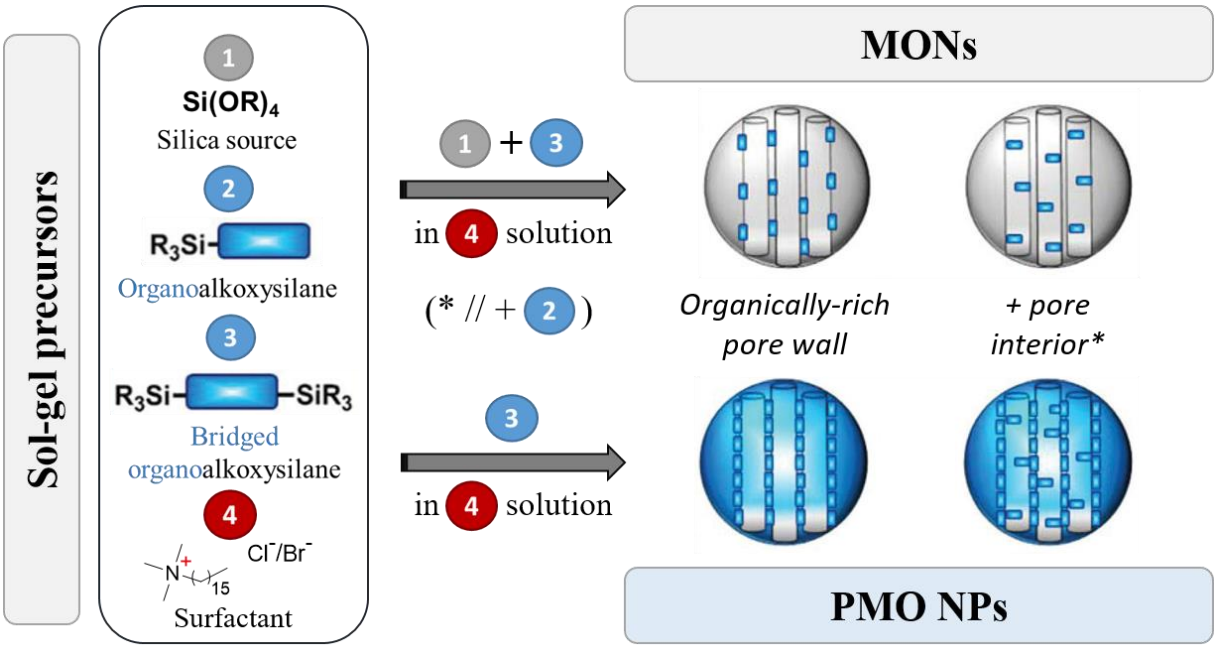

Figure 4: Synthesis conditions and structure specificities of mesoporous organosilica and periodic mesoporous organosilica nanoparticles. Similar to Figure 2, nanoparticle surface can also be further modified by direct grafting or post-grafting with an organoalkoxysilane before removal of surfactant. MONs: Mesoporous Organosilica Nanoparticles; PMO NPs: Periodic Mesoporous Organosilica nanoparticles. Adapted from Croissant *et al.* (2016).[27]

1.3.2 Morphology and structure

The design of porous organosilica NPs relies on pore and particle size control as well as framework and structure adjustment. With the rich chemistry and versatility of MONs synthesis, several morphologies have been developed so far to address specific needs in terms of physicochemical, morphological and structural properties for biomolecule delivery and for use as active therapeutic platforms (**Figure 5)**.

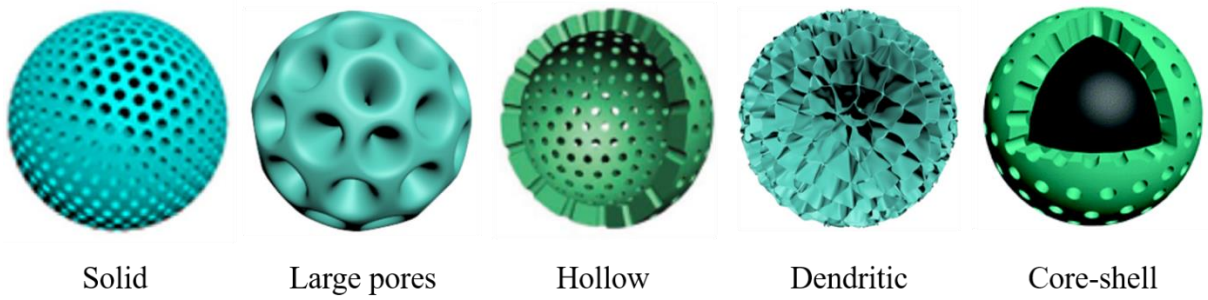

Figure 5: Mesoporous organosilica nanoparticles with various structural and morphological features for optimal drug transport and therapeutic activity. Models are adapted from different research groups.[40-43]

Large-pore MONs are obtained by increasing the catalyst amount or the ratio between organosilica and silica precursors. In fact, organoalkoxysilanes can be integrated into the micelles, thus expanding the pore size due to steric hindrance coming from the organic

spacers.[44] As an example, the studies of Shi and coworkers on large pore ultrasmall mesoporous organosilica nanosystems demonstrated this characteristic. They could manipulate MON structure by tuning triethanolamine (basic catalyst) and bis[3-(triethoxysilyl)propyl]tetrasulfide (4S) amounts. When mixing TEOS with increased 4S ratio and elevated triethanolamine amount, up to 6.2 nm pore sizes were obtained for ultrasmall MON of 30 nm.[45] Another notable work was performed by Yu's team which prepared well-dispersed periodic MONs with only benzene-bridged precursor, producing NPs with average diameters of 50 nm and large pores of 7.6 nm.[46] These MONs with regular large pores are often confused with the so-called dendritic MONs due to very similar topology, especially for particle size below 50 nm.

A dendritic arborization describes the tree-like branching out of dendrites architectures with hierarchical branch size. Du *et al.* pioneered this concept to design MSNs with a dendritic texture and gradual pore sizes.[47] To date, three types of synthesis have been described to prepare dendritic MONs.[41] The first one employs cetyltrimethylammonium or equivalent surface active agent in water without organic co-solvent. The second one relies on a biphasic system in which the reaction happens within the stratification interface between water and oil phases. Finally, the third strategy remains on a bicontinuous microemulsion phase with a mixture of surfactants.

According to a late review, research works including dendritic MONs mostly find their use in biochemistry applications, with many studies for cancer therapy and for the delivery of protein, ribonucleic acid and drug.[41] As a whole, the wide pore channels of dendritic and large-pore materials enable them suitable for the safe transport of large biomolecules with high molecular weight.

Hollow MONs are another class of special nanostructures that have recently sparked interest because of the gigantic empty space they have in their interior. Since mesoporous organosilica shells are permeable to biomolecules *in vivo*, hollow nanoparticles would theoretically be better to confine guest compounds. The preparation of hollow MONs can be divided in three approaches.[48]

The most widely used method, known as hard-core templating, involves the synthesis of hard-core templates, the coating of mesoporous organosilica shell and the removal of the initial template. Up to now, polystyrene latex beads and hematite, carbon, metallic and silica NPs were reported in studies related to hollow MONs.[49-53] With such portfolio of core templates, precise control over the void shape and size is achievable. However, most of removal procedures are environmentally unfriendly and involve acids and bases that can be toxic for biological

applications even in trace amounts. Thus, finding greener and more biocompatible etching agents would allow for better expansion of these materials.

Other syntheses of hollow MONs are performed by liquid-interface assembly where the mesoporous organosilica layer grow in liquid medium around the interfaces made of micelles, vesicles or oil/water emulsions. These conditions offer more tunability of internal and external structural composition but less control over size and shape because most interfaces are thermodynamically unstable.[48] **Figure 6** illustrates an outstanding example of hollow MONs prepared in an oil-in-water emulsion using decane as the oil phase. By this strategy, Teng and coworkers synthesized ethylene-based (E) NPs with an enormous pore volume of 3.96 cm^3 g^{-1}, an average diameter of about 560 nm and a gigantic void size of 480 nm. Mesoporosity and size were confirmed by transmission electronic microscopy (TEM) and nitrogen sorption measurements also demonstrated the large hollow morphology because of the delayed N_2 evaporation from the voids blocked by the mesopores during the desorption step.[54]

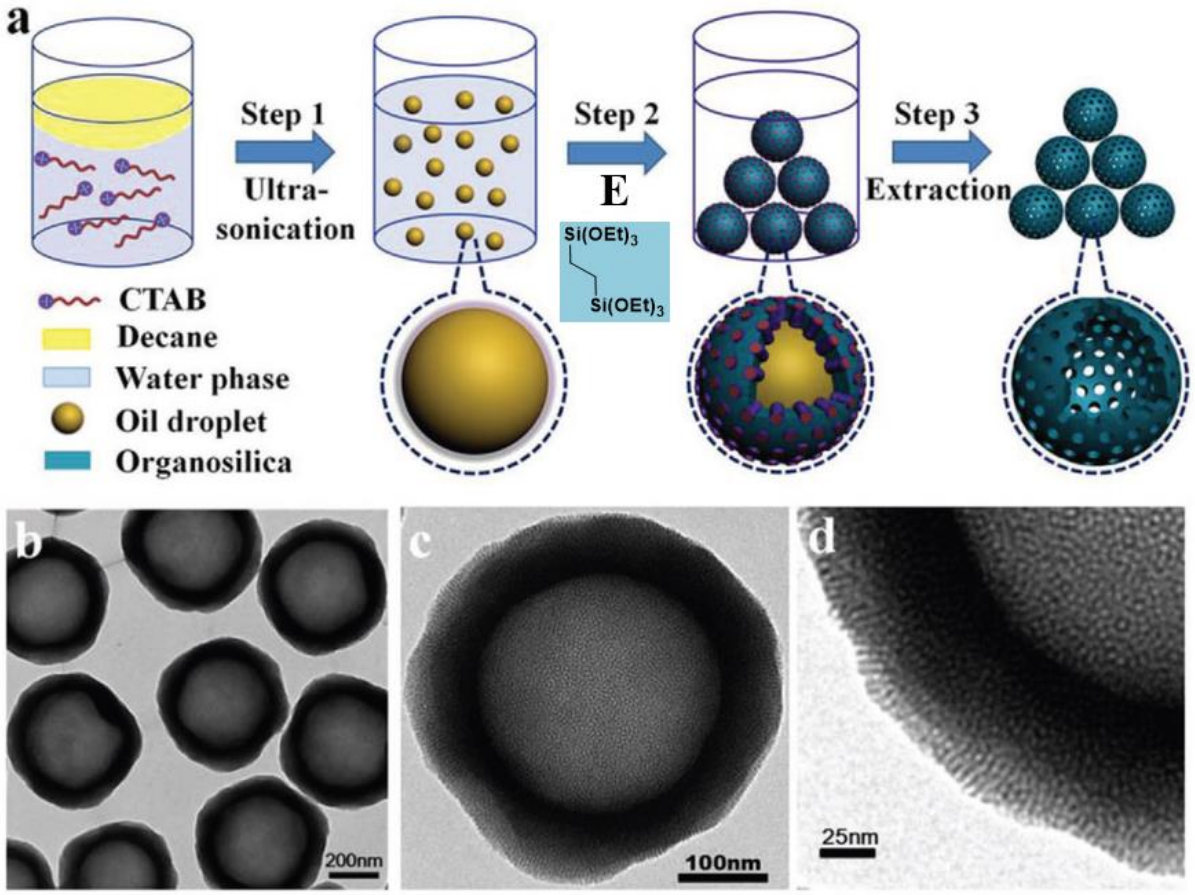

Figure 6: Synthesis of hollow MONs by liquid-interface assembly in an oil/water emulsion. (a) Schematic illustration of the process; (b-d) Transmission electronic microscopy (TEM) images of ethane-bridged hollow MONs. CTAB: Cetyltrimethylammonium bromide; E: 1,2-bis(triethoxysilyl)ethane. Adapted from Ma *et al.* (2016).[54]

Moreover, the synthesized NPs showed low cytotoxicity in human embryonic kidney 293 cells as well as low haemolysis, demonstrating the biocompatibility of such MONs for biomedical applications.

Finally, a third approach was investigated by the same group. It consists of the interfacial reassembly and transformation of early prepared MONs. By such process, the drawbacks of hard templates and unstable liquid interfaces can be avoided. Indeed, the researchers found that the inner core of MONs could be removed by hydrothermal treatment because the internal cross-linking degree is lower than the external one, which is thus more stable after a certain time of sol-gel condensation reaction.[43]

In parallel to hollow MONs, yolk-shell NPs (also known as nanorattles) have been designed to form various core-shell MONs. Such systems are resumed as NP core@void@MON. Several types of nanometric cores have been encapsulated so far, including upconversion nanoparticles made of fluorides, metals, metal oxides, SiO_2 and polystyrene.[55-57] Other studies presented core-shell MONs without void space. For instance, Knezevic *et al.* prepared ethane-based (E) PMO NPs with multiple magnetite cores in their inner structure and uniform pore morphology.[58]

Altogether, the large exploration of MONs rich chemistry in the last two decades prove to what extent these biocompatible materials are capable to serve as passive or active nanoplatforms for the safe transport and controlled delivery of all sorts of biomolecules and drugs. Combinations of the presented morphologies and structures are also increasingly considered to build advanced materials with multiple features for application in nanomedicine. In particular, PMO NPs with unique properties hold great promises for theranostic applications.

1.3.3 Periodic mesoporous organosilica nanoparticles

The first PMO syntheses were reported in 1999 independently by Ozin, Stein and Inagaki groups.[59-61] Ozin and Stein described the synthesis of bulk amorphous ethylene-based PMO (E PMO) and ethenylene-based (ENE) PMO materials from the corresponding symmetrical bis-organoalkoxysilane precursor reacting in the presence of cetyltrimethylammonium bromide (CTAB) surfactant. Inagaki and coworkers chose octadecyltrimethylammonium to prepare two or three-dimensional structures with small hexagonal mesopores from 2.7 to 3.1 nm. Later in 2002, they obtained larger pore arrays with phenylene-bridged PMO materials that interestingly displayed crystal-like pore walls with

regular benzene-based rows, distant of 0.76 nm from silicate moieties along the channel direction (**Figure 7**).[62]

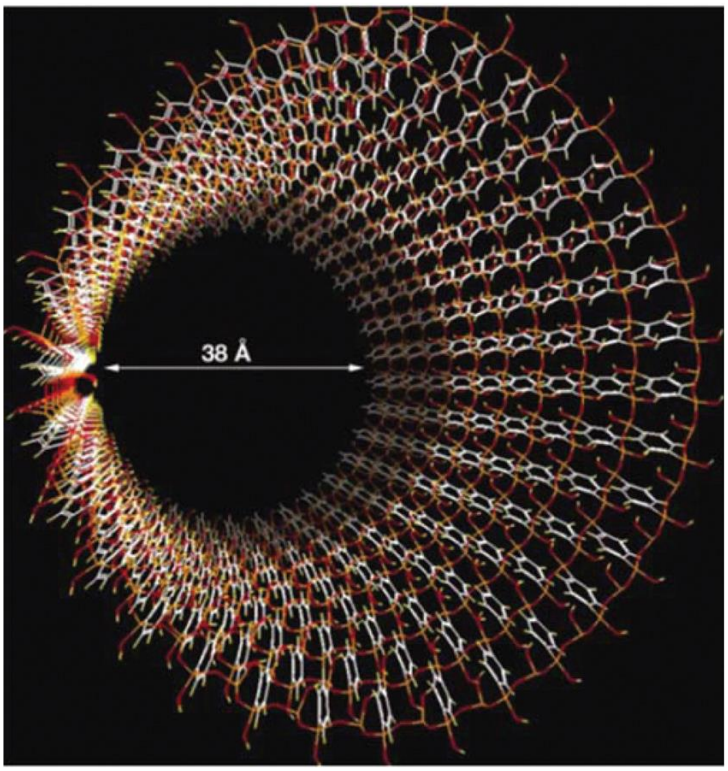

Figure 7: Pore surface modelization of phenylene-bridged PMO structure. The distance between hydrophobic benzene layers and hydrophilic silicates was estimated to be 7.6 Å. 1 nm = 10 Å. Reproduced from Inagaki *et al.* (2002).[62]

In short, the supramolecular assembly of PMO precursors can result either in amorphous or crystal-like walls, depending on the catalyst and the nature of the organic moieties that are integrated into the framework. Well-organized PMO NPs structures with crystalline lattices are mostly obtained under basic conditions and from bridged organoalkoxysilane source with a rigid and planar organic bridge (e.g. ethylene, benzene and phenylbenzene).[37]

Thus, PMO nanomaterials fundamentally possess unique features with respect to other inorganic MSNs and hybrid MONs. First, they share the numerous properties and assets of silica-based NPs:

- Tunable pore morphology, structure and size for drug delivery and for better accessibility and interaction with active functions incorporated in the three-dimensional organosilica framework such as magneto-, thermo- and photo-responsive moieties;
- Biocompatibility, largely demonstrated in the literature, but still important to check for any biological study;
- Versatile surface engineering due to the extended knowledge of scientists in the silica chemistry concerning material post-treatment and synthesis of almost any organoalkoxysilane compounds that can be employed in the preparation of PMO NPs.

Second, the organic bridges from the precursors provide infinite possibilities of applications. The biological and physicochemical features are emphasized as the organic content in PMO NPs can be maximized.[63] In addition, hybrid PMO NPs can display synergistic features, thus enabling these nanomaterials even greater candidate for bioapplications. As an example, aggregation-induced emission and quenching behaviors of chromophores embedded in the framework can be finely controlled to build highly-performant bioimaging probes.[64]

Third, the grafting of organosilica NPs *via* the reaction with free surface silanol groups (Si-OH) provides a further possibility of tailoring their properties in respect to the biological environment associated with the application that is targeted (**Figure 8**).

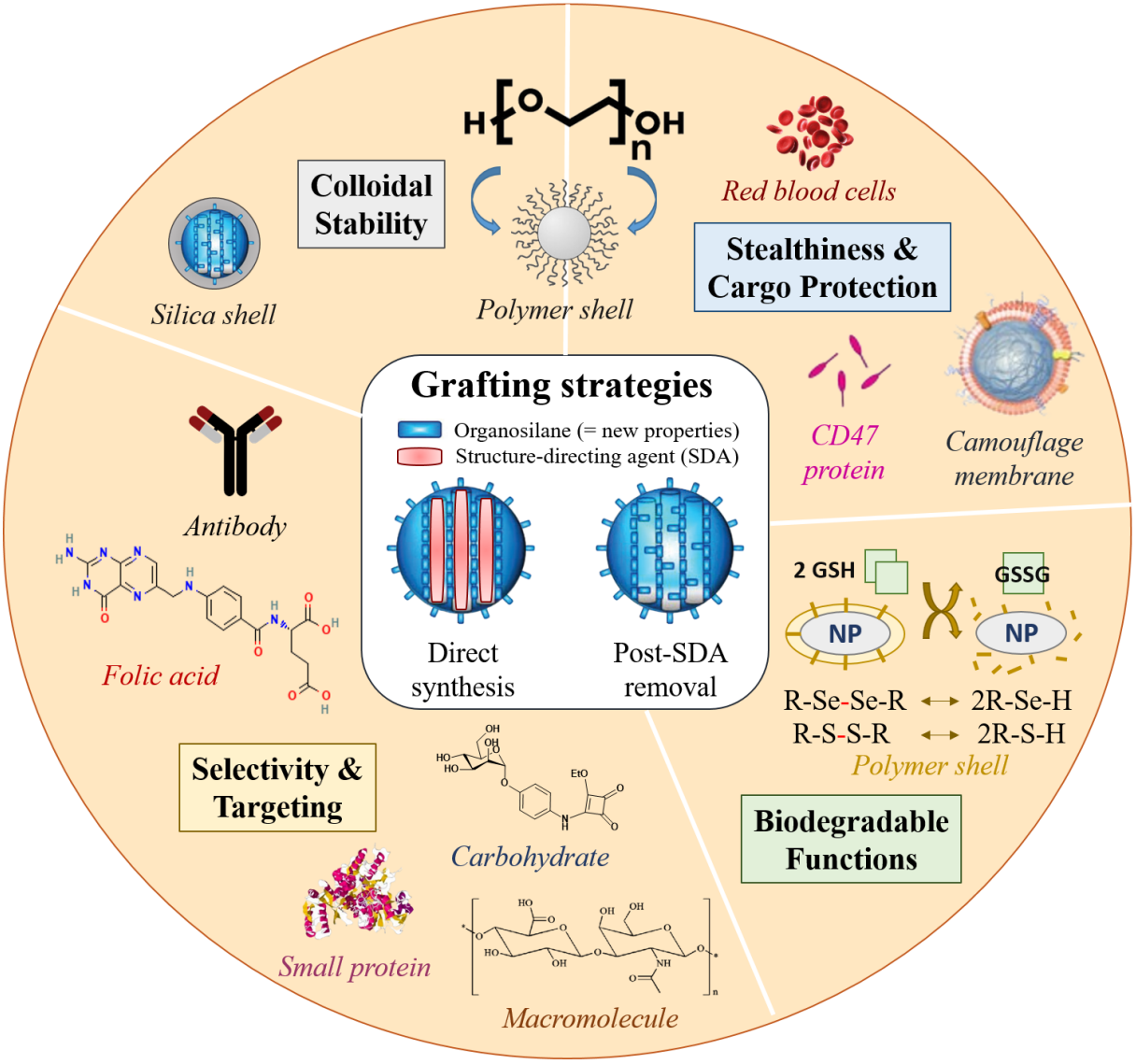

Figure 8: Surface grafting of various biomolecules and materials, associated strategies and advantages for bioapplications. GSH/GSSG: Glutathione redox couple; SDA: Structure-directing agent.

New functionalities can be grafted by co-condensation during the sol-gel reaction. Also known as direct synthesis, this process is performed with structure-directing agent still present in the pores, thus only the external surface is modified with organosilane grafts. The other strategy consists in post-grafting after removal of the structure-directing agent by washing steps. This time, in addition to the external surface, the pore walls and the pore interior are also functionalized.

The immune system is one important functional limit of nanomaterials. Thus, stealthiness can enhance *in vivo* stability and retention of NPs, thus providing protection of the cargo and of the NPs themselves.[65]

Cellular surface receptor CD47 protein is known to activate the transduction of the "don't-eat-me" signal to avoid phagocytosis and other immune responses. Surface covering with CD47 demonstrated good potency to mimic its biochemical behavior and make the NPs bioinert.[66] The design of bio-inspired membranes extracted from red blood cells, platelet, stem cells, dendritic cells and even cancer cells and bacteria have received a lot of attention due to their natural capability of camouflage from the immune system, with extensive applicability, in particular for immunotherapy and vaccines.[67-68] Another widespread practice is the direct grafting of polyethylene glycol (PEG) chains to prevent the adsorption of complement proteins.[69] Instead of having these proteins forming a corona around NPs, it was reported that, in the presence of PEG, clusterin proteins are attached to NPs surface and can enhance NPs stability in physiological media.[70]

Altogether, PEG contribution to stealthiness and colloidal stability is a main asset for organosilica NPs. Alternatively, a coverage with silica shell or other polymeric shells such as polyglycerol and poly(methyl methacrylate) increases the stability of the colloidal suspensions.[71]

Multifunctional nanomaterials are also covered with targeting functions to increase NPs biodistribution and selectivity towards diseased cells. Indeed, antibodies are specifically used for immunotherapy against cancer cells, and many proteins are over-expressed by cancer cells and microbes in comparison with healthy cells.[72] Famous examples of grafted ligands for targeted therapy are folic acid and hyaluronic acid fixing respectively on the folate receptors and CD44 receptors of many tumor cells, but also transferrin for brain cancer and carbohydrates interaction with bacteria and tumor lectins.[73]

Finally, PMO NPs biodegradability and fate *in vivo* are of major importance; first, to properly control drug and biomolecule delivery depending on the needs (burst release or prolonged action), and second to avoid NPs accumulation in the organs, which is a big challenge to address to properly reveal their efficacy and impact on health.[74]

Nanoparticles can liberate encapsulated drugs and reduce their size for proper clearance by means of several internal and external stimuli (**Figure 9**). First, as shown in **Figure 8**, oxydo-reduction reaction between the reduced form of glutathione (GSH) and diselenide or disulfide groups produces bond cleavage.[75] Glutathione is a natural tripeptide intervening, *inter alia*, in hydrogen transport. It was demonstrated that GSH concentration is compounded in the close environment of several bacteria and in the cytosol of cancer cells, compared to the extracellular media, making biodegradable PMO (BPMO) NPs containing sulfide or selenide bonds very promising materials for the previously mentioned applications.[76]

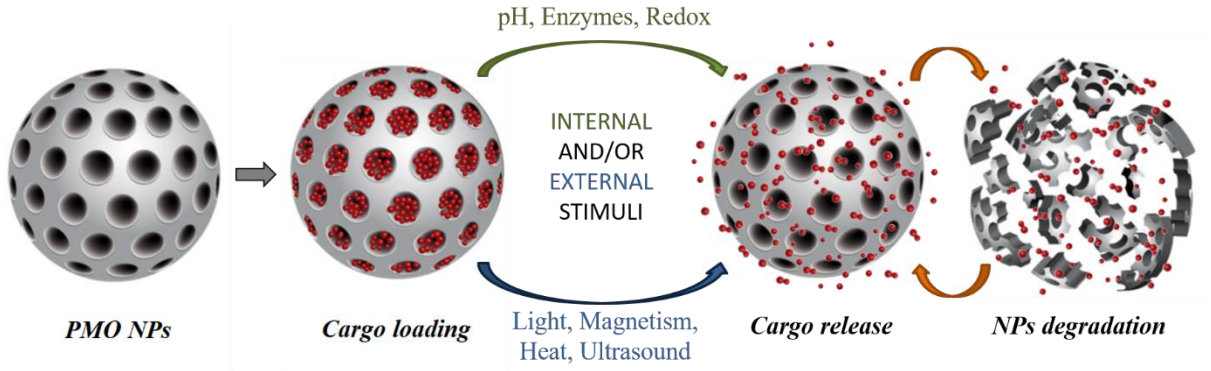

Figure 9: Versatile PMO nanoplatforms for the controlled delivery of drugs and biomolecules. Cargo release and NPs degradation can be individually or simultaneously triggered by biological internal stimuli and non-invasive external stimuli depending on PMO functionalities sensitiveness. Adapted from Poscher *et al.* (2020).[77]

Multifunctional PMO NPs can also possess grafted or framework-integrated moieties that are responsive and sensitive to change in pH and interactions with specific enzymes.

Several studies have also been dedicated to the design of PMO NPs which are sensitive to external stimuli (**Figure 9**). In particular, this strategy allows performing combined therapy. On one hand, a controlled drug delivery is possible under the influence of an external magnetic field or an irradiation, with tracking using magnetic or luminescent probes. On the other hand, the therapy associated with this stimuli (e.g. magnetic hyperthermia, phototherapies, sonodynamic therapy) can enhance the killing activity using sensitive moieties (e.g. the NPs themselves or the grafted compounds).

In the next section, some relevant examples of PMO nanoparticles applied in theranostics are presented, with a special focus on cancer therapy and against bacterial infections.

1.4 Biological applications of PMO-based nanomaterials

1.4.1 Anticancer therapy

According to the World Health Organization, cancer is a leading cause of premature death worldwide, representing one over six deaths in 2020. Recent trends are even suggesting that cancer may surpass cardiovascular diseases as the first cause of premature death in most developing and developed countries.[78]

There is a constant need to develop more robust and adapted therapeutic systems for both rare metastatic tumors and more common cancers. The key issues could be seen from different point of views. On one hand, there are economic issues with the need to develop more affordable treatments, and on the other hand, investing money in research to find solutions where there is none yet.

Recent studies based on disulfide or tetrasulfide-bridged BPMO nanoplatforms showed great efficiency to deliver genes, chemotherapeutic agents, and also boron within the context of cancer therapy.[79-83] For this purpose, biodegradation and drug release assays were performed to confirm the controlled GSH-responsiveness of the nanosystems in tumor environment.

Other release modes were tested with MONs. Rao and coworkers prepared biodegradable MONs composed of bis(cysteine-modified)disulfide organic moieties along with inorganic siloxanes from TEOS.[84] The loading and release properties of doxorubicin were studied. Up to 50.6% loading was obtained, and the release was pH-dependent, with higher efficiency for acidic pH. All in all, knowing the high intracellular GSH concentration and acidity in tumor cells, these systems appear to be promising drug delivery candidates.

A study conducted by Shao *et al.* explored the potential synergy of chemotherapy and photothermal therapy (PTT). Briefly, PMO NPs, loaded or not with doxorubicin anticancer drug (16% loading), were modified with photothermal responsive MoS_2 nanosheets wrapped around them. Besides that, post-functionalization with PEG enhanced the colloidal stability of the materials. Without doxorubicin, PTT study at 808 nm demonstrated limited killing efficiency of cancer cells *in vitro*, whereas an excellent synergy was observed by fluorescence imaging during a live/dead staining assay (**Figure 10**). Indeed, only 13% cells were remaining after

irradiation, while individual chemotherapy or PTT respectively reduced the viability to 59 and 74%. Similar results were obtained on MCF-7 breast cancer cells.

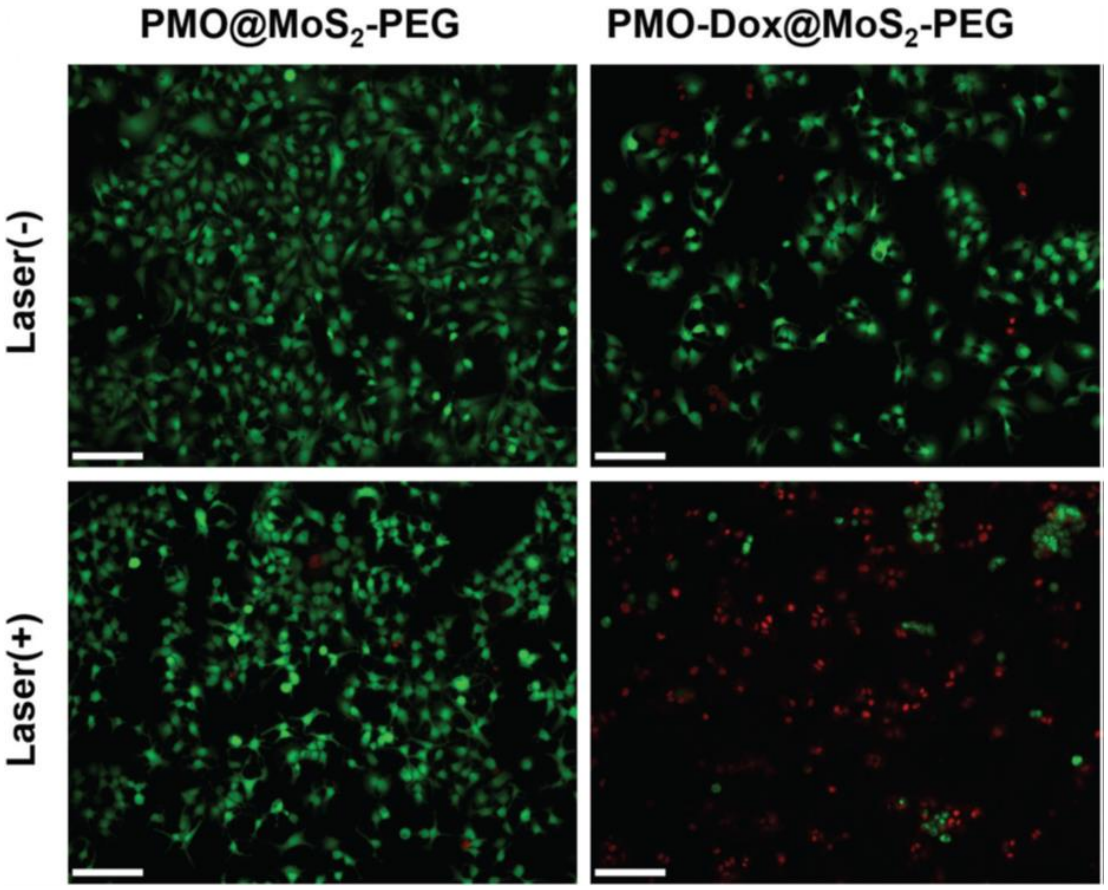

Figure 10: Fluorescence imaging of human liver Huh-7 cancer cells after live/dead staining assays. Cells were incubated with PMO@MoS_2-PEG or PMO-doxorubicin@MOS_2-PEG NPs and irradiated for 5 min at 808 nm (2 W cm^{-2}) or not. Doxorubicin (Dox) concentration loaded in PMO NPs (1 mg mL^{-1}) was 160 µg mL^{-1}. Cells were stained with calcein (green, living cells) and propidium iodide (red, dead cells) 24 h after incubation with NPs; scale bar: 100 µm. Adapted from Shao *et al.* (2016).[85]

In another work, Liu *et al.* prepared Fe_3O_4@PMO core-shell NPs coated with a cysteine-based dye and loaded with doxorubicin for the treatment of hepatocellular carcinoma.[86] High drug loading and release efficiencies were observed in a pH-responsive manner in MDA-MB-231 breast cancer cells. Magnetite NP cores allowed performing magnetic resonance imaging studies before and after treatment to track the evolution of liver tumors sizes in rabbit. In combination with Lipiodol® embolic agent, the transcatheter arterial chemoembolization technique induced significant tumor volume reduction, whereas free doxorubicin, Lipiodol® alone, and PMO NPs with only of the two elements showed limited efficiency.

In conclusion, mesoporous organosilica-based nanosystems appear to be efficient and biocompatible platforms for innovative drug delivery strategies in cancer therapy. Clinical translation is now necessary and could be valuable.

1.4.2 Antibacterial treatments

i. Context of antimicrobial resistance

There is an urgent need for developing more advanced therapeutic strategies regarding antimicrobial resistance (AMR). Indeed, AMR results from bacteria, viruses, fungi and parasites evolution over time making current medicines obsolete. Based on scenarios with high risk levels, if no satisfying efforts are made in the coming years, a continued rise in resistance by 2050 would led to 10 million deaths per year imputable to AMR (**Figure 11**).[87] If this happens, antimicrobial resistant infections would become the most non-natural common cause of death.

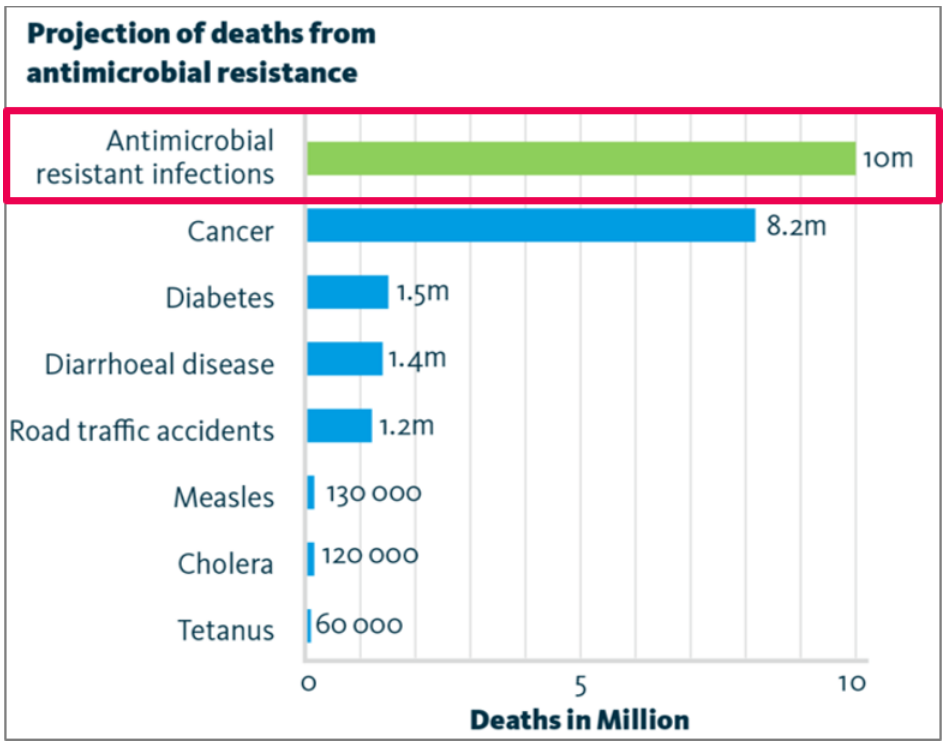

Figure 11: Death prospects attributable to AMR compared to other major causes of death for year 2050. Adapted from O'Neill (2014).[87]

Recent years have witnessed an unprecedented growth both in terms of incidences and intensity of ineffectiveness of commonly available antibiotics against microbial infections. For example, 1.27 million deaths were attributable to bacterial AMR for year 2019, with 73% of them attributable to six bacterial strains, *Escherichia coli* and *Staphylococcus aureus* pathogens being on the top of that list.[88] AMR is increasingly spreading with resistant bacteria giving their advantage to non-resistant bacteria due to the overuse and misuse of antibiotics (**Figure 12**).[89]

New therapeutic references with low potential of developing resistance and effective killing of pathogenic microbes are now required. Some promising solutions are emerging, in particular combination therapies including sets of drugs instead of an individual type of drug.[90]

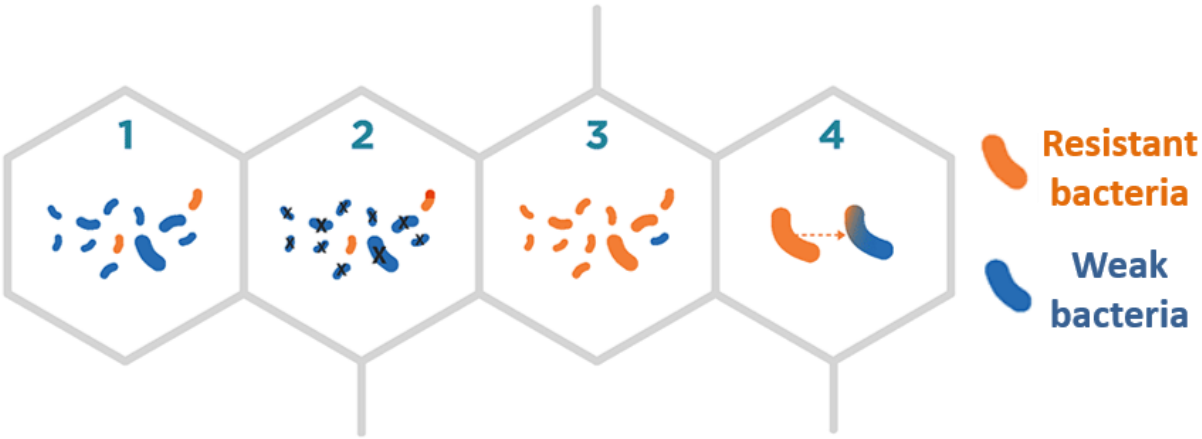

Figure 12: Cyclic process underlying antibacterial resistance development and spreading. 1: Coexistence of healthy and pathogenic bacteria; 2: Antibiotic use; 3: Growth and spreading of resistant bacteria; 4: Resistance transfer to other bacteria. Adapted from Centers for Disease Control and Prevention (2021).[89]

A good example of organosilica NPs employment for tackling antibacterial resistance was reported by Hasanzadeh and coworkers.[91] Briefly, the NPs were prepared by co-condensation of TEOS and symmetrical bis[3-(triethoxysilyl)propyl]urea precursors, and silver NPs were grafted on the surface by biosynthesis using euphorbia leaf polyphenol. Toxicity studies on mouse embryonic fibroblast NIH-3T3 cells showed good biocompatibility up to a concentration of 100 µg mL^{-1} in Ag-PMO NPs (1.27% silver atoms). Interestingly, antibacterial assays presented similar minimum bactericidal concentrations (MBCs) as gentamycin antibiotic positive control against planktonic gram-positive *Staphylococcus aureus* (*S. aureus*) and gram-negative *Pseudonomas aeruginosa* (*P. aeruginosa*) strains. MBC values for the NPs were 4.8 and 39 µg mL^{-1} against *S. aureus* and *P. aeruginosa*, while gentamycin MBCs were 8 and 16 µg mL^{-1}. The group highlighted the potential of these materials for treating nosocomial infections that are increasingly developed in hospital environments.[91]

Nevertheless, the future therapeutic systems should be even more efficient than is the previously cited work. According to the National Institutes of Health, 65% of microbial infections and 80% of chronic infections are associated with biofilm formation.[92] Biofilms are architectural assemblies of bacteria growing within a matrix of extracellular polymeric substance, and they are known to be incredibly more resistant that planktonic bacteria colonies (**Figure 13).** As a consequence, early treatment of biofilms during the initial step of development is highly recommended to encompass their strong antibacterial resistance.

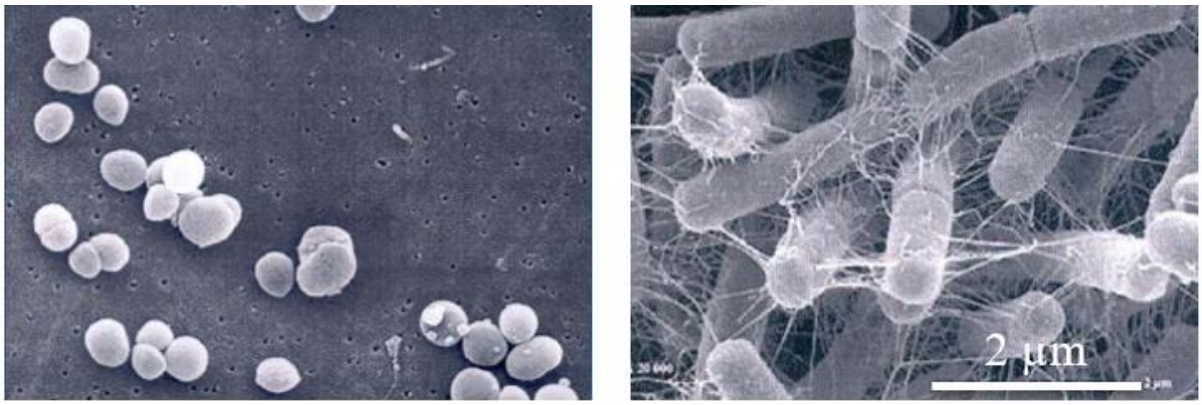

Figure 13: Scanning electronic microscopy representing bacteria phenotypes, either planktonic or as a biofilm within an extracellular polymeric matrix self-produced by bacteria. Adapted from Delorme (2012).[93]

ii. Bacterial infections

In the post-antibiotic era, nanoparticle-based systems hold significant advantages to build advanced treatments against bacterial infections. Multifunctional platforms such as PMO-based nanomaterials can guarantee better drug selectivity to the pathogen and enable drug-free approaches to efficiently eradicate microbes and ensure the long-term integrity of the body.[94]

Each species of bacteria has the ability to infect certain organs and not others. Bacterial infections-related diseases are caused by different responses from the body. Indeed, the organism can destroy body cells or initiate the immune response to the infection. This latter can result in systemic inflammatory response syndrome, and patients can develop sepsis. More serious side effects, including organ failure and death, are also possible.[95]

In this context, modulating cell proliferation and cell enrichment before or during infection is a serious research problem. Kehr prepared alginate hydrogel scaffolds containing PMO NPs grafted with either penicillamine or mannose pentaacetate to simultaneously control cell enrichment and drug delivery. For each bioactive molecule, the two enantiomeric forms were compared regarding the affinity of 3T3 fibroblasts and human cervix epithelial HeLa cells with the hydrogel surface. Results with a 1:1 heterogeneous mixture of HeLa and 3T3 cells showed 90% enrichment in HeLa cells over 3T3 cells when using a dextrorotatory-penicillamine-containing composite, whereas only 65% enrichment was observed for the levorotatory isomer form. These experiments highlighted that a cell mixture can be manipulated, especially with the stereochemistry of the materials. Furthermore, fluorescence imaging illustrated the capability of the PMO NPs to release dyes from their pores to the hydrogel scaffold.[96] In this way, such

nanomaterials could be used to specifically isolate cells from blood and tissues while delivering antibacterial compounds.

In another study, Kehr and coworkers further assessed of similar hydrogels as bioimplants. Biomaterial-related infections are a major cause of biomaterial implant failure, and potentially of severe side effects.[97] Finding the right balance between tissue integration of the implant and bacterial colonization is not an easy task. The group developed PMO NPs loaded with antibacterial tetracycline and poly-D-lysine, this latter being also cell-adhesive. On one hand, proliferation assays showed enhanced fibroblasts amounts (involved in tissue adhesion with the implant) after different incubation times in the presence of drug-loaded PMO compared to the free drugs (**Figure 14a**). On the other band, antibacterial activity was observed on gram-negative *E. coli* (planktonic) using tetracycline-loaded PMO NPs in alginate-laponite-based hydrogel. A synergistic efficiency of tetracycline and poly-D-lysine-containing nanocomposites was even observed on early stage biofilm of gram-negative *P. aeruginosa*, compared to the hydrogel alone and each individual drug (**Figure 14b**).

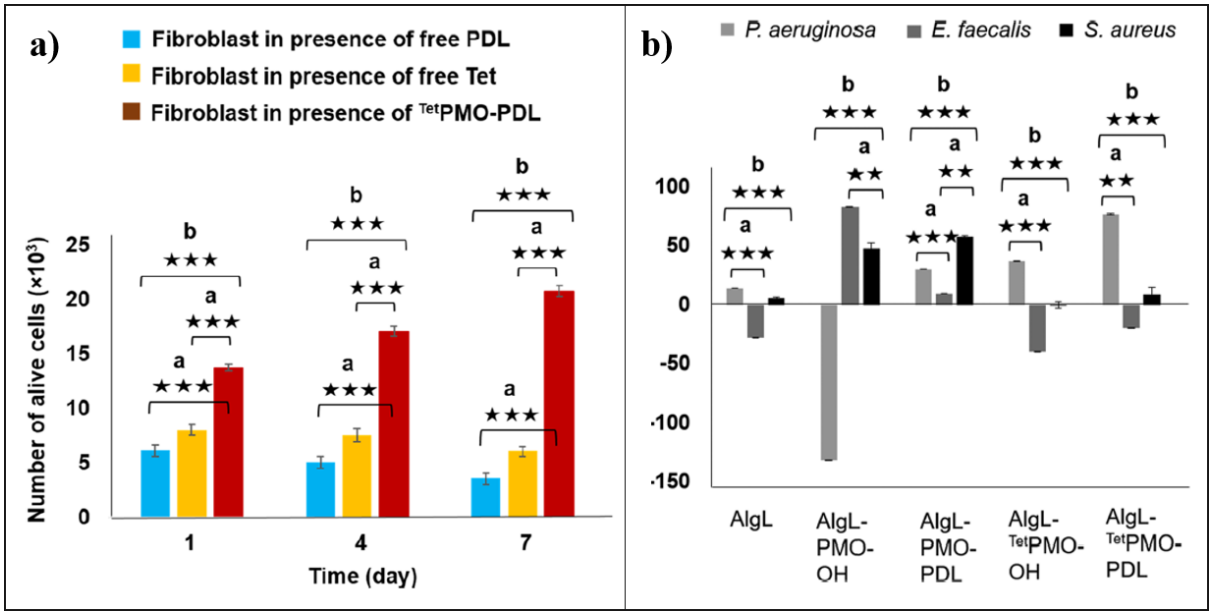

Figure 14: Cell enrichment and antibiofilm assays using tetracycline and poly-D-lysine-loaded PMO nanoparticles. (a) Fibroblast amounts in the presence of free bioactive drugs and drug-loaded PMO NPs during 1 day, 4 days and 7 days incubation time; (b) Percentage reduction of different bacterial biofilms incubated with hydrogels. Statistical methods were employed (**: $p < 0.01$; ***: $p < 0.001$; a = significant difference between two groups; b = significant difference between all groups). AlgL: Alginate-laponite-based hydrogel scaffold obtained by three-dimensional printing; PDL: Biopolymer poly-D-lysine; Tet: Tetracycline. Adapted from Motealleh *et al.* (2021).[97]

The higher antibiofilm activities for gram-positive strains in the case of alginate-PMO and alginate-PMO-poly-D-lysine composites were attributed to cations release from the hydrogel and the lysine, interfering with tetracycline.[98]

Among all pathologies presenting a particular risk of infection, research for non-healing wounds is receiving a lot of attention, in particular with the ever-growing bad health practices in developed countries.

iii. Focus on non-healing wounds

Skin is an important natural barrier against dehydration and external environment. When it is damaged, it results in protection loss and micro-organism colonies development, leading to severe wound infections and co-morbid conditions. The classic wound healing (WH) process is a succession of biochemical reactions and overlapping stages such as haemostasis, inflammation, proliferation and tissue remodelling or resolution.[99] When this mechanism is not properly sequenced (**Figure 15**), wounds are exhibiting impaired healing.[100] These non-healing wounds, acute or chronic, affect 3-6 million people in the US alone, mainly due to ulcers that are associated with ischemia, diabetes mellitus or venous stasis disease.[101]

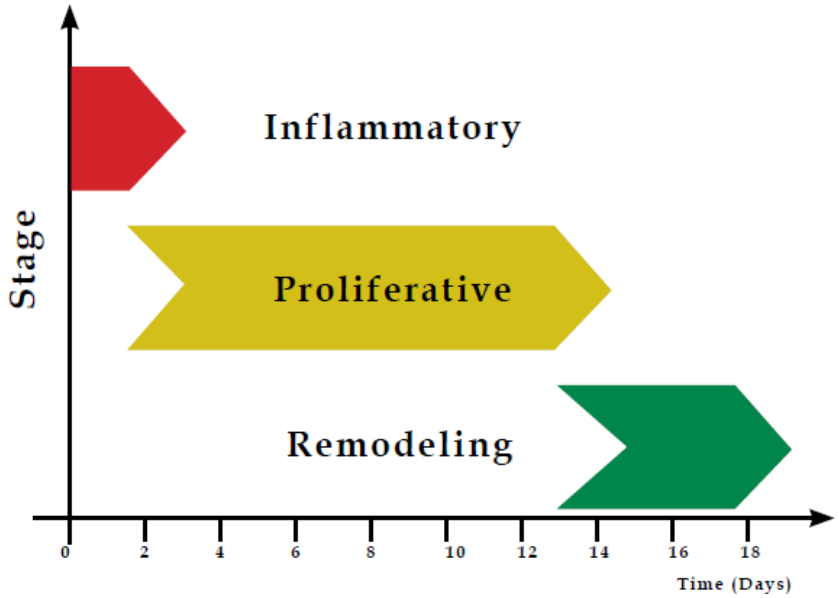

Figure 15: Simplified illustration of tissue repairment steps. The reality is that the stages are not taking place successively but to a certain extent conjointly, causing impaired wound healing (WH). Reproduced from de Oliveira Gonzalez *et al.* (2016).[100]

As a consequence of rising prevalence of lifetime diseases such as diabetes, further wound care expenditures would probably be needed in the short run. For example, the population affected by diabetes mellitus was estimated to be 37.3 million in the US[102] and 59.3 million in Europe, and the number of diabetics is expected to reach 66 million in Europe in 2030.[103] Moreover, chronic diabetic wounds - that are defined as wounds that are opened for more than a month[104] - and decubiti are important long-term sequalae of both type I diabetes mellitus, and they often lead to traumatic side effects and complications.[105] This underlines the importance of developing more advanced strategies for non-healing chronic wounds.

In this context, the desired long-term application of our project is to focus on the development of innovative antibacterial topical treatment of non-healing wounds. An early bacterial eradication at the injured site would allow better control of the infection and enhanced tissue reconstruction by the immune system.

Despite the large exploration of organosilica-based nanomaterials for cancer therapy, their application to WH has been poorly described. Nonetheless, two noteworthy studies were recently reported.

First, Wang *et al.* described the synthesis of ethane-based hollow MONs prepared by etching of the MSN core of MSN@MONs.[106] Thermosensitive phase-change materials made of a proton-responsive spirolactone with strong absorption in the near-infrared (NIR) were loaded into the void space. The hybrid nanomaterials, which showed high photothermal conversion, were tested against methicillin-resistant *S. aureus* (MRSA) strain. They displayed high antibacterial activity with a bacteria eradication of 99.99% under 808 nm NIR laser irradiation at a power density of 1.5 W cm^{-2}, compared to non-irradiated systems that were not toxic. As a positive control, indocyanine green photothermal agent (not embedded in the NPs) caused 99.9999% reduction in viability at the same concentration as the photothermal phase-change material in the NPs. Moreover, *in vivo* WH assays were performed on mice (**Figure 16a**).

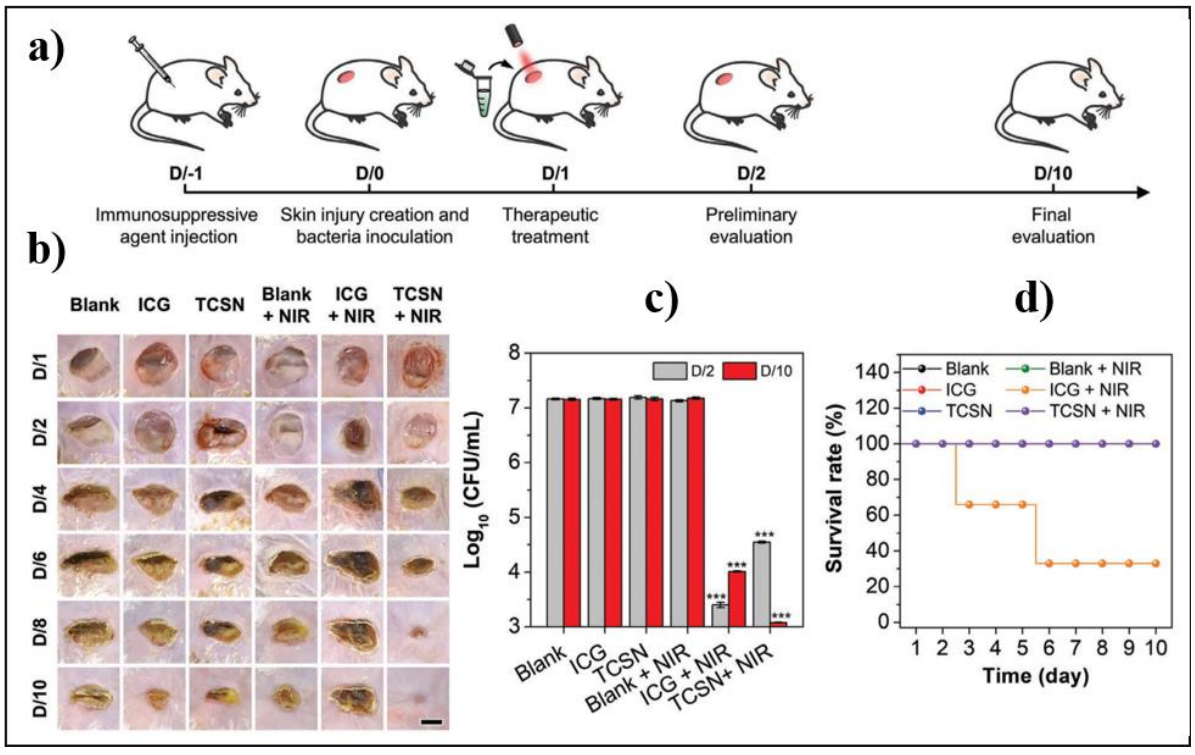

Figure 16: *In vivo* antibacterial studies without irradiation and with photothermal treatment using NIR irradiation. (a) Experimental timeline; (b) Photographs of MRSA-infected wounds after different treatments; (c) Bacterial viability expressed in log_{10} CFU mL^{-1} (CFU: Colony-Forming Unit; ***: p <

0.001); (d) Mice survival as a function of time after wound creation. ICG: Indocyanine Green; TCSN: Thermosensitive MONs. Adapted from Wang *et al.* (2022).[106]

Briefly, an immunosuppressive agent was injected in the animals, followed by skin injury creation and inoculation with the *S. aureus* strain. PTT efficiency in the presence of MONs was confirmed by the 100% survival rate observed during the final evaluation nine days later (**Figure 16d**). Moreover, wound areas were almost fully closed without infection. In contrast, PTT on indocyanine-treated wounds showed some side-effect with eschar formation caused by burn injury (**Figure 16b and c**).[106]

Second, Zeng and coworkers presented the synthesis and application of GSH-responsive BPMO NPs prepared by condensation of E and 4S organoalkoxysilane precursors (**Figure 17a and b**).[107] The NPs were modified with a guanidinated-fluorinated α-polylysine and demonstrated high biocompatibility up to 800 µg mL^{-1} and high potential as gene carriers. Indeed, efficient transfection in the targeted DNA model (e.g. green fluorescent protein plasmid) was shown by fluorescence imaging in human embryonic kidney 293T and human cervix epithelial HeLa cells in which higher fluorescence, thus protein expression, was observed.

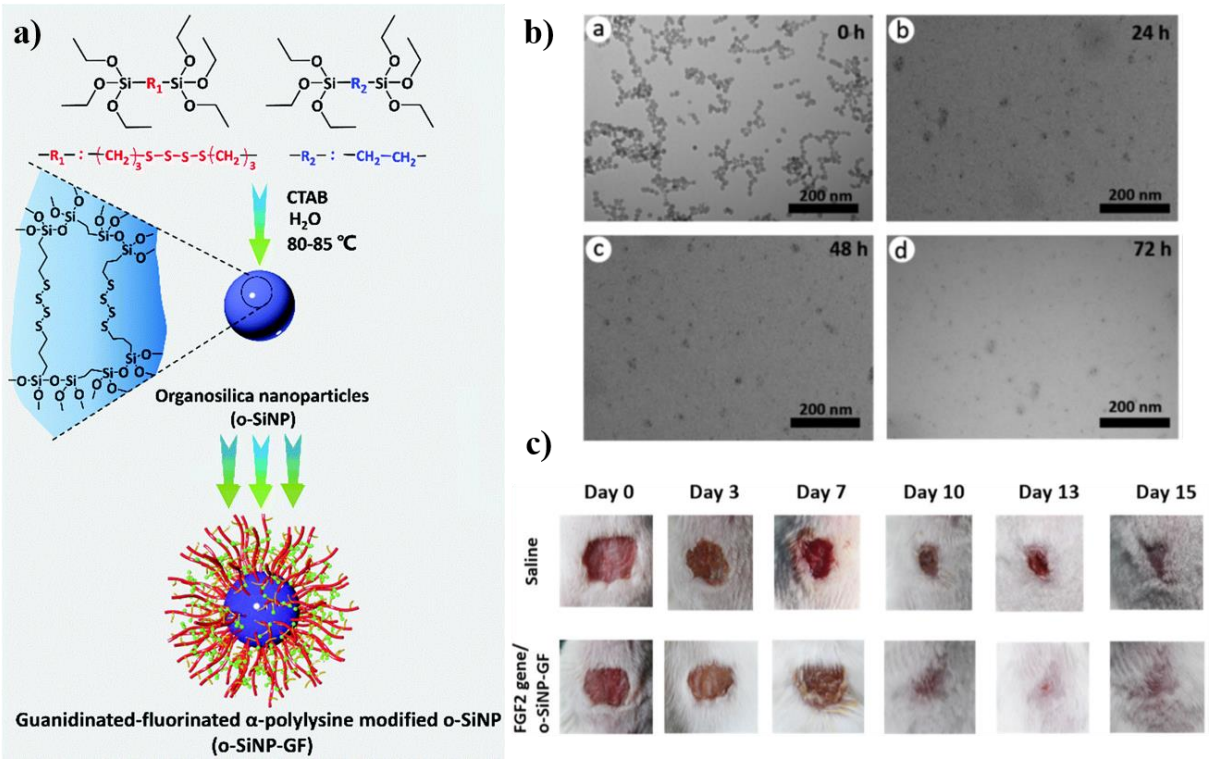

Figure 17: Synthesis, characterization and biological studies of BPMO NPs as gene carriers for WH. (a) Multistep synthesis of o-SiNP-GF (organosilica NPs modified with guanidinated-fluorinated α-polylysine); (b) TEM images of o-SiNPs after suspension into phosphate buffer saline (PBS) with GSH (10 mm) for different times, illustrating NPs biodegradation; (c) Photographs of wounds (1 x 1 cm *ab* initio) after gene therapy (FGF2: fibroblast growth factor-2). Adapted from Zeng *et al.* (2020).[107]

In vivo WH studies on mature mice were then performed to assess the transfection efficiency of fibroblasts growth factor-2 complexed with the multifunctional PMO NPs. Fifteen days after treatment, wound closure was more advanced than the saline control (**Figure 17c**), confirming the excellent capacity of these nanosystems to deliver genes and activate the immune response.[107]

As a conclusion, hybrid inorganic-organic organosilica nanostructures with high biocompatibility and versatile internal and external surface composition hold great potency for biomedical applications. They can virtually comprise any organic function and organic compound in their framework walls, and also carry any molecule or material of interest. The different examples of PMO-based nanosystems that were presented symbolize their excellent features for cancer and infection-associated therapeutic applications.

In the last decades, the use of photon-responsive compounds for photodynamic therapy has emerged as a firm candidate for becoming a forerunner in future theranostics. However, organosilica-based nanomaterials and especially PMO nanoparticles have been scarcely reported in two-photon excitation fluorescence imaging and photodynamic therapy, which are advantageous for several reasons.

An overview of two-photon principles and potential is described in the next section.

2. Two-photon responsive materials applied to theranostics based on two-photon excitation

2.1 Introduction to nonlinear optics

When subjected to a dielectric medium, a defined material generally exhibits an optical response that is linearly proportional with the polarization of the electric field. However, at high laser power values, several intrinsic properties of the material can be modulated. Nonlinear optics (NLO) regroups a large bench of optical phenomena originating from the interaction of light with matter associated with nonlinear response in terms of polarization density.[108-109]

Considering nonlinear optical behavior requires a very intense light source, modern NLO appeared with experimental demonstrations, especially with the invention of the optical laser by Maiman in 1960[110] and the discovery of second-harmonic generation by Franken's team one year after, by focusing a pulsed ruby laser into crystalline quartz.[111] Those discoveries constituted the starting materials of NLO research field, which has known lots of technical improvements in the last decades, being beneficial to several fields, including optical data storage, telecommunications and health care.[112]

2.2 Two-photon absorption

2.2.1 History

One of the most famous nonlinear effects discovered since the first laser construction is two-photon absorption (TPA), a third order nonlinear optical phenomenon. The process was firstly predicted by Göppert-Mayer in the 1930s during her PhD.[113] It was then evidenced in 1961 by Kaiser and Garrett experimentations on inorganic Eu^{2+}:CaF_2 material[114] and in 1963 by Peticolas and coworkers on organic polycyclic aromatic crystals derived from the anthracene family by two-photon excitation fluorescence (TPEF) microscopy with a ruby laser at 694 nm.[115]

TPA corresponds to the simultaneous absorption of two photons by the same molecule or material. TPA study was facilitated by the emergence of sub-picosecond pulsed lasers in the 1990s, inspired by the Ti:sapphire model invented by Peter Moulton in 1982.[116] With such focused and intense beams, a huge instantaneous photon density can be generated.[117]

2.2.2 Principle and challenges

TPA can be defined as degenerate or non degenerate depending on whether the two involved photons have the same or different energies, respectively. This energy is about half that required to reach a given excited electronic state e_n through an intermediate virtual state (**Figure 18**).

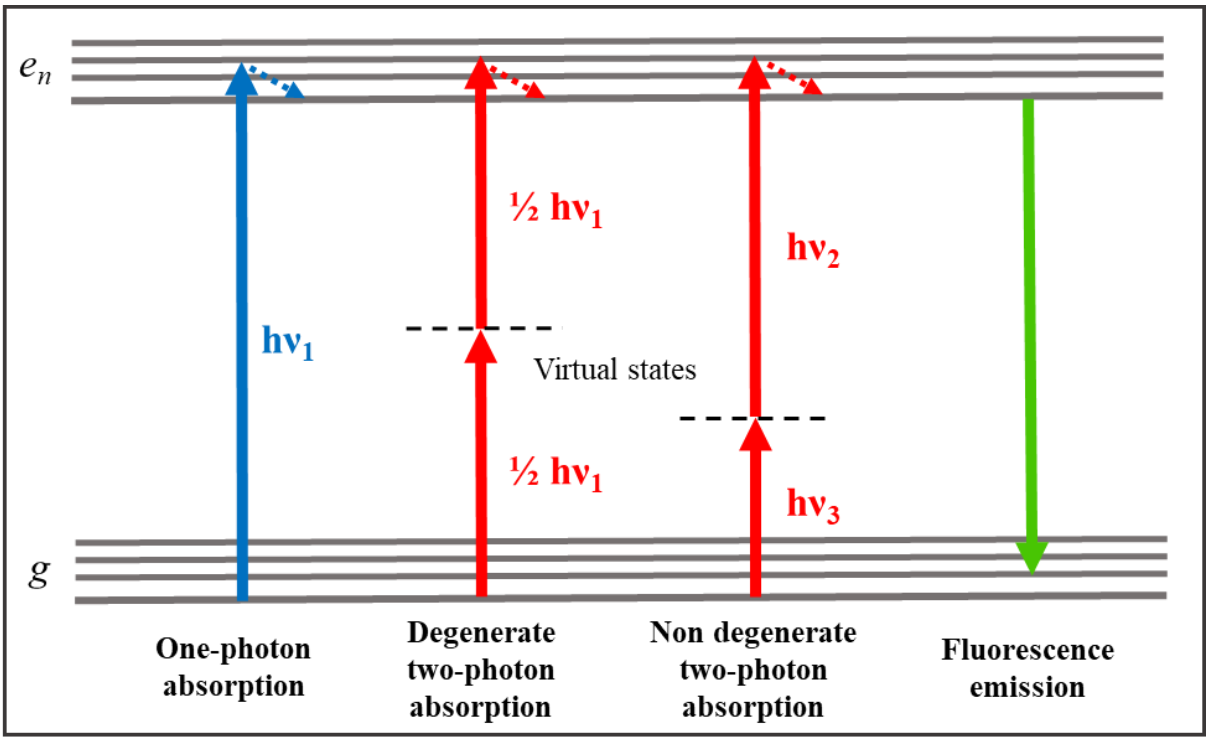

Figure 18: Simplified Jablonski energy level diagram of one-photon and two-photon absorption. Fluorescence emission takes place from the most stable excited state. Adapted from Pascal *et al.* (2021)[112] and Wu *et al.* (2021).[118]

Compared to one-photon absorption process varying linearly with light intensity, TPA is proportional to the square of excitation intensity. Thus, the probability of a molecule to absorb two photons simultaneously is given by the following equation:

$$n_{TPA} = \frac{1}{2}\sigma_{TPA}(\nu)N_g\left(\frac{I}{h\nu}\right)^2,$$

where n_{TPA} is the number of molecules excited by TPA per units of volume and time, σ_{TPA} is the two-photon absorption cross-section of the absorption process at frequency ν quoted in the units of Göppert-Mayer (GM) with 1 GM = 10^{-50} $cm^4.s.photon^{-1}$, N_g is the density of molecules in the ground state g, I is the laser intensity and hν the energy of one photon.[119]

Since the 1960s discoveries, the design of efficient chromophores for NLO application has known a great expansion. Nonetheless, the large development and access to femtosecond

pulsed lasers in the 1990s is a fundamental step in the research area, as it allowed deeper studies of two-photon dyes potential. Indeed, two-photon excitation (TPE) is functional with high temporal photon density (short pulse duration and high repetition level) from the laser as it becomes possible for the two-photon molecule to absorb two photons at once.[120]

However, samples can be damaged by too high laser power values, so there is a quest for molecules and materials exhibiting large σ_{TPA} values to facilitate the practical applications, especially biomedical ones. Accordingly, by using molecules with large two-photon cross-sections at a fixed lower power value, photodamages to the sample are minimized with similar efficiency for the selected employment or better signal-to-noise ratio in the case of microscopy.[119]

As TPA scales quadratically with light intensity, it can allow the transition from ground state g to specific excited states e_n that are in some cases forbidden with one-photon transition. Consequently, TPA enabled the growth of a broad range of applications based on mechanisms triggered by two-photon irradiation, including optical data storage,[121-122] optical power limiting to protect optical detectors[123-124] and photochemical relaxation processes such as guided photopolymerization with a fluorophore as photoinitiator for 3D nano- or micro-fabrication,[125-128] but also high resolution fluorescence imaging by confocal laser scanning microscopy[129-132] and ROS generation for TPE-PDT.[133-134]

2.3 Two-photon organic fluorophores

The need for two-photon organic fluorophores with large σ_{TPA} values is still one of today's challenges as their multistep synthesis is generally difficult. Several families of aromatic and cyclic organic dyes have been extensively studied to better understand the structure-properties relationships in the backbone of such fluorophores to optimize their performances.

2.3.1 Photophysical properties

Two-photon markers and probes are generally classified by their photophysical properties. These parameters will define their suitability for selected applications.

The fluorescence quantum yield (Φ_f) is an important criterion to assess the potential of a two-photon probe, as there is a competition between fluorescence emission and other photophysical processes. Φ_f is the ratio of emitted photons to absorbed photons.

As mentioned before, the TPA cross-section value (σ_{TPA}) is also crucial to meet good optical sensitivity of fluorophores for bio-imaging. σ_{TPA} can be measured by several methods, the most common being by excited-state method using TPEF,[135] or by nonlinear transmission methods,[136] such as z-scan technique.[137]

Other parameters such as fluorescence lifetime, and photostability need to be considered when performing imaging through two-photon microscopy.[138]

In our study, the goal is to build systems for theranostics with a right balance between ROS generation through non radiative processes for PDT combined with radiative fluorescence emission for localizing the materials in the tested biological environments.

2.3.2 Structure-performance relationships

The organic structure of a two-photon fluorophore can be described as an "electron donor-π-electron acceptor" system (D-π-A) which can be subsided in various one-dimensional and multi-dimensional organizations.[117, 139]

Performances of two-photon responsive molecules and materials can be tuned by the modulation of their band gap, so to say, the modulation of their TPA cross-section. To do so, the three molecular units constituting the fluorophore, namely electron donor groups, electron acceptor groups and conjugated π-linkers, have to be finely adjusted. Larger σ_{TPA} is often connected with longer length of the π-electron conjugation, strong donor and acceptor units and good sample polarizability.[140-142] Moreover, molecules exhibiting a planar geometry are known to have enhanced electronic delocalization, leading to more rigid structure with higher fluorescence quantum yield.[143-144]

As one of the multi-dimensional TPA materials, organic multi-branched fluorophores exhibit increased structure-performance relationships compared to most classes of fluorophores. The branching strategy is very efficient for designing two-photon responsive materials with high Φ_f intensity and large σ_{TPA}.

In 1999, Prasad's group discovered that multi-branched planar two-photon chromophores not only display an additive effect of the responses of every single component to the TPA cross-section. In fact, the synthesized triphenylamine-cored materials showed a cooperative enhancement between dipolar branches, leading to much larger σ_{TPA} when brought back to the equivalent value for one branch.[145] This phenomenon is related to intramolecular charge transfer (ICT) in the structure.

As an example, Opatz's team showed the contribution of multi-branching to the enhancement of the relative TPA cross-section value in star-shaped triazine-based derivatives. By comparison with its one-dimensional analog, the three-branched fluorophore showed a 7.1-fold enhancement in σ_{TPA} instead of a 3-fold increase if coupling properties were only additive (**Figure 19**).[146]

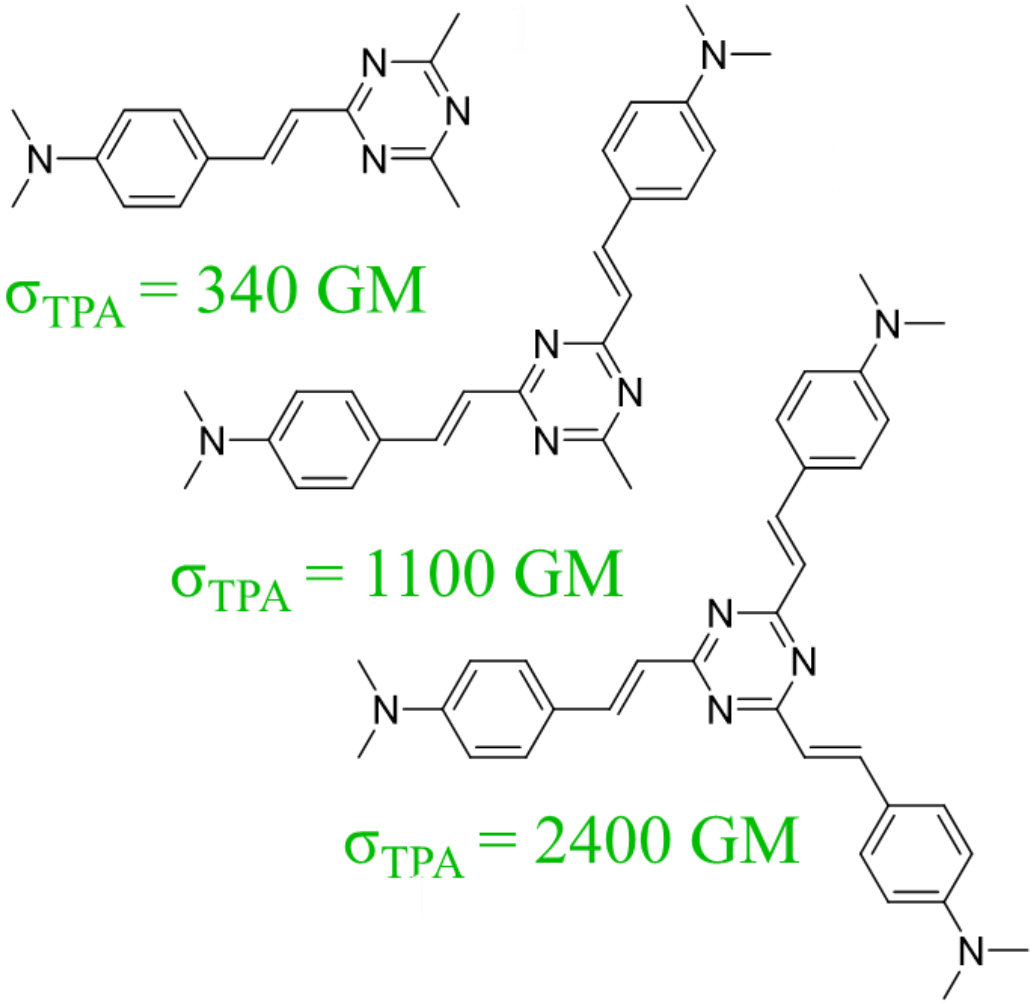

Figure 19: Cooperative effect of branching on the two-photon absorption cross-section values of triazine-cored derivatives excited at 800 nm. The relative contributions calculated for one branch gives a 3.2-fold and a 7.1-fold increase for two- and three-branched dyes, respectively. Adapted from Gorelik *et al.* (2018).[146]

This interesting strategy using a push-pull behavior has been extensively studied to make multi-branched two-photon fluorophores with excellent TPA properties. In such excited systems, energy and electrons are transferred from peripheral electron donors to core electron acceptors (or inversely). Moreover, the branch moieties can act as a shell to the core moiety, thus protecting from self-quenching and aggregation.[147]

2.3.3 Summary of prerequisites for bioapplications

Two-photon responsive fluorophores are gaining increasing attention in the biomedical sector since the last two decades as they fulfill most of the specifications required for such applications.

First of all, it is of great importance that newly produced two-photon materials entail high Φ_f and σ_{TPA} to generate bright images, as the brightness parameter is equal to their product.[118] As these parameters would generally evolve diametrically, a compromise between good fluorescence emission intensity for tracking and non-radiative processes such as reactive species generation for cell eradication should be found. Nevertheless, such very conjugated multi-branched structures with exceptional TPA properties and high molecular weights have poor solubility in water, resulting in aggregation and self-quenching issues upon fluorescence and other photophysical mechanisms.[120] Considering that, the final systems should remain photostable upon irradiation in the targeted biological media.

Furthermore, TPA provides highly selective excitation in the biological window, intrinsic three-dimensional resolution for two-photon microscopy and considerable reduction of photodamage by the use of lower excitation intensity.

As the absorption and autofluorescence of biomolecules in the ultraviolet (UV) region is very high,[148-149] attention must be payed to designing TP-responsive materials with excitation and emission wavelengths in the NIR region. In fact, a shift to longer wavelengths provides better penetration in the tissues, up to 2 cm, as well as lower photobleaching and reduced autofluorescence of the tissues. Since 2010, there has been greater emphasis on NIR fluorophores overlapping with biological windows of interest. They are generally divided in two categories, namely the NIR-I and NIR-II regions, from 700 to 950 nm and from 1000 to 1700 nm, respectively.[150]

From a biomedical point of view, more general requirements are the use of non-toxic and stealth platforms, with good sensitivity and selectivity. To meet the needs of medicine, one good strategy currently in great expansion is based on the integration of fluorophores in biocompatible and dispersible nanocarriers such as dendrimeric,[151] silica-based[29] or PMO nanoparticles,[152-153] with great potential for diagnosis and therapy.

2.4 Two-photon excitation photodynamic therapy

2.4.1 Generalities about photodynamic therapy

Photodynamic therapy (PDT) is an emerging clinically approved and non-invasive treatment for cancer and various non-malignant diseases, including infections.[154] PDT consists of the light excitation of photosensitive molecules or materials triggering the activation of photochemical processes which participate in specific biological reactions to cells or tissues.

The therapy is based on the interaction of three mandatory elements: a light source, an oxygen-rich environment, and a photosensitizer (PS) which will react with oxygen to generate highly cytotoxic reactive oxygen species (ROS).[155-156] First clinical attempts using PDT strategy were carried on by Von Tappeiner and Jesionek in 1903. Eosin PS was exposed to light irradiation in contact with a tumor located on the lip.[157-158] Thereafter, the two consecutive world wars and the rise of pharmaceutical industry delayed the launching of new PDT studies. New impetus was provided in the 1970s with the discovery of haematoporphyrin derivatives (HpDs), largely driven by Thomas Dougherty and collaborators.[154] After several pre-clinical and clinical studies, the purified version of a HpD, which was named Photofrin®, became in 1993 the first government-approved PS for cancer treatment by the mean of PDT and is currently approved for various types of cancer by Food and Drug Administration (FDA).[159-160]

To date, several PSs have been clinically validated for the treatment of solid tumors, precancers and non-oncological pathologies. PDT showed good potency in atherosclerosis,[161] cancer,[162] ophthalmology,[163] dermatology,[164-165], and multidrug-resistant infectious diseases.[166-168] In particular, antimicrobial photodynamic therapy (aPDT) has recently emerged as an interesting alternative over antibiotics because of its broader spectrum of action since PSs can operate on diverse microbes and because it will cause reduced adverse effects and damages.[169] For instance, aPDT has shown effectiveness in the treatment of abrasion, burns and excisional wounds. Oyama and collaborators proposed a summary of the potential PDT contributions in the WH process (**Figure 20**).[170] Many *in vivo* studies used the similar protocols demonstrating PDT involvement, such as active killing bacteria and proliferation enhancement of fibroblasts, thus of collagen and elastin, that are essential elements in extracellular collagen remodeling.[171-173]

The mechanisms of one-photon and two-photon PDT are described in **Figure 21**.[174-175] Upon irradiation, a PS in its singlet lowest or singlet ground state ($^1PS_0$) energy level can be excited to a higher-energy singlet excited state (^1PS_n). This very unstable excited state can

encompass short-lived internal conversion phenomenon to reach its lowest singlet excited state ($^1PS_1$) before transition to a relatively long-lived electronically triplet excited state ($^3PS_1$) by another non-radiative process known as intersystem crossing (ISC).[176]

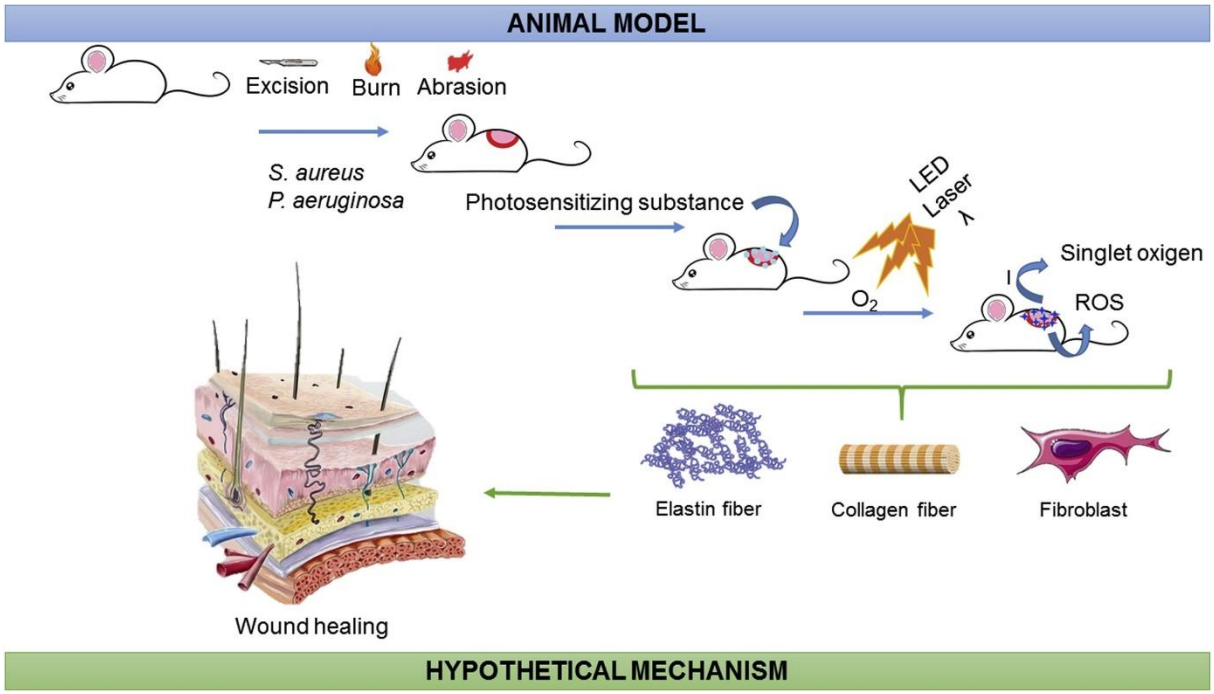

Figure 20: Schematic representation of the potential mechanisms associated with PDT treatment applied to WH *in vivo*. After receiving a specific wound and being infected or not by bacteria, the animals are subject to the administration of photosensitizing substance. Then, the wound area is irradiated and the excited PS interacts with surrounding oxygen to generate ROS for bacteria eradication. The irradiation also contributes to the stimulation of the immune response, reflected in the proliferation of different biomaterials involved in the WH process. Reproduced with permission from Oyama *et al.* (2020).[170]

The triplet excited state can undergo different photophysical and photochemical processes involved in PDT, which can be classified into three types.[177] In type-I mechanism, PS can react with biological substrates via electronic transfer to form radicals that will interact with $^3O_2$ to generate ROS such as $O_2^{\bullet-}$, $HO^{\bullet}$ and H_2O_2. In type-II process, the PS directly convert molecular oxygen into singlet oxygen ($^1O_2$) through energy transfer, going back to its ground singlet state. Type-II mechanism has been clearly identified as the main source of the photodynamic effect, mainly because $^1O_2$ can easily diffuse in cellular tissues to trigger death through oxidation of amino and nucleic acids ending in the denaturation of proteins, RNA and DNA.[178] Less common type-III reactions can occur under hypoxic conditions as they are only based on electron transfer to biomolecules causing cellular damages. These three mechanisms can induce cell death, either by cell necrosis or by causing cell apoptosis.

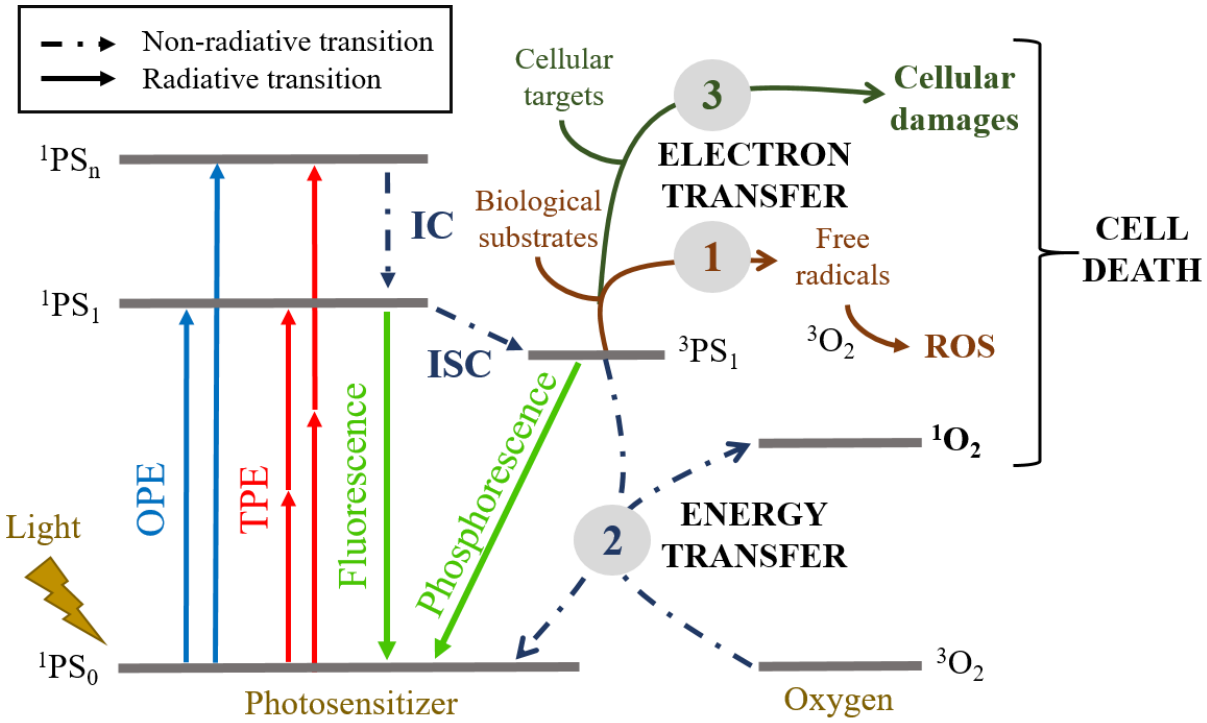

Figure 21: Jablonski diagram applied to PDT. From its triple excited state, the PS can undergo three types of photochemical mechanisms that can all trigger cell death in the irradiated environment. IC: Internal Conversion; ISC: Intersystem crossing; OPE: One-Photon Excitation; ROS: Reactive Oxygen Species; TPE: Two-Photon Excitation. Adapted from Sun *et al.* (2017).[176]

2.4.2 Challenges with two-photon excitation therapy

PDT presents significant advantages compared to surgery, chemotherapy or radiotherapy due to spatial and temporal resolution, poor invasiveness, minimal toxicity to healthy tissue, low systemic toxicity, great organ function sparing and reduced long-term morbidity. In addition to this potential for precision therapy, PDT is not much affected by intrinsic or acquired resistance issues.[179-180] For all these reasons, PDT generally does not require sedation or hospitalization, which can improve patient comfort and reduced economical costs. However, when using the one-photon strategy, PDT has been limited for a long time by light delivery and penetration depth. The influence of excitation wavelength and light intensity towards light penetration is substantial, with very poor efficacy in UV and best results attained in the NIR up to 2 cm and 21% light transmission (**Figure 22**).[181] In addition to that, one-photon excitation (OPE) is provoking photodamages all along the laser path. Conversely in TPE, the irradiation is limited to the laser focal point with a resolution at the μm^3 level.[182]

All these drawbacks can be overcome by the design of new PSs sensitive to TPE in the NIR region and characterized by high TPA cross-sections, photostability, dark toxicity and great ROS production quantum yield (Φ_Δ).[183]

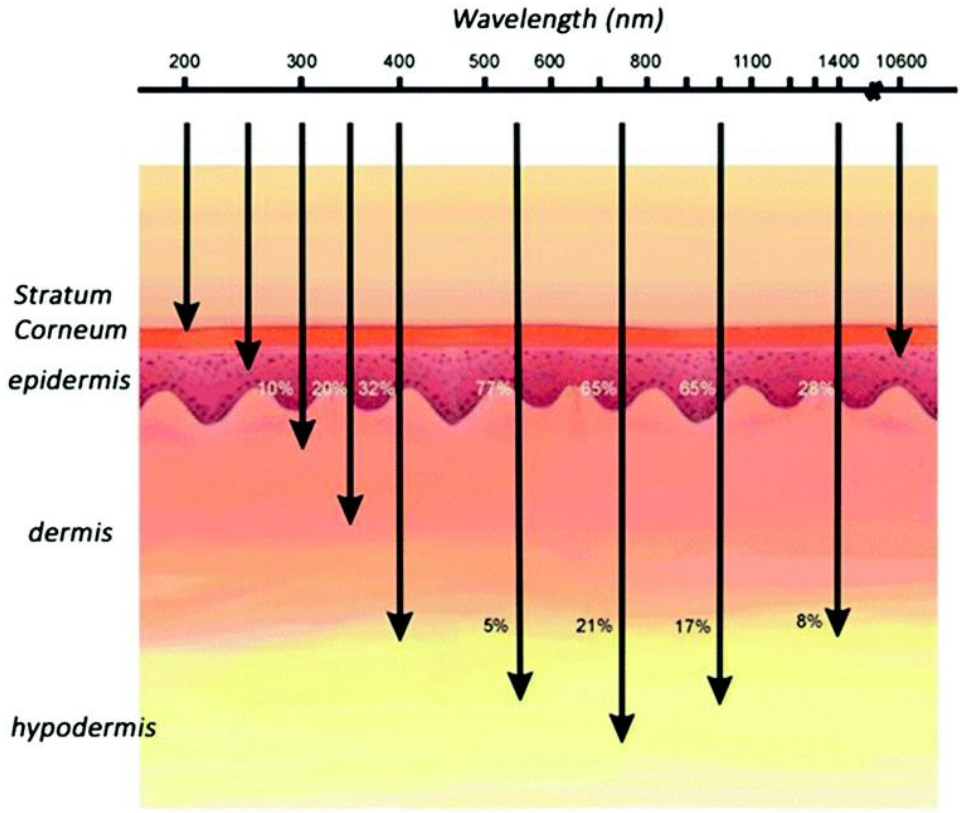

Figure 22: Schematic representation of skin layers showing the influence of wavelength excitation to light transmission. Reproduced with permission from Bolze *et al.* (2017).[181]

Up to now, some promising results have already been obtained *in vivo* with TPE-PDT. The main light sources currently employed within the phototherapeutic window (780-950 nm) are femtosecond lasers based on Ti:sapphire technology, which most effective excitation conditions are in the 780-820 nm region. Nevertheless, most of the studies propose PSs with large σ_{TPA} out of this window, thus, developing new systems in this suitable window would be relevant, especially for economic reasons considering the currently available equipments.[176]

The ideal PS structure and TPE-PDT conditions appear to be very different between topical and systemic PSs drug delivery. On one hand, cancer therapy and diseases generally require systemic administration, hence, good penetration in the tissues is crucial. On the other hand, this factor is less predominant for antimicrobial treatments that tends to be more superficial. Therefore, efficiency could be increased by elaborating materials with high affinity for the diseased tissues or cells, using targets for specific molecular recognition and by integrating PSs in nanotechnologies to limit their aggregation.[184] For anticancer cure, suitable PS-based platforms should be lipophilic with little to no overall charge. To treat bacterial infections, cationic materials are largely described, especially for eradicating gram-negative bacteria populations due to the good interaction with their negatively-charged external membrane.[154]

Taking into account the spotlighted advantages of TPE-PDT, a list of the future directions to undertake could be seen as followed:

- Theranostic strategy using PSs fluorescence for live tracking or biomolecule recognition leading to more accurate results;
- Treatment of diseases accompanied by small lesions in some important organs;
- Adjuvant therapy to heal residual lesions in tissues after surgery or conventional treatments;
- More efficient systems were PSs are assembled with innovative materials like quantum dots, liposomes and NPs. Careful attention should be placed in the composites synthesis reproducibility, as well as their composition and stability in biological media.[176] Notably, Förster resonance energy transfer (FRET) is one emerging strategy that could be worth the effort if properly quantified. Its principles and some good case studies from the literature will be presented in the next sections.

2.4.3 FRET-enhanced strategy

Förster-type energy transfer is a non-radiative mechanism characterized by the interaction of two electric dipoles in their singlet states at large distances, in other words from 1 to 10 nm (**Figure 23a**).[185-186] For this to happen, a spectral overlap between the emission spectrum of a highly fluorescent two-photon fluorophore (the energy donor, abbreviated as D) and the absorption spectrum of a PS element possessing intrinsic high ROS quantum yield (the energy acceptor, abbreviated as A) is required (**Figure 23b**). Hence, a right choice of donor/acceptor couple is fundamental. This spectral overlap should be wide enough to cover a broad range of biological environments (whose polarity is very variable), so that the FRET could remain exalted.

Alongside with the development of more and more efficient TPA materials, FRET-enhanced TPE-PDT is being largely tested since the last decade. Contrary to the trivial (radiative) energy transfer mechanism accompanied by photon emission and reabsorption, FRET is maximized in diluted media, thus well adapted for biological applications. Some of the best examples from the literature of materials applied to TPE-PDT and possessing high FRET efficiencies have been summarized in **Table 1**, indicating the nature of D/A pairs and the results from photophysical studies and *in vitro*/*in vivo* biological experiments.

Several characterization methods exist to confirm the FRET efficiency, either qualitatively or quantitatively. Before this, a wide range wavelength scanning is generally performed in the NIR to find the best conditions for having light upconversion from D to A parts. Then, by one or

two-photon excitation around D maximum absorption wavelength, fluorescence lifetime or fluorescence intensities of a similar system possessing only D units or both D and A units can be compared to establish of a FRET quantum yield synonym of D fluorescence quenching for the benefit of A (**Figure 23c and d**).

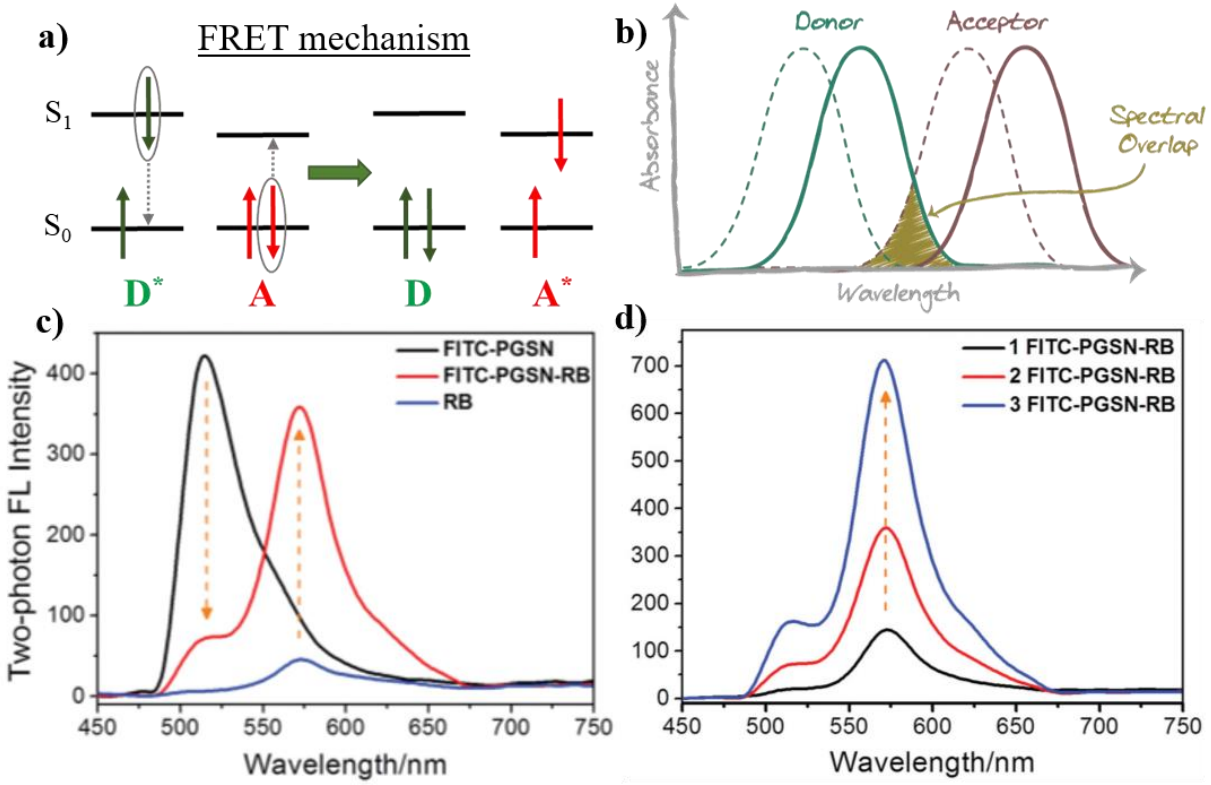

Figure 23: Fundamental FRET principles and example of FRET confirmation. (a) Simplified energy level diagram presenting FRET mechanism; (b) Illustration of the spectral overlap FRET condition between donor D and acceptor A; (c) Example of TPE fluorescence spectra showing fluorescein (FITC, D) fluorescence quenching and Rose Bengal (RB, A) fluorescence enhancement in the presence of (d) increasing concentrations of donor D ($\lambda_{exc.}$ = 920 nm). PGSN: Polyglycerol mesoporous silica nanoparticles. Adapted from Liu *et al.* (2016).[187]

Direct evaluation of photosensitizing enhancement can be performed by evaluation of singlet oxygen generation. Because $^1O_2$ has short lifetime,[29] the use of fluorescent oxidizable "chemical traps" (ABDA, ADPA, DPBF, etc.) is very common. The method evaluates the fluorophore photobleaching by monitoring the fluorescence decrease rate after irradiation in D absorption domain either in the presence of D, A or both D and A, making the parallel with singlet oxygen production level.[188]

Biological studies can be even more significant to evaluate two-photon materials dependence. Intracellular or extracellular energy transfer quantum yields can be assessed by fluorescence imaging, in addition to the killing efficiency under TPE.

Table 1: Overview of innovative systems exhibiting FRET properties for TPE-PDT and associated photophysical and biological studies.

Global system	Donor (D)	Acceptor (A)	FRET confirmation method ($\lambda_{exc.}$, nm)	FRET efficiency / Photophysical studies: system *vs.* system without D (unless otherwise specified)	$\lambda_{TP,exc.}$ (nm)	Biological model(s)	Intracellular FRET / TPE-PDT biological results by CLSM imaging (irradiation time, laser power/ intensity)	Refs
Water-soluble dendrimeric structure integrating $(AF\text{-}343)_8$ with TPP core	AF-343 (DPA-derivative)	TPP	OP/TP-induced fluorescence spectra (390/780); $^1O_2$ generation (780): ADPA fluorescence intensity.	$\Phi_{OP} > 99\%$; $\Phi_{TP} > 99\%$; Higher $^1O_2$ generation.	780	n.d.	n.d.	189-190
44 nm (DLS) (CdSe/ZnS)-PMAO-PEG-MPyP	CdSe/ZnS QDs	Tris-MPyP-COOH	TP-induced fluorescence spectra (800); $^1O_2$ generation (800): ADPA fluorescence intensity.	D fluorescence quenched by A; $^1O_2$ generation 2 times higher.	800	n.d.	n.d.	191
30 ± 6 nm (TEM) Organically-modified MSN encapsulating BDSA/HPPH	BDSA	HPPH	TP-induced fluorescence spectra (850); $^1O_2$ generation (850): ADPA fluorescence intensity.	Emission of A 30 times more intense; Very higher $^1O_2$ generation.	850	HeLa cervical CCs	36% intracellular FRET efficiency; Important cell necrosis after irradiation (30 x 3 s, 10 s interval, 1.4 mW cm^{-2}).	29
80 nm (DLS) TPP dispersed in PFEMO-conjugated polymer NPs	PFEMO	TPP	TP-induced fluorescence spectra (800); $^1O_2$ generation (800): ABDA fluorescence intensity.	Emission of A 20 times more intense; ABDA photobleached 5 times higher.	800	$HepG_2$ human liver CCs	42% $HepG_2$ mortality after irradiation (630 J cm^{-2}).	192
80 nm (TEM) PdTPP-grafted FITC@MSN	FITC	PdTPP	OP and TP-induced fluorescence spectra (460/920); $^1O_2$ generation (920): DPBF fluorescence intensity.	Emission of A more intense; Very higher $^1O_2$ generation.	920	MDA-MB-231 breast CCs, Nude mice bearing MDA	89% intracellular FRET efficiency; High level of cell apoptosis after irradiation (15 min); Important cell apoptosis and necrosis in mice tissues after irradiation (15 min, 150 J cm^{-2}).	193
5 nm (DLS) Hydrophilic CD-PpIX	CDs	PpIX	TP-induced fluorescence spectra (800); $^1O_2$ generation (365): DPBF fluorescence intensity.	Emission of A more intense; Normalized DPBF intensity decrease: 0.70 *vs.* 0.91.	800	HeLa CCs, CeH/HeN mice bearing RIF-1	Low dark toxicity and 82% killing efficiency after irradiation (1 µM). 60% of tumor-size reduction after 4 days (3 x 3 min, 3 min interval, 20 J cm^{-2}). Opposite effect of A alone.	194
8 x 2.5 nm (AFM) CDs-TMPyP disks	CDs	TMPyP	Fluorescence lifetime (360); OP-induced fluorescence spectra (360); $^1O_2$ generation (700): DPBF fluorescence intensity.	$\Phi_{OP} = 47\%$; Emission of A more intense; Very higher $^1O_2$ generation.	700	HeLa cervical CCs	No dark toxicity and 80% killing efficiency after irradiation (45 min, 16 W cm^{-2}).	195
80 nm (TEM) Fluorophore-PMO@8-Br-quinoline NPs	Alkoxy-silylated fluorophore	8-Br-quinoline derivative	TP-induced fluorescence spectra (715-980): determination of best σ_{TPA} and photophysical measurements.	Best conditions at 760 nm. 2.5-fold higher brightness even if Φ_f is 2.5-fold lower (compared to D-based NPs)	760	MCF-7 breast CCs	47% killing efficiency after irradiation with 40 µg mL^{-1} (3 x 1.57 s, 3W) and no toxicity without A grafting.	196

80 nm (TEM) FITC@PG-MSN@RB NPs	FITC	RB	Fluorescence lifetime (455); OP and TP-induced fluorescence spectra (455/920); $^1O_2$ generation (480): ABDA fluorescence intensity.	Φ_{OP} = 59%; Emission of A more intense with increasing D rates; Normalized ABDA intensity decrease: 0.03 *vs.* 0.66.	920	HeLa cervical CCs	Very high killing efficiency after irradiation (20 min, 2% laser intensity) and no toxicity without D or A.	187
200−300 nm (TEM) BP-CDPNP@RB	BP	RB	Fluorescence lifetime (344); $^1O_2$ generation (480): ABDA fluorescence intensity.	Φ_{OP} = 47%; Normalized ABDA intensity decrease: 0.35 *vs.* 0.64.	810	MCF-7 breast CCs	High toxicity level after irradiation (50 min, 5% laser intensity) and no toxicity with only laser.	197
70 nm (TEM) PAH-RB-coated carboxylated BP nanocomplexes	BP	RB	Fluorescence lifetime: (370); OP and TP-induced fluorescence spectra (405/810); $^1O_2$ generation (480): ABDA fluorescence intensity.	Φ_{OP} = 80% Emission of A more intense; Normalized ABDA intensity decrease: 0.26 *vs.* 0.65.	810	MCF-7 breast CCs	High toxicity level after irradiation (20 min, 5% laser intensity) and no toxicity with A alone.	198
300 nm (TEM) FITC/RB-CAT-VN NPs	FITC	RB	Fluorescence lifetime: (455); OP and TP-induced fluorescence spectra (480/880); $^1O_2$ generation (480): ABDA fluorescence intensity.	Φ_{OP} = 53%; Emission of A more intense; Normalized ABDA intensity decrease: 0.09 *vs.* 0.16 (A alone).	880	MCF-7 breast CCs	High toxicity level after irradiation (20 min, 5% laser intensity) and no toxicity with A alone.	199
10 ± 3 nm (TEM) Antibody-conjugated GQD-GNC	GQDs	GNCs	Fluorescence lifetime: (380); OP and TP-induced fluorescence spectra (380/860); $^1O_2$ generation (860): ABDA fluorescence intensity.	Φ_{OP} = 57%; Emission of A more intense; Φ_{1O2} = 97% (44%: D, 15%: A, 75%: RB reference).	860	MRSA	100% MRSA eradication after irradiation (10 min), 50% with D and 15% with A.	200
Ace-DAN-ZnTPP	Ace-DAN	*t*Bu-ZnTPP	OP-induced (370) and TP-induced fluorescence spectra (720-880): determination of best σ_{TPA}; $^1O_2$ generation (370): DPBF fluorescence intensity.	Φ_{OP} = 98%; Best conditions at 740 nm; $^1O_2$ generation two times higher than A.	740	A549 CCs	No dark toxicity (0 min) and increasing cell damage with irradiation time (10 to 30 min, < 5% laser intensity).	201-202
PTX-loaded POEGMA dendritic structure incorporating imidazole and PPa	Imidazole derivative	PPa	TP-induced fluorescence spectra (800); $^1O_2$ generation (808): ADPA fluorescence intensity.	Emission of A 20 times more intense; Very higher $^1O_2$ generation.	808	4T1 murine breast CCs, Nude mice bearing 4T1 xenografts	High toxicity after various irradiation times and intensities compared to HELF control cells. 67% tumor growth inhibition after irradiation (3 x 10 min, 5 min interval, 0.5 W cm^{-2}). Only 49% with A.	203

ABDA: 9,10-anthracenediyl-bis(methylene)dimalonic acid; Ace-DAN: 2-Acetyl-6-dimethyl-aminonaphtalene; ADPA: 9,10-anthracene-dipropionic acid disodium salt; AFM: Atomic Force Microscopy; BDSA: 9,10-bis[4'-(4''-aminostyryl)styryl]anthracene; BP: Bispyrene; CAT: Catalase; CC: Cancer Cell; CD: Carbon Dot; CDPNP: Cationic Dipeptide NP; CLSM: Confocal Light Scanning Microscopy; DPA: Diphenylamine; DPBF: 1,3-diphenylisobenzofuran; FITC: Fluorescein; GNC: Gold Nanocluster; GQD: Graphene Quantum Dot; HELF: Human Embryonic Lung Fibroblasts; HPPH: 2-devinyl-2-(1-hexyloxyethyl)pyropheophorbide; OP: One-Photon; PAH: Polyallylamine; PFEMO: Poly[9,9-dibromohexylfluorene-2,7-ylenethylene-alt-1,4-(2,5-dimethoxy)phenylene]; PG: Polyglycerol; PMAO: Poly(maleic anhydride-alt-1-octadecene); POEGMA: Poly[oligo(ethylene glycol)methylethermethacrylate]; PPa: Pyreophorbide a; PpIX: Protoporphyrin IX; PTX: Paclitaxel; QD: Quantum Dot; RB: Rose Bengal; RIF-1: Radiation-induced Fibrosarcoma; TMPyP: 5,10,15,20-tetrakis(1-methyl,4-pyridinio) porphyrin tetra(*p*-toluenesulfonate); TP: Two-Photon; TPP: Tetraphenylporphyrin derivative; TrisMPyP: 5,10,15-tris(1-methyl,4-pyridinio) porphyrin tri(*p*-toluenesulfonate); VN: Vaterite NP.

As indicated in **Table 1**, donor moieties are mainly organic TPA fluorophores, quantum dots and carbon-based materials, while acceptor PSs are mostly porphyrin derivatives. The gathering of these FRET pairs in stable nanostructures with good properties for biomedical use can improve the transfer efficiency.[187, 192, 198] Furthermore, as molecular oxygen is a fundamental element for PDT proficiency, employment of a polymer matrix can be very relevant due to porosity allowing easier in and out diffusion.[204]

Thus, while addressing the biological requirements for a controlled and personalized medicine, some effort should be placed in developing adaptable and effective TPA-responsive nanomaterials through FRET-enhanced PDT.

2.5 Two-photon photosensitizers

2.5.1 Generations of photosensitizers

Previous sections gave a preview of the properties that a PS should possess so the treatment efficiency could be maximized, and inversely, the side effects, minimized. To summarize those conditions, photosensitizing elements should be pure (in the case of a molecule), homogeneously distributed (in the case of material structure), water-soluble, biocompatible and should present selective accumulation in the tissues, no dark toxicity and fast clearance.[205] To achieve these specifications while holding high absorption capacity and ROS production quantum yields, the formulation of PSs has been in constant evolution since the early days of PDT. Three generations of materials have been explored over time.

First generation PSs were mainly HpDs featuring excellent affinity and accumulation in diseased tissues along with superior absorbance and $^1O_2$ production rates due to their physicochemical properties. While this first crop led to the commercialization of Photofrin®, some of the above announced settings were not fulfilled yet: NIR absorption capability was not high enough and PS half-life was too long, resulting in widespread photosensitization for one to three months when the patient needs to avoid prolonged exposure to light.[206]

Consequently, new approaches were examined during the 1980s. TPA cross-sections values were increased in the NIR domain by slight structural modifications in different kinds of macrocycles. The use of harmless and selective prodrugs (becoming active under metabolism action and showing good body clearance) partially addressed the long-term photosensitivity issue. This second generation of PSs is principally composed of chlorin, bacteriochlorin, which

belong to the porphyrin family, and polysulfonated metallic phthalocyanine families.[207-209] Different molecules obtained a marketing authorization, mostly during the 2000s and 2010s.

The third generation of photosensitizing materials has to deal with today's orientation toward personalized and mild medicine. The lack of specificity of PSs for infected and tumor tissues is a major obstacle to reach the clinic or ever make it to the market. Bioconjugation and encapsulation with targeting moieties appear as the main strategies for the development of optimal PS-based systems.[210-211] A large variety of biomolecules already showed their efficiency, such as antibodies and oligosaccharides,[212-213] but further work is imperative to enhance TPE-PDT risk-benefit ratio with reduced dosage of photoactive drug.

The coupling of targeting strategy with TPE will be presented in the next sections by means of various examples. The discussion will be focused on the families of components that were chosen during this research project for their suitability in TPE-PDT: on one hand, porphyrin and nanodiamond-based PSs, and on the other hand, PS-PMO nanoplatforms combining imaging capacity and therapeutic activity against cancer or infections.

2.5.2 Porphyrin derivatives

i. Generalities

Regarding their good safety proven with several market authorizations, porphyrins and theirs derivatives (notably chlorins and bacteriochlorins) are the most described macrocyclic tetrapyrroles in the literature for biomedical applications. They are an important class of molecules naturally present in various biological processes. Some bacteria can form porphyrin in their metabolism (which was used upon PDT via auto-photosensitization to eradicate bacterial cells).[214] Porphyrins have special absorption, emission and charge transfer features (photosynthetic ability). They can also transport small molecules, as heme (a ferrous porphyrin responsible for blood color) does in blood vessels to transport oxygen.[215] This latter was originally used for the design of the first artificial porphyrins starting with an acidic treatment for Fe removal.

The porphyrin core is composed of four pyrrole units connected by methene bridges between pyrrolic C_α atoms, in addition to two protonable central nitrogen atoms bringing diacid or dibasic character depending on the pH value (**Figure 24a**). Twelve positions of the structure can be functionalized (8 β-pyrrolic and 4 meso), and its center can be metallated to form a metalloporphyrin. With such modifications, chromophore geometry and photophysical properties can drastically change.[216]

Through their aromatic structure, porphyrins are very stable compared to other macrocyclic dyes. Their rigid and planar geometry, as well as their good absorption in the visible range, originates from their 22 π electrons, where 18 of them can be easily delocalized. This aromaticity is characterized by a very intense absorption band in the UV region (390-430 nm), namely the Soret band, with an electronic transition from ground singlet state S_0 to excited singlet state S_2. Furthermore, the color of porphyrin comes from weaker absorption bands at higher wavelengths (500-700 nm), called the Q bands, and associated with different energy levels of transition from S_0 to S_1. Porphyrins also possess good fluorescence properties with two characteristic bands, the most intense being located between 600 and 700 nm (**Figure 24b**). Substitution will cause hypsochromic (blue) or bathochromic (red) shift of these emission wavelengths.

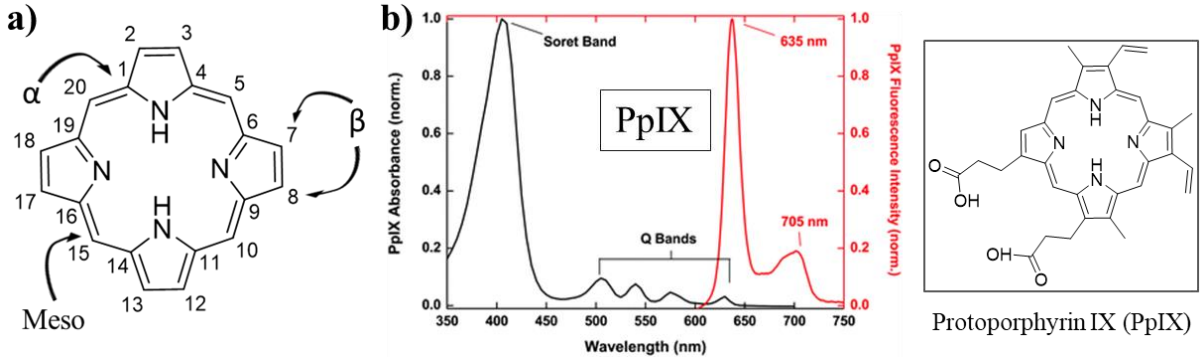

Figure 24: Fundamentals about porphyrins. (a) Chemical structure of the porphyrin core; (b) Absorption and emission spectra of protoporphyrin IX (PpIX) displaying an intense UV band (Soret) and four weaker absorption bands at higher wavelengths (Q4 to Q1), as well as NIR fluorescence peaks with a maximum at 635 nm. Adapted from Valentine et al. (2013).[217]

Altogether, the performances of porphyrins (and of all PSs) for TPE-PDT are evaluated by using the two-photon figure of merit, which is the product of σ_{TPA} and Φ_{Δ}. One good way to achieve the best figure of merit is the ability of porphyrins to behave like building-blocks to form supramolecular assemblies. Type H aggregates correspond to macrocycles piling in columns, and type J aggregates designate stair-shaped assemblies. This latter implies red shift of absorption and emission spectra, thus strongly increasing TPA cross-sections and ROS generation.[218-219]

ii. Examples of photodynamic activity

The first TPE-PDT experiments were performed with some clinically approved one-photon porphyrin derivatives. However, their TPA cross-sections were very limited (σ_{TPA} (Photofrin®) = 10 GM at 800 nm and σ_{TPA} (Visudyne®) = 51 GM at 900 nm).[220] Consequently, the strategy of expanded π-conjugation and polymerization was developed to improve the TPA

absorption properties. Ogawa and coworkers prepared self-assembled conjugated derivatives via ethyne or butadiyne bonding, forming porphyrin dimers through imidazolyl coordination to each zinc metal center. With values up to 3.3 x 10^4 GM in the NIR, their TPA cross-sections in water were greatly enhanced, allowing good performances for killing HeLa cancer cells under TPE-PDT at 780 nm.[221-222] Among the first two-photon *in vivo* PDT studies, Collins' group used another porphyrin dimer to selectively cause the occlusion of blood vessels in three mice treated with the PS and irradiated at 920 nm. Conversely, no effect was observed without photoactive drug or with Verteporfin, the active compound in commercially available Visudyne® for OPE-PDT.[223]

Another challenge that needs to be solved for applying porphyrins and their derivatives in two-photon-based therapy is their hydrophobicity causing aggregation and limited cellular uptake. The addition of hydrophilic functions in the porphyrin structures can increase the solubility in biological media,[224] but would not be enough to meet the clinical specifications. As mentioned before with the FRET strategy, multifunctional nanoparticles are great candidates to safely integrate and convey PSs to tumor or bacterial cells via target recognition groups, while retaining their photoactivity level. Encapsulation of porphyrin derivatives in polymeric framework or in silica-based nanoparticles is a good way to maintain their two-photon phototherapeutic effect, as proven by several *in vitro* and *in vivo* experiments.[225-231] Increasingly, the capacity of such systems for combined therapy is investigated, with concomitant drug or biomolecule delivery, TPEF bio-imaging and photodynamic therapy.[232]

2.5.3 The case of nanodiamonds

While some nanomaterials only have a passive role, some others can also display intrinsic photoactivity. This is notably the case for gold nanoclusters, quantum dots, fullerenes, carbon nanodots and nanodiamonds.

i. Generalities

Nanodiamonds (NDs) tiny gems are one-dimensional carbon-based materials possessing great mechanical and optical properties, along with high surface area and easily tunable surface structure.

Several types of NDs with various production methods are already on the market.[233] Detonation nanodiamond (DND) synthesis by shocks compression of explosives precursors or graphite was discovered accidentally during the study of diamond synthesis by Volkov, Danilenko and Elin in 1963.[234-235] Pulsed laser ablation was first described by Liu's group in

1998 and originates from graphitic and hydrocarbon reactants.[236] High-energy ball milling of micron-sized diamonds at high pressure and high temperature (HPHT) was presented by Boudou and collaborators in 2009.[237] Natural NDs have also been isolated from primitive carbonaceous meteorites and detected in protoplanetary disks of various kinds of stars.[238-239]

NDs properties are associated with some characteristic features, including shape, surface functional groups, sp^2 and sp^3 carbon contents and core impurities, which are mainly nitrogen vacancies known for bringing fluorescence to the material.[240] Moreover, their surface exhibits various oxygen and nitrogen-based functional groups, thus, nanodiamonds have a non-zero zeta potential value in water, giving them colloidal stability in water and also some polar solvents. Those parameters can be controlled by the nature of synthetic pathway, the purification protocols and also the facile particles post-modification (**Figure 25**).

Altogether, non-toxic NDs have been extensively employed in the last decades for a large bench of biological applications,[241] mainly bio-imaging and labelling,[242-244] cancer therapy,[245-247] tissue engineering[248-249] and bacteria killing.[250-252] A review paper written during my PhD years was published in *Journal of Materials Chemistry B*. This work presents the recent studies where ND was used as vector, passive or active element, and give a large overview of their contribution to biomedical research (see in **Annexes**).[253]

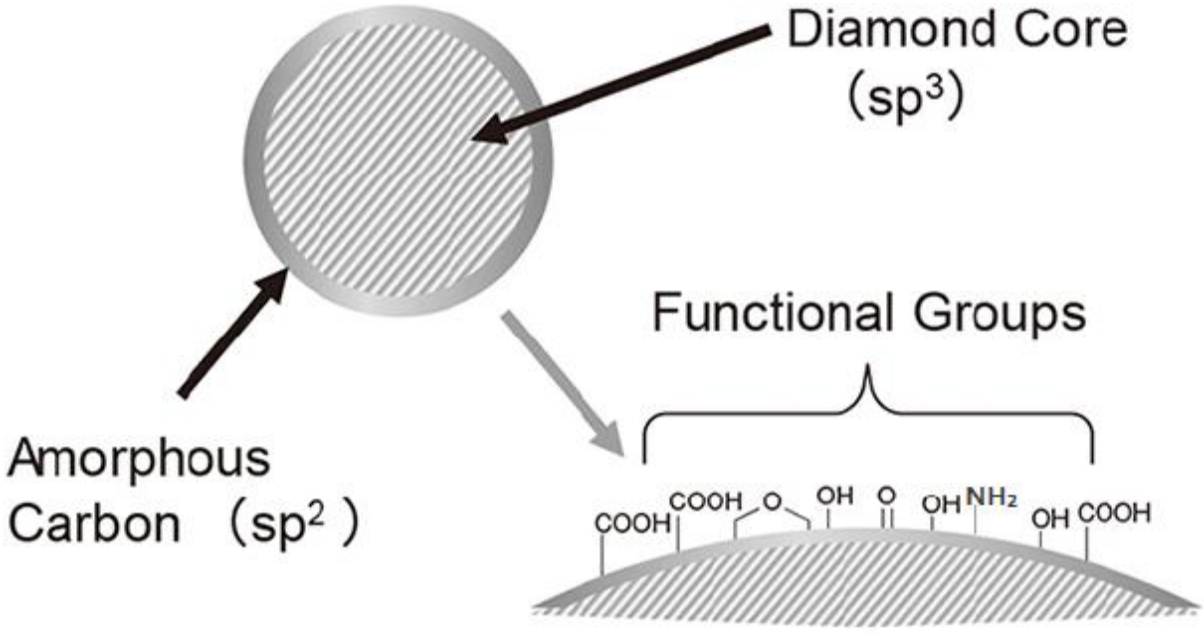

Figure 25: Generic nanodiamond structure. The nature and abundance of core defects and surface functional groups are factors of synthesis, purification and washing steps, and their surface is easily tunable for multistep post-modifications. Adapted from reference 254.

ii. Examples of photodynamic activity

As introduced in the literature review, ND optical properties have recently started to be explored in PDT. Enhanced killing efficiency was obtained under OPE as a global activity of NDs with other PSs capable to generate ROS.[255-257] NDs alone or encapsulated in biocompatible ethenylene PMO NPs even showed significant death of MCF-7 breast cancer cells by TPE-PDT at 800 nm.[258]

An early comprehensive study about NDs-TiO_2 composites demonstrated their potential for PDT under visible light by ROS generation testing in a cell free system or in human cancer cervical cells with good internalization by endocytosis. The authors also proposed a mechanism for explaining the cooperative interaction between the two elements where NDs can absorb photons in visible-NIR region and produce large amounts of electron/hole pairs, due to their sp^2 content and surface functionalities.[259] By this process, TiO_2 semi-conductors NPs could accumulate electrons for enhanced ROS production.[260]

Diamond NPs or ND-based composites skills for phototherapy combined with NDs fluorescence and magnetism characteristics for biological screening are very promising for future theranostic developments. In that respect, we decided to further explore NDs potential for TPEF imaging and TPE-PDT when encapsulated in biocompatible multifunctional PMO nanometric shells (Chapter 2).

2.6 PMO nanoplaftorms in PDT-based strategies

For the last two decades, much effort has been placed in developing efficient PDT systems. One potential outcome of all this research work could be to develop simple and generic vectorization platforms suitable for all biological media. Among the candidates, MON and PMO NPs are characterized by good colloidal stability (contrary to molecular TP-responsive PSs) and easily tunable surface and porosities which can bring stealthiness and targeting properties for bioapplications.

The design of organosilica-based NPs for TPE-PDT is scarcely reported. To our knowledge, only our group reported anticancer *in vitro* and *in vivo* testing using multifunctional PS-PMO systems with PS moieties either homogeneously integrated into the three-dimensional NP framework or encapsulated as cores on which the organosilica shell grows.

Croissant *et al.* designed Au@PMO NPs with a PMO shell containing ethenylene or benzene bridges and two-photon responsive PS units made up of a diaminodiphenylbutadiene core structure. With a concentration of 40 µg mL^{-1}, NPs showed zero dark toxicity and

significant efficiency against MCF-7 cancer cells after 760 nm two-photon irradiation was attributed to the synergy between gold nanospheres and PSs, with respectively 40% and 27% cell death for ethylene and benzene-based core-shell particles. Addition of doxorubicin in the pores led to increased toxicity, both in dark and under irradiation.[261] In another work, they prepared various Au@MON and MON@Au using TEOS, mercaptopropyltrimethoxysilane or the same silylated PS as sol-gel precursors. Interestingly, in the same spirit as for ND@PMO NPs, when gold NPs were post-grafted (MON@Au) on the surface of MON, they displayed significant photoactivity against MCF-7 cancer cell line without any PS in the shell.[262]

Another study reported fluorophore-PMO@PS NPs with a tetrasilylated two-photon donor and ENE as precursors, and a star-shaped bromoquinoline PS grafted by copper catalyzed azide-alkyne click reaction on the surface of the particles. While TPE-PDT experiments without PS confirmed that the two-photon fluorophore was not toxic, fluorophore-PMO@PS NPs caused about 40% cell death under 760 nm irradiation.[196]

Notably, two different studies demonstrated that porphyrins form J-aggregates when covalently integrated into the walls of organosilica NPs by the sol-gel procedure. This was evidenced by comparing the UV-visible absorption spectra of silylated porphyrin precursor and final NPs. After reaction, the Soret band and the Q bands were red shifted, which is a typical sign of J-aggregation. Such constitution endows the NPs of two-photon sensitivity (**Figure 26a**). Aggad and collaborators synthesized PMO NPs with tetrasilylated 5,10,15,20-tetrakis(4-aminophenyl)porphyrin (P) and 1,2-bis(triethoxysilyl)ethane (E) precursors for one or two-photon excitation PDT combined with the delivery of gemcitabine anticancer drug. [263] Unloaded NPs were biocompatible and showed 30% MCF-7 killing after 750 nm two-photon irradiation at 80 µg mL^{-1}. With the loading of gemcitabine, a synergistic effect was observed with 62% cell death. Mauriello Jimenez and coworkers developed 100-300 nm spherical and porous porphyrin-PMO NPs by only using a silylated octapropargyl porphyrin derivative (**Figure 26b**). Amine-functionalized PMO NPs displayed high TPE-PDT efficiency *in vitro* on MDA-MB-231 breast cancer cells (800 nm, 40 µg mL^{-1}). More importantly, the two-photon activity was monitored in zebrafish embryos injected with MDA-MB-231 cancer cells expressing the green fluorescent protein (**Figure 26c**). Without NPs, confocal light scanning microscopy imaging revealed green fluorescence of the embryos, either with laser irradiation or not. Now with incubation with the PMO nanospheres, the larvae showed bright green fluorescence without irradiation and high fluorescence extinction after 800 nm TPE, synonym of high rates of cancer cell death.[264]

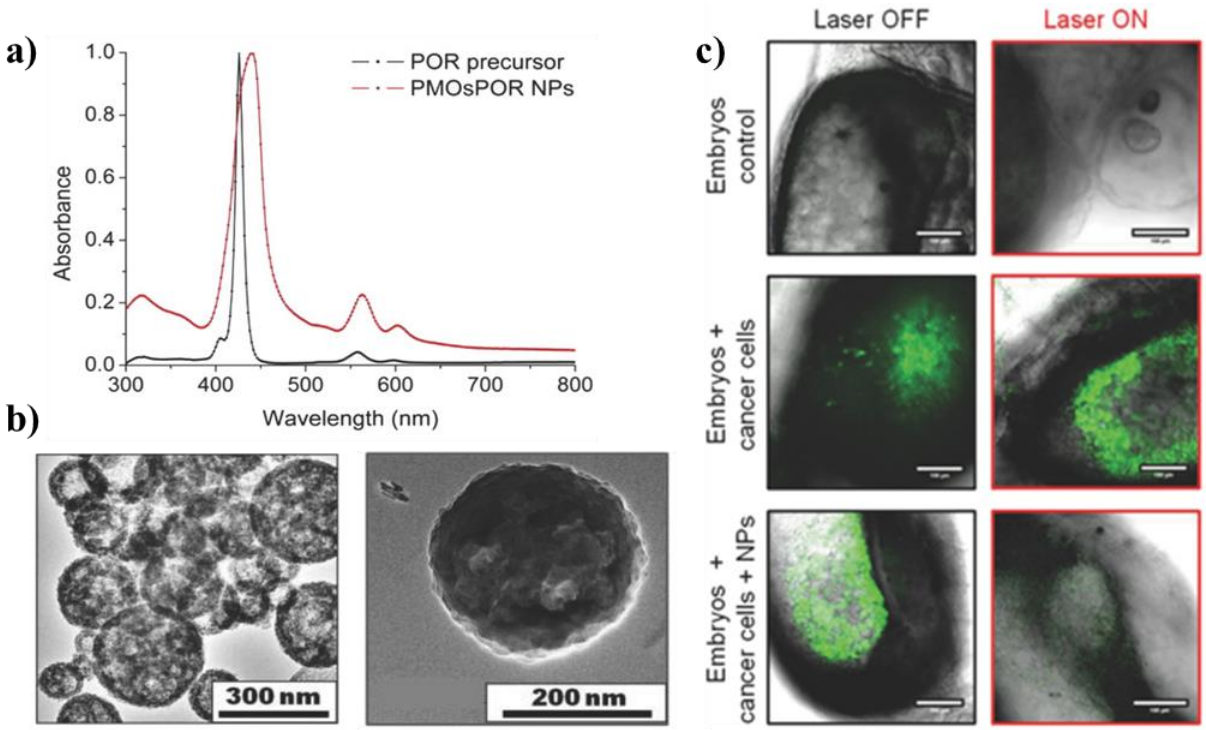

Figure 26: Example of Porphyrin-PMO NPs and their characterization for TPE-PDT. (a) Comparison of absorbance profiles of porphyrin precursor (POR) and associated NPs (PMOsPOR NPs); (b) High-Resolution TEM images of Porphyrin-PMO NPs displaying a spherical shape with cavities inside; (c) Bio-imaging of zebrafish embryos before and after two-photon irradiation (800 nm) in the absence or presence of MDA-MB-231 cancer cells, and with both cancer cells and NPs. Adapted from Mauriello Jimenez *et al.* **(**2018).[264]

While mesoporous organosilica NPs have shown prospective assets for anticancer TPE-PDT, they never have been tested to fight bacterial infections by two-photon irradiation. Because the penetration depth is generally less crucial for topical treatments, most reported aPDT assays in the literature deal with OPE. It would, however, be appropriate to assess the potential of TPE-aPDT to favor the healing of fairly deep skin lesions.

3. Towards combination therapy against infectious diseases

From the literature survey, it is obvious that there is a vital need for the development of alternative antimicrobial approaches for patients where standard therapy does not give positive results. In this section, several examples of recently considered multitherapies to fight infectious diseases will be presented.

3.1 Delivery of multiple antimicrobial drugs

Increasing bacterial resistance calls for the simultaneous delivery of multiple antibiotics and antibacterial agents. As mentioned before (1. of Chapter 1), MSNs and MON NPs have been widely studied for drug or biomolecule transport, including antibiotic delivery for several biomedical applications. As bacteria can be inhibited and killed by various biochemical mechanisms, combining several antimicrobial peptides and antibiotics with different physicochemical properties would much more endanger bacterial cells integrity.

Gounani and coworkers studied the efficiency of MSNs for the simultaneous delivery of vancomycin and polymixin B antibiotics to improve the local drug concentration and reduce the systemic one. Vancomycin prevents assembly of the peptidoglycan scaffold that constitutes bacterial cell envelope, and polymyxin B affects the outer membrane.[265-266] With 45.3% total DLC, the carboxyl-grafted NPs showed synergistic efficiency towards *E. coli*, *P. aeruginosa* and *S. aureus* strains compared to a mixture of free antibiotics at equivalent doses.[267] When adsorbed on the surface of nanoparticles, the antibiotics demonstrated enhanced biocompatibility towards three different human cell lines.

The combination of conventional antibiotics with silver ions have also been tested. In fact, some metals possess intrinsic antibacterial activity and are employed since ancient times. Şen Karaman *et al.* developed chitosan-coated and silver-doped MSNs that showed little antibacterial activity against gram-negative *Vibrio cholerae*. Then, after incubation with kanamycin, the eradication level was significantly increased.[268] Rahmani and collaborators synthesized hollow degradable organosilica nanoparticles loaded with amoxicillin and Ag^+ ions, respectively with 30% and 0.8% DLC in weight. A synergistic effect in reducing *E. coli* growth was observed, while amoxicillin-loaded NPs showed none effect.[269] Li and coworkers studied the delivery of silver ions and gentamycin from biodegradable nanosilver-decorated MON against four different antibiotic resistant strains and their sensitive counterparts. Triggered by GSH, the simultaneous release was very efficient and showed long-term antibacterial capacity in a dose-dependent manner. Notably, the different MIC values obtained

with the whole system were far lower than the one of individual elements, especially against the resistant bacteria.[270]

One of the most recurrent issue with antibiotics is their poor ability to eradicate complex bacterial microenvironments. Wan and collaborators created nanocomposites of silver and biodegradable mesoporous organosilica for a controlled release of alginate lyase enzyme and ceftazidime to eradicate *Pseudomonas aeruginosa* biofilms. They presented high biocompatibility and high DLC, yielding 38.1% in ceftazidime. With such organosilica shell, good antibacterial effects were obtained, including the enzymatic degradation of alginate from the biofilm. Moreover, NPs incubated in mouse lungs at different times after establishment of bacteria beads showed significant eradication levels and WH properties.[271]

3.2 Synergistic photodynamic/antibiotic therapy

Assuming that aPDT is not restrained by AMR issues itself and does not induce resistance towards antibiotics,[272] its combination with antibiotic loading could be an adapted solution to face bacterial infections, either as a second-wave treatment or as a first-line strategy.

Engineered multifunctional nanoparticles have shown their high efficiency for targeted anticancer drug delivery and confinement of PSs for enhanced ROS generation in PDT. While largely used for cancer therapy, their applications for the treatment of bacterial infections have been much less described. It is timely to investigate the efficiency of different organosilica nanoparticles as antibiotic delivery platform as well as alternatives to antibiotics such as photodynamic therapy or combined approaches.

As good example of synergistic antibiotherapy and PDT using nanocarriers, Liu and coworkers prepared MSN@carbon dot-rose bengal loaded with ampicillin (18.3% DLC). Without antibiotic, *E. coli* incubated with nanoparticles and irradiated with green light were inhibited for about 12 hours when the concentration was increased to 100 µg mL^{-1}. When ampicillin was loaded, complete bacteria eradication was visible even after 24 hours.[273] In another study, Valenzuela-Valderrama *et al.* used cationic PSs because of their good interaction with bacterial envelope for antibacterial purpose. They coupled Ir (III)-based compounds with imipenem - able to inhibit bacterial cell wall development - against multidrug resistant *Klebsiella pneumoniae*. Compared to 3 $\log_{10}$ step reduction (> 99.9% killing efficiency) with only ROS generation via PS elements, a cooperative effect was observed with up to 6 $\log_{10}$ reduction rate in colony-forming unit (CFU) per milliliter, with experimental conditions adaptable to *in vivo* or clinical work.[274]

An increasing number of clinical aPDT studies have also been conducted these last years, notably in oral infections. One of them reported that 17 of 18 patients which received both antibiotic and PDT treatment did not have to endure limb amputation. In contrast, all 16 patients that only followed antibiotherapy were subjected to amputation, demonstrating the impact of PDT.[275]

3.3 Photodynamic therapy alongside other treatments

For the post antibiotic-era, combination of several alternative therapies with low risks of acquired resistance would be required. Some research groups already proposed combinations of aPDT with radio-, immuno-, sonodynamic or photothermal therapy, to name a few.

Xu and collaborators obtained encouraging results with upconversion nanoparticles for combined sonodynamic/photodynamic therapy. The system, composed of two different PSs encapsulated within a yolk-structured core covered by a SiO_2 shell, was tested against MRSA and extended spectrum beta-lactamase-producing *E. coli*. This latter type of strain is an important threat since decades causing community-acquired and nosocomial urinary tract infections in hospitals. After optimization, the final conditions tested were 20 min at 1 W cm^{-2} and 10 min at 2 W cm^{-2}, respectively for PDT ($\lambda_{exc.}$ = 980 nm) and sonodynamic therapy. The materials incubated at 125 µg mL^{-1} with 0.5 10^9 CFU mL^{-1} bacteria suspension displayed ≥ 3 $\log_{10}$ reduction rate of the gram-positive strain, and about 2 $\log_{10}$ reduction for the negative one, which was far above each individual therapy.[276]

On a larger scale, Li and coworkers presented promising data in a study about infections on titanium-based medical implants combining sputtered MOS_2 photothermal and NIR PS photodynamic activities. The antibacterial activity was evaluated by spread plate method on *S. aureus* biofilm-infected rats with subcutaneous implementation of biocompatible implants. After 808 nm irradiation for 20 min, a synergistic effect was well visible (**Figure 27a and b**). High efficiency was notably demonstrated by histological analysis using haematoxylin and eosin staining. The results suggested no obvious organ damage after culture for three days and good biofilm eradication compared to dark control and bare titanium implant (**Figure 27c**).[277]

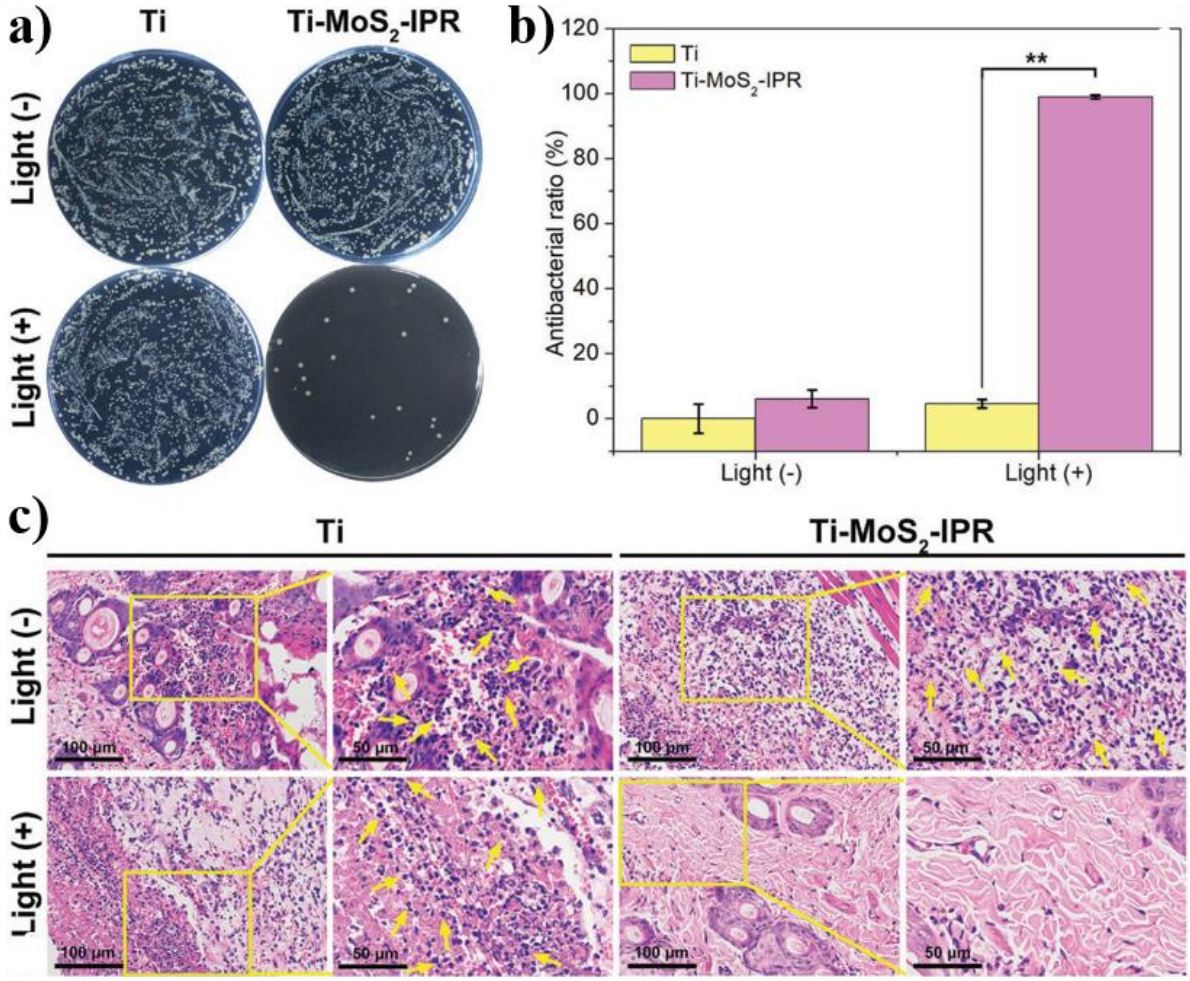

Figure 27: Antibacterial activity assessment *in vivo* after PDT-PTT treatment. (a) Spread plate results of SA biofilm implant in dark or after 808 nm irradiation for 20 min; (b) Antibacterial efficiency of implants calculated by multiple comparison tests; (c) Haematoxylin and eosin staining images in rat tissues illustrating bacterial infection by the rate of neutrophils leucocytes (yellow arrows). IPR: Infrared PS-Polydopamine-RGDC; RGDC: arginine–glycine–aspartic acid–cysteine. **: $p < 0.01$. Adapted from Li *et al.* (2019)**.**[277]

As a conclusion, the future of antimicrobial therapy will certainly lie in such innovative strategies. Nonetheless, there are still a lot of things to investigate in the mechanisms of actions towards planktonic bacteria and biofilm. Mimicking human infections environment would be of great interest to better understand bacteria behavior and development.[278]

Based on the different strategies presented all along this state-of-art introduction for the treatment of cancer or bacterial infections, we tried to develop innovative two-photon responsive systems with a PMO matrix as the common denominator that could be closer to the present therapeutic requirements.

Thus, the experimental part of this thesis work will be separated in four chapters.

A first study about the design of various nanodiamond-organosilica core-shell nanoparticles and their application to *in vitro* anticancer photodynamic therapy will be reported in chapter 2.

Moving to another strategy, chapter 3 will discuss the synthesis of innovative fluorescent three-branched octupolar fluorophores possessing great photophysical properties for biomedical applications.

In chapter 4, one of these newly-synthesized two-photon fluorophores along with a two-photon porphyrin photosensitizer will be integrated in the framework of multifunctional PMO nanoparticles to perform a FRET-enhanced therapeutic strategy. Nanoparticles design and characterization as well as energy transfer quantum yields will be fully detailed.

Then, chapter 5 will be dedicated to the presentation of biological testing with the above materials. It will include results about their ability for two-photon excitation fluorescence imaging, anticancer and antibacterial two-photon excitation photodynamic therapy and antibiotic delivery.

Finally, the strategies and findings of this project will be resumed and some perspectives of potent optimization and bioapplications will be tackled.

Bibliography

1. Agyeman, A. A.; Ofori-Asenso, R., Perspective: Does personalized medicine hold the future for medicine? *Journal of pharmacy & bioallied sciences* **2015,** *7* (3), 239-44.

2. Alshamrani, M., Broad-Spectrum Theranostics and Biomedical Application of Functionalized Nanomaterials. *Polymers* **2022,** *14* (6), 1221.

3. Wang, X.; Liu, L. H.; Ramström, O.; Yan, M., Engineering nanomaterial surfaces for biomedical applications. *Experimental Biology and Medicine* **2009,** *234* (10), 1128-39.

4. Lim, E. K.; Kim, T.; Paik, S.; Haam, S.; Huh, Y. M.; Lee, K., Nanomaterials for Theranostics: Recent Advances and Future Challenges. *Chemical Reviews* **2015,** *115* (1), 327-394.

5. Bertrand, N.; Wu, J.; Xu, X.; Kamaly, N.; Farokhzad, O. C., Cancer nanotechnology: The impact of passive and active targeting in the era of modern cancer biology. *Advanced Drug Delivery Reviews* **2014,** *66*, 2-25.

6. Yao, Y.; Zhou, Y.; Liu, L.; Xu, Y.; Chen, Q.; Wang, Y., et al., Nanoparticle-Based Drug Delivery in Cancer Therapy and Its Role in Overcoming Drug Resistance. *Frontiers in Molecular Biosciences* **2020,** *7*.

7. Jiang, Q.; Liu, Y.; Guo, R.; Yao, X.; Sung, S.; Pang, Z., et al., Erythrocyte-cancer hybrid membrane-camouflaged melanin nanoparticles for enhancing photothermal therapy efficacy in tumors. *Biomaterials* **2019,** *192*, 292-308.

8. Morones, J. R.; Elechiguerra, J. L.; Camacho, A.; Holt, K.; Kouri, J. B.; Ramirez, J. T., et al., The bactericidal effect of silver nanoparticles. *Nanotechnology* **2005,** *16* (10), 2346-2353.

9. Liu, Z.; Tabakman, S.; Welsher, K.; Dai, H. J., Carbon Nanotubes in Biology and Medicine: In vitro and in vivo Detection, Imaging and Drug Delivery. *Nano Research* **2009,** *2* (2), 85-120.

10. Perevedentseva, E.; Lin, Y. C.; Jani, M.; Cheng, C. L., Biomedical applications of nanodiamonds in imaging and therapy. *Nanomedicine* **2013,** *8* (12), 2041-2060.

11. Singh, R. K.; Kumar, R.; Singh, D. P.; Savu, R.; Moshkalev, S. A., Progress in microwave-assisted synthesis of quantum dots (graphene/carbon/semiconducting) for bioapplications: a review. *Materials Today Chemistry* **2019,** *12*, 282-314.

12. Yang, P. P.; Gai, S. L.; Lin, J., Functionalized mesoporous silica materials for controlled drug delivery. *Chemical Society Reviews* **2012,** *41* (9), 3679-3698.

13. Lemière, J.; Carvalho, K.; Sykes, C., Chapter 14 - Cell-sized liposomes that mimic cell motility and the cell cortex. In *Methods in Cell Biology*, Ross, J.; Marshall, W. F., Eds. Academic Press: **2015**; Vol. 128, 271-285.

14. Dash, M.; Chiellini, F.; Ottenbrite, R. M.; Chiellini, E., Chitosan-A versatile semi-synthetic polymer in biomedical applications. *Progress in Polymer Science* **2011,** *36* (8), 981-1014.

15. Burglova, K.; Noureddine, A.; Hodacova, J.; Toquer, G.; Cattoen, X.; Wong Chi Man, M., A General Method for Preparing Bridged Organosilanes with Pendant Functional Groups and Functional Mesoporous Organosilicas. *Chemistry - A European Journal* **2014,** *20* (33), 10371-10382.

16. Kneuer, C.; Sameti, M.; Haltner, E. G.; Schiestel, T.; Schirra, H.; Schmidt, H., et al., Silica nanoparticles modified with aminosilanes as carriers for plasmid DNA. *International Journal of Pharmaceutics* **2000,** *196* (2), 257-61.

17. Stöber, W.; Fink, A.; Bohn, E., Controlled growth of monodisperse silica spheres in the micron size range. *Journal of Colloid and Interface Science* **1968,** *26* (1), 62-69.

18. Chang, J.-H.; Chandrasekar, N.; Shen, S.-Y.; Shkir, M.; Kumar, M., 13 - Biomedical applications. In *Silicon-Based Hybrid Nanoparticles*, Thomas, S.; Nguyen, T. A.; Ahmadi, M.; Yasin, G.; Joshi, N., Eds. Elsevier: **2022**; 277-323.

19. Singh, B.; Na, J.; Konarova, M.; Wakihara, T.; Yamauchi, Y.; Salomon, C., et al., Functional Mesoporous Silica Nanomaterials for Catalysis and Environmental Applications. *Bulletin of the Chemical Society of Japan* **2020,** *93* (12), 1459-1496.

20. Liang, X. J.; Wang, X. S.; Ren, H. X.; Jiang, S. X.; Wang, L. C.; Liu, S. J., Gold nanoparticle decorated graphene oxide/silica composite stationary phase for high-performance liquid chromatography. *Journal of Separation Science* **2014,** *37* (12), 1371-1379.

21. Yadav, A.; Gerislioglu, B.; Ahmadivand, A.; Kaushik, A.; Cheng, G. J.; Ouyang, Z. B., et al., Controlled self-assembly of plasmon-based photonic nanocrystals for high performance photonic technologies. *Nano Today* **2021,** *37*, 101072.

22. Chen, F.; Hableel, G.; Zhao, E. R.; Jokerst, J. V., Multifunctional nanomedicine with silica: Role of silica in nanoparticles for theranostic, imaging, and drug monitoring. *Journal of Colloid and Interface Science* **2018,** *521*, 261-279.

23. Wu, J., The Enhanced Permeability and Retention (EPR) Effect: The Significance of the Concept and Methods to Enhance Its Application. *Journal of Personalized Medicine* **2021,** *11* (8), 771.

24. Pandit, S.; Dutta, D.; Nie, S., Active transcytosis and new opportunities for cancer nanomedicine. *Nature Materials* **2020,** *19* (5), 478-480.

25. Poscher, V.; Teasdale, I.; Salinas, Y., Surfactant-Free Synthesis of Cyclomatrix and Linear Organosilica Phosphazene-Based Hybrid Nanoparticles. *ACS Applied Nano Materials* **2019,** *2* (2), 655-660.

26. Song, Y. P.; Cheng, D.; Luo, J. Q.; Zhang, M.; Yang, Y. N., Surfactant-free synthesis of monodispersed organosilica particles with pure sulfide-bridged silsesquioxane framework chemistry *via* extension of Stober method. *Journal of Colloid and Interface Science* **2021,** *591*, 129-138.

27. Croissant, J. G.; Cattoen, X.; Durand, J. O.; Man, M. W. C.; Khashab, N. M., Organosilica hybrid nanomaterials with a high organic content: syntheses and applications of silsesquioxanes. *Nanoscale* **2016,** *8* (48), 19945-19972.

28. Boday, D. J.; Tolbert, S.; Keller, M. W.; Li, Z.; Wertz, J. T.; Muriithi, B., et al., Non-hydrolytic formation of silica and polysilsesquioxane particles from alkoxysilane monomers with formic acid in toluene/tetrahydrofuran solutions. *Journal of Nanoparticle Research* **2014,** *16* (3), 2313.

29. Kim, S.; Ohulchanskyy, T. Y.; Pudavar, H. E.; Pandey, R. K.; Prasad, P. N., Organically Modified Silica Nanoparticles Co-encapsulating Photosensitizing Drug and Aggregation-Enhanced Two-Photon Absorbing Fluorescent Dye Aggregates for Two-Photon Photodynamic Therapy. *Journal of the American Chemical Society* **2007,** *129* (9), 2669-2675.

30. Arkhireeva, A.; Hay, J. N., Synthesis of sub-200 nm silsesquioxane particles using a modified Stöber sol–gel route. *Journal of Materials Chemistry* **2003,** *13* (12), 3122-3127.

31. Mochizuki, C.; Nakamura, J.; Nakamura, M., Development of Non-Porous Silica Nanoparticles towards Cancer Photo-Theranostics. *Biomedicines* **2021,** *9* (1), 73.

32. Fatieiev, Y.; Croissant, J. G.; Alsaiari, S.; Moosa, B. A.; Anjum, D. H.; Khashab, N. M., Photoresponsive Bridged Silsesquioxane Nanoparticles with Tunable Morphology for Light-Triggered Plasmid DNA Delivery. *ACS Applied Materials & Interfaces* **2015,** *7* (45), 24993-24997.

33. Kim, H.; Röth, D.; Isoe, Y.; Hayashi, K.; Mochizuki, C.; Kalkum, M., et al., Protein corona components of polyethylene glycol-conjugated organosilica nanoparticles modulates macrophage uptake. *Colloids and Surfaces B: Biointerfaces* **2021,** *199*, 111527.

34. Hoffmann, F.; Fröba, M., Vitalising porous inorganic silica networks with organic functions—PMOs and related hybrid materials. *Chemical Society Reviews* **2011,** *40* (2), 608-620.

35. Tsuneo, Y.; Toshio, S.; Kazuyuki, K.; Chuzo, K., The Preparation of Alkyltrimethylammonium–Kanemite Complexes and Their Conversion to Microporous Materials. *Bulletin of the Chemical Society of Japan* **1990,** *63* (4), 988-992.

36. Beck, J. S.; Chu, C. T.-W.; Johnson, I. D.; Kresge, C. T.; Leonowicz, M. E.; Roth, W. J., et al. Synthetic porous crystalline material: its synthesis and use. WO Patent 91/11390, **1991**.

37. Nunes, S. C.; Almeida, P.; de Zea Bermudez, V., Ordered Mesoporous Sol–Gel Materials: From Molecular Sieves to Crystal-Like Periodic Mesoporous Organosilicas. In *The Sol-Gel Handbook*, **2015**; 575-604.

38. Wu, S.-H.; Mou, C.-Y.; Lin, H.-P., Synthesis of mesoporous silica nanoparticles. *Chemical Society Reviews* **2013,** *42* (9), 3862.

39. Koike, N.; Chaikittisilp, W.; Shimojima, A.; Okubo, T., Surfactant-free synthesis of hollow mesoporous organosilica nanoparticles with controllable particle sizes and diversified organic moieties. *RSC Advances* **2016,** *6* (93), 90435-90445.

40. Wang, B.; Wei, Y.; Wang, Q.; Di, J.; Miao, S.; Yu, J., Superhydrophobic magnetic core–shell mesoporous organosilica nanoparticles with dendritic architecture for oil–water separation. *Materials Chemistry Frontiers* **2020,** *4* (7), 2184-2191.

41. Wang, Y.; Zhang, B.; Ding, X.; Du, X., Dendritic mesoporous organosilica nanoparticles (DMONs): Chemical composition, structural architecture, and promising applications. *Nano Today* **2021,** *39*, 101231.

42. Yang, Y.; Wan, J.; Niu, Y.; Gu, Z.; Zhang, J.; Yu, M., et al., Structure-Dependent and Glutathione-Responsive Biodegradable Dendritic Mesoporous Organosilica Nanoparticles for Safe Protein Delivery. *Chemistry of Materials* **2016,** *28* (24), 9008-9016.

43. Teng, Z.; Wang, S.; Su, X.; Chen, G.; Liu, Y.; Luo, Z., et al., Facile Synthesis of Yolk-Shell Structured Inorganic-Organic Hybrid Spheres with Ordered Radial Mesochannels. *Advanced Materials* **2014,** *26* (22), 3741-3747.

44. Zhang, L.; Wang, L.; Yao, H.; Xu, F.; Chen, Y., Biodegradable and biocompatible monodispersed hollow mesoporous organosilica with large pores for delivering biomacromolecules. *Journal of Materials Chemistry B* **2017,** *5* (39), 8013-8025.

45. Wu, M. Y.; Meng, Q. S.; Chen, Y.; Du, Y. Y.; Zhang, L. X.; Li, Y. P., et al., Large-Pore Ultrasmall Mesoporous Organosilica Nanoparticles: Micelle/Precursor Co-templating Assembly and Nuclear-Targeted Gene Delivery. *Advanced Materials* **2015,** *27* (2), 215-222.

46. Yang, Y.; Niu, Y.; Zhang, J.; Meka, A. K.; Zhang, H.; Xu, C., et al., Biphasic Synthesis of Large-Pore and Well-Dispersed Benzene Bridged Mesoporous Organosilica Nanoparticles for Intracellular Protein Delivery. *Small* **2015,** *11* (23), 2743-2749.

47. Du, X.; Shi, B.; Liang, J.; Bi, J.; Dai, S.; Qiao, S. Z., Developing Functionalized Dendrimer-Like Silica Nanoparticles with Hierarchical Pores as Advanced Delivery Nanocarriers. *Advanced Materials* **2013,** *25* (41), 5981-5985.

48. Teng, Z.; Li, W.; Tang, Y.; Elzatahry, A.; Lu, G.; Zhao, D., Mesoporous Organosilica Hollow Nanoparticles: Synthesis and Applications. *Advanced Materials* **2018**, 1707612.

49. Guo, W.; Wang, J.; Lee, S.-J.; Dong, F.; Park, S. S.; Ha, C.-S., A General pH-Responsive Supramolecular Nanovalve Based on Mesoporous Organosilica Hollow Nanospheres. *Chemistry - A European Journal* **2010,** *16* (29), 8641-8646.

50. Koike, N.; Ikuno, T.; Okubo, T.; Shimojima, A., Synthesis of monodisperse organosilica nanoparticles with hollow interiors and porous shells using silica nanospheres as templates. *Chemical Communications* **2013,** *49* (44), 4998.

51. Shi, J. Y.; Wang, C. A.; Li, Z. J.; Wang, Q.; Zhang, Y.; Wang, W., Heterogeneous Organocatalysis at Work: Functionalization of Hollow Periodic Mesoporous Organosilica Spheres with MacMillan Catalyst. *Chemistry – A European Journal* **2011,** *17* (22), 6206-6213.

52. Wu, M.; Chen, Y.; Zhang, L.; Li, X.; Cai, X.; Du, Y., et al., A salt-assisted acid etching strategy for hollow mesoporous silica/organosilica for pH-responsive drug and gene co-delivery. *Journal of Materials Chemistry B* **2015,** *3* (5), 766-775.

53. Chen, Y.; Xu, P.; Chen, H.; Li, Y.; Bu, W.; Shu, Z., et al., Colloidal HPMO Nanoparticles: Silica-Etching Chemistry Tailoring, Topological Transformation, and Nano-Biomedical Applications. *Advanced Materials* **2013,** *25* (22), 3100-3105.

54. Ma, X.; Zhang, J.; Dang, M.; Wang, J.; Tu, Z.; Yuwen, L., et al., Hollow periodic mesoporous organosilica nanospheres by a facile emulsion approach. *Journal of Colloid and Interface Science* **2016,** *475*, 66-71.

55. Norouzi, M.; Elhamifar, D., Magnetic yolk-shell structured methylene and propylamine based mesoporous organosilica nanocomposite: A highly recoverable and durable nanocatalyst with improved efficiency. *Colloids and Surfaces A: Physicochemical and Engineering Aspects* **2021,** *615*, 126226.

56. Li, Q.; Zhao, A. F.; Zhang, N.; Li, X. M.; Zhang, X. T.; Wang, Y., et al., Semi-aromatic polyamide membrane incorporated with yolk-shell mesoporous hybrid nanospheres for ultrahigh permeability and improving comprehensive property. *Journal of Membrane Science* **2022,** *655*, 120612.

57. Zhang, X.; Zhao, Y.; Xu, S.; Yang, Y.; Liu, J.; Wei, Y., et al., Polystyrene sulphonic acid resins with enhanced acid strength *via* macromolecular self-assembly within confined nanospace. *Nature Communications* **2014,** *5* (1).

58. Knezevic, N. Z.; Mauriello Jimenez, C.; Albino, M.; Vukadinovic, A.; Mrakovic, A.; Illes, E., et al., Synthesis and Characterization of Core-Shell Magnetic Mesoporous Silica and Organosilica Nanostructures. *MRS Advances* **2017,** *2* (19-20), 1037-1045.

59. Asefa, T.; MacLachlan, M. J.; Coombs, N.; Ozin, G. A., Periodic mesoporous organosilicas with organic groups inside the channel walls. *Nature* **1999,** *402* (6764), 867-871.

60. Melde, B. J.; Holland, B. T.; Blanford, C. F.; Stein, A., Mesoporous Sieves with Unified Hybrid Inorganic/Organic Frameworks. *Chemistry of Materials* **1999,** *11* (11), 3302-3308.

61. Inagaki, S.; Guan, S.; Fukushima, Y.; Ohsuna, T.; Terasaki, O., Novel Mesoporous Materials with a Uniform Distribution of Organic Groups and Inorganic Oxide in Their Frameworks. *Journal of the American Chemical Society* **1999,** *121* (41), 9611-9614.

62. Inagaki, S.; Guan, S.; Ohsuna, T.; Terasaki, O., An ordered mesoporous organosilica hybrid material with a crystal-like wall structure. *Nature* **2002,** *416* (6878), 304-307.

63. Croissant, J. G.; Cattoën, X.; Wong Chi Man, M.; Durand, J.-O.; Khashab, N. M., Syntheses and applications of periodic mesoporous organosilica nanoparticles. *Nanoscale* **2015,** *7* (48), 20318-20334.

64. Li, D.; Zhang, Y.; Fan, Z.; Chen, J.; Yu, J., Coupling of chromophores with exactly opposite luminescence behaviours in mesostructured organosilicas for high-efficiency multicolour emission. *Chemical Science* **2015,** *6* (11), 6097-6101.

65. Butcher, N. J.; Mortimer, G. M.; Minchin, R. F., Unravelling the stealth effect. *Nature Nanotechnology* **2016,** *11* (4), 310-311.

66. Gheibi Hayat, S. M.; Bianconi, V.; Pirro, M.; Sahebkar, A., Stealth functionalization of biomaterials and nanoparticles by CD47 mimicry. *International Journal of Pharmaceutics* **2019,** *569*, 118628.

67. Jin, J.; Bhujwalla, Z. M., Biomimetic Nanoparticles Camouflaged in Cancer Cell Membranes and Their Applications in Cancer Theranostics. *Frontiers in Oncology* **2019,** *9*, 1560.

68. Xiang, W.; Liu, X.; Zhang, L.; Liu, C.; Liu, G., Cell membrane-encapsulated nanoparticles for vaccines and immunotherapy. *Particuology* **2022,** *64*, 35-42.

69. Grenier, P.; Viana, I. M. O.; Lima, E. M.; Bertrand, N., Anti-polyethylene glycol antibodies alter the protein corona deposited on nanoparticles and the physiological pathways regulating their fate in vivo. *Journal of Controlled Release* **2018,** *287*, 121-131.

70. Su, X. D.; Tao, J.; Wang, Q.; Xu, P.; Luo, W.; Dang, M., et al., Controlled PEGylation of periodic mesoporous organosilica nanospheres for improving their stability in physiological solutions. *Chinese Chemical Letters* **2019,** *30* (4), 929-932.

71. Panja, P.; Das, P.; Mandal, K.; Jana, N. R., Hyperbranched Polyglycerol Grafting on the Surface of Silica-Coated Nanoparticles for High Colloidal Stability and Low Nonspecific Interaction. *ACS Sustainable Chemistry & Engineering* **2017,** *5* (6), 4879-4889.

72. Yu, M. K.; Park, J.; Jon, S., Targeting strategies for multifunctional nanoparticles in cancer imaging and therapy. *Theranostics* **2012,** *2* (1), 3-44.

73. Pardhi, D. M.; Şen Karaman, D.; Timonen, J.; Wu, W.; Zhang, Q.; Satija, S., et al., Anti-bacterial activity of inorganic nanomaterials and their antimicrobial peptide conjugates against resistant and non-resistant pathogens. *International Journal of Pharmaceutics* **2020,** *586*, 119531.

74. Ajdary, M.; Moosavi, M. A.; Rahmati, M.; Falahati, M.; Mahboubi, M.; Mandegary, A., et al., Health Concerns of Various Nanoparticles: A Review of Their in Vitro and in Vivo Toxicity. *Nanomaterials* **2018,** *8* (9), 634.

75. Tan, X.; Yang, L.; Huang, Z.; Yu, Y.; Wang, Z.; Zhang, X., Amphiphilic diselenide-containing supramolecular polymers. *Polymer Chemistry* **2015,** *6* (5), 681-685.

76. Chinnathambi, S.; Tamanoi, F., Recent Development to Explore the Use of Biodegradable Periodic Mesoporous Organosilica (BPMO) Nanomaterials for Cancer Therapy. *Pharmaceutics* **2020,** *12* (9), 890.

77. Poscher, V.; Salinas, Y., Trends in Degradable Mesoporous Organosilica-Based Nanomaterials for Controlling Drug Delivery: A Mini Review. *Materials* **2020,** *13* (17), 3668.

78. Bray, F.; Laversanne, M.; Weiderpass, E.; Soerjomataram, I., The ever-increasing importance of cancer as a leading cause of premature death worldwide. *Cancer* **2021,** *127* (16), 3029-3030.

79. Wu, J.; Bremner, D. H.; Niu, S.; Shi, M.; Wang, H.; Tang, R., et al., Chemodrug-Gated Biodegradable Hollow Mesoporous Organosilica Nanotheranostics for Multimodal Imaging-Guided Low-Temperature Photothermal Therapy/Chemotherapy of Cancer. *ACS Applied Materials & Interfaces* **2018,** *10* (49), 42115-42126.

80. Wu, M.; Meng, Q.; Chen, Y.; Zhang, L.; Li, M.; Cai, X., et al., Large Pore-Sized Hollow Mesoporous Organosilica for Redox-Responsive Gene Delivery and Synergistic Cancer Chemotherapy. *Advanced Materials* **2016,** *28* (10), 1963-1969.

81. Mai, N. X. D.; Birault, A.; Matsumoto, K.; Ta, H. K. T.; Intasa-Ard, S. G.; Morrison, K., et al., Biodegradable Periodic Mesoporous Organosilica (BPMO) Loaded with Daunorubicin: A Promising Nanoparticle-Based Anticancer Drug. *ChemMedChem* **2020,** *15* (7), 593-599.

82. Tamanoi, F.; Chinnathambi, S.; Laird, M.; Komatsu, A.; Birault, A.; Takata, T., et al., Construction of Boronophenylalanine-Loaded Biodegradable Periodic Mesoporous Organosilica Nanoparticles for BNCT Cancer Therapy. *International Journal of Molecular Sciences* **2021,** *22* (5), 2251.

83. Vu, B. T.; Shahin, S. A.; Croissant, J.; Fatieiev, Y.; Matsumoto, K.; Le-Hoang Doan, T., et al., Chick chorioallantoic membrane assay as an in vivo model to study the effect of nanoparticle-based anticancer drugs in ovarian cancer. *Scientific Reports* **2018,** *8* (1), 8524.

84. Rao, K. M.; Parambadath, S.; Kumar, A.; Ha, C.-S.; Han, S. S., Tunable Intracellular Degradable Periodic Mesoporous Organosilica Hybrid Nanoparticles for Doxorubicin Drug Delivery in Cancer Cells. *ACS Biomaterials Science & Engineering* **2018,** *4* (1), 175-183.

85. Shao, T.; Wen, J.; Zhang, Q.; Zhou, Y.; Liu, L.; Yuwen, L., et al., NIR photoresponsive drug delivery and synergistic chemo-photothermal therapy by monodispersed MoS_2 nanosheets wrapped periodic mesoporous organosilicas. *Journal of Materials Chemistry B* **2016,** *4* (47), 7708-7717.

86. Liu, L.; Xu, X. X.; Liang, X. X.; Zhang, X.; Wen, J.; Chen, K., et al., Periodic mesoporous organosilica-coated magnetite nanoparticles combined with lipiodol for transcatheter arterial chemoembolization to inhibit the progression of liver cancer. *Journal of Colloid and Interface Science* **2021,** *591*, 211-220.

87. O'Neill, J. Antimicrobial Resistance: Tackling a Crisis for the Health and Wealth of Nations; *Review on Antimicrobial Resistance*; **2014**.

88. Murray, C. J.; Ikuta, K. S.; Sharara, F.; Swetschinski, L.; Robles Aguilar, G.; Gray, A., et al., Global burden of bacterial antimicrobial resistance in 2019: a systematic analysis. *The Lancet* **2022,** *399* (10325), 629-655.

89. Centers for Disease Control and Prevention, How Antibiotic Resistance Happens. cdc.gov/antibiotic-use, **2021** (accessed 3d November 2022).

90. Fischbach, M. A., Combination therapies for combating antimicrobial resistance. *Current opinion in microbiology* **2011,** *14* (5), 519-23.

91. Hasanzadeh, A.; Gholipour, B.; Rostamnia, S.; Eftekhari, A.; Tanomand, A.; Valizadeh. K, A., et al., Biosynthesis of AgNPs onto the urea-based periodic mesoporous organosilica (Ag_xNPs/Ur-PMO) for antibacterial and cell viability assay. *Journal of Colloid and Interface Science* **2021,** *585*, 676-683.

92. Jamal, M.; Ahmad, W.; Andleeb, S.; Jalil, F.; Imran, M.; Nawaz, M. A., et al., Bacterial biofilm and associated infections. *Journal of the Chinese Medical Association* **2018,** *81* (1), 7-11.

93. Delorme, L. Biofilms : nouvelle approche dans la guérison des plaies [Online], **2012**, docplayer.fr/18979696-Biofilms-nouvelle-approche-dans-la-guerison-des-plaies.html (accessed 14th November 2022).

94. Gao, W.; Chen, Y.; Zhang, Y.; Zhang, Q.; Zhang, L., Nanoparticle-based local antimicrobial drug delivery. *Advanced Drug Delivery Reviews* **2018,** *127*, 46-57.

95. Doron, S.; Gorbach, S. L., Bacterial Infections: Overview. In *International Encyclopedia of Public Health*, Heggenhougen, H. K., Ed. Academic Press: Oxford, **2008**; 273-282.

96. Kehr, N. S., Enantiomorphous Periodic Mesoporous Organosilica-Based Nanocomposite Hydrogel Scaffolds for Cell Adhesion and Cell Enrichment. *Biomacromolecules* **2016,** *17* (3), 1117-1122.

97. Motealleh, A.; Kart, D.; Czieborowski, M.; Kehr, N. S., Functional Nanomaterials and 3D-Printable Nanocomposite Hydrogels for Enhanced Cell Proliferation and for the Reduction of Bacterial Biofilm Formation. *ACS Applied Materials & Interfaces* **2021,** *13* (36), 43755-43768.

98. Quinlan, G. J.; Gutteridge, J. M. C., Hydrixyl radical generation by the tetracycline antibiotics with free radical damage to DNA, lipids and carbohydrate in the presence of iron and copper salts. *Free Radical Biology and Medicine* **1988,** *5* (5), 341-348.

99. Mathieu, D.; Linke, J.-C.; Wattel, F., Non-Healing Wounds. In *Handbook on Hyperbaric Medicine*, Springer Netherlands: Dordrecht, **2006**; 401-428.

100. de Oliveira Gonzalez, A. C.; Costa, T. F.; de Araújo Andrade, Z.; Medrado, A. R. A. P., Wound healing - A literature review. *Anais Brasileiros de Dermatologia* **2016,** *91* (5), 614-620.

101. Finnerty, N. A.; Weinstock, M. B.; Kaide, C. G., Nonhealing wounds, part 1: diagnosis in the urgent care center. *The Journal of Urgent Care Medicine* **2016**.

102. National Center for Health Statistics; Department of Health and Human Services, National Health and Nutrition Examination Survey Data. cdc.gov/diabetes/pdfs/data/statistics/national-diabetes-statistics-report.pdf, **2020** (accessed 15th July 2022).

103. Saeedi, P.; Petersohn, I.; Salpea, P.; Malanda, B.; Karuranga, S.; Unwin, N., et al., Global and regional diabetes prevalence estimates for 2019 and projections for 2030 and 2045: Results from the International Diabetes Federation Diabetes Atlas, 9th edition. *Diabetes Research and Clinical Practice* **2019,** *157*, 107843.

104. Sen, C.; Roy, S.; Gordillo, G., Wound Healing. In *Neligan Plastic Surgery: Volume One*, Elsevier: **2017**.

105. Zhang, P.; Lu, J.; Jing, Y.; Tang, S.; Zhu, D.; Bi, Y., Global epidemiology of diabetic foot ulceration: a systematic review and meta-analysis. *Annals of Medicine* **2017,** *49* (2), 106-116.

106. Wang, J.; Hao, B.; Xue, K.; Fu, H.; Xiao, M.; Zhang, Y., et al., A Smart Photothermal Nanosystem with an Intrinsic Temperature-Control Mechanism for Thermostatic Treatment of Bacterial Infections. *Advanced Materials* **2022,** *34* (44), 2205653.

107. Zeng, K.; Ma, L.; Yang, W.; Lei, S.; Wang, M.; You, Y., et al., Biodegradable nano-organosilica gene carrier for high-efficiency gene transfection. *Journal of Materials Chemistry B* **2020,** *8* (12), 2483-2494.

108. Pinnow, M., Materials for nonlinear optics: Chemical perspectives. *Acta Polymerica* **1993,** *44* (2), 112-112.

109. Rigamonti, L., Schiff base metal complexes for second order nonlinear optics. *La Chimica e l'Industria – Rivista della Società Chimica Italiana* **2010,** *Aprile 2010*, 118-122.

110. Maiman, T. H., Stimulated Optical Radiation in Ruby. *Nature* **1960,** *187* (4736), 493-494.

111. Franken, P. A.; Hill, A. E.; Peters, C. W.; Weinreich, G., Generation of Optical Harmonics. *Physical Review Letters* **1961,** *7* (4), 118-119.

112. Pascal, S.; David, S.; Andraud, C.; Maury, O., Near-infrared dyes for two-photon absorption in the short-wavelength infrared: strategies towards optical power limiting. *Chemical Society Reviews* **2021,** *50* (11), 6613-6658.

113. Göppert-Mayer, M., Über Elementarakte mit zwei Quantensprüngen. *Annalen der Physik* **1931,** *401* (3), 273-294.

114. Kaiser, W.; Garrett, C. G. B., Two-Photon Excitation in CaF_2: Eu^{2+}. *Physical Review Letters* **1961,** *7* (6), 229-231.

115. Peticolas, W. L.; Goldsborough, J. P.; Rieckhoff, K. E., Double Photon Excitation in Organic Crystals. *Physical Review Letters* **1963,** *10* (2), 43-45.

116. Moulton, P. F., Spectroscopic and laser characteristics of Ti:Al2O3. *The Journal of Optical Society of America B* **1986,** *3* (1), 125-133.

117. Pawlicki, M.; Collins, H. A.; Denning, R. G.; Anderson, H. L., Two-Photon Absorption and the Design of Two-Photon Dyes. *Angewandte Chemie International Edition* **2009,** *48* (18), 3244-3266.

118. Wu, L.; Liu, J.; Li, P.; Tang, B.; James, T. D., Two-photon small-molecule fluorescence-based agents for sensing, imaging, and therapy within biological systems. *Chemical Society Reviews* **2021,** *50* (2), 702-734.

119. Rumi, M.; Barlow, S.; Wang, J.; Perry, J. W.; Marder, S. R., Two-Photon Absorbing Materials and Two-Photon-Induced Chemistry. Springer Berlin Heidelberg: **2008**; 1-95.

120. Liu, H. W.; Liu, Y. C.; Wang, P.; Zhang, X. B., Molecular engineering of two-photon fluorescent probes for bioimaging applications. *Methods and Applications in Fluorescence* **2017,** *5* (1), 012003.

121. Strickler, J. H.; Webb, W. W., Three-dimensional optical data storage in refractive media by two-photon point excitation. *Optics Letters* **1991,** *16* (22), 1780-1782.

122. Dvornikov, A. S.; Walker, E. P.; Rentzepis, P. M., Two-Photon Three-Dimensional Optical Storage Memory. *The Journal of Physical Chemistry A* **2009,** *113* (49), 13633-13644.

123. He, G. S.; Xu, G. C.; Prasad, P. N.; Reinhardt, B. A.; Bhatt, J. C.; Dillard, A. G., Two-photon absorption and optical-limiting properties of novel organic compounds. *Optics Letters* **1995,** *20* (5), 435-437.

124. W. Spangler, C., Recent development in the design of organic materials for optical power limiting. *Journal of Materials Chemistry* **1999,** *9* (9), 2013-2020.

125. Maruo, S.; Nakamura, O.; Kawata, S., Three-dimensional microfabrication with two-photon-absorbed photopolymerization. *Optics Letters* **1997,** *22* (2), 132-134.

126. Cumpston, B. H.; Ananthavel, S. P.; Barlow, S.; Dyer, D. L.; Ehrlich, J. E.; Erskine, L. L., et al., Two-photon polymerization initiators for three-dimensional optical data storage and microfabrication. *Nature* **1999,** *398* (6722), 51-54.

127. Lee, K.-S.; Kim, R. H.; Yang, D.-Y.; Park, S. H., Advances in 3D nano/microfabrication using two-photon initiated polymerization. *Progress in Polymer Science* **2008,** *33* (6), 631-681.

128. Belqat, M.; Wu, X. Y.; Gomez, L. P. C.; Malval, J. P.; Dominici, S.; Leuschel, B., et al., Tuning nanomechanical properties of microstructures made by 3D direct laser writing. *Additive Manufacturing* **2021,** *47*, 102232.

129. Yang, Z.; Zhao, N.; Sun, Y.; Miao, F.; Liu, Y.; Liu, X., et al., Highly selective red- and green-emitting two-photon fluorescent probes for cysteine detection and their bio-imaging in living cells. *Chemical Communications* **2012,** *48* (28), 3442-3444.

130. Mao, G.-J.; Wei, T.-T.; Wang, X.-X.; Huan, S.-y.; Lu, D.-Q.; Zhang, J., et al., High-Sensitivity Naphthalene-Based Two-Photon Fluorescent Probe Suitable for Direct Bioimaging of H_2S in Living Cells. *Analytical Chemistry* **2013,** *85* (16), 7875-7881.

131. Sun, W.; Fan, J.; Hu, C.; Cao, J.; Zhang, H.; Xiong, X., et al., A two-photon fluorescent probe with near-infrared emission for hydrogen sulfide imaging in biosystems. *Chemical Communications* **2013,** *49* (37), 3890-3892.

132. Tang, Y.; Kong, X.; Xu, A.; Dong, B.; Lin, W., Development of a Two-Photon Fluorescent Probe for Imaging of Endogenous Formaldehyde in Living Tissues. *Angewandte Chemie International Edition* **2016,** *55* (10), 3356-3359.

133. Celli, J. P.; Spring, B. Q.; Rizvi, I.; Evans, C. L.; Samkoe, K. S.; Verma, S., et al., Imaging and photodynamic therapy: mechanisms, monitoring, and optimization. *Chemical Reviews* **2010,** *110* (5), 2795-838.

134. Shen, Y.; Shuhendler, A. J.; Ye, D.; Xu, J.-J.; Chen, H.-Y., Two-photon excitation nanoparticles for photodynamic therapy. *Chemical Society Reviews* **2016,** *45* (24), 6725-6741.

135. Hermann, J. P.; Ducuing, J., Absolute Measurement of Two-Photon Cross Sections. *Physical Review A* **1972,** *5* (6), 2557-2568.

136. He, G. S.; Tan, L.-S.; Zheng, Q.; Prasad, P. N., Multiphoton Absorbing Materials: Molecular Designs, Characterizations, and Applications. *Chemical Reviews* **2008,** *108* (4), 1245-1330.

137. Sheik-Bahae, M.; Said, A.; Wei, T.-H.; Hagan, D. J.; Van Stryland, E., Sensitive Measurement of Optical Nonlinearities Using a Single Beam. *IEEE Journal of Quantum Electronics* **1990,** *26*, 760-769.

138. Kobayashi, H.; Ogawa, M.; Alford, R.; Choyke, P. L.; Urano, Y., New Strategies for Fluorescent Probe Design in Medical Diagnostic Imaging. *Chemical Reviews* **2010,** *110* (5), 2620-2640.

139. Xu, L.; Lin, W.; Huang, B.; Zhang, J.; Long, X.; Zhang, W., et al., The design strategies and applications for organic multi-branched two-photon absorption chromophores with novel cores and branches: a recent review. *Journal of Materials Chemistry C* **2021,** *9* (5), 1520-1536.

140. Morales, A. R.; Belfield, K. D.; Hales, J. M.; Van Stryland, E. W.; Hagan, D. J., Synthesis of Two-Photon Absorbing Unsymmetrical Fluorenyl-Based Chromophores. *Chemistry of Materials* **2006,** *18* (20), 4972-4980.

141. Yao, S.; Belfield, K. D., Two-Photon Fluorescent Probes for Bioimaging. *European Journal of Organic Chemistry* **2012,** *2012* (17), 3199-3217.

142. Le Droumaguet, C.; Sourdon, A.; Genin, E.; Mongin, O.; Blanchard-Desce, M., Two-Photon Polarity Probes Built from Octupolar Fluorophores: Synthesis, Structure-Properties Relationships, and Use in Cellular Imaging. *Chemistry - An Asian Journal* **2013,** *8* (12), 2984-3001.

143. Ren, Y.; Xin, Q.; Tao, X.-T.; Wang, L.; Yu, X.-Q.; Yang, J.-X., et al., Novel multi-branched organic compounds with enhanced two-photon absorption benefiting from the strong electronic coupling. *Chemical Physics Letters* **2005,** *414* (1), 253-258.

144. Wang, D.; Wang, X.; He, Q.; Zhou, M.; Rui, W.; Tao, X., et al., Enhanced two-photon absorption of novel four-branched chromophore *via* vibronic coupling. *Tetrahedron Letters* **2008,** *49* (41), 5871-5876.

145. Chung, S.-J.; Kim, K.-S.; Lin, T.-C.; He, G. S.; Swiatkiewicz, J.; Prasad, P. N., Cooperative Enhancement of Two-Photon Absorption in Multi-branched Structures. *The Journal of Physical Chemistry B* **1999,** *103* (49), 10741-10745.

146. Gorelik, T. E.; van de Streek, J.; Meier, H.; Andernach, L.; Opatz, T., Crystal structure analysis of a star-shaped triazine compound: a combination of single-crystal three-dimensional electron diffraction and powder X-ray diffraction. *Acta Crystallographica Section B* **2018,** *74* (3), 287-294.

147. Wan, Y.; Yan, L.; Zhao, Z.; Ma, X.; Guo, Q.; Jia, M., et al., Gigantic Two-Photon Absorption Cross Sections and Strong Two-Photon Excited Fluorescence in Pyrene Core Dendrimers with Fluorene/Carbazole as Dendrons and Acetylene as Linkages. *The Journal of Physical Chemistry B* **2010,** *114* (36), 11737-11745.

148. D. Nolting, D.; C. Gore, J.; Pham, W., Near-Infrared Dyes: Probe Development and Applications in Optical Molecular Imaging. *Current Organic Synthesis* **2011,** *8* (4), 521-534.

149. Yuan, L.; Lin, W.; Zheng, K.; He, L.; Huang, W., Far-red to near infrared analyte-responsive fluorescent probes based on organic fluorophore platforms for fluorescence imaging. *Chemical Society Reviews* **2013,** *42* (2), 622-661.

150. Cao, J.; Zhu, B.; Zheng, K.; He, S.; Meng, L.; Song, J., et al., Recent Progress in NIR-II Contrast Agent for Biological Imaging. *Frontiers in Bioengineering and Biotechnology* **2019,** *7*, 487.

151. Sourdon, A.; Gary-Bobo, M.; Maynadier, M.; Garcia, M.; Majoral, J. P.; Caminade, A. M., et al., Dendrimeric Nanoparticles for Two-Photon Photodynamic Therapy and Imaging: Synthesis, Photophysical Properties, Innocuousness in Daylight and Cytotoxicity under Two-Photon Irradiation in the NIR. *Chemistry – A European Journal* **2019,** *25* (14), 3637-3649.

152. Lu, D. L.; Chen, H.; Yan, X. F.; Wang, L. Z.; Zhang, J. L., Ratiometric Hg2+ Sensor Based on Periodic Mesoporous Organosilica Nanoparticles and Forster Resonance Energy Transfer. *Journal of Photochemistry and Photobiology A: Chemistry* **2015,** *299*, 125-130.

153. Nakamura, M.; Hayashi, K.; Nakano, M.; Kanadani, T.; Miyamoto, K.; Kori, T., et al., Identification of Polyethylene Glycol-Resistant Macrophages on Stealth Imaging in Vitro Using Fluorescent Organosilica Nanoparticles. *ACS Nano* **2015,** *9* (2), 1058-1071.

154. Abrahamse, H.; Michael, H. R., New photosensitizers for photodynamic therapy. *Biochemical Journal* **2016,** *473* (4), 347-364.

155. Wang, S.; Wu, W.; Manghnani, P.; Xu, S.; Wang, Y.; Goh, C. C., et al., Polymerization-Enhanced Two-Photon Photosensitization for Precise Photodynamic Therapy. *ACS Nano* **2019,** *13* (3), 3095-3105.

156. Zheng, Z.; Liu, H.; Zhai, S.; Zhang, H.; Shan, G.; Kwok, R. T. K., et al., Highly efficient singlet oxygen generation, two-photon photodynamic therapy and melanoma ablation by rationally designed mitochondria-specific near-infrared AIEgens. *Chemical Science* **2020,** *11* (9), 2494-2503.

157. von Tappeiner, H., Therapeutische Versuche mit fluoreszierenden Stoffen. *Munchener Medizinische Wochenschrift 1* **1903**, 2042-2044.

158. von Tappeiner, H., Die photodynamische Erscheinung (Sensibilisierung durch fluoreszierende Stoffe). *Ergebnisse der Physiologie* **1909,** *8* (1), 698-741.

159. Dougherty, T. J., A brief history of clinical photodynamic therapy development at Roswell Park Cancer Institute. *Journal of Clinical Laser Medicine and Surgery* **1996,** *14* (5), 219-21.

160. Dougherty, T. J., Photodynamic therapy (PDT) of malignant tumors. *Critical Reviews in Oncology/Hematology* **1984,** *2* (2), 83-116.

161. Chou, T. M.; Woodburn, K. W.; Cheong, W. F.; Lacy, S. A.; Sudhir, K.; Adelman, D. C., et al., Photodynamic therapy: applications in atherosclerotic vascular disease with motexafin lutetium. *Catheterization and Cardiovascular Interventions* **2002,** *57* (3), 387-94.

162. Wang, J.; Zheng, M.; Xie, Z., Carrier-free core-shell nanodrugs for synergistic two-photon photodynamic therapy of cervical cancer. *Journal of Colloid and Interface Science* **2019,** *535*, 84-91.

163. Bressler, N. M., Photodynamic therapy of subfoveal choroidal neovascularization in age-related macular degeneration with verteporfin: two-year results of 2 randomized clinical trials-tap report 2. *Archives of Ophthalmology* **2001,** *119* (2), 198-207.

164. Smits, T.; Kleinpenning, M. M.; van Erp, P. E.; van de Kerkhof, P. C.; Gerritsen, M. J., A placebo-controlled randomized study on the clinical effectiveness, immunohistochemical changes and protoporphyrin IX accumulation in fractionated 5-aminolaevulinic acid-photodynamic therapy in patients with psoriasis. *The British Journal of Dermatology* **2006,** *155* (2), 429-36.

165. Tschen, E. H.; Wong, D. S.; Pariser, D. M.; Dunlap, F. E.; Houlihan, A.; Ferdon, M. B., Photodynamic therapy using aminolaevulinic acid for patients with nonhyperkeratotic actinic keratoses of the face and scalp: phase IV multicentre clinical trial with 12-month follow up. *The British Journal of Dermatology* **2006,** *155* (6), 1262-9.

166. Kuo, W.-S.; Chang, C.-Y.; Chen, H.-H.; Hsu, C.-L. L.; Wang, J.-Y.; Kao, H.-F., et al., Two-Photon Photoexcited Photodynamic Therapy and Contrast Agent with Antimicrobial Graphene Quantum Dots. *ACS Applied Materials & Interfaces* **2016,** *8* (44), 30467-30474.

167. Kuo, W.-S.; Shao, Y.-T.; Huang, K.-S.; Chou, T.-M.; Yang, C.-H., Antimicrobial Amino-Functionalized Nitrogen-Doped Graphene Quantum Dots for Eliminating Multidrug-Resistant Species in Dual-Modality Photodynamic Therapy and Bioimaging under Two-Photon Excitation. *ACS Applied Materials & Interfaces* **2018,** *10* (17), 14438-14446.

168. Niavarzi, S.; Pourhajibagher, M.; Khedmat, S.; Ghabraei, S.; Chiniforush, N.; Bahador, A., Effect of ultrasonic activation on the efficacy of antimicrobial photodynamic therapy: Evaluation of penetration depth of photosensitizer and elimination of Enterococcus faecalis biofilms. *Photodiagnosis and Photodynamic Therapy* **2019,** *27*, 362-366.

169. Ghorbani, J.; Rahban, D.; Aghamiri, S.; Teymouri, A.; Bahador, A., Photosensitizers in antibacterial photodynamic therapy: an overview. *Laser Therapy* **2018,** *27* (4), 293-302.

170. Oyama, J.; Fernandes Herculano Ramos-Milaré, Á. C.; Lopes Lera-Nonose, D. S. S.; Nesi-Reis, V.; Galhardo Demarchi, I.; Alessi Aristides, S. M., et al., Photodynamic therapy in wound healing in vivo: a systematic review. *Photodiagnosis and Photodynamic Therapy* **2020,** *30*, 101682.

171. Garcia, V. G.; De Lima, M. A.; Okamoto, T.; Milanezi, L. A.; Júnior, E. C. G.; Fernandes, L. A., et al., Effect of photodynamic therapy on the healing of cutaneous third-degree-burn: histological study in rats. *Lasers in Medical Science* **2010,** *25* (2), 221-228.

172. Garrier, J.; Bezdetnaya, L.; Barlier, C.; Gräfe, S.; Guillemin, F.; D'Hallewin, M.-A., Foslip®-based photodynamic therapy as a means to improve wound healing. *Photodiagnosis and Photodynamic Therapy* **2011,** *8* (4), 321-327.

173. Rudenko, T. G.; Shekhter, A. B.; Guller, A. E.; Aksenova, N. A.; Glagolev, N. N.; Ivanov, A. V., et al., Specific Features of Early Stage of the Wound Healing Process Occurring Against the Background of Photodynamic Therapy Using Fotoditazin Photosensitizer–Amphiphilic Polymer Complexes. *Photochemistry and Photobiology* **2014,** *90* (6), 1413-1422.

174. Yano, S.; Hirohara, S.; Obata, M.; Hagiya, Y.; Ogura, S.-i.; Ikeda, A., et al., Current states and future views in photodynamic therapy. *Journal of Photochemistry and Photobiology C: Photochemistry Reviews* **2011,** *12* (1), 46-67.

175. Shen, Y. Z.; Shuhendler, A. J.; Ye, D. J.; Xu, J. J.; Chen, H. Y., Two-photon excitation nanoparticles for photodynamic therapy. *Chemical Society Reviews* **2016,** *45* (24), 6725-6741.

176. Sun, Z. Y.; Zhang, L. P.; Wu, F. P.; Zhao, Y. X., Photosensitizers for Two-Photon Excited Photodynamic Therapy. *Advanced Functional Materials* **2017,** *27* (48), 1704079.

177. Horne, T. K.; Cronjé, M. J., Mechanistics and photo-energetics of macrocycles and photodynamic therapy: An overview of aspects to consider for research. *Chemical Biology & Drug Design* **2017,** *89* (2), 221-242.

178. DeRosa, M. C.; Crutchley, R. J., Photosensitized singlet oxygen and its applications. *Coordination Chemistry Reviews* **2002,** *233*, 351-371.

179. Spring, B. Q.; Rizvi, I.; Xu, N.; Hasan, T., The role of photodynamic therapy in overcoming cancer drug resistance. *Photochemical & Photobiological Sciences* **2015,** *14* (8), 1476-1491.

180. Agostinis, P.; Berg, K.; Cengel, K. A.; Foster, T. H.; Girotti, A. W.; Gollnick, S. O., et al., Photodynamic therapy of cancer: An update. *CA: A Cancer Journal for Clinicians* **2011,** *61* (4), 250-281.

181. Bolze, F.; Jenni, S.; Sour, A.; Heitz, V., Molecular photosensitisers for two-photon photodynamic therapy. *Chemical Communications* **2017,** *53* (96), 12857-12877.

182. Li, L.; Fourkas, J. T., Multiphoton polymerization. *Materials Today* **2007,** *10* (6), 30-37.

183. Mallidi, S.; Anbil, S.; Bulin, A.-L.; Obaid, G.; Ichikawa, M.; Hasan, T., Beyond the Barriers of Light Penetration: Strategies, Perspectives and Possibilities for Photodynamic Therapy. *Theranostics* **2016,** *6* (13), 2458-2487.

184. Kim, M.; Jung, H. Y.; Park, H. J., Topical PDT in the Treatment of Benign Skin Diseases: Principles and New Applications. *International Journal of Molecular Sciences* **2015,** *16* (10), 23259-23278.

185. Valeur, B., Resonance Energy Transfer and Its Applications. In *Molecular Fluorescence*, **2001**; 247-272.

186. Förster, T., Zwischenmolekulare Energiewanderung und Fluoreszenz. *Annalen der Physik* **1948,** *437* (1-2), 55-75.

187. Liu, H. L.; Yang, Y.; Wang, A. H.; Han, M. J.; Cui, W.; Li, J. B., Hyperbranched Polyglycerol-Doped Mesoporous Silica Nanoparticles for One- and Two-Photon Activated Photodynamic Therapy. *Advanced Functional Materials* **2016,** *26* (15), 2561-2570.

188. Lindig, B. A.; Rodgers, M. A. J.; Schaap, A. P., Determination of the lifetime of singlet oxygen in water-d2 using 9,10-anthracenedipropionic acid, a water-soluble probe. *Journal of the American Chemical Society* **1980,** *102* (17), 5590-5593.

189. Tan, L.-S.; Kannan, R.; Matuszewski, M. J.; Khur, I. J.; Feld, W. A.; Dang, T. D., et al. In *Functionalization of heterocyclic diphenylamino-based two-photon absorbing materials for microfabrication, data storage, and upconverted imaging*, Multiphoton Absorption and Nonlinear Transmission Processes: Materials, Theory, and Applications, SPIE: 2003; pp 171-178.

190. Oar, M. A.; Serin, J. M.; Dichtel, W. R.; Fréchet, J. M. J.; Ohulchanskyy, T. Y.; Prasad, P. N., Photosensitization of Singlet Oxygen *via* Two-Photon-Excited Fluorescence Resonance Energy Transfer in a Water-Soluble Dendrimer. *Chemistry of Materials* **2005,** *17* (9), 2267-2275.

191. Qi, Z.-D.; Li, D.-W.; Jiang, P.; Jiang, F.-L.; Li, Y.-S.; Liu, Y., et al., Biocompatible CdSe quantum dot-based photosensitizer under two-photon excitation for photodynamic therapy. *Journal of Materials Chemistry* **2011,** *21* (8), 2455.

192. Shen, X.; Li, L.; Wu, H.; Yao, S. Q.; Xu, Q.-H., Photosensitizer-doped conjugated polymer nanoparticles for simultaneous two-photon imaging and two-photon photodynamic therapy in living cells. *Nanoscale* **2011,** *3* (12), 5140-5146.

193. Cheng, S.-H.; Hsieh, C.-C.; Chen, N.-T.; Chu, C.-H.; Huang, C.-M.; Chou, P.-T., et al., Well-defined mesoporous nanostructure modulates three-dimensional interface energy transfer for two-photon activated photodynamic therapy. *Nano Today* **2011,** *6* (6), 552-563.

194. Fowley, C.; Nomikou, N.; McHale, A. P.; McCaughan, B.; Callan, J. F., Extending the tissue penetration capability of conventional photosensitisers: a carbon quantum dot–protoporphyrin IX conjugate for use in two-photon excited photodynamic therapy. *Chemical Communications* **2013,** *49* (79), 8934.

195. Wang, J.; Zhang, Z.; Zha, S.; Zhu, Y.; Wu, P.; Ehrenberg, B., et al., Carbon nanodots featuring efficient FRET for two-photon photodynamic cancer therapy with a low fs laser power density. *Biomaterials* **2014,** *35* (34), 9372-81.

196. Croissant, J. G.; Picard, S.; Aggad, D.; Klausen, M.; Mauriello Jimenez, C.; Maynadier, M., et al., Fluorescent periodic mesoporous organosilica nanoparticles dual-functionalized *via* click chemistry for two-photon photodynamic therapy in cells. *Journal of Materials Chemistry B* **2016,** *4* (33), 5567-5574.

197. Sun, B.; Wang, L.; Li, Q.; He, P.; Liu, H.; Wang, H., et al., Bis(pyrene)-Doped Cationic Dipeptide Nanoparticles for Two-Photon-Activated Photodynamic Therapy. *Biomacromolecules* **2017,** *18* (11), 3506-3513.

198. Cao, H. Q.; Qi, Y. F.; Yang, Y.; Wang, L.; Sun, J. H.; Li, Y., et al., Assembled Nanocomplex for Improving Photodynamic Therapy through Intraparticle Fluorescence Resonance Energy Transfer. *Chemistry - An Asian Journal* **2018,** *13* (22), 3540-3546.

199. Cao, H. Q.; Yang, Y.; Qi, Y. F.; Li, Y.; Sun, B. B.; Li, Y., et al., Intraparticle FRET for Enhanced Efficiency of Two-Photon Activated Photodynamic Therapy. *Advanced Healthcare Materials* **2018,** *7* (12), 1701357.

200. Vangara, A.; Pramanik, A.; Gao, Y.; Gates, K.; Begum, S.; Ray, P. C., Fluorescence Resonance Energy Transfer Based Highly Efficient Theranostic Nanoplatform for Two-Photon Bioimaging and Two-Photon Excited Photodynamic Therapy of Multiple Drug Resistance Bacteria. *ACS Applied Bio Materials* **2018,** *1* (2), 298-309.

201. Zhu, M.; Su, C.; Xing, P.; Zhou, Y.; Gong, L.; Zhang, J., et al., An AceDAN–porphyrin(Zn) dyad for fluorescence imaging and photodynamic therapy *via* two-photon excited FRET. *Inorganic Chemistry Frontiers* **2018,** *5* (12), 3061-3066.

202. Zhu, M.; Zhang, J.; Zhou, Y.; Xing, P.; Gong, L.; Su, C., et al., Two-Photon Excited FRET Dyads for Lysosome-Targeted Imaging and Photodynamic Therapy. *Inorganic Chemistry* **2018,** *57* (18), 11537-11542.

203. Luo, L.; Yin, Z.; Qi, Y. M.; Liu, S.; Yi, Y.; Tian, X. H., et al., An intracellular enzyme-responsive polymeric prodrug with synergistic effect of chemotherapy and two-photon photodynamic therapy. *Applied Materials Today* **2021,** *23*, 100996.

204. Roy, I.; Ohulchanskyy, T. Y.; Pudavar, H. E.; Bergey, E. J.; Oseroff, A. R.; Morgan, J., et al., Ceramic-based nanoparticles entrapping water-insoluble photosensitizing anticancer drugs: a novel drug-carrier system for photodynamic therapy. *Journal of the American Chemical Society* **2003,** *125* (26), 7860-5.

205. Boyle, R. W.; Dolphin, D., Structure and Biodistribution Relationships of Photodynamic Sensitizers. *Photochemistry and Photobiology* **1996,** *64* (3), 469-485.

206. Monnereau, C.; Andraud, C., Thérapie photodynamique : évolution chimique des photosensibilisateurs. *Techniques de l'Ingenieur* **2013,** *IN161*, 1.

207. Ogura, S.-i.; Tabata, K.; Fukushima, K.; Kamachi, T.; Okura, I., Development of phthalocyanines for photodynamic therapy. *Journal of Porphyrins and Phthalocyanines* **2006,** *10* (09), 1116-1124.

208. Wang, S.; Bromley, E.; Xu, L.; Chen, J. C.; Keltner, L., Talaporfin sodium. *Expert Opinion on Pharmacotherapy* **2010,** *11* (1), 133-140.

209. Schuitmaker, J. J.; van Best, J. A.; van Delft, J. L.; Dubbelman, T. M.; Oosterhuis, J. A.; de Wolff-Rouendaal, D., Bacteriochlorin a, a new photosensitizer in photodynamic therapy. In vivo results. *Investigative Ophthalmology & Visual Science* **1990,** *31* (8), 1444-50.

210. Sharman, W. M.; van Lier, J. E.; Allen, C. M., Targeted photodynamic therapy *via* receptor mediated delivery systems. *Advanced Drug Delivery Reviews* **2004,** *56* (1), 53-76.

211. Mfouo-Tynga, I. S.; Dias, L. D.; Inada, N. M.; Kurachi, C., Features of third generation photosensitizers used in anticancer photodynamic therapy: Review. *Photodiagnosis and Photodynamic Therapy* **2021,** *34*, 102091.

212. Hino, S.; Funada, R.; Sugikawa, K.; Kawasaki, R.; Koumoto, K.; Suzuki, T., et al., Mechanism toward Turn-on of Polysaccharide-Porphyrin Complexes for Fluorescence Probes and Photosensitizers in Photodynamic Therapy in Living Cells. *ChemMedChem* **2021,** *16* (5), 793-803.

213. Plekhova, N.; Shevchenko, O.; Korshunova, O.; Stepanyugina, A.; Tananaev, I.; Apanasevich, V., Development of Novel Tetrapyrrole Structure Photosensitizers for Cancer Photodynamic Therapy. *Bioengineering* **2022,** *9* (2), 82.

214. Cieplik, F.; Späth, A.; Leibl, C.; Gollmer, A.; Regensburger, J.; Tabenski, L., et al., Blue light kills *Aggregatibacter actinomycetemcomitans* due to its endogenous photosensitizers. *Clinical Oral Investigations* **2014,** *18* (7), 1763-9.

215. Dixon, D. W., The Colours of Life: An Introduction to the Chemistry of Porphyrins and Related Compounds. Lionel R. Milgrom. *The Quarterly Review of Biology* **2000,** *75* (1), 45-46.

216. Kingsbury, C. J.; Senge, M. O., The shape of porphyrins. *Coordination Chemistry Reviews* **2021,** *431*, 213760.

217. Valentine, R. M.; Ibbotson, S. H.; Wood, K.; Brown, C. T. A.; Moseley, H., Modelling fluorescence in clinical photodynamic therapy. *Photochemical & Photobiological Sciences* **2013,** *12* (1), 203-213.

218. Biswas, S.; Ahn, H.-Y.; Bondar, M. V.; Belfield, K. D., Two-Photon Absorption Enhancement of Polymer-Templated Porphyrin-Based J-Aggregates. *Langmuir* **2012,** *28* (2), 1515-1522.

219. Ray, P. C.; Sainudeen, Z., Very Large Infrared Two-Photon Absorption Cross Section of Asymmetric Zinc Porphyrin Aggregates: Role of Intermolecular Interaction and Donor−Acceptor Strengths. *The Journal of Physical Chemistry A* **2006,** *110* (44), 12342-12347.

220. Khurana, M.; Collins, H. A.; Karotki, A.; Anderson, H. L.; Cramb, D. T.; Wilson, B. C., Quantitative In Vitro Demonstration of Two-Photon Photodynamic Therapy Using Photofrin®and Visudyne®. *Photochemistry and Photobiology* **2007,** *83* (6), 1441-1448.

221. Ogawa, K.; Hasegawa, H.; Inaba, Y.; Kobuke, Y.; Inouye, H.; Kanemitsu, Y., et al., Water-soluble bis(imidazolylporphyrin) self-assemblies with large two-photon absorption cross sections as potential agents for photodynamic therapy. *Journal of Medicinal Chemistry* **2006,** *49* (7), 2276-83.

222. Ogawa, K.; Dy, J. T.; Kobuke, Y.; Ogura, S.-i.; Okura, I., Singlet Oxygen Generation and Photocytotoxicity against Tumor Cell by Two-Photon Absorption. *Molecular Crystals and Liquid Crystals* **2007,** *471* (1), 61-67.

223. Collins, H. A.; Khurana, M.; Moriyama, E. H.; Mariampillai, A.; Dahlstedt, E.; Balaz, M., et al., Blood-vessel closure using photosensitizers engineered for two-photon excitation. *Nature Photonics* **2008,** *2* (7), 420-424.

224. Zhang, T.; Lan, R.; Gong, L.; Wu, B.; Wang, Y.; Kwong, D. W. J., et al., An Amphiphilic BODIPY-Porphyrin Conjugate: Intense Two-Photon Absorption and Rapid Cellular Uptake for Two-Photon-Induced Imaging and Photodynamic Therapy. *ChemBioChem* **2015,** *16* (16), 2357-2364.

225. Qian, J.; Wang, D.; Cai, F.; Zhan, Q.; Wang, Y.; He, S., Photosensitizer encapsulated organically modified silica nanoparticles for direct two-photon photodynamic therapy and In Vivo functional imaging. *Biomaterials* **2012,** *33* (19), 4851-4860.

226. Chen, N.-T.; Tang, K.-C.; Chung, M.-F.; Cheng, S.-H.; Huang, C.-M.; Chu, C.-H., et al., Enhanced plasmonic resonance energy transfer in mesoporous silica-encased gold nanorod for two-photon-activated photodynamic therapy. *Theranostics* **2014,** *4* (8), 798-807.

227. Zhao, T.; Yu, K.; Li, L.; Zhang, T.; Guan, Z.; Gao, N., et al., Gold Nanorod Enhanced Two-Photon Excitation Fluorescence of Photosensitizers for Two-Photon Imaging and Photodynamic Therapy. *ACS Applied Materials & Interfaces* **2014,** *6* (4), 2700-2708.

228. Croissant, J. G.; Mauriello-Jimenez, C.; Maynadier, M.; Cattoen, X.; Wong Chi Man, M.; Raehm, L., et al., Synthesis of disulfide-based biodegradable bridged silsesquioxane nanoparticles for two-photon imaging and therapy of cancer cells. *Chemical Communications* **2015,** *51* (61), 12324-12327.

229. Shen, X.; Li, S.; Li, L.; Yao, S. Q.; Xu, Q.-H., Highly Efficient, Conjugated-Polymer-Based Nano-Photosensitizers for Selectively Targeted Two-Photon Photodynamic Therapy and Imaging of Cancer Cells. *Chemistry – A European Journal* **2015,** *21* (5), 2214-2221.

230. Dib, S.; Aggad, D.; Jimenez, C.; Lakrafi, A.; Hery, G.; Nguyen, C., et al., Porphyrin-based bridged silsesquioxane nanoparticles for targeted two-photon photodynamic therapy of zebrafish xenografted with human tumor. *Cancer Reports* **2019,** *2* (5).

231. Shi, L.; Nguyen, C.; Daurat, M.; Richy, N.; Gauthier, C.; Rebecq, E., et al., Encapsulation of Hydrophobic Porphyrins into Biocompatible Nanoparticles: An Easy Way to Benefit of Their Two-Photon Phototherapeutic Effect without Hydrophilic Functionalization. *Cancers* **2022,** *14* (10), 2358.

232. Li, S.; Zhang, Y.; He, X.-W.; Li, W.-Y.; Zhang, Y.-K., Multifunctional mesoporous silica nanoplatform based on silicon nanoparticles for targeted two-photon-excited fluorescence imaging-guided chemo/photodynamic synergetic therapy in vitro. *Talanta* **2020,** *209*, 120552.

233. Shenderova, O.; Nunn, N., Production and purification of nanodiamonds. In *Nanodiamonds: Advanced Material Analysis, Properties and Applications*, Micro and Nano Technologies ed.; Arnault, J.-C., Ed. Elsevier: Amsterdam, **2017**; 25-56.

234. Volkov, K.; Danilenko, V.; Elin, V., Synthesis of diamonds from the carbon in explosive detonation products. *Fizika Goreniya Vzryva* **1990,** *26* (3), 123-125.

235. Danilenko, V. V., On the history of the discovery of nanodiamond synthesis. *Physics of the Solid State* **2004,** *46* (4), 595-599.

236. Yang, G.-Y.; Wang, J.-B.; Liu, Q.-X., Preparation of nano-crystalline diamonds using pulsed laser induced reactive quenching. *Journal of Physics: Condensed Matter* **1998,** *10* (35), 7923.

237. Boudou, J.-P.; Curmi, P. A.; Jelezko, F.; Wrachtrup, J.; Aubert, P.; Sennour, M., et al., High yield fabrication of fluorescent nanodiamonds. *Nanotechnology* **2009,** *20* (23), 235602.

238. Daulton, T. L.; Eisenhour, D. D.; Bernatowicz, T. J.; Lewis, R. S.; Buseck, P. R., Genesis of presolar diamonds: Comparative high-resolution transmission electron microscopy study of meteoritic and terrestrial nano-diamonds. *Geochimica et Cosmochimica Acta* **1996,** *60* (23), 4853-4872.

239. Goto, M.; Henning, T.; Kouchi, A.; Takami, H.; Hayano, Y.; Usuda, T., et al., Spatially resolved 3 μm spectroscopy of ELIAS 1: origin of diamonds in protoplanetary disks. *The Astrophysical Journal* **2009,** *693* (1), 610-616.

240. Mochalin, V. N.; Shenderova, O.; Ho, D.; Gogotsi, Y., The properties and applications of nanodiamonds. *Nature Nanotechnology* **2012,** *7* (1), 11-23.

241. Bondar', V. S.; Puzyr', A. P., Nanodiamonds for biological investigations. *Physics of the Solid State* **2004,** *46* (4), 716-719.

242. Jung, H.-S.; Neuman, K. C., Surface Modification of Fluorescent Nanodiamonds for Biological Applications. *Nanomaterials* **2021,** *11* (1), 153.

243. Lien, Z. Y.; Hsu, T. C.; Liu, K. K.; Liao, W. S.; Hwang, K. C.; Chao, J. I., Cancer cell labeling and tracking using fluorescent and magnetic nanodiamond. *Biomaterials* **2012,** *33* (26), 6172-6185.

244. Rosenholm, J. M.; Vlasov, I. I.; Burikov, S. A.; Dolenko, T. A.; Shenderova, O. A., Nanodiamond-Based Composite Structures for Biomedical Imaging and Drug Delivery. *Journal of Nanoscience and Nanotechnology* **2015,** *15* (2), 959-971.

245. Ali, M. S.; Metwally, A. A.; Fahmy, R. H.; Osman, R., Chitosan-coated nanodiamonds: Mucoadhesive platform for intravesical delivery of doxorubicin. *Carbohydrate Polymers* **2020,** *245*, 116528.

246. Lee, H.; Lee, J. S.; Moor, K. J.; Kim, H. I.; Kim, S. R.; Gim, G., et al., Hand-ground fullerene-nanodiamond composite for photosensitized water treatment and photodynamic cancer therapy. *Journal of Colloid and Interface Science* **2021,** *587*, 101-109.

247. Li, Y. J.; Su, Y. P.; Pan, H.; Deng, W. B.; Wang, J. H.; Liu, D. D., et al., Nanodiamond-based multifunctional platform for oral chemo-photothermal combinational therapy of orthotopic colon cancer. *Pharmacological Research* **2022,** *176*, 106080.

248. Fox, K.; Ratwatte, R.; Booth, M. A.; Tran, H. M.; Tran, P. A., High Nanodiamond Content-PCL Composite for Tissue Engineering Scaffolds. *Nanomaterials* **2020,** *10* (5), 948.

249. Luo, X.; Zhang, H.; Cao, Z.; Cai, N.; Xue, Y.; Yu, F., A simple route to develop transparent doxorubicin-loaded nanodiamonds/cellulose nanocomposite membranes as potential wound dressings. *Carbohydrate Polymers* **2016,** *143*, 231-238.

250. Norouzi, N.; Ong, Y.; Damle, V. G.; Habibi Najafi, M. B.; Schirhagl, R., Effect of medium and aggregation on antibacterial activity of nanodiamonds. *Materials Science and Engineering: C* **2020,** *112*, 110930.

251. Ong, S. Y.; van Harmelen, R. J. J.; Norouzi, N.; Offens, F.; Venema, I. M.; Habibi Najafi, M. B., et al., Interaction of nanodiamonds with bacteria. *Nanoscale* **2018,** *10* (36), 17117-17124.

252. Rifai, A.; Tran, N.; Reineck, P.; Elbourne, A.; Mayes, E.; Sarker, A., et al., Engineering the Interface: Nanodiamond Coating on 3D-Printed Titanium Promotes Mammalian Cell Growth and Inhibits *Staphylococcus aureus* Colonization. *ACS Applied Materials & Interfaces* **2019,** *11* (27), 24588-24597.

253. Bondon, N.; Raehm, L.; Charnay, C.; Boukherroub, R.; Durand, J.-O., Nanodiamonds for bioapplications, recent developments. *Journal of Materials Chemistry B* **2020,** *8*, 10878-10896.

254. Dinnovare™, What is Nanodiamond? daicel.com/en/business/new-solution/dinnovare/ (accessed 22th August 2022).

255. Matshitse, R.; Managa, M.; Nyokong, T., The modulation of the photophysical and photodynamic therapy activities of a phthalocyanine by detonation nanodiamonds: Comparison with graphene quantum dots and carbon nanodots. *Diamond and Related Materials* **2020,** *101*, 107617.

256. Matshitse, R.; Ngoy, B. P.; Managa, M.; Mack, J.; Nyokong, T., Photophysical properties and photodynamic therapy activities of detonated nanodiamonds-BODIPY-phthalocyanines nanoassemblies. *Photodiagnosis and Photodynamic Therapy* **2019,** *26*, 101-110.

257. Ryu, T. K.; Baek, S. W.; Kang, R. H.; Jeong, K. Y.; Jun, D. R.; Choi, S. W., Photodynamic and photothermal tumor therapy using phase-change material nanoparticles containing chlorin e6 and nanodiamonds. *Journal of Controlled Release* **2018,** *270*, 237-245.

258. Mauriello Jimenez, C.; Knezevic, N. Z.; Rubio, Y. G.; Szunerits, S.; Boukherroub, R.; Teodorescu, F., et al., Nanodiamond-periodic mesoporous organosilica nanoparticles (PMO) for two-photon photodynamic therapy (PDT) and drug delivery. *Journal of Materials Chemistry B* **2016,** *4* (35), 5803-5808.

259. Kim, H. i.; Kim, H.-n.; Weon, S.; Moon, G.-h.; Kim, J.-H.; Choi, W., Robust Co-catalytic Performance of Nanodiamonds Loaded on WO3 for the Decomposition of Volatile Organic Compounds under Visible Light. *ACS Catalysis* **2016,** *6* (12), 8350-8360.

260. Li, J.; Liu, R.; Zhao, Q.; Shi, Y.; Gao, G.; Zhi, J., Nanodiamond-based photosensitizer: Enhancing photodynamic therapy and inhibiting tumor metastasis. *Carbon* **2021,** *174*, 90-97.

261. Croissant, J.; Salles, D.; Maynadier, M.; Mongin, O.; Hugues, V.; Banchard-Desce, M., et al., Mixed Periodic Mesoporous Organosilica Nanoparticles and Core-Shell Systems, Application to in Vitro Two-Photon Imaging, Therapy, and Drug Delivery. *Chemistry of Materials* **2014,** *26* (24), 7214-7220.

262. Croissant, J. G.; Qi, C.; Maynadier, M.; Cattoen, X.; Man, M. W. C.; Raehm, L., et al., Multifunctional Gold-Mesoporous Silica Nanocomposites for Enhanced Two-Photon Imaging and Therapy of Cancer Cells. *Frontiers in Molecular Biosciences* **2016,** *3*.

263. Aggad, D.; Mauriello Jimenez, C.; Dib, S.; Croissant, J. G.; Lichon, L.; Laurencin, D., et al., Gemcitabine Delivery and Photodynamic Therapy in Cancer Cells *via* Porphyrin-Ethylene-Based Periodic Mesoporous Organosilica Nanoparticles. *ChemNanoMat* **2018,** *4* (1), 46-51.

264. Mauriello Jimenez, C.; Aggad, D.; Croissant, J. G.; Tresfield, K.; Laurencin, D.; Berthomieu, D., et al., Porous Porphyrin-Based Organosilica Nanoparticles for NIR Two-Photon Photodynamic Therapy and Gene Delivery in Zebrafish. *Advanced Functional Materials* **2018,** *28* (21), 1800235.

265. Velkov, T.; Thompson, P. E.; Nation, R. L.; Li, J., Structure--activity relationships of polymyxin antibiotics. *Journal of Medicinal Chemistry* **2010,** *53* (5), 1898-916.

266. Hubbard, B. K.; Walsh, C. T., Vancomycin assembly: nature's way. *Angewandte Chemie* **2003,** *42* (7), 730-65.

267. Gounani, Z.; Asadollahi, M. A.; Pedersen, J. N.; Lyngso, J.; Pedersen, J. S.; Arpanaei, A., et al., Mesoporous silica nanoparticles carrying multiple antibiotics provide enhanced synergistic effect and improved biocompatibility. *Colloids and Surfaces B: Biointerfaces* **2019,** *175*, 498-508.

268. Şen Karaman, D.; Sarwar, S.; Desai, D.; Björk, E. M.; Odén, M.; Chakrabarti, P., et al., Shape engineering boosts antibacterial activity of chitosan coated mesoporous silica nanoparticle doped with silver: a mechanistic investigation. *Journal of Materials Chemistry B* **2016,** *4* (19), 3292-3304.

269. Rahmani, S.; Bouchmella, K.; Budimir, J.; Raehm, L.; Cardoso, M. B.; Trens, P., et al., Degradable Hollow Organosilica Nanoparticles for Antibacterial Activity. *ACS Omega* **2019,** *4* (1), 1479-1486.

270. Li, H.; Li, D.; Chen, F.; Yang, C.; Li, X.; Zhang, Y., et al., Nanosilver-Decorated Biodegradable Mesoporous Organosilica Nanoparticles for GSH-Responsive Gentamicin Release and Synergistic Treatment of Antibiotic-Resistant Bacteria. *International Journal of Nanomedicine* **2021,** *16*, 4631-4642.

271. Wan, B.; Zhu, Y.; Tao, J.; Zhu, F. P.; Chen, J. Q.; Li, L., et al., Alginate Lyase Guided Silver Nanocomposites for Eradicating Pseudomonas aeruginosa from Lungs. *ACS Applied Materials & Interfaces* **2020,** *12* (8), 9050-9061.

272. Cassidy, C. M.; Donnelly, R. F.; Tunney, M. M., Effect of sub-lethal challenge with Photodynamic Antimicrobial Chemotherapy (PACT) on the antibiotic susceptibility of clinical bacterial isolates. *Journal of photochemistry and photobiology. B, Biology* **2010,** *99* (1), 62-6.

273. Liu, Y.; Liu, X.; Xiao, Y.; Chen, F.; Xiao, F., A multifunctional nanoplatform based on mesoporous silica nanoparticles for imaging-guided chemo/photodynamic synergetic therapy. *RSC Advances* **2017,** *7* (49), 31133-31141.

274. Valenzuela-Valderrama, M.; Bustamante, V.; Carrasco, N.; Gonzalez, I. A.; Dreyse, P.; Palavecino, C. E., Photodynamic treatment with cationic Ir(III) complexes induces a synergistic antimicrobial effect with imipenem over carbapenem-resistant Klebsiella pneumoniae. *Photodiagnosis and Photodynamic Therapy* **2020,** *30*.

275. Tardivo, J. P.; Adami, F.; Correa, J. A.; Pinhal, M. A.; Baptista, M. S., A clinical trial testing the efficacy of PDT in preventing amputation in diabetic patients. *Photodiagnosis and Photodynamic Therapy* **2014,** *11* (3), 342-50.

276. Xu, F.; Hu, M.; Liu, C.; Choi, S. K., Yolk-structured multifunctional up-conversion nanoparticles for synergistic photodynamic–sonodynamic antibacterial resistance therapy. *Biomaterials Science* **2017,** *5* (4), 678-685.

277. Li, M.; Li, L. Q.; Su, K.; Liu, X. M.; Zhang, T. J.; Liang, Y. Q., et al., Highly Effective and Noninvasive Near-Infrared Eradication of a *Staphylococcus aureus* Biofilm on Implants by a Photoresponsive Coating within 20 Min. *Advanced Science* **2019,** *6* (17), 1900599.

278. Cieplik, F.; Deng, D.; Crielaard, W.; Buchalla, W.; Hellwig, E.; Al-Ahmad, A., et al., Antimicrobial photodynamic therapy – what we know and what we don't. *Critical Reviews in Microbiology* **2018,** *44* (5), 571-589.

CHAPTER 2: Photosensitive nanodiamond-PMO core-shell nanoparticles for two-photon excitation PDT

1. Introduction

We report here the design of nanodiamond-periodic mesoporous organosilica core-shell nanoparticles (ND@PMO NPs) with two-photon photosensitizing property due to nanodiamonds cores integrated in the PMO frameworks.

NDs with tunable surface chemistry and core defects composition can be prepared through a large range of processes.[1-2] Luminescence properties of NDs are generally correlated with the proportion of nitrogen vacancy (NV) centers in the nanocrystals. Starting from this, NDs are extensively reported as bio-imaging probes. However, their employment as photoactive species for therapy has been scarcely described with only a few recent studies.[3-8] Just like other carbon-based semiconductors (f.i. carbon quantum dots or single-walled carbon nanotubes), NDs are mostly presented as electron donor agents for photodynamic and photothermal therapies, combined with phthalocyanine or porphyrin photosensitizers, but not as direct sensitizing drugs.

NDs ability to generate reactive oxygen species (ROS) for two-photon excitation photodynamic therapy (TPE-PDT) has been demonstrated recently for the first time. Briefly, NDs alone and NDs covered by an ethenylene-based PMO shell were irradiated at 800 nm with a pulsed femtosecond laser and induced 32 ± 6 and 39 ± 10% mortality on MCF-7 breast cancer cells, respectively.[5] Moreover, PMO NPs without NDs displayed no toxicity upon two-photon irradiation or not, which is characteristic of organosilica-based materials.[9-10] Negatively-charged nitrogen vacancy (NV^-) centers located in the core of diamond particles are probably at the origin of the two-photon PDT effect observed. As expressed by the energy-level diagram of such centers (**Figure 1**), the zero-phonon line (ZPL) in NV^- centers between ground state $^3A_2$ and excited state ^3E equates 1.95 eV (637 nm).[11] When performing two-photon irradiation at 800 nm (1.55 eV/photon), the selection rules are allowing the electronic transition from ground to excited state with absorption energy calculated to be 2.33 eV (533 nm).[12] Then, PDT principle is applicable with non-radiative degeneration from m = ± 1 sub-levels of ^3E to $^1E'$ by ISC.[13] Finally, a transition from $^1E'$ to $^1A_1$ could result in the production of ROS through reaction with surrounding oxygen in biological media.

In this context, we decided to assess the TPE sensitiveness of three different commercially available hydroxylated NDs (including the same NDs that the one that were used

in the previously outlined *in vitro* studies) with variable NV^- centers contents, size and shape that could influence their optical properties.[14]

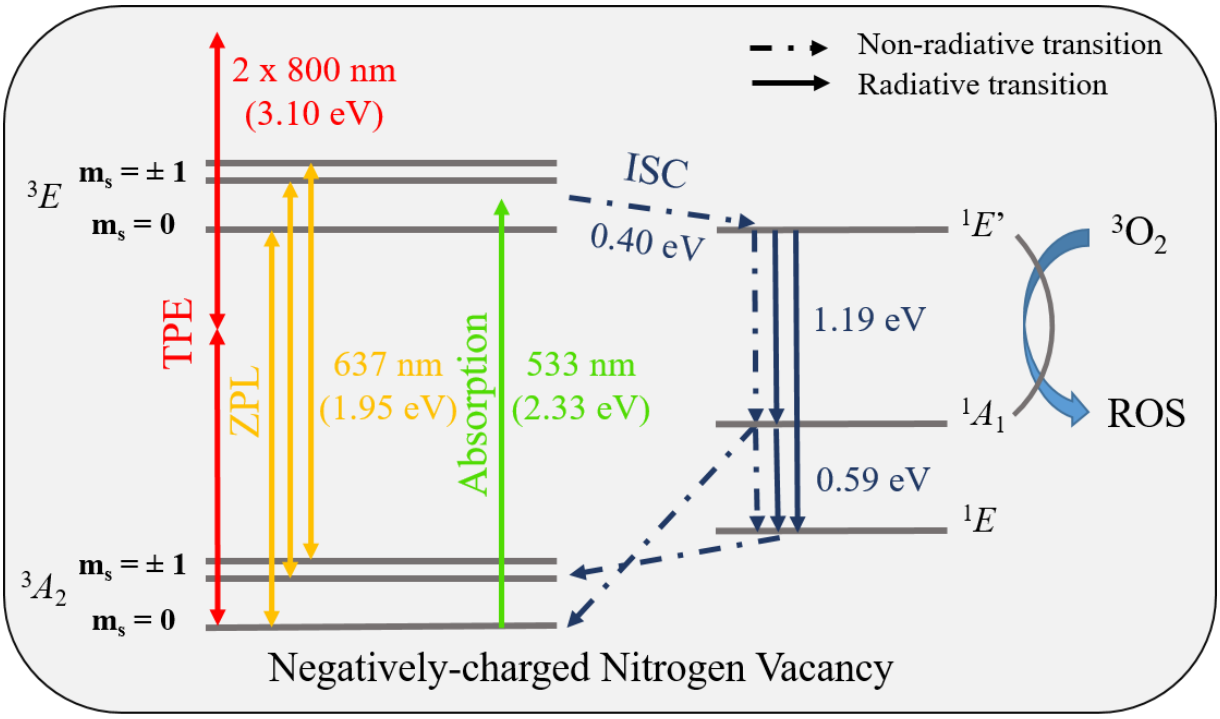

Figure 1: Energy-level diagram of NV^- centers in typical NDs for potential interaction with surrounding molecular oxygen. Adapted from reference 12.

2. Results and discussion

2.1 Nanodiamonds characterization and TPE-PDT potential against cancer

Before performing *in cellulo* TPE-PDT, NDs were further characterized to have a better knowledge about their physico-chemical properties.

2.1.1 Size and morphology

Hydrodynamic diameter distributions of three different hydroxylated NDs samples were recorded by dynamic light scattering (DLS) measurements after sonication for a couple minutes. For the three samples, statistical results showed average sizes in number of 107, 36 and 20 nm, respectively (**Table 1**). Therefore, NDs were called FND100 (for fluorescent NDs), DND30 and DND20. In addition, the average sizes, calculated from cumulants model, displayed higher hydrodynamic diameters due to the presence of some NDs aggregates in the suspensions.

Table 1: Size and surface charge measurements of three different commercial hydroxylated NDs. [a] Hydrodynamic diameters in number or z average size. Measurements were performed at 100 µg mL^{-1} in water. [b] Zeta potential (1 mM NaCl aqueous solutions) with pH tuned by adding aliquots of HCl or NaOH. Measurements of DND20 were performed with 1% DMSO in volume.

	Hydrodynamic size[a] (nm)			**ζ[b] (mV)**		
Samples	**Statistical size (nb)**	**z average size (cumulants)**	**PDI**	**pH = 4**	**pH = 8**	**pH = 11**
FND100	107 ± 32	231.1 ± 1.6	0.267	-11.3 ± 0.3	-12.2 ± 0.2	-15.6 ± 0.7
DND30	36 ± 16	88.2 ± 1.6	0.178	+36.6 ± 0.6	+33.4 ± 1.0	-5.4 ± 0.3
DND20	20 ± 3	42.0 ± 0.4	0.232	+32.4 ± 0.4	+23.7 ± 0.5	-15.5 ± 0.5

FND100 were obtained from phase transformation of graphite at high pressure and high temperature (HPHT) by grinding procedure. By this procedure, they are holding intrinsic fluorescence with at least 900 nitrogen-vacancies (NVs) per particle. DND30 and DND20 are detonation nanodiamonds (DNDs) synthesized by shocks of trinitrotoluene-like explosives and hexogen, prior to purification and washing steps. TEM images (**Figure 2**) confirmed the better dispersion of DNDs which synthesis pathway is more controlled than HPHT for FNDs.

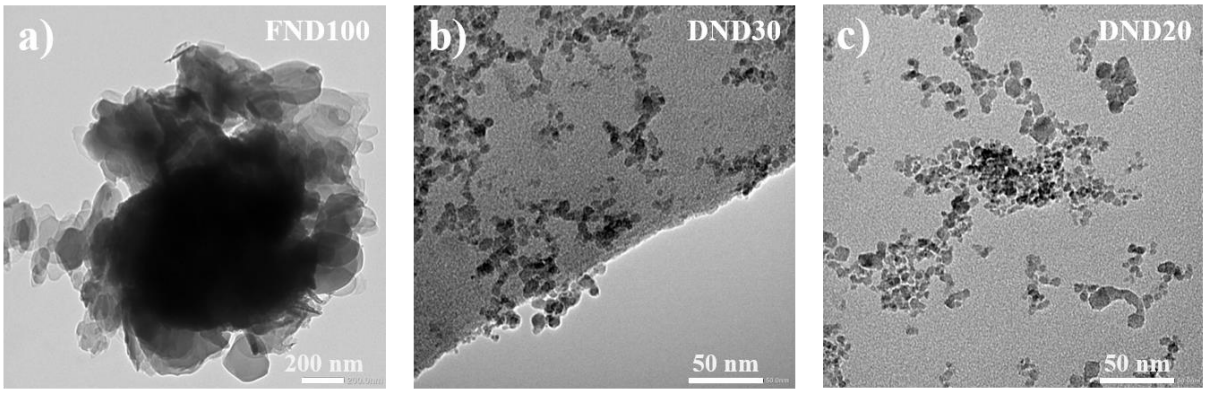

Figure 2: TEM micrographs of different hydroxylated NDs. (a) FND100, (b) DND30, and (c) DND20.

2.1.2 Surface and structural properties

Depending on synthesis and purification stages, NDs exhibit a large variety of surface functionalities (f.i. -OH, -COOH, $-NH_2$ and anhydride). In order to have a better knowledge of NDs surface chemistry, their surface charge was assessed by zeta potential measurements. NDs were dispersed in 1 mM NaCl aqueous solution in order to achieve enough conductivity to provide reliable data.

At pH 4 and 8, FND100 displayed a slightly negative surface, contrary to DND30 and DND20 which were positively charged (**Table 1**). This difference between FND100 and DNDs surface charge environment has been associated with surface functionalities content as NDs are holding hydroxyls groups, and also amine and carboxyl moieties. NH_2 groups are easily protonated in

ammonium ions at acidic to neutral pH and generally confer very positive zeta potential values. In comparison, carboxyl groups are responsible for negative surface charge, upon deprotonation ($–COO^-$) even at low pH.[15] According to this behavior, $\frac{R-COOH}{R-NH2}$ and $\frac{R-COOH}{R-OH}$ ratios could be higher at FND100's surface than at DNDs' surface. This is confirmed at pH ≈ 11 where NDs are all negatively charged, with absence of ammonium and predominance of OH and COO^-.

To further assess NDs properties, their structural composition was studied by X-ray Photoelectron Spectroscopy (XPS). DND30 nanodiamonds revealed a higher atomic concentration in nitrogen compared to DND20 analogues, with respectively 1.16 and 0.77 at. % (**Table 2**). This difference might be responsible for the more positive charge of surface at basic pH for DND30 (i.e. -5.4 ± 0.3 mV) than for DND20 (-15.5 ± 0.5 mV).[16]

Table 2: Structural composition studies of DND30 and DND20 hydroxylated NDs by XPS. [a] Atomic percentage of different elements. [b] Binding energy (E_b) and atomic percentage of different carbon environments obtained after deconvolution of the C_{1s} spectra. Measurements were performed at 100 µg mL^{-1} in water, with 1% DMSO in volume for DND20.

Samples	**C_{1s}[a] (at. %)**	**O_{1s} (at. %)**	**N_{1s} (at. %)**	**C_{1s}[b]**	**sp^2 C=C**	**sp^3 C-C**	**C-O**	**C=O**	**O-C=O**
DND30	90.65	8.19	1.16	E_b (eV)	284.3	285.3	286.5	288.2	/
				At. %	24.56	40.30	32.78	2.37	/
DND20	87.57	11.66	0.77	E_b (eV)	284.6	285.2	286.4	288.9	290.1
				At. %	18.99	36.56	36.43	6.83	1.18

C_{1s} core level XPS spectra revealed similar bands for the two DNDs at about 284.5 eV (sp^2 C=C), 285.3 eV (sp^3 C-C/C-H), 286.5 eV (C-O) and 288.6 eV (C=O), with also a band at 290.1 eV for DND20 indicating the presence of ester groups (**Figure 3**). Surface functionalities are known to be more abundant for small NPs than for larger ones. This characteristic was confirmed by increased at. % of oxygen-based functions (**Table 2**). Moreover, after deconvolution of the O_{1s} spectra (not shown) it appeared that the highest binding energy corresponding to OH groups (531.6 or 533.4 eV, respectively for DND30 and DND20) was the most abundant with 58.7 at. %, confirming the predominance of surface hydroxyl groups.[17]

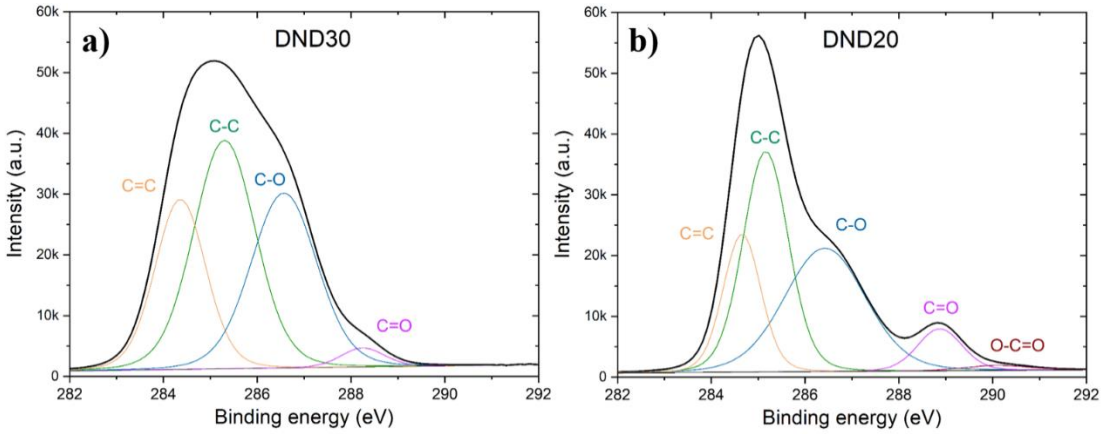

Figure 3: C_{1s} XPS spectra of (a) DND30 and (b) DND20 hydroxylated NDs.

2.1.3 Optical properties

Absorption and fluorescence properties of DNDs were studied to compare their potential for imaging and photodynamic therapy. Firstly, UV-visible absorption spectra in water revealed that the light absorption is proportional to ND30 concentration due to diffusion effects, with a maximum efficiency in the UV regions (**Figure 4a**). Moreover, for a same concentration, light absorption of DND20 was reduced compared to DND30.

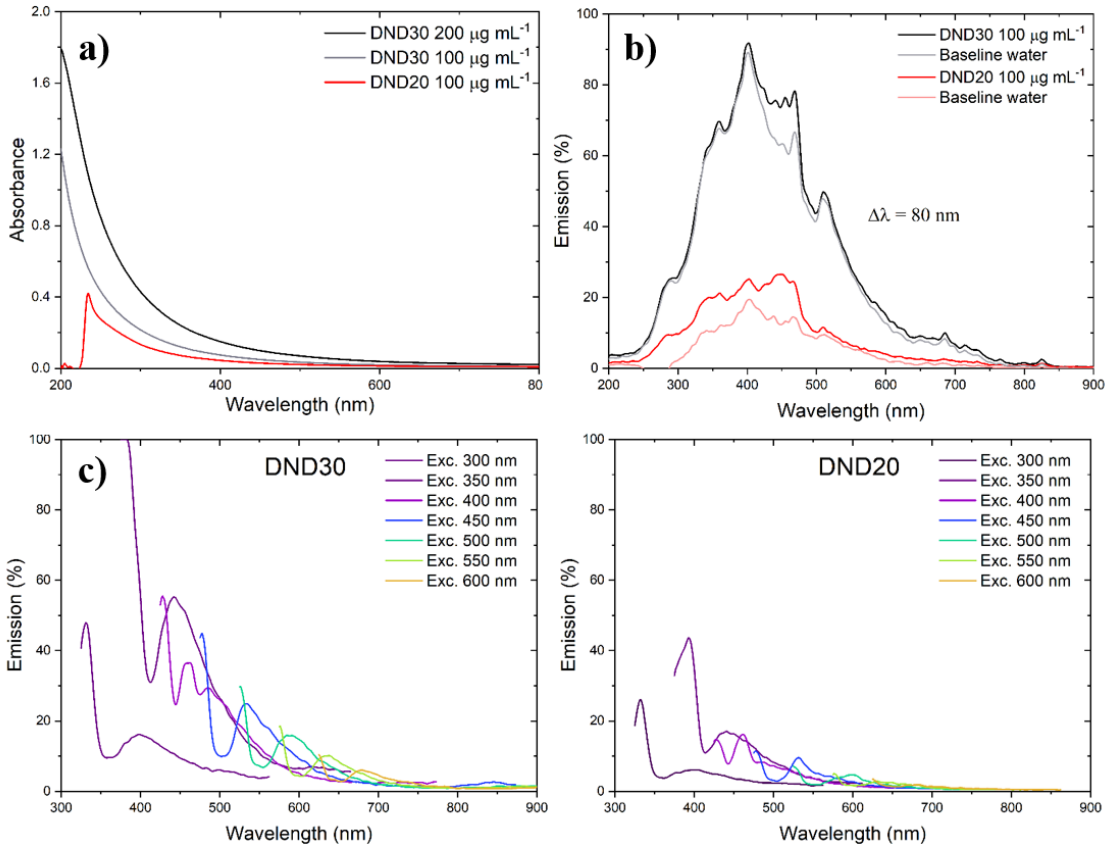

Figure 4: Optical characterization of detonation nanodiamonds in water. (a) UV-visible absorption spectra; (b) Synchronous fluorescence spectra and the corresponding baseline ($\Delta\lambda = \lambda_{em.} - \lambda_{exc.}$); (c) Fluorescence spectra with different excitation wavelengths ($\lambda_{exc.}$ = 300-600 nm, step = 50 nm). NB: DND20 aqueous suspensions contained 1% DMSO in volume.

Accordingly, studies of fluorescence emission at various wavelengths and synchronous fluorescence spectroscopy with a $\Delta\lambda$ of 80 nm applied between excitation and emission wavelengths were performed. They displayed much lower fluorescence intensities for DND20 in the 300-700 nm region (**Figure 4b and c**). The fluorescence emission of NDs appeared to be dependent on excitation wavelength, with a maximum emission obtained at $\lambda_{exc.}$ = 350 or 400 nm. By comparing the synchronous spectra of NDs and the corresponding baseline of signal in water, the most intense emission was observed in the 430-470 nm region ($\lambda_{exc.}$ = 350-390 nm). All for all, the lower absorption and fluorescence of DND20 could be related to the number of NV^- color centers per particle. Due to their smaller average size, a lower number of vacancies per particle is expected, thus bringing a low global TPA cross-section per object.[18]

2.1.4 Photosensitizing ability of NDs for anticancer TPE-PDT

With the background knowledge that DND30 nanodiamonds can be used as active photosensitizing agents for TPE-PDT on MCF-7 breast cancer cells[5], FND100, DND30 and DND20 were incubated at a concentration of 80 µg mL^{-1} for 24 h with MDA-MB-231 epithelial human breast cancer cell populations.

As shown by 3-(4,5-dimethylthiazol-2-yl)-2,5-diphenyl tetrazolium bromide (MTT) assay data presented in **Figure 5**, a killing activity upon two-photon irradiation at 800 nm was observed with FND100 and DND30 nanodiamonds with 40% and 18% cell death, respectively. Therefore, DND20 seemed to be ineffective upon excitation, which can be associated with their smaller size as presented above.

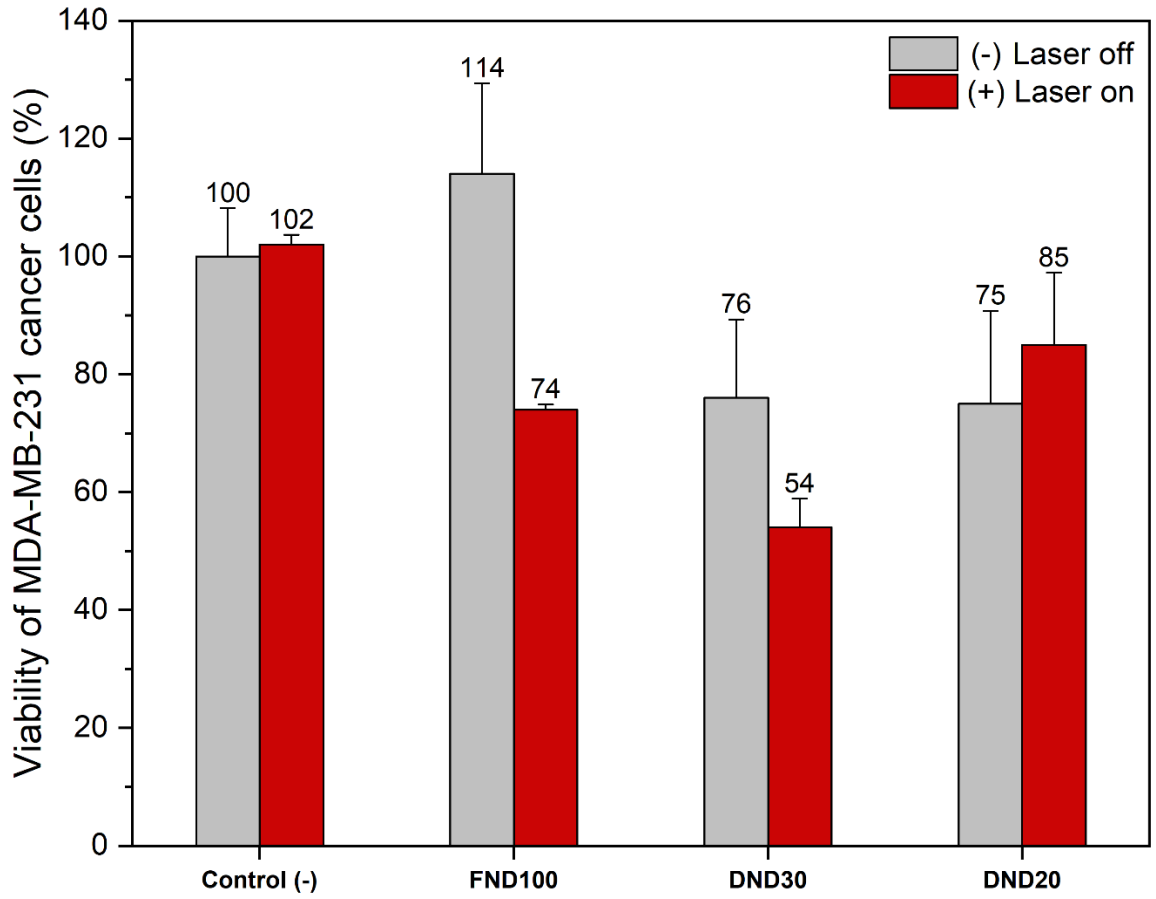

Figure 5: TPE-PDT studies of different NDs. TPE-triggered cancer cell killing (MDA-MB-231 epithelial human breast cancer cells) after incubation with NPs 80 µg mL^{-1} for 20 h and irradiation at 800 nm (3 x 1.57 s). Lines represent standard deviations of three independent experiments.

The optical features of NDs are generally attributable to their size and to the excitation wavelength of the light source. In the case of large FND100, photoluminescence and thus toxicity by TPE is related to NV^- centers and other defects participating in ROS generation through ISC.[19] For smaller NDs, the best excitation wavelength have been associated with surface chemical composition, but the exact origins are still source of debate.[20-21]

On the basis of these results, we decided to keep only FND100 and ND30 diamond gems for further work.

2.2 Synthesis of ND-silica core-shell nanoparticles and associated grafting strategies

After selection of FND100 and DND30 as the two best candidates to yield good photosensitizing capability for ROS generation applied to TPE-PDT, they were encapsulated in biocompatible PMO shells to avoid their intrinsic toxicity.

2.2.1 Design of ND@PMO nanoparticles

First and foremost, we had to deal with the spontaneous aggregation of carbon-based materials in aqueous media, which is mainly due to van der Waals forces.[22] The reaction mixture is indeed basic as ammonium hydroxide was used as the sol-gel catalyst and cetyltrimethylammonium bromide (CTAB) cationic surfactant was applied as porogen agent. To face this, we adapted a reported procedure on the preparation of nanodiamond-mesoporous silica core-shell nanoparticles (ND@MSN) where the continuous sonication of mixture reaction allowed for better dispersion of NDs in CTAB micelles in order to limit size polydispersity issues.[23-24] ND@PMO core-shell nanocapsules were then prepared by a modified Stöber process. The addition of organoalkoxysilane sol-gel precursors under ultrasonication in a water bath (1000 W, 25 kHz) leads to shell growth around NDs by concomitant condensation and hydrolysis.

i. Impact of sonication time during sol-gel

As sol-gel is mainly kinetic-dependent, the impact of sonication time during reaction was evaluated. DND30@PMO NPs with PMO shell grown from 90:10 molar ratio of 1,2-bis(triethoxysilyl)ethylene (ENE) and bis[3-(triethoxysilyl)propyl]tetrasulfide (4S) mixture (**Figure 6**) were prepared with 0, 5, 15 or 30 min sonication time after addition of the last drop of premix.

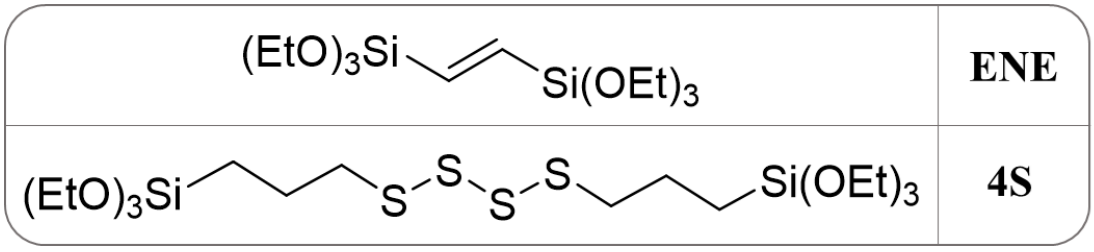

Figure 6: Simplified structures of the organoalkoxysilane precursors used.

Notably, without any sonication during precursors addition, very monodisperse PMO NPs and very large NDs aggregates (covered or not with a small silica layer) were visible by TEM imaging.

According to DLS results (**Figure 7b**), the final average size of NPs was increased from 286 to 440 nm, with polydispersity index (PDI) slightly rising with prolonged sonication time. The proposed explanation is that sonication could have lowered hydrophobic interactions and repulsive electrostatic interactions between micelles, and thus, favoured the growth of bigger ND-based cores with a lot of NDs. Indeed, as seen in TEM micrographs (**Figure 7a**), while PMO shell thickness is quite constant, the capsule-like cores are getting more and more

polydisperse in size with longer sonication times. All bare DND30@PMO exhibited a negative surface charge, which originates from silanolate functions –Si-O$^-$, yielding zeta potential values around -35 mV.

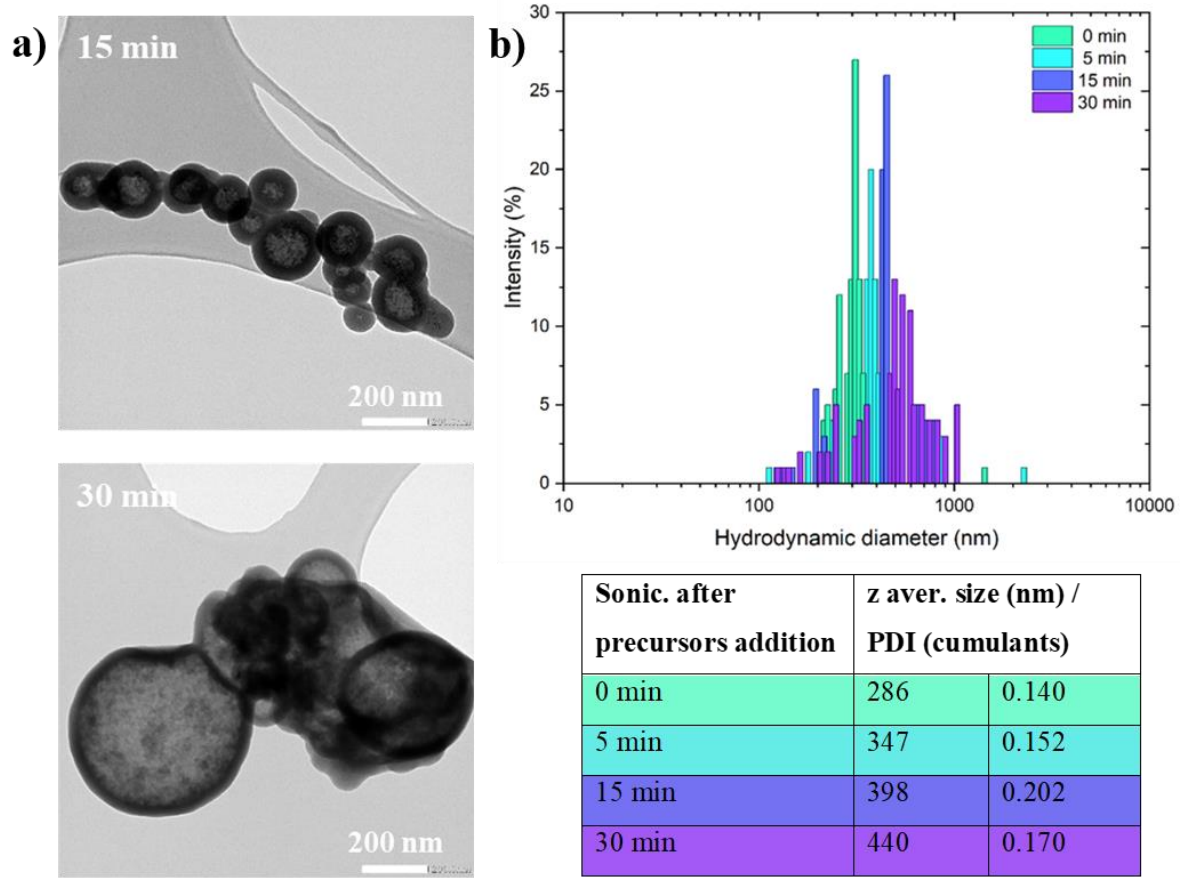

Sonic. after precursors addition	z aver. size (nm) / PDI (cumulants)	
0 min	286	0.140
5 min	347	0.152
15 min	398	0.202
30 min	440	0.170

Figure 7: Morphology and size evaluation of DND30@ENE 4S NPs. (a) TEM micrographs (b) and size distributions for different sonication times after precursors addition.

On one hand, when stopping sonication right after precursors addition (t = 0), sol-gel kinetics are at the most critical stage, thus, synthesis would not be sufficiently reproducible. On the other hand, after long sonication time, larger and more polydisperse NPs are less suitable for bioapplications. Altogether, a timing of 5 minutes seemed to be a good compromise and was chosen for the next work.

ii. Synthesis and characterization of ND@PMO nanoparticles

Different ND@PMO NPs were synthesized and functionalized in a one-pot strategy. Core-shell nano-sized particles were formed under ultrasonication for five minutes. The reaction mixture was removed from the bath and NPs were allowed to grow for 24h under stirring (**Figure 8,** 1-2). Then, the direct grafting of short-chain silylated polyethylene glycol (PEG-Si, M_w = 410.62 g mol^{-1}) and aminoundecyltriethoxysilane (AUTES, M_w = 333.59 g mol^{-1}) was performed with a precursor:PEG-Si:AUTES molar ratio of 9.6:2:1 (**Figure 8,** 3). After

separation by centrifugation, SN2 reaction in a 50:50 (v:v) H_2O/EtOH medium enabled squarate mannose derivate (sqMAN) grafting onto amine functions (**Figure 8,** 4).[25]

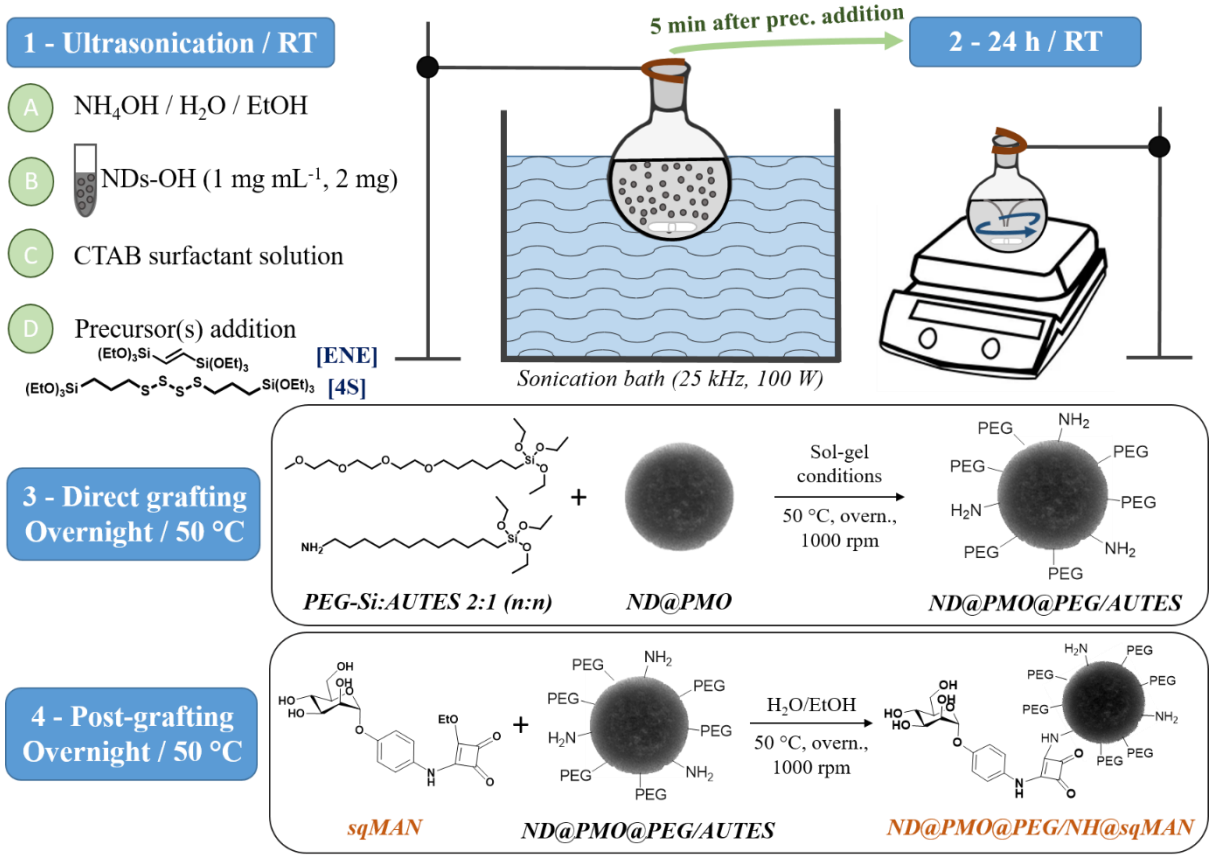

Figure 8: Typical synthesis and functionalization steps of ND@PMO NPs.

We then investigated the functionalization of ND@PMO NPs with PEG-Si, AUTES and sqMAN by several characterization techniques.

ND@PMO@PEG/AUTES hydrodynamic sizes obtained by Padé-Laplace (statistical size) and cumulants-based algorithms displayed similar average values, with PDI ≤ 0.20 for all samples (**Table 4**). NPs with 10% 4S molar ratio were smaller than the one prepared with only ENE as sol-gel precursor, with z average decreasing from 339 to 259 nm for FND100-based NPs and from 323 to 260 nm for DND30-based NPs. Similarly, measured diameters from TEM images showed significant variations from 137 ± 83 to 106 ± 69 nm and from 147 ± 86 to 132 ± 52 nm for FND100-based NPs and DND30-based NPs, respectively. This could be explained by a better integration of 4S compared to ENE in CTAB micelle cores during hydrolysis-condensation reactions, leading to an enlarged nuclei growth.

In addition, after post-grafting of sqMAN onto NPs surface, their size and colloidal stability were conserved as DLS measurements in ethanol showed analogous hydrodynamic sizes and PDI.

Table 4: Size measurements of different ND@PMO@PEG/AUTES NPs. [a] Statistical hydrodynamic diameter. [b] z average hydrodynamic diameter, n = 3 independent experiments. PDI ≤ 0.20 indicates good size monodispersity. [c] Average diameters of n ≥ 100 counts determined on TEM images. Hydrodynamic diameters were determined from suspensions in ethanol; n.d.: non-determined.

ND@PMO@PEG/AUTES NPs	Statistical size[a] (intensity, nm)	z average size[b] (nm)	PDI	Size[c] (nm)
FND100@ENE	350 ± 40	339	0.108	137 ± 83
DND30@ENE	342 ± 50	323	0.140	147 ± 86
// @sqMAN (10:4 m:m)	327 ± 30	299	0.108	119 ± 58
// @sqMAN (10:4 m:m)	342 ± 100	302	0.195	148 ± 80
FND100@ENE 4S	250 ± 100	259	0.149	106 ± 69
DND30@ENE 4S	271 ± 30	260	0.129	132 ± 52
// @sqMAN (10:1 m:m)	271 ± 20	247	0.147	n.d.
// @sqMAN (10:1 m:m)	284 ± 10	263	0.150	n.d.

To go further, TEM micrographs revealed that FND100@PMO NPs display either spherical nanocapsule-like morphologies or distorted spherical core-shell morphologies with large FNDs with flake shapes (**Figure 9a and b**). Easy aggregation of ND particles and thus, variable aggregate sizes, are responsible for the polydisperse sizes of the final ND@PMO nanocapsules. Moreover, by screening the different sizes of NPs populations, it was observed that NPs with diameter below 60 nm were not encapsulating ND (**Figure 9a and d**), even in the case of small DND30, thus, these objects were simple PMO NPs spheres. This can be explained by the heterogeneous repartition of NDs in the micelles before initiating the sol-gel process.

Scanning transmission electron microscopy energy-dispersive X-ray spectroscopy (STEM-EDX) elemental mapping of ND@ENE@PEG/AUTES NPs revealed the presence of nitrogen on the PMO surface, which is suggesting AUTES grafting. Moreover, the presence of low amount of bromide confirms that CTAB was properly removed (after synthesis and surface modification) by NH_4NO_3 extraction and washing steps using ion exchange technique between nitrate NO_3^- and Br^- (**Figure 9c and f**).

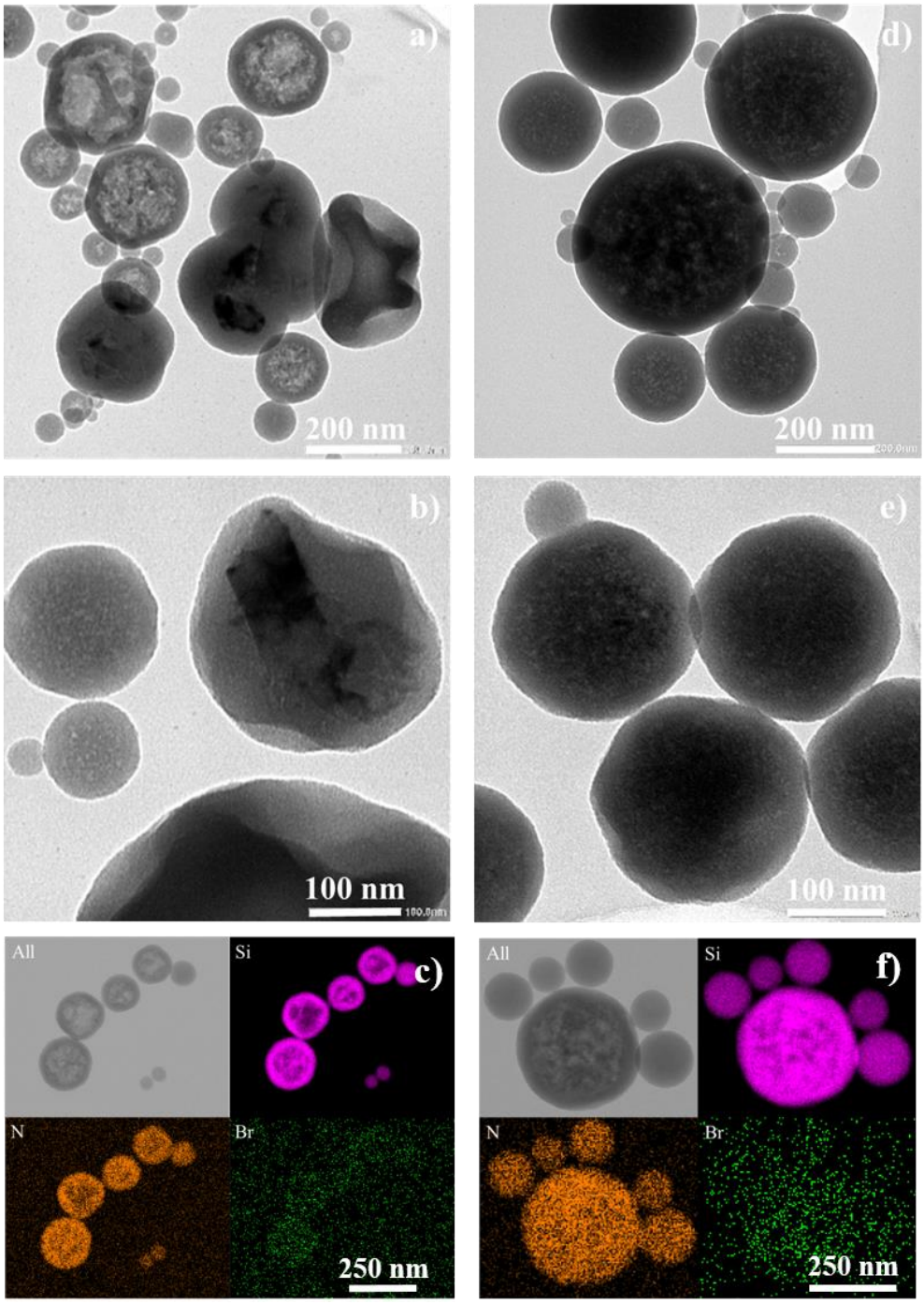

Figure 9: TEM and STEM-EDX micrographs of ND@ENE@PEG/AUTES NPs. (a, b) Spherical nanocapsules containing multiple FND100 or distorted core-shell NPs with large FND100 and (c) the corresponding STEM-EDX elemental mapping; (d, e) Spherical nanocapsules containing multiple DND30 and (f) the corresponding STEM-EDX elemental mapping. PMO NPs < 60 nm do not possess NDs.

Bands corresponding to the covalent grafting of PEG-Si, AUTES and sqMAN were identified by infrared spectroscopy (**Figure 10a**). For FND100@ENE bare NPs, the signals at 2977, 1634 and 922 cm^{-1} correspond to the C=C bond in ethene bridges. The appearance of asymmetric and symmetric stretching vibration mode of aliphatic carbons (ν_{CH2}) at 2929 and

2859 cm^{-1} confirmed the coupling of both PEG-Si and AUTES. At 1350 cm^{-1}, another symmetrical stretching mode of alkane (δ_{CH2}) was also detected. Moreover, the band observed at 1558 cm^{-1} corresponds to the angular deformation of the primary N–H bond (δ_{NH2}). After functionalization with the sqMAN, Fourier transform infrared (FTIR) spectra seems more complex with different bands between 1800 cm^{-1} and 1500 cm^{-1}, which can be assigned to the C=C bond of the phenyl and of the squarate moiety of the mannose. In addition, before and after SN2 reaction, there is a slight shift from 1247 to 1235 cm^{-1}, which can be linked with the bending vibration mode of primary and secondary amine (ν_{NH2} and ν_{NH}).

After PEG-Si and AUTES direct grafting, surface charge were strongly positive with zeta potential ranging from +19.7 to +26.0 mV due to protonation of amine moieties to generate NH_3^+ ions. When adding different %wt. ratios of sqMAN through amine functions, the charge decreased proportionally due to partial or total disappearance of ammonium ions and appearance of deprotonated hydroxyls $-O^-$ from the grafted mannose derivative. For instance, in the case of FND100-based PMO NPs, for 10:1 NPs:sqMAN (m:m) ratio, zeta potential value was equal to +6.9 ± 0.2 mV, and for 10:4 NPs:sqMAN (m:m) ratio, it was even lower with z = -6.5 ± 0.5 mV (**Figure 10d**). Moreover, the negative surface charge coming from the large amount of surface silanolate -Si-O^- obtained after sol-gel is more predominant when grafted primary amines are substituted with sqMAN in secondary amines.

We then evaluated sqMAN grafted amounts by UV-visible titration of the centrifugation supernatant after reaction. sqMAN standards were prepared to fit within the working range of absorbance (A < 2). They revealed high linear correlation for $\lambda_{abs.,\,max}$ = 296 nm (**Figure 10c**). Note that the other absorbance maximum at 221 nm was not used to determinate sqMAN concentration due to scattering effect of organosilica-based NPs in the UV region, which were present as traces in the supernatant's samples.

Results showed that an initial 10:1 ratio resulted in 42 and 30 µg sqMAN/mg of FND100@ENE 4S@PEG/AUTES and DND30@ENE 4S@PEG/AUTES, respectively. Interestingly, for an initial 10:4 ratio, the amount grafted was not multiplied by 4, yielding 86 and 88 µg sqMAN/mg of FND100@ENE@PEG/AUTES and DND30@ENE@PEG/AUTES, respectively (**Figure 10d**). This is suggesting that all amine-terminated chains were covalently bonded with sqMAN in that case, and that the maximum required amount of sqMAN would be comprised between 10:2 and 10:3 NPs:sqMAN weight ratio. This hypothesis was reinforced by FTIR comparison of FND100-based NPs, with at least two times reduction in the transmittance intensity between the two samples (**Figure 10b**).

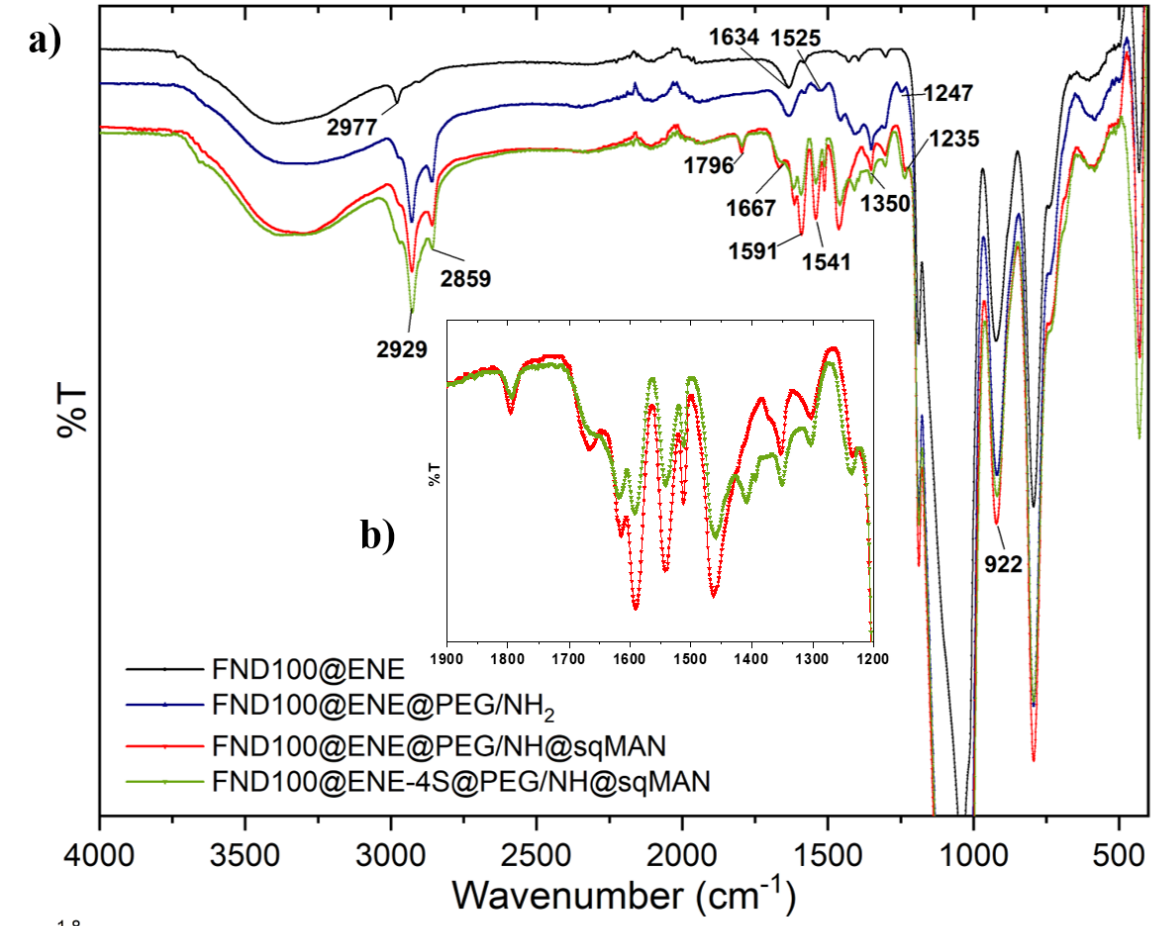

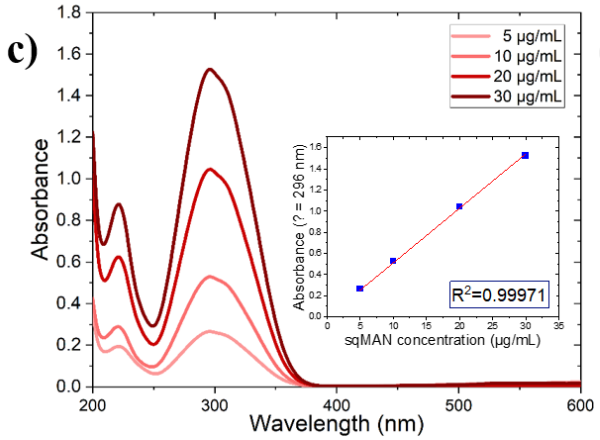

d)

ND@PMO @PEG/AUTES-grafted NPs	Zeta pot. (0.5 mM PBS, mV)	sqMAN *vs.* NPs	
		mg g^{-1}	mmol g^{-1}
FND100@ENE	+19.7 ± 0.4	86	2.2 10^{-1}
// @sqMAN (10:4 m:m)	-6.5 ± 0.5		
DND30@ENE	+26.0 ± 0.9	88	2.2 10^{-1}
// @sqMAN (10:4 m:m)	-7.9 ± 0.4		
FND100@ENE-4S	+22.5 ± 2.1	42	1.1 10^{-1}
// @sqMAN (10:1 m:m)	+6.9 ± 0.2		
DND30@ENE-4S	+25.0 ± 0.8	30	7.5 10^{-2}
// @sqMAN (10:1 m:m)	+5.9 ± 0.1		

Figure 10: Characterization for grafting confirmation on ND@PMO NPs. (a) Infrared spectra of FND100@ENE (black line), FND100@ENE@PEG/AUTES (blue line) and FND100@ENE@PEG/AUTES@sqMAN (red line); (b) qualitative comparison of sqMAN grafting with FND100@ENE 4S@PEG/AUTES@sqMAN NPs (green line); (c) UV-visible absorption profile of sqMAN in 50:50 (v:v) H_2O:EtOH mixture and affiliated correlation curve with n = 4 standards for $\lambda_{abs.,\,max}$ = 296 nm; (d) Zeta potential values of ND@PMO@PEG/AUTES NPs with various initial weight ratios of sqMAN and estimated final grafting by UV-visible standard curve with linear correlation.

2.2.2 Design of ND@MSN@ENE nanoparticles

Similarly to the previous protocol, ND@MSN@ENE@PEG/AUTES (*in fine* ND@MON@PEG/AUTES) hybrid NPs were prepared. Briefly, TEOS was added under

sonication, and then, after 30 min, ENE was introduced under stirring at room temperature. After 24h, PEG-Si and AUTES were then directly grafted in the sol-gel mixture with a 4.53:5.2:2:1 molar ratio of TEOS:ENE:PEG-Si:AUTES.

According to TEM images (**Figure 11**), the use of TEOS and the separation of precursors addition was beneficial as it gave more control to nucleation and growth, thus, ND@MSN@ENE NPs were more monodisperse in size compared to ND@PMO NPs. The newly formed NPs exhibited well-defined morphologies, either spherical or ellipsoidal, depending on the ND content that was encapsulated. Then, a mesoporous organosilica shell with constant thickness of 40 nm was formed around ND@MSN core-shells.

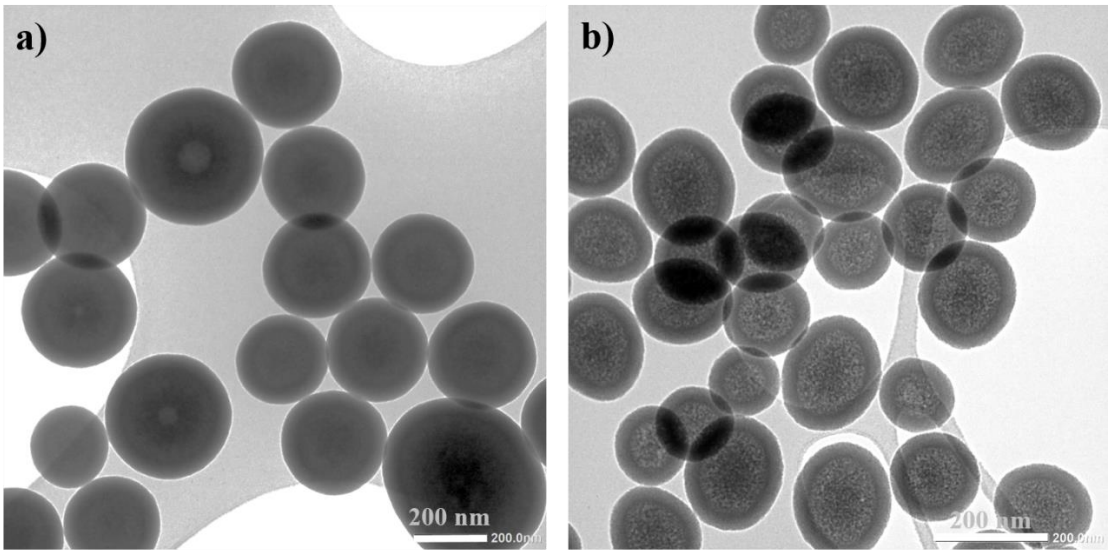

Figure 11: TEM micrographs of ND@MSN@ENE@PEG/AUTES NPs. Spherical or ellipsoidal nanocapsules containing FND100@MSN core (a) or DND30@MSN core (b) with an external PMO shell were obtained. For FND100-based NPs, an ellipsoidal morphology was obtained when a large ND was encapsulated.

Notably, FND100@MSN@ENE NPs display larger diameters than DND30@MSN@ENE NPs (**Table 5**), with respectively 407 and 195 nm calculated from DLS measurement. In comparison, FND100@ENE and ND30@ENE were much more comparable. This shift of average particle size to higher numbers is suggesting that a higher yield of FND100 was encapsulated.

Table 5: Size and surface charge measurements of different ND@MSN@ENE@PEG/AUTES NPs. [a] z average hydrodynamic diameter in ethanol, n = 3 independent experiments. PDI ≤ 0.20 indicates good size monodispersity. [b] Average diameters of n ≥ 100 counts determined on TEM images. [c] Zeta potential (0.5 mM PBS aqueous solutions).

NPs@PEG/AUTES	Hydrodynamic size[a] (nm)	PDI	Size[b] (nm)	ζ[c] (mV)
With FND100	407	0.181	291 ± 44	+32.9 ± 0.5
With DND30	195	0.118	165 ± 26	+23.4 ± 0.4

Hence, having higher encapsulation yield of ND and more monodisperse core-shell particle sizes would be of great interest for further TPE-PDT treatment.

2.3 Biological studies of functionalized ND@PMO nanoparticles

2.3.1 TPEF imaging of NDs and ND@ENE

The internalization of NPs into cancer cells was screened by two-photon excitation fluorescence (TPEF). NPs were incubated at 50 µg mL^{-1} for 20h. Fifteen minutes before the imaging experiments, the cell membranes were stained with Cell Mask™ Orange Plasma Membrane. All NPs were successfully endocytosed by cancer cells, as shown by TPEF appearance at 800 nm inside the cytosol (**Figure 12**).

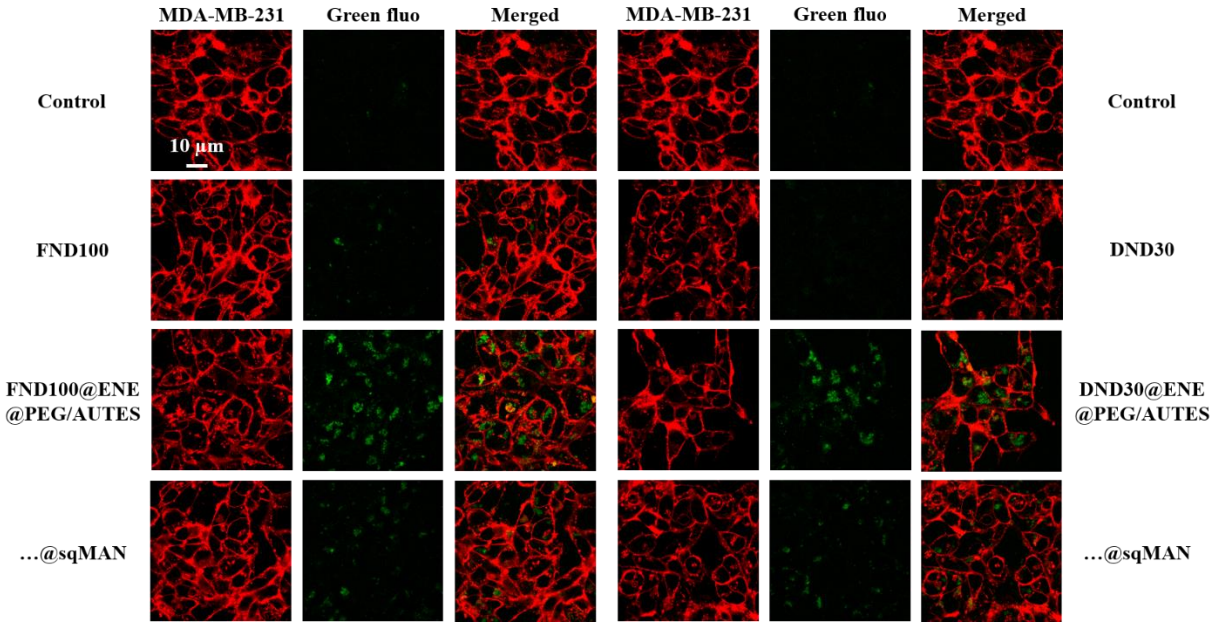

Figure 12: Cell internalization study of different functionalized ND@ENE core-shell NPs and NDs at 50 µg mL^{-1} using confocal microscopy imaging. After incubation for 20 h, MDA-MB-231 cancer cells were stained with Cell Mask™ Orange Plasma Membrane and then visualized at 561 nm (membrane) or 800 nm (NPs, green fluorescence). Images were obtained with Carl Zeiss LSM780 confocal fluorescence microscope using a high magnification (63x/1.4 OIL Plan-Apo).

The remarkable level of internalization observed for FND100@ENE@PEG/AUTES and DND30@ENE@PEG/AUTES NPs compared to NDs can be associated with the suitable interaction between negatively charged MDA-MB-231 cells and positively charged NPs because of surface amine functionalities. It is commonly accepted that neutralization of cell membrane can promote endocytosis.[26-28]

2.3.2 Phototoxicity studies of ND@ENE

Preliminary testing by MTT assay revealed the photosensitizing property of DND30 and FND100 under two-photon excitation at 800 nm.

For ND@PMO NPs, the values obtained after reading the absorbance with MTT do not seem to be representative of the results observed when examining the cell density under the microscope. Cell death was therefore assessed 48 h after irradiation by nuclear labelling with Hoechst 33342™ which is a DNA intercalant that will bind to DNA and stain the nuclei of living cells in blue. Thus, the phototoxicity of ND@PMO@PEG/AUTES towards MDA-MB-231 breast cancer cells was studied in the presence and in the absence of sqMAN and compared to non-encapsulated NDs. For all samples, cancer cells were incubated with NPs (80 µg mL^{-1}) for 20 h. **Figure 13** illustrates some images of wells after staining and from which data are collected after counting of living cells.

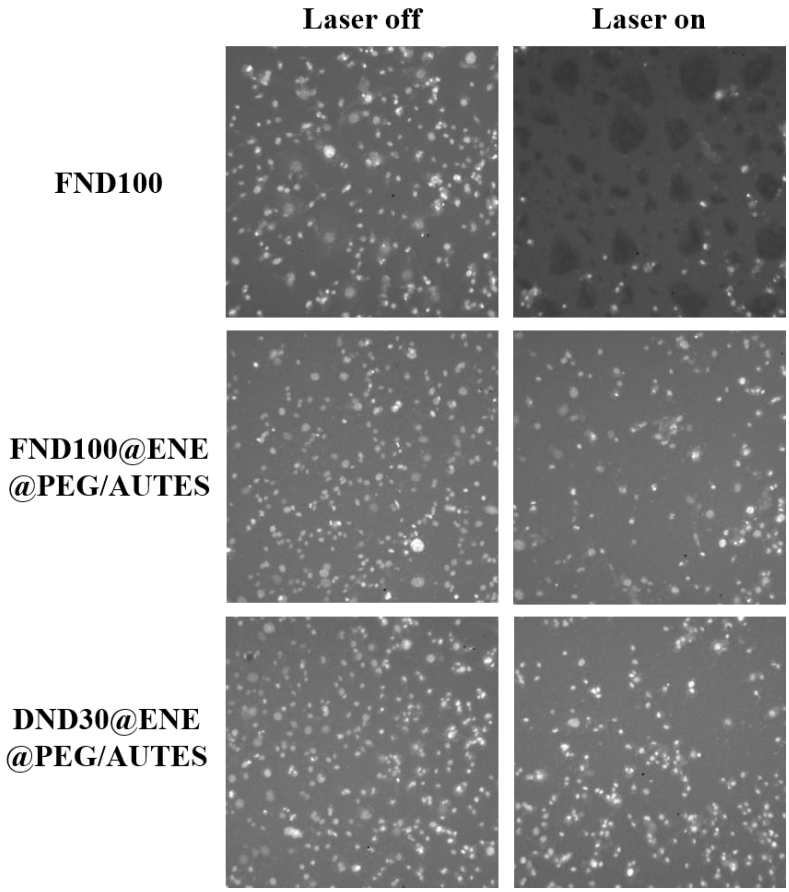

Figure 13: Images of wells obtained by fluorescence microscopy. Extracted images represent wells area that have been subjected or not to two-photon irradiation (3 x 1.57 s) at 800 nm. White dots correspond to living MDA-MB-231 cancer cells.

As revealed by the well image after irradiation, FND100 found to be very efficient, causing 74% of cell death, whereas DND30 photosensitizing activity only killed 10% more cells (**Figure 14**).

Interestingly, when NDs were encapsulated at low concentration level in ENE shell covered by PEG-Si and AUTES, TPE-PDT killing efficiency was remarkably efficient with 46 and 36% mortality, respectively with FND100 and DND30-based nanoparticles. With no irradiation, all ND@ENE NPs revealed high biocompatibility, which can be associated with the organosilica matrix. When adding sqMAN onto the surface, better internalization was expected as mannose is well-known for its ability to specifically and selectively bind onto lectins of cancer cells.[29-31] However, results demonstrated low cell death in those cases, with 26% and 9% killing for ENE@PEG/AUTES@sqMAN NPs containing FND100 and DND30, respectively. This reduced efficiency seems to be proportional to NPs internalization rate as visible in TPEF images.

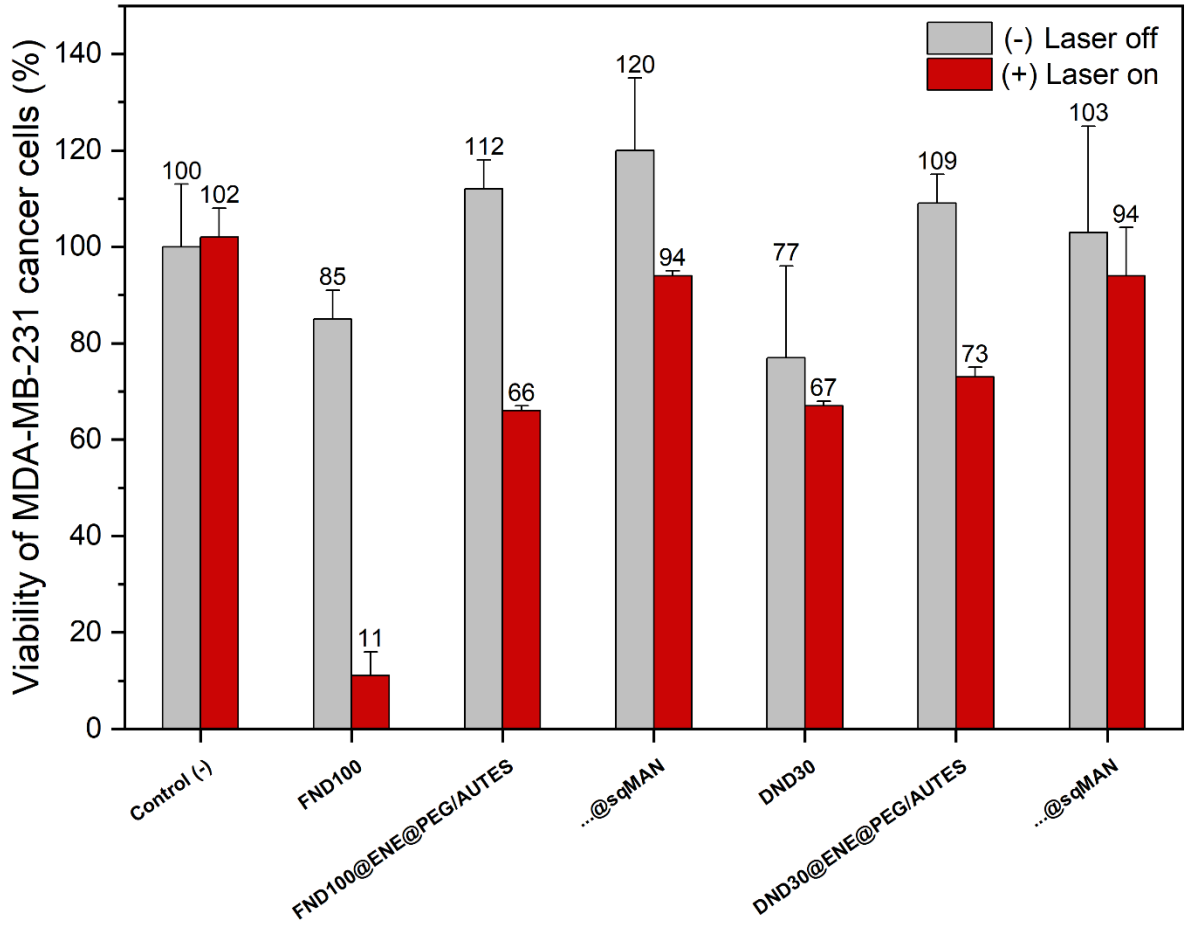

Figure 14: TPE-PDT studies of different ND@ENE@PEG/AUTES core-shell NPs and the corresponding NDs. TPE-triggered cancer cell killing (MDA-MB-231 epithelial human breast cancer cells) after incubation with NPs at 80 µg mL^{-1} for 20 h and irradiation at 800 nm (3 x 1.57 s). Lines represent standard deviations of three independent experiments.

These results suggest that NDs with different morphologies and sizes can be employed for TPE-PDT, but a protective shell is necessary to enhance biocompatibility and ensure endocytosis through surface functionalization.

2.3.3 Phototoxicity studies of ND@ENE 4S

Similarly, 4S-based ND@PMO NPs were tested *in vitro*. They revealed high cytotoxicity towards MDA-MB-231 cancer cells with or without laser irradiation, except DND30@ENE 4S@PEG/AUTES NPs with 26% reduction in cell viability after TPE-PDT treatment (**Figure 15**).

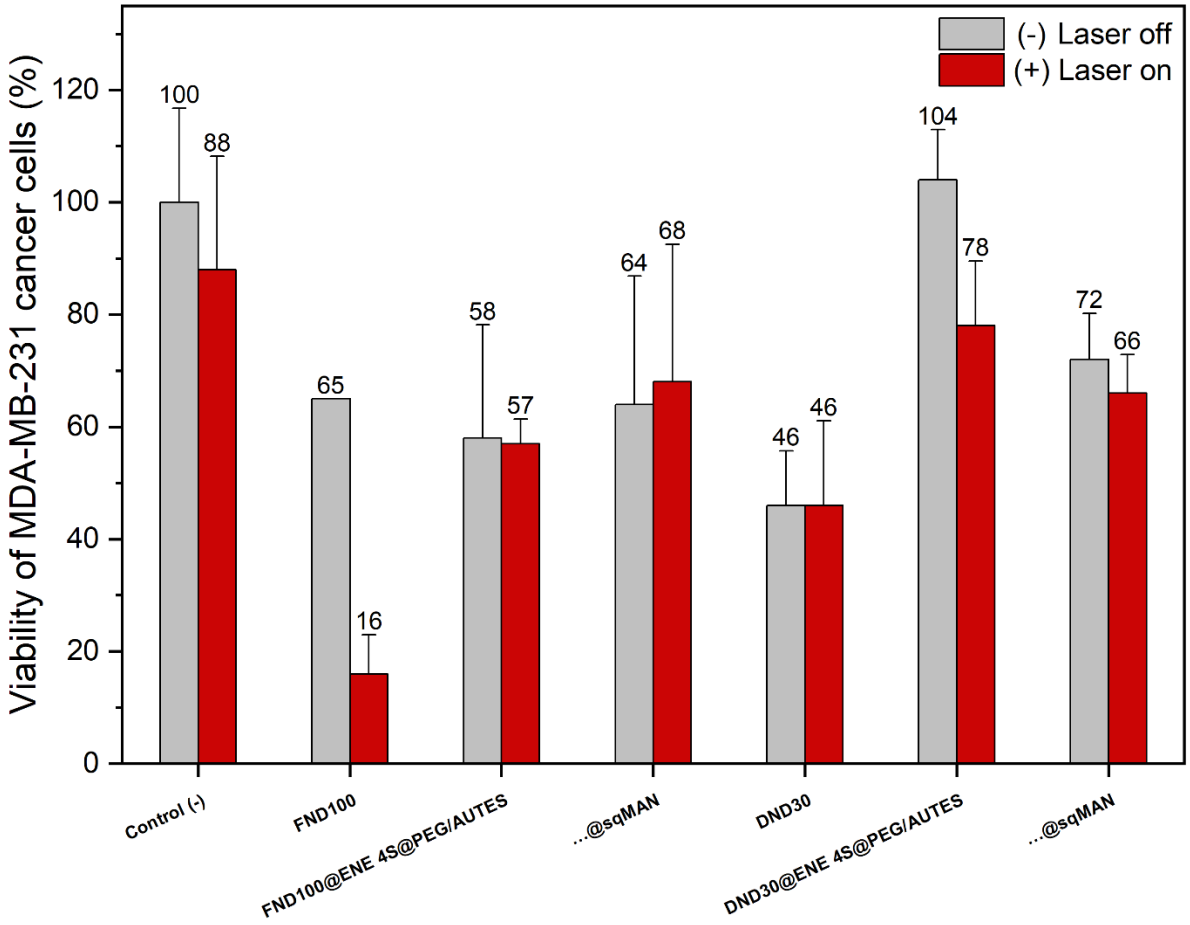

Figure 15: TPE-PDT studies of different ND@ENE 4S@PEG/AUTES core-shell NPs and the corresponding NDs. TPE-triggered cancer cell killing (MDA-MB-231 epithelial human breast cancer cells) after incubation with NPs at 80 µg mL^{-1} for 20 h and irradiation at 800 nm (3 x 1.57 s). Lines represent standard deviations of three independent experiments.

To summarize, mixing molecular ENE precursors with little portion of 4S precursors is assumed to change both TPE-PDT capability and dark toxicity of ND@PMO core-shell NPs. Nonetheless, as visible on viability counting results, the reproducibility of the experiments was limited (error bars in **Figure 15**).

3. Conclusions and perspectives

The toxicity studies of three hydroxylated NDs references revealed that two of them display a PS behavior by TPE-PDT on MDA-MB-231 cancer cells. The selected FND and DND were encapsulated by formation of biocompatible PMO shell using ENE or ENE 4S mixture for sol-gel reaction under ultrasonication for better disaggregation of the ND gems, in order to have better core-shell yields and more monodisperse colloidal suspension. Confocal imaging of the prepared ND@ENE core-shell systems functionalized with short PEG and amine functions revealed efficient internalization in MDA-MB-231 cancer cells. Their biological testing upon TPE-PDT showed their high biocompatibility and noteworthy levels of mortality, with 46 and 36% cell death respectively with FND100 and DND30-based nanoparticles. In contrast, less internalized sqMAN-grafted objects were less toxic towards cancer cells. Parallel to that, the toxicity of multifunctional ND@ENE 4S NPs was unclear with high mortality rates without irradiation and no real photosensitizing effect.

The results presented in this work pave the way to further optimization of the core-shell-based systems. NDs with various surface environments, sizes and morphologies could be compared. Furthermore, a large variety of process conditions could be tested to build multifunctional ND@PMO structures, in order to find in which configuration the photosensitizing effect could be the most powerful, while keeping an eye on potent ND intrinsic biocompatibility without irradiation. Thus with large PMO shell porosities, such multifunctional materials would be suitable for targeted and selective drug delivery and combinatory TPE-PDT/chemotherapy.

Nanodiamond particles alone are otherwise easily tunable platforms for vectorization. One potential good strategy to explore would be the covalent coupling of NDs with efficient organic photosensitizers for energy transfer and with grafted moieties bringing more specificity and selectivity to targeted biomedical applications.

4. Experimental section

Materials

Unless otherwise specified, ACS reagent grade starting materials and solvents were used as received from commercial suppliers without further purification.

Deionized water (resistivity = 18.2 MΩ cm) obtained from an Aquadem™ system (Veolia Water Technologies, Saint-Maurice, France) was used in all experiments. Hydroxylated nanodiamonds in powder (DND30, 4 nm average primary particle size, 30 nm average particle size, z > +30 mV, > 98%) were obtained from International Technology Center (Raleigh, NC, USA). Fluorescent hydroxylated nanodiamonds (FND100, > 900 NV/particle, 1 mg mL^{-1} H_2O, 100 nm average particle size, z < -20 mV), hydroxylated nanodiamonds (ND20, 10 mg mL^{-1} DMSO, 5 nm average primary particle size, 20 nm average particle size, z > +25 mV), bis[3-(triethoxysilyl)propyl]tetrasulfide (4S, ≥ 90%), cetyltrimethylammonium bromide (CTAB, > 98%), sodium hydroxide pellets (NaOH, ≥ 98%), ammonium nitrate (NH_4NO_3, > 98%) and 3-(4,5-dimethylthiazol-2-yl)-2,5-diphenyl tetrazolium bromide (MTT) were purchased from Merck (Saint-Quentin-Fallavier, France). Chlorhydric acid (HCl, ≥ 37%) was purchased from Thermo Fisher Scientific (Illkirch-Graffenstaden, France). Sodium chloride (NaCl) was obtained from VWR (Radnor, PA, USA). 1,2-Bis(triethoxysilyl)ethylene (ENE, 95%, 80% trans-isomer) and tetraethyl orthosilicate (TEOS, 99%) were obtained from abcr GmbH (Karlsruhe, Germany). Ammonium hydroxide (28%), absolute ethanol (EtOH) and ethanol (96%) were obtained from Carlo Erba Reagents (Cornaredo, MI, Italy). (6-{2-[2-(2-Methoxy-ethoxy) ethoxy]ethoxy}hexyl)triethoxysilane (PEG-Si, > 98%) and 11-aminoundecyltriethoxysilane (AUTES, > 97%) were purchased from Sikemia (Montpellier, France). Cell Mask™ Orange Plasma Membrane was obtained from Invitrogen (Cergy-Pontoise, France). p-[N-(2-Ethoxy-3,4-dioxocyclobut-1-enyl)amino]phenyl-α-D-mannopyranoside (sqMAN) was synthesized following Sperling *et al.* protocol.[32] Glass bottom 8-well tissue culture chambers were purchased from Sarstedt (Marnay, France).

Analytical techniques

Samples for transmission electron microscopy (TEM) measurements were deposited from suspensions on Cu Formvar/C holey grids and left to dry before observation. The main TEM images were acquired using a JEOL 1200 EXII (Tokyo, Japan) operated at 120 kV. The quantification of the nanoparticles diameters was performed with the Image*J* software with at

least 100 counts. The elemental mapping was recorded in STEM mode with an Oxford Instruments XMaxN 100 TLE (100 mm^2, windows less) EDX detector with a JEOL 2200 FS (FEG) Transmission Electron Microscope operated at 200 kV with a Gatan UltraScan 4000 (4k x 4k) CCD camera.

Hydrodynamic diameters of ND@PMO NPs were obtained on a Cordouan Technologies (Pessac, France) DL135 Particle Size Analyzer and data were treated by NanoQ software using a statistical or a cumulant-based model. Hydrodynamic diameters of NDs and ND@MSN@ENE NPs and all zeta potential measurements were recorded on Malvern NanoSeries (Malvern, UK) Zetasizer NanoZS (model ZEN3600) in a DTS1060C Zetacell (for zeta potential) at 25 °C, with an equilibration time of 60 s and with automatic measurement, and data were treated by Zetasizer software using a Smoluchowski model. All zeta potentials and hydrodynamic diameters were obtained with nanoparticles suspensions at 100 µg mL^{-1}.

XPS measurements were performed on dried samples (after washing steps including centrifugation in the case of ND20). Data were collected on a VG Escalab 220XL spectrometer from Vacuum Generators (Hailsham, UK) featuring a monochromatic Al Kα X-ray source (1486.6 eV) and a spherical energy analyzer operated in the constant analyzer energy (CAE) mode (CAE = 100 eV for survey spectra and CAE = 40 eV for high-resolution spectra), using the electromagnetic lens mode. The angle between the incident X-rays and the analyzer is 58° and the detection angle of the photoelectrons is 30°.

Emission and synchronous fluorescence spectra were recorded with a Xenius XC fluorimeter (Monaco, Monaco) were performed in Type I ultrapure water (or 1% DMSO) at 100 µg mL^{-1} (excitation and emission bandwidth = 10 nm, step = 1 nm, PMT voltage = 600 V). Emission fluorescence spectra were recorded in the range from 325 to 900 nm at excitation wavelengths from 300 to 600 nm, spaced by 50 nm intervals in the excitation domain. For synchronous fluorescence spectra, the difference value (Δλ) between the emission and excitation wavelengths was fixed at 80 nm and water (or 1% DMSO) was used as baseline.

UV-visible absorption spectra were determined in water with a Jasco V-770 spectrophotometer (Mary's Court Easton, MD, USA) using quartz cells of 1 cm path length.

FTIR spectra were recorded on a PerkinElmer Spectrum Two (Waltham, MA, USA) spectrometer with four acquisitions at a resolution of 4 cm^{-1}.

ND@PMO syntheses were performed at 25 °C using a FisherBrand™ (Illkirch-Graffenstaden, France) TI-H10 MF2 ultrasonic bath (1000 W, 25 kHz in normal mode).

Zeta potential of NDs at different pH values

NDs were suspended in 1 mM NaCl aqueous solutions, yielding a concentration of 100 µg mL^{-1}. After quick sonication, the pH value was tuned with 20 or 50 mM NaOH or HCl aqueous solutions, using a pH probe, and zeta potential (n = 5) was recorded on the Malvern Zetasizer. For each NPs, pH was first fixed to 4, and then increased to 8 and 11 for the next measurements.

Synthesis of ND-silica core-shell nanoparticles and associated grafting strategies

Preparation of functionalized ND@ENE (4S) PMO NPs

Sonication time impact on the synthesis of ND30@ENE 4S PMO NPs

Absolute ethanol (5.8 mL), deionized water (10.1 mL) and ammonium hydroxide (NH_4OH (2 M), 0.6 mL) were added in a 50 mL round bottom flask. Then, an aqueous solution of DND30 (2 mg, previously dispersed at 1 mg mL^{-1} and sonicated for 30 min) was added dropwise under 25 kHz sonication. After 30 min, a surfactant solution of CTAB (80 mg, 0.22 mmol) dissolved in absolute ethanol (0.6 mL) and deionized water (1.3 mL) was added dropwise under powerful sonication. After 60 min stabilization, a mixture of 1,2-bis(triethoxysilyl)ethylene (227 µL, 0.65 mmol) and bis[3-(triethoxysilyl)propyl]tetrasulfide (36 µL, 72 µmol) was introduced dropwise in the solution under powerful sonication. After a certain time (respectively, 0, 5, 15 and 30 min), the resultant suspension was stirred at 1400 rpm and room temperature overnight. Fractions were gathered in propylene tubes and collected by centrifugation for 10 min at 14k rpm. Subsequently, the still surfactant-filled particles were solvent-extracted three times with ammonium nitrate solution (20 g L^{-1} ethanol) in order to remove the CTAB template, and washed two times with ethanol. Each extraction and washing involved 20 min sonication and centrifugation for 10 min at 10k rpm. The nanoparticles were finally redispersed in ethanol and stored at +4 °C.

Synthesis of ND@ENE (4S) PMO NPs

Absolute ethanol (5.8 mL), deionized water (10.1 mL) and ammonium hydroxide (NH_4OH (2 M), 0.6 mL) were added in a 50 mL round bottom flask. Then, an aqueous solution

of FND100 (2 mL at 1 mg mL^{-1} and sonicated for 30 min) or DND30 (2 mg, previously dispersed at 1 mg/mL and sonicated for 30 min) was added dropwise under 25 kHz sonication. After 30 min, a surfactant solution of CTAB (80 mg, 0.22 mmol) dissolved in absolute ethanol (0.6 mL) and deionized water (1.3 mL) was added dropwise under powerful sonication. After 60 min stabilization, a mixture of 1,2-bis(triethoxysilyl)ethylene and bis[3-(triethoxysilyl)propyl]tetrasulfide (100:0 or 90:10, total 0.72 mmol) was introduced dropwise in the solution under powerful sonication. After 5 min, the resultant suspension was stirred at 1400 rpm and room temperature overnight.

Direct grafting of PEG-Si and AUTES on ND@ENE (4S) PMO NPs

After 24 h condensation process of core-shell NPs, temperature was increased to 50 °C. Then, a 2:1 (n:n) mix of PEG-Si (61.6 mg, 150 µmol) and 11-aminoundecyltriethoxysilane (25.0 mg, 75 µmol) was dissolved in 1 mL of deionized water and added to the sol-gel preparation. The reaction was kept under stirring at 1000 rpm and 50 °C overnight. Then, the solution was cooled to room temperature while stirring; fractions were gathered in propylene tubes and collected by centrifugation for 10 min at 14k rpm. Some part of the NPs was not treated with ammonium nitrate and only redispersed in ethanol and stored at +4 °C for further sqMAN grafting step. In the other part, CTAB was extracted and NPs were washed according to the previously described protocol.

Squarate mannose derivative post-grafting

The targeted ND@PMO@PEG/AUTES NPs:sqMAN ratio for post-grafting of sqMAN was 10:4 (m:m) for NPs containing only ENE and 10:1 (m:m) for NPs containing both ENE and 4S. Briefly, a mixture of ND@PMO@PEG/AUTES NPs in EtOH (previously sonicated for 30 min and not extracted in CTAB to avoid grafting in the pore walls) and sqMAN aqueous solution was stirred at 750 rpm and 50 °C overnight in a 50 mL round bottom flask (50:50 (v:v) H_2O:EtOH). CTAB was extracted and NPs were washed according to the previously described protocol. UV-visible spectra of sqMAN standards from 5 to 30 µg mL^{-1} (n = 4 standards) in a 50:50 (v:v) H_2O:EtOH medium displayed a high linear correlation at $\lambda_{abs.}$ = 296 nm ($R^2 \geq 0.999$). Supernatants were diluted by 10 or 40 to reach the concentration range of the standards. After baseline correction, sqMAN grafting contents (µg sqMAN mg^{-1} ND@PMO@PEG/AUTES) were calculated with the following equation:

$$GC = \frac{m(ini\ sqMAN) - m(free\ sqMAN)}{m(ini\ NPs)}.$$

Preparation of ND@MSN@ENE@PEG/AUTES PMO NPs

Synthesis of ND@MSN@ENE PMO NPs

Absolute ethanol (6.0 mL), deionized water (10.7 mL) and ammonium hydroxide (NH_4OH (2 M), 0.35 mL) were added in a 50 mL round bottom flask. Then, an aqueous solution of FND100 (2 mL at 1 mg mL^{-1} and sonicated for 30 min) or DND30 (2 mg, previously dispersed at 1 mg/mL and sonicated for 30 min) was added dropwise under 25 kHz sonication. After 30 min, a surfactant solution of CTAB (80 mg, 0.22 mmol) dissolved in absolute ethanol (0.5 mL) and deionized water (1.05 mL) was added dropwise under powerful sonication. After 60 min stabilization, tetraorthosilicate (75 µL, 0.34 mmol) was introduced dropwise in the solution under powerful sonication. After 5 min, the resultant suspension was stirred at 1400 rpm and RT. 60 min after tetraorthosilicate addition, 1,2-bis(triethoxysilyl)ethylene (150 µL, 0.39 mmol) was added and the sol-gel process was conducted overnight.

Direct grafting of PEG-Si and AUTES on ND@MSN@ENE NPs

After 24 h condensation process of core-shell NPs, temperature was increased to 50 °C. Then, a 2:1 (n:n) mix of PEG-Si (61.6 mg, 150 µmol) and 11-aminoundecyltriethoxysilane (25.0 mg, 75 µmol) was dissolved in 1 mL of deionized water and added to the sol-gel preparation. The reaction was kept under stirring at 1000 rpm and 50 °C overnight. Then, the solution was cooled to room temperature while stirring; fractions were gathered in propylene tubes and collected by centrifugation for 10 min at 14k rpm. Subsequently, the still surfactant-filled particles were solvent-extracted three times with ammonium nitrate solution (20 g L^{-1} ethanol) in order to remove the CTAB template, and washed three times with water, ethanol and ethanol. Each extraction and washing involved 20 min sonication and centrifugation for 10 min at 20k rpm. The nanoparticles were finally redispersed in ethanol and stored at +4 °C.

Biological studies of NDs and multifunctional ND@PMO NPs

Cell line

MDA-MB-231 human breast cancer cells were cultured in Dulbecco's Modified Eagle's Medium (DMEM) supplemented with 10 % fetal bovine serum and 50 µg mL^{-1} gentamycin. All cells were allowed to grow in humidified atmosphere at 37 °C under 5 % CO_2.

Cell internalization study using confocal microscopy

MDA-MB-231 cells were seeded in glass bottom 8-well tissue culture chambers. Twenty-four hours after seeding, cells were treated or not with 50 µg mL^{-1} of nanoparticles for 24 h. Fifteen minutes before the end of incubation, cells were treated with CellMask™ Orange Plasma Membrane stain at a final concentration of 5 µg mL^{-1}. Cells were washed two times with culture medium before observation with confocal fluorescence microscope LSM780 (Carl Zeiss, France) at 800 nm for fluorescent NPs (TPEF) and 561 nm for CellMask™ Orange Plasma Membrane stain, using a high magnification (63x/1.4 OIL Plan-Apo).

Two-photon excitation photodynamic therapy

MDA-MB-231 cells were seeded into a 384-multiwell glass-bottomed plate (thickness = 0.17 mm), with a black polystyrene frame, 2000 cells per well in 50 µL of culture medium, and allowed to grow for 24 h. NPs were dispersed under ultrasounds in PBS at a concentration of 1 mg mL^{-1} and cells were then incubated for 20 h with nanoparticles at a final concentration of 80 µg mL^{-1} in supplemented DMEM. Non-treated cells were considered as a control. After incubation with NPs, cells were maintained in fresh culture medium, and then submitted (or not) to TPE with the LSM780 live confocal microscope (Carl Zeiss Microscope). Half of the wells were irradiated at 800 nm by three scans of 1.57 s duration in four different areas of the well with a focused laser at a maximum laser power (laser power input = 3 W). The laser beam was focused by a microscope objective lens (Carl Zeiss 10×/0.3 EC Plan-Neofluar).

Preliminary testing of NDs using MTT

The photosensitizing ability of all NDs was evaluated by MTT assay 48 h after TPE and values were corrected according to the following formula:

(Non-irradiated viability – 2 × (non-irradiated viability – irradiated viability)).

Data are mean values standard deviation from three independent experiments.

Anticancer potential of NDs and ND@PMO NPs using Hoechst staining

Fifteen minutes before the end of incubation for two days, cells were treated with Hoechst 33342™ at a final concentration of 10 µg mL^{-1}. Cells were washed two times with culture medium before photo shooting with a fluorescent microscope LEICA DM IRB at 340/380 nm. The quantification of the living cells was performed with the Image*J* software by analyzing pictures of the different wells taken at a magnification of 4X. A specific method was defined and reproduced on all images in an identical way to count the nuclei and to establish a percentage of cell viability according to the following equation:

$$\frac{Number\ of\ nuclei\ in\ the\ well}{Number\ of\ nuclei\ in\ the\ control\ well} \times 100,$$

then, the viability was corrected according to the following formula:

(Non-irradiated viability – 2 × (non-irradiated viability – irradiated viability).

Data are mean values standard deviation from three independent experiments.

Bibliography

1. Mochalin, V. N.; Shenderova, O.; Ho, D.; Gogotsi, Y., The properties and applications of nanodiamonds. *Nature Nanotechnology* **2012,** *7* (1), 11-23.

2. Bondon, N.; Raehm, L.; Charnay, C.; Boukherroub, R.; Durand, J.-O., Nanodiamonds for bioapplications, recent developments. *Journal of Materials Chemistry B* **2020,** *8*, 10878-10896.

3. Hou, Z. S.; Wang, Z. Z.; Wang, P. W.; Chen, F.; Luo, X. L., Near-infrared light-triggered mild-temperature photothermal effect of nanodiamond with functional groups. *Diamond and Related Materials* **2022,** *123*, 108831.

4. Li, J.; Liu, R.; Zhao, Q.; Shi, Y.; Gao, G.; Zhi, J., Nanodiamond-based photosensitizer: Enhancing photodynamic therapy and inhibiting tumor metastasis. *Carbon* **2021,** *174*, 90-97.

5. Mauriello Jimenez, C.; Knezevic, N. Z.; Rubio, Y. G.; Szunerits, S.; Boukherroub, R.; Teodorescu, F., et al., Nanodiamond-periodic mesoporous organosilica nanoparticles (PMO) for two-photon photodynamic therapy (PDT) and drug delivery. *Journal of Materials Chemistry B* **2016,** *4* (35), 5803-5808.

6. Matshitse, R.; Managa, M.; Nyokong, T., The modulation of the photophysical and photodynamic therapy activities of a phthalocyanine by detonation nanodiamonds: Comparison with graphene quantum dots and carbon nanodots. *Diamond and Related Materials* **2020,** *101*, 107617.

7. Matshitse, R.; Ngoy, B. P.; Managa, M.; Mack, J.; Nyokong, T., Photophysical properties and photodynamic therapy activities of detonated nanodiamonds-BODIPY-phthalocyanines nanoassemblies. *Photodiagnosis and Photodynamic Therapy* **2019,** *26*, 101-110.

8. Ryu, T. K.; Baek, S. W.; Kang, R. H.; Jeong, K. Y.; Jun, D. R.; Choi, S. W., Photodynamic and photothermal tumor therapy using phase-change material nanoparticles containing chlorin e6 and nanodiamonds. *Journal of Controlled Release* **2018,** *270*, 237-245.

9. Chen, Y.; Meng, Q.; Wu, M.; Wang, S.; Xu, P.; Chen, H., et al., Hollow Mesoporous Organosilica Nanoparticles: A Generic Intelligent Framework-Hybridization Approach for Biomedicine. *Journal of the American Chemical Society* **2014,** *136* (46), 16326-16334.

10. Fatieiev, Y.; Croissant, J. G.; Alamoudi, K.; Khashab, N. M., Cellular Internalization and Biocompatibility of Periodic Mesoporous Organosilica Nanoparticles with Tunable Morphologies: From Nanospheres to Nanowires. *ChemPlusChem* **2017,** *82* (4), 631-637.

11. Davies, G.; Hamer, M. F., Optical studies of the 1.945 eV vibronic band in diamond. *Proceedings of the Royal Society of London. A. Mathematical and Physical Sciences* **1976,** *348* (1653), 285-298.

12. Ma, Y.; Rohlfing, M.; Gali, A., Excited states of the negatively charged nitrogen-vacancy color center in diamond. *Physical Review B* **2010,** *81* (4), 041204.

13. Nam, J. S.; Hong, Y.; Lee, C. G.; Kim, T. I.; Lee, C.; Roh, D.-H., et al., Singlet Oxygen Generation from Polyaminoglycerol by Spin-Flip-Based Electron Transfer. *JACS Au* **2022,** *2* (4), 933-942.

14. Plakhotnik, T.; Aman, H., NV-centers in nanodiamonds: How good they are. *Diamond and Related Materials* **2018,** *82*, 87-95.

15. Szunerits, S.; Barras, A.; Boukherroub, R., Antibacterial Applications of Nanodiamonds. *International Journal of Environmental Research and Public Health* **2016,** *13* (4), 413-413.

16. Bilyy, R.; Pagneux, Q.; François, N.; Bila, G.; Grytsko, R.; Lebedin, Y., et al., Rapid Generation of Coronaviral Immunity Using Recombinant Peptide Modified Nanodiamonds. *Pathogens* **2021,** *10* (7), 861.

17. Lan, G.; Qiu, Y.; Fan, J.; Wang, X.; Tang, H.; Han, W., et al., Defective graphene@diamond hybrid nanocarbon material as an effective and stable metal-free catalyst for acetylene hydrochlorination. *Chemical Communications* **2019,** *55* (10), 1430-1433.

18. Wee, T. L.; Tzeng, Y. K.; Han, C. C.; Chang, H. C.; Fann, W.; Hsu, J. H., et al., Two-photon excited fluorescence of nitrogen-vacancy centers in proton-irradiated type Ib diamond. *The Journal of Physical Chemistry A* **2007,** *111* (38), 9379-86.

19. Chung, P. H.; Perevedentseva, E.; Cheng, C. L., The particle size-dependent photoluminescence of nanodiamonds. *Surface Science* **2007,** *601* (18), 3866-3870.

20. Xiao, J.; Liu, P.; Li, L.; Yang, G., Fluorescence Origin of Nanodiamonds. *The Journal of Physical Chemistry C* **2015,** *119* (4), 2239-2248.

21. Reineck, P.; Lau, D. W. M.; Wilson, E. R.; Fox, K.; Field, M. R.; Deeleepojananan, C., et al., Effect of Surface Chemistry on the Fluorescence of Detonation Nanodiamonds. *ACS Nano* **2017,** *11*, 10924-10934.

22. Desai, C.; Chen, K.; Mitra, S., Aggregation behavior of nanodiamonds and their functionalized analogs in an aqueous environment. *Environmental Science: Processes & Impacts* **2014,** *16* (3), 518-523.

23. Bumb, A.; Sarkar, S. K.; Billington, N.; Brechbiel, M. W.; Neuman, K. C., Silica Encapsulation of Fluorescent Nanodiamonds for Colloidal Stability and Facile Surface Functionalization. *Journal of the American Chemical Society* **2013,** *135* (21), 7815-7818.

24. Von Haartman, E.; Jiang, H.; Khomich, A. A.; Zhang, J.; Burikov, S. A.; Dolenko, T. A., et al., Core–shell designs of photoluminescent nanodiamonds with porous silica coatings for bioimaging and drug delivery I: fabrication. *Journal of Materials Chemistry B* **2013,** *1* (18), 2358.

25. Daurat, M.; Nguyen, C.; Dominguez Gil, S.; Sol, V.; Chaleix, V.; Charnay, C., et al., The mannose 6-phosphate receptor targeted with porphyrin-based periodic mesoporous organosilica nanoparticles for rhabdomyosarcoma theranostics. *Biomaterials Science* **2020,** *8* (13), 3678-3684.

26. Gaspar, D.; Veiga, A. S.; Sinthuvanich, C.; Schneider, J. P.; Castanho, M., Anticancer Peptide SVS-1: Efficacy Precedes Membrane Neutralization. *Biochemistry* **2012,** *51* (32), 6263-6265.

27. Figueira, T. N.; Oliveira, F. D.; Almeida, I.; Mello, E. O.; Gomes, V. M.; Castanho, M., et al., Challenging metastatic breast cancer with the natural defensin PvD(1). *Nanoscale* **2017,** *9* (43), 16887-16899.

28. Oliveira, F. D.; Cavaco, M.; Figueira, T. N.; Valle, J.; Neves, V.; Andreu, D., et al., The antimetastatic breast cancer activity of the viral protein-derived peptide vCPP2319 as revealed by cellular biomechanics. *The FEBS Journal* **2022,** *289* (6), 1603-1624.

29. East, L.; Isacke, C. M., The mannose receptor family. *Biochimica et Biophysica Acta - General Subjects* **2002,** *1572* (2), 364-386.

30. Sturge, J.; Wienke, D.; East, L.; Jones, G. E.; Isacke, C. M., GPI-anchored uPAR requires Endo180 for rapid directional sensing during chemotaxis. *Journal of Cell Biology* **2003,** *162* (5), 789-794.

31. Brevet, D.; Gary-Bobo, M.; Raehm, L.; Richeter, S.; Hocine, O.; Amro, K., et al., Mannose-targeted mesoporous silica nanoparticles for photodynamic therapy. *Chemical Communications* **2009,** (12), 1475.

32. Sperling, O.; Fuchs, A.; Lindhorst, T. K., Evaluation of the carbohydrate recognition domain of the bacterial adhesin FimH: design, synthesis and binding properties of mannoside ligands. *Organic & Biomolecular Chemistry* **2006,** *4* (21), 3913.

CHAPTER 3: Synthesis and photophysics of new two-photon responsive octupolar fluorophores

1. Introduction

The design of molecular chromophores possessing enhanced TPA properties has been extensively studied in the past few years.[1-6] TPA presents several advantages for biomedical applications, such as excitation with high selectivity levels in biological environment and photodamage reduction by the use of lower excitation intensities.[7]

However, the direct use of two-photon dyes in biological media is often limited by their unstable photophysical properties and poor solubility in aqueous media. Considering that, water-dispersible nanoparticles integrating such small organic molecules already proved their efficiency in solving those issues while keeping a right balance between biocompatibility and performance. Ying and coworkers reported multi-branched probes based on polycyclic aromatic hydrocarbon naphthalene indenofluorene groups encapsulated in an ethylene oxide/propylene oxide/F127 matrix by nanoprecipitation, with still suitable photophysical characteristics.[8]

Among the different organic dyes families, octupolar chromophores possessing non-centrosymmetric structure can be attractive for their multiphoton absorption properties. In our study, we report the synthesis of two new fluorescent two-photon absorbing octupolar compounds that can be described as $D(-\pi-A)_3$ systems, constituted of three push-pull branches, where D is an electron donor, π a conjugated system and A an electron acceptor.[9] The intrinsic TPA of those materials is resulting from ICT from triphenylamine (TPAM) donor core to sulfone-based peripheral groups that are strongly electron-withdrawing. Phenylene-vinylene conjugated linkers allow efficient electron communication between the electro-active groups.[10] Branching leads to cooperative enhancement of the TPA properties, in relation with coherent excitonic coupling between the branches.[11]

This fluorophore family has great potential for theranostics as it already displayed high TPA cross-sections in the biological window (700-1000 nm) and almost no toxicity in human embryonic kidney 293 cells.[12] In this context, the aim of this work was to prepare new three-branched molecules bearing hydroxyl end-groups to induce increased solubility in polar solvents or biological media and allow further trisilylation with isocyanatopropyltriethoxysilane. By this strategy, a silylated fluorophore would be easily

incorporable in PMO NPs frameworks during sol-gel process to obtain multifunctional nanoplatforms for TPEF imaging and PDT bioapplications.

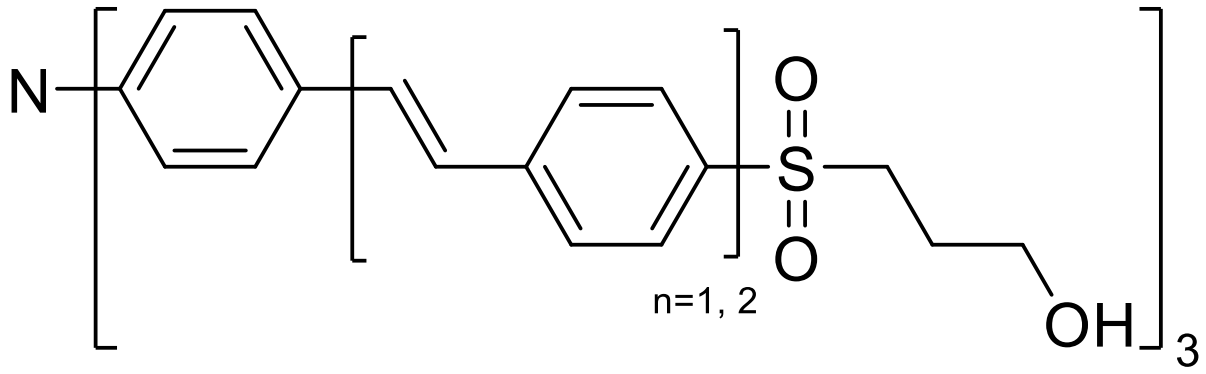

Figure 1: Simplified chemical formula of F and F2 new two-photon responsive three-branched dyes.

In there, we describe the multistep synthesis protocols of F and F2 (**Figure 1**) fluorophores, possessing one or two phenylene-vinylene spacers, respectively. Then, their photophysical properties in low- to medium-polarity solvents are presented and compared to the literature.

2. Results and discussion

2.1 Synthesis of new two-photon responsive fluorophores

The tripodal fluorophores F and F2 could be obtained by Heck reaction. Discovered by Mizoroki, Heck and Julia, the Heck coupling is basically a palladium-catalyzed vinylation between an unsaturated halogen derivative and an alkene in the presence of a base, generally triethylamine, potassium carbonate or sodium acetate.[13-15]

In our case, TPAM cores and sulfonyl-based branches were modified to bear either a halogen or alkene function for a final coupling yielding fluorescent products.

All new molecules were fully characterized by NMR spectroscopy (^{1}H and ^{13}C), HRMS and elemental analysis to confirm their purity.

Firstly, TPAM moieties were uniformly modified in para positions (**Scheme 1**). Compound **1a** was obtained by a two-step trisformylation in Vilsmeier-Haack conditions *via* the bisaldehyde compound to allow higher yield for the third substitution.[16] Then, trisalkene **1b** was formed by classic Wittig reaction with methyltriphenylphosphonium iodide.[12] In another

process pathway, tris(4-iodophenyl)amine **2** was produced in acidic medium by an adapted procedure.[17]

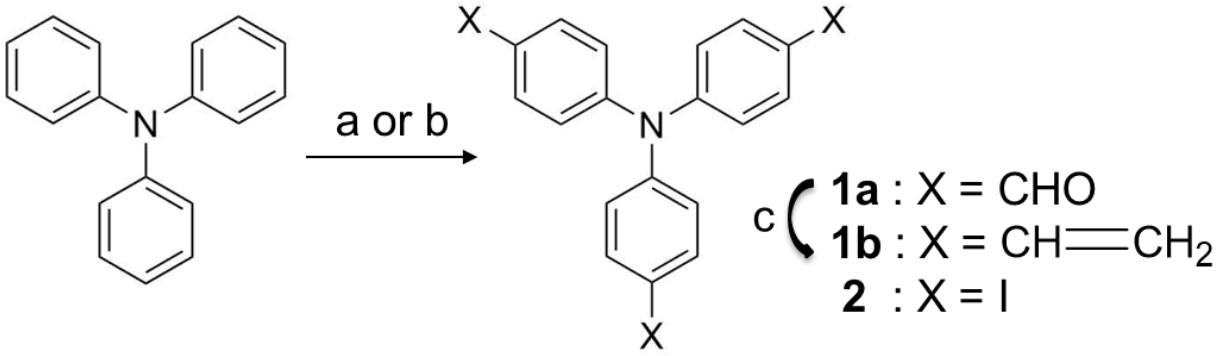

Scheme 1: Reagents and conditions for the preparation of TPAM-based cores. (a) TPAM, $POCl_3$ (25 eq.), DMF (23 eq.), 95 °C, 4 h, then $POCl_3$ (50 eq.), DMF (49 eq.), 95 °C, 2h (41% of **1a**); (b) TPAM, KI, HIO_4, acetic acid, 85 °C, 14 h (65% of **2**) ; (c) methyltriphenylphosphonium iodide, NaH, THF, rt, 15 h (94% of **1b**).

Secondly, after alkylation of *p*-bromothiophenol with 3-bromopropanol, resulting thioether **3** was oxidized by *m*-CPBA to reach the corresponding sulfone **4** (**Scheme 2**).[18] Then, the Heck coupling between **4** and *p*-vinylbenzaldehyde **5**[19] under Jeffery's conditions using tetrabutylammonium bromide salt granted better reactivity and selectivity with 43% yield of intermediate compound **6**.[20]

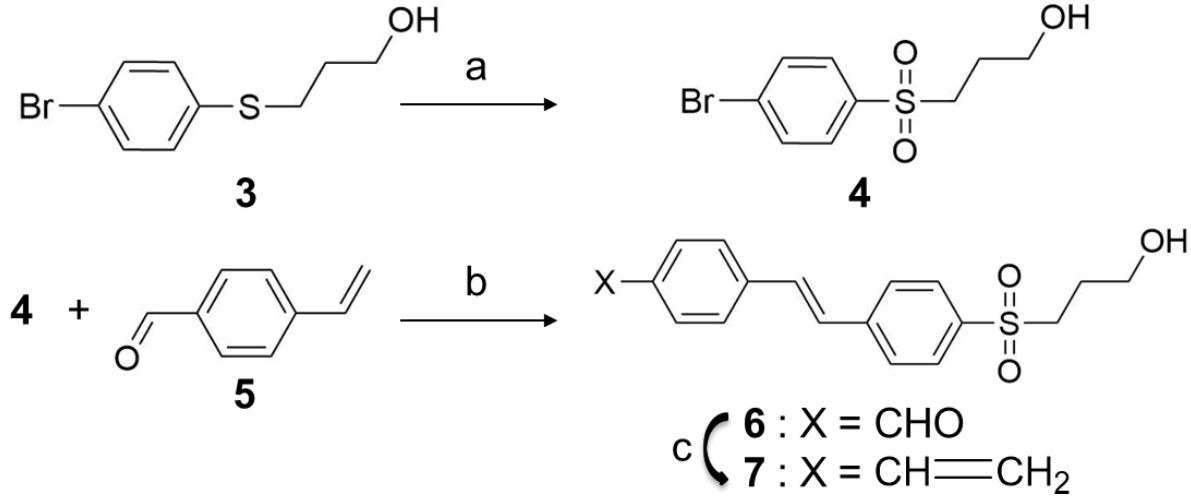

Scheme 2: Reagents and conditions for the preparation of branches with hydroxyl-ending group. (a) *m*-CPBA, DCM, rt, 15 h (79% of **4**); (b) **4** (1.00 eq.), **5** (1.45 eq.), $Pd(OAc)_2$, PPh_3, K_2CO_3, *n*-Bu_4NBr, DMF, 90 °C, 20 h (43% of **6**); (c) methyltriphenylphosphonium iodide, *t*-BuOK, DCM, rt, 15 h (13% of **7**).

The proton NMR spectrum in **Figure 2** confirmed the presence of aldehyde function with a singlet signal at δ = 10.05 ppm, and signal integration showed good correlation of the

different equivalent protons in the structure. Intermediate **6** was then condensed with methyltriphenylphosphonium iodide to afford the vinyl product **7** with *E* stereochemistry, in pure and isolated form, as confirmed by ^{1}H NMR (**Figure 3**). The reaction yielded only 13% of distyrene derivative as $OPPh_3$ by-product presented similar polarity and solubility than **7** in the different solvent mixtures and chromatographic conditions tested.

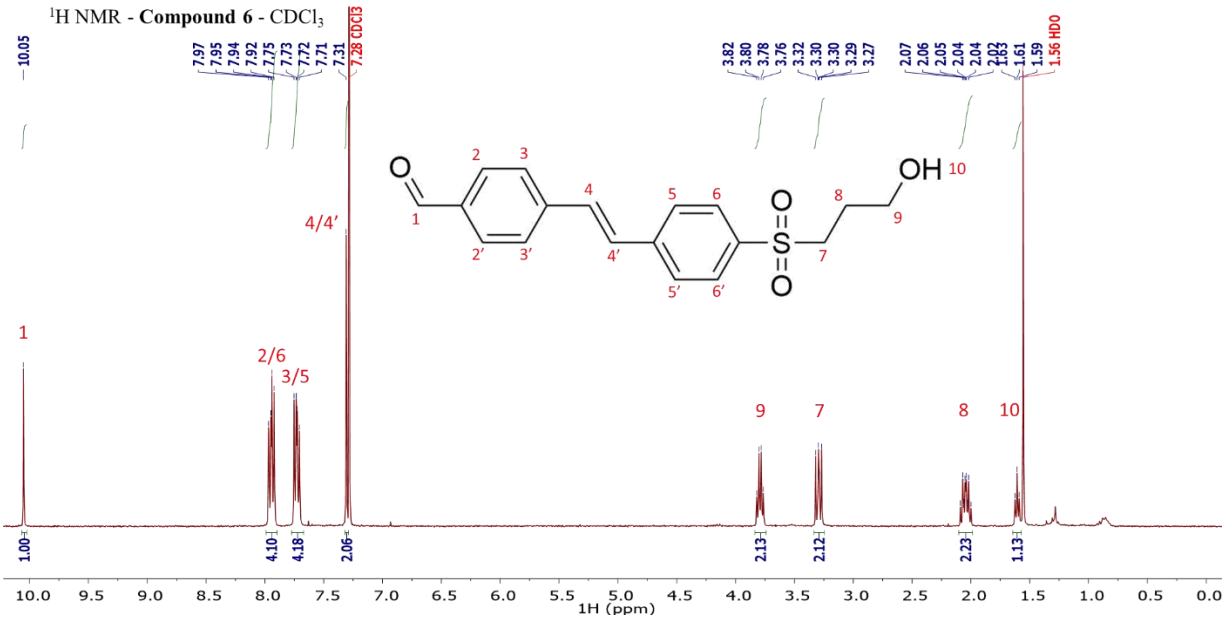

Figure 2: ^{1}H NMR spectrum of intermediate compound 6 (in $CDCl_3$).

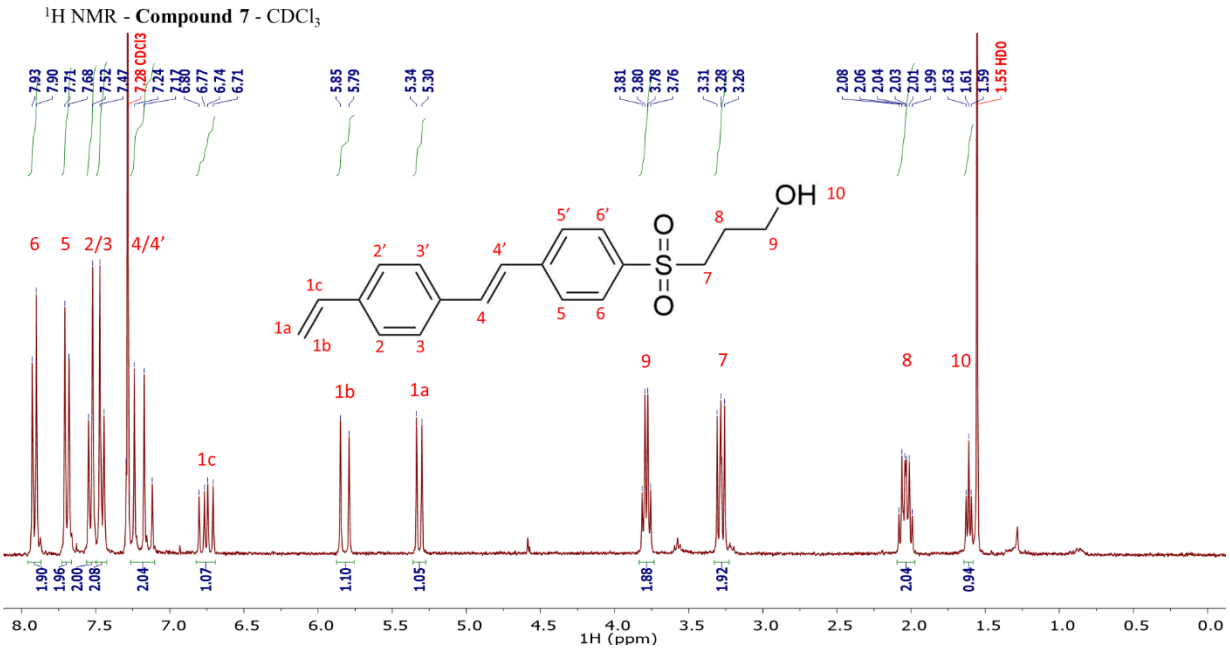

Figure 3: ^{1}H NMR spectrum of intermediate compound 7 (in $CDCl_3$).

Finally, treatment of trivinyl core **1b** with brominated derivative **4** by classic Heck reaction afforded octupole **8**, namely fluorophore F (**Scheme 3**). Conversely, fluorophore **9** (F2)

bearing an extended spacer of two phenylene-vinylene units was obtained in Jeffery's conditions by condensing triiodinated TPAM core **2** with vinyl intermediate **7**. The two dyes exclusively presented *E* stereochemistry. Olefinic protons visible on NMR spectra were all detected at higher chemical shifts than if they were displaying a *Z* stereochemistry (**Figure 4a-b**). In addition, the vicinal $^{3}J_{HH}$ coupling constants of all doublets were around 16.4 Hz (see in Experimental Section), which is characteristic of *trans* configuration.[21]

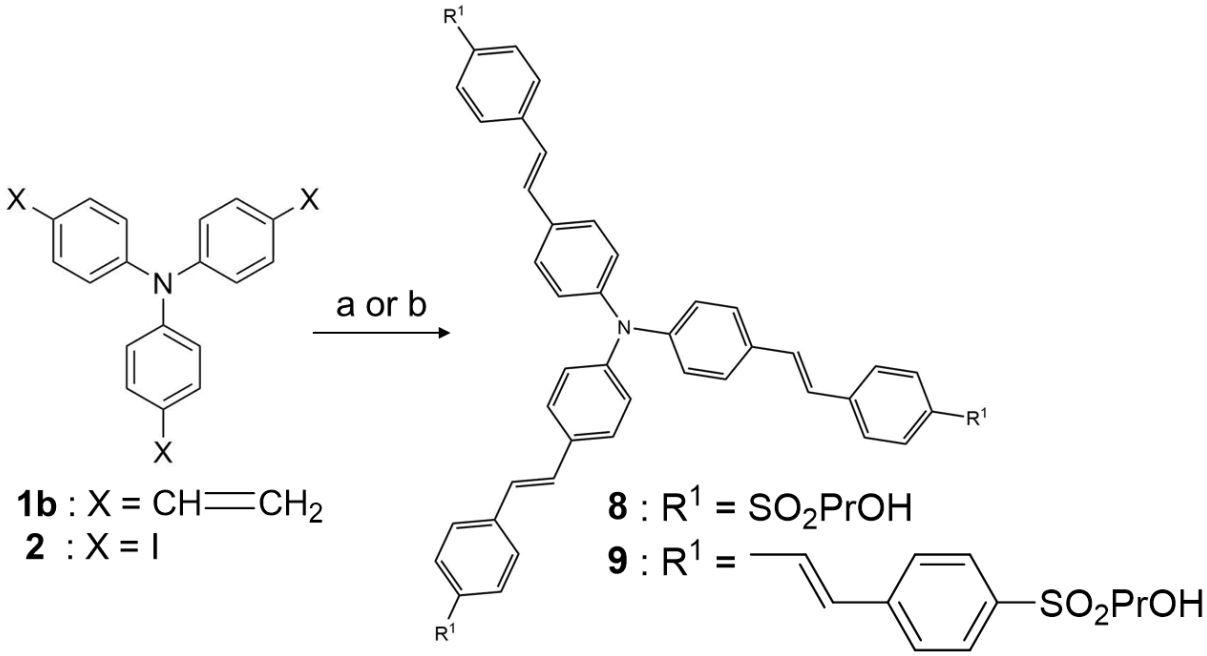

Scheme 3: Reagents and conditions for the preparation of F and F2 three-branched fluorophores. (a) **1b** (1.00 eq.), **4** (3.50 eq.), $Pd(OAc)_2$, (*o*-tol)$_3$P, Et_3N, DMF, 100 °C, 4 h (31% of **8**); (b) **2** (1.00 eq.), **7** (4.50 eq.), $Pd(OAc)_2$, PPh_3, K_2CO_3, *n*-Bu_4NBr, DMF, 90 °C, 16 h (26% of **9**).

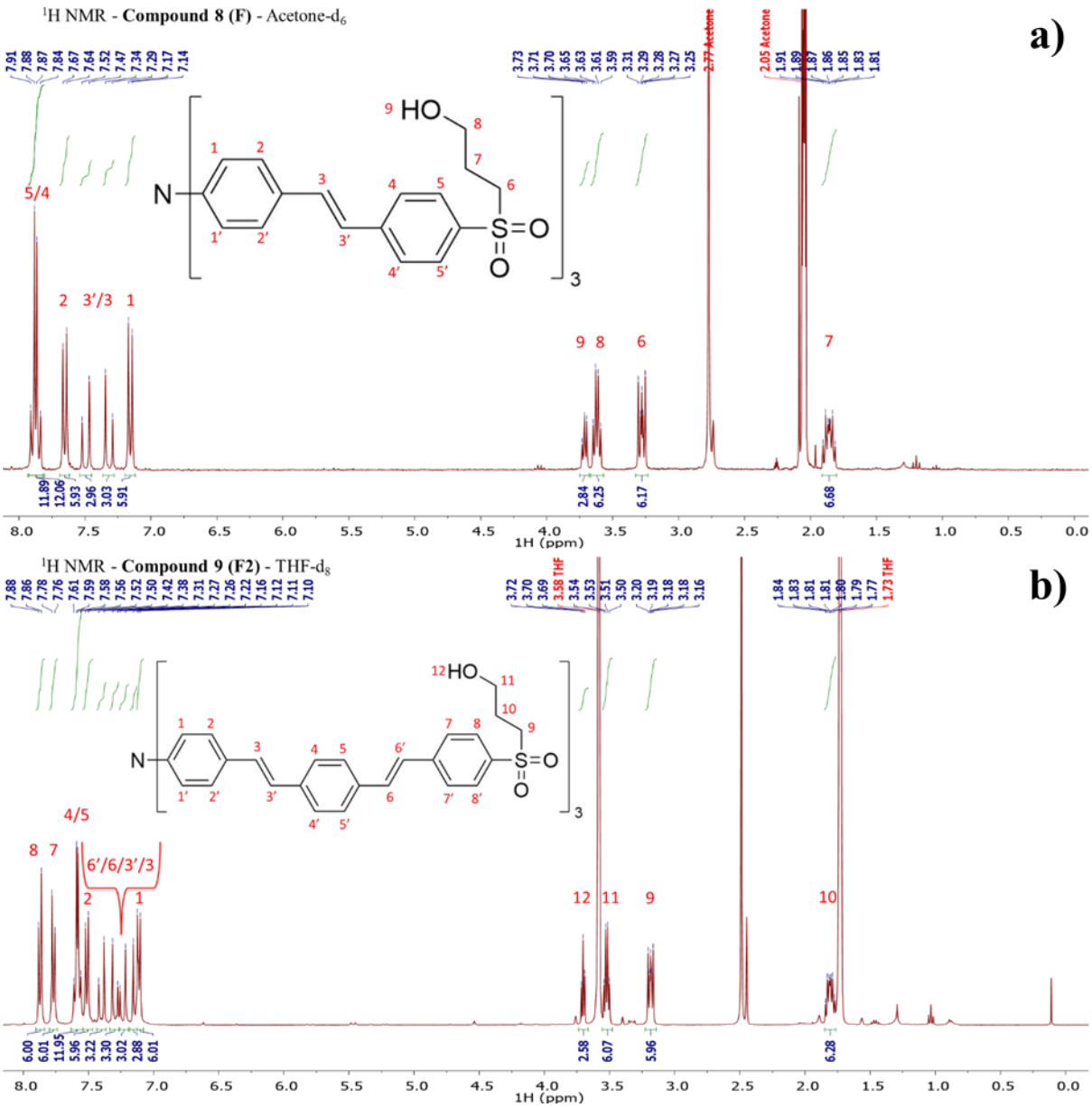

Figure 4: ^{1}H NMR spectra of three-branched fluorophores. (a) Compound **8** (F) bearing one phenylene-vinylene linker (in acetone-d_6); (b) Compound **9** (F2) bearing two phenylene-vinylene linkers (in THF-d_8)**.**

2.2 Photophysical studies of synthesized fluorophores

2.2.1 Solvatochromic studies

After synthesis, the photophysical properties of fluorophores were studied upon one-photon excitation.

Solvent effects on absorbance and fluorescence of the octupoles were first investigated in THF, DCM, EtOH and DMSO. Due to their three alcohol functions, both compounds were insoluble in solvents of low polarity, such as toluene and pentane.

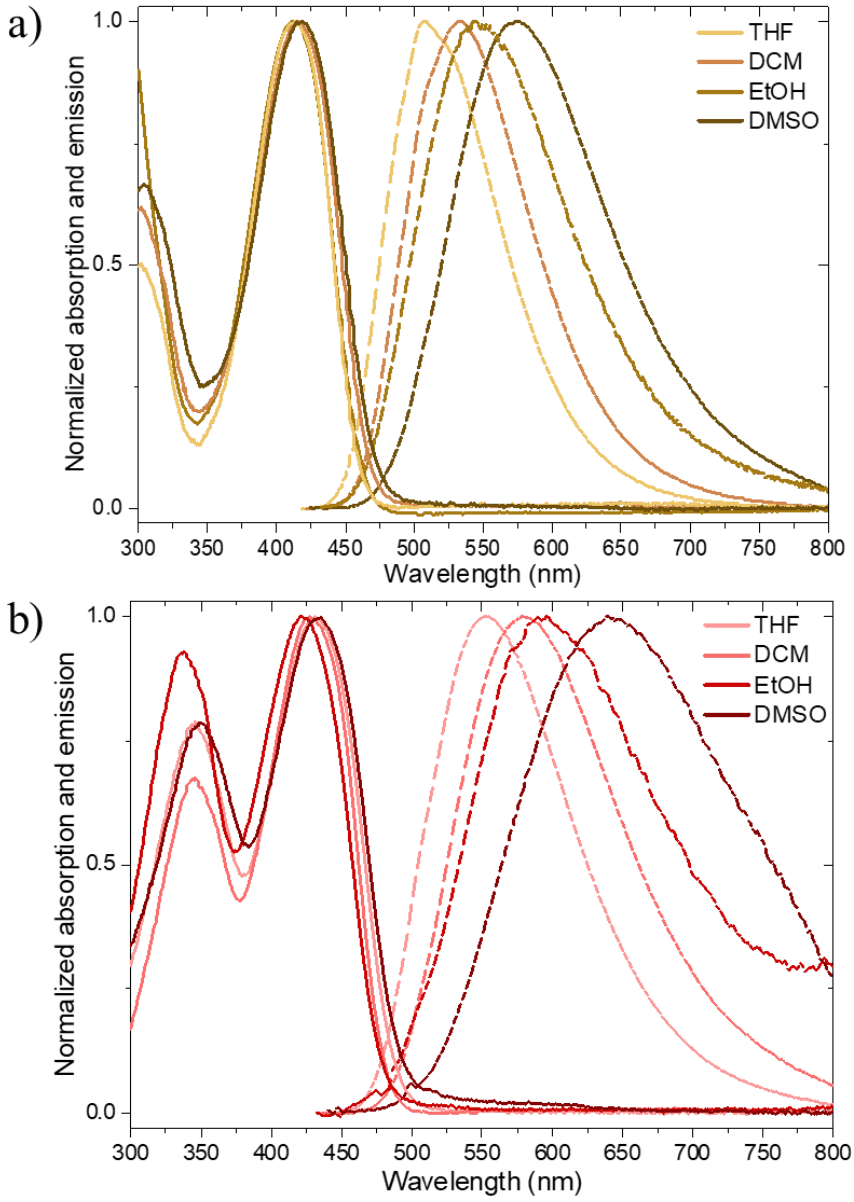

Figure 5: Normalized absorption and emission spectra of (a) F and (b) F2. Increased solvent polarity induces the bathochromic shift of fluorescence emission.

By increasing solvent polarity, a strong bathochromic shift of the fluorescence emission band was observed, whereas little to no shift of the absorption band was detected (**Figure 5a-b**). Consequently, Stokes shift $\Delta\lambda$ values increased and emission bands remarkably broadened with increasing polarity, from 93 to 155 nm (4431 to 6418 cm^{-1}) and from 106 to 204 nm (4657 to 7339 cm^{-1}) in the case of F and F2, respectively (**Table 1**). This effect is characteristic of ICT mechanism taking place upon excitation with fluorescence emission originating from a relaxed excited state localized on one of the dipolar branches. This phenomenon is particularly interesting when $\Delta\lambda \geq 80$ nm for biological applications such as TPEF imaging, because of the variability of biological media polarities.[10, 12, 22-23] For instance, such probes could serve in biodistribution studies or localization of materials used in theranostics.

As shown in **Table 1**, the fluorescence quantum yields decreased along with the increase of solvent polarity. This result could be mostly associated to the solvatochromic behavior of excited-state dipole moments that have variable interaction with solvent molecules, and also to the decrease of solubility (well-visible in the case of DMSO).

Now comparing F and F2, the longer conjugated system of F2 induces significant red shift of absorption and emission bands, as well as increase of fluorescence quantum yields in THF and DCM. F and F2 exhibit molar extinction coefficients in DCM of $\varepsilon_{max} = 8.1 \times 10^4$ and $\varepsilon_{max} = 1.1 \times 10^5$ M^{-1} cm^{-1}, respectively. Hence, the insertion of more phenylene-vinylene units improved the brightness ($B = \varepsilon_{max}\ \Phi_f$) of the longest fluorophore (in DCM: $B_F = 5.1 \times 10^4$; $B_{F2} = 7.5 \times 10^4$ M^{-1} cm^{-1}).

Table 1: Solvatochromic studies of F and F2 upon one-photon excitation. [a-b] Maximum absorbance (used for excitation) and emission wavelengths measured in solvents of various polarity. [c] Stokes shift ($1/\lambda_{abs.} - 1/\lambda_{em.}$). [d] Fluorescence quantum yields obtained using quinine bisulfate (QBS) in 0.5 M H_2SO_4 as a standard ($\Phi_{QBS} = 0.546$).

Compound	Solvent	$\lambda_{abs.,\ max}$ [a] (nm)	$\lambda_{em.,\ max}$ [b] (nm)	$\Delta\bar{\nu}$ [c] (cm^{-1})	Φ_f [d]
F	THF	414	507	4431	0.65
	DCM	417	533	5219	0.63
	EtOH	411	544	5949	0.44
	DMSO	420	575	6418	0.35
F2	THF	427	533	4657	0.75
	DCM	431	579	5931	0.70
	EtOH	422	589	6719	0.18
	DMSO	435	639	7339	0.06

2.2.2 Fluorescence lifetime measurements

The fluorescence lifetimes were determined by using time-correlated single-photon counting. Both compounds displayed monoexponential fluorescence decays. F2 lifetime was found to be shorter than that of F, with respectively 2.2 ns and 2.5 ns decay times (**Table 2**). Although the non-radiative decay rate is unchanged with longer conjugated system, the radiative decay rate is clearly enhanced in F2. One could associate this result to the hyperchromic shift observed, thus explaining the better fluorescence quantum yield.

Table 2: Experimental fluorescence lifetimes and the corresponding radiative ($k_{2r} = \Phi / \tau$) and non-radiative ($k_{2nr} = (1-\Phi) / \tau$) decay rates. Samples were tested in THF.

Compound	τ (ns)	k_r (10^9 s^{-1})	k_{nr} (10^9 s^{-1})
F	2.5	0.26	0.14
F2	2.2	0.34	0.11

3. Conclusions and perspectives

In conclusion, two new push-pull three-branched TPA fluorophores possessing a triphenylamine core were synthesized by multistep synthesis involving different Heck coupling strategies. They revealed similar structure-property behavior as other trigonal $A(–\pi–D)_3$ and $D(–\pi–A)_3$ octupoles described in the literature, with strong influence of conjugation length and aromaticity, as well as donor and acceptor strengths.[24-25]

F and F2 dyes are good candidates for bioapplications as they exhibit suitable photophysical properties in the NIR region, including tunable emission wavelength due to solvatochromic character, high TPA cross-sections values and fluorescence quantum yield in biological environments, thus providing efficient intrinsic three-dimensional resolution.

With hydroxyl end-groups, the newly synthesized fluorophores will be integrated in biocompatible PMO NPs vectors for a large bench of bioapplications. Considering their excellent TPA and TPEF properties, they could serve as bioimaging probes in combination with drug delivery and also as energy transfer source for FRET-enhanced strategies in anticancer and antibacterial TPE-PDT treatments. These aspects will be discussed in chapter 4.

4. Experimental section

Materials

Unless otherwise specified, ACS reagent grade starting materials and solvents were used as received from commercial suppliers without further purification.

Dimethylformamide (DMF, distilled using CaH_2), tetrahydrofuran (THF, distilled using sodium-benzophenone), dichloromethane (DCM), dimethylsulfoxide (DMSO), ethyl acetate (EtOAc), absolute ethanol (EtOH), diethyl ether (Et_2O), pentane, heptane, petroleum ether, acetonitrile (CH_3CN), sodium thiosulfate ($Na_2S_2O_3$), sodium bicarbonate ($NaHCO_3$), sodium sulfate (Na_2SO_4), magnesium sulfate ($MgSO_4$), palladium (II) acetate ($Pd(OAc)_2$), tri(*o*-tolyl)phosphine ($(o\text{-tol})_3P$), potassium carbonate (K_2CO_3), potassium iodide (KI, 99%), phosphoryl chloride ($POCl_3$, 99%), sodium hydroxide pellets (NaOH, ≥ 98%), sodium hydride (NaH, 60% dispersion in mineral oil), sulfuric acid (H_2SO_4), quinine bisulfate (QBS), 3-bromopropanol (97%), $CDCl_3$ (99.9 atom% D), dimethylsulfoxide-d_6 (99.9 atom% D), acetone-d_6 (99.9 atom% D) and tetrahydrofuran-d_8 (99.9 atom% D) were purchased from Merck (Saint-Quentin-Fallavier, France). Acetic acid, periodic acid (HIO_4), *m*-chloroperoxybenzoic acid (*m*-CPBA, 70-75%), terephtalaldehyde (98%), potassium *tert*-butoxide (*t*-BuOK), *p*-bromothiophenol (98%) tetrabutylammonium chloride ($n\text{-}Bu_4Br$), triphenylamine (TPAM), methyltriphenylphosphonium iodide (≥ 98%), triphenylphosphine and triethylamine (Et_3N, > 99%) were purchased from Thermo Fisher Scientific (Illkirch-Graffenstaden, France). Celite S® was obtained from VWR (Radnor, PA, USA). Silica for chromatography (0.04-0.63 mm silica gel, 60 Å pores, 40-60 μm) was purchased from Macherey-Nagel (Düren, Germany).

Analytical techniques

^1H and ^{13}C NMR spectra were obtained with a Bruker Avance III (300 or 400 MHz) NMR spectrometer (Billerica, MA, USA). CHNS elemental analysis and high resolution mass spectrometry (HRMS) analyses were performed at the Centre Régional de Mesures Physiques de l'Ouest (C.R.M.P.O., Rennes) either with a Bruker MaXis 4G (ES^+, Methanol:DCM 90:10 (v:v)) or with a Bruker Ultraflex III (MALDI, DCTB matrix).

Melting points were determined using a Kofler bench (Wagner & Munz).

All photophysical measurements were performed with freshly prepared air-equilibrated solutions of THF, DMSO, EtOH, DMF or DCM (HPLC grade) at room temperature (20 °C).

UV–Vis absorption spectra were recorded on dilute solutions (ca. 10^{-6} M) by using a Jasco V-770 spectrophotometer (Mary's Court Easton, MD, USA). Steady-state fluorescence studies were performed in quartz cells of 1 cm path length (ca. 1×10^{-6} M, optical density < 0.1) using an Edinburgh Instruments FLS920 fluorimeter (Edinburgh, UK) in photon-counting mode or a Jasco FP-8300 fluorimeter (Mary's Court Easton, MD, USA).

Multistep synthesis of fluorophores

*Tris(4-formylphenyl)amine (**1a**)*

$POCl_3$ (28.6 mL, 305.72 mmol, 25 eq.) was added portionwise at 0 °C to anhydrous DMF (21.8 mL, 23 eq.). After 1h stirring, triphenylamine (3.00 g, 12.23 mmol, 1 eq.) was quickly added. The temperature was immediately shifted to 95 °C, and the reaction mixture was stirred for 4h (solidification after 3-4h). Then, the reaction mixture was transferred to an ice bath and neutralized with 6M $NaOH_{aq.}$ solution. After addition of water, extractions in DCM, and drying over Na_2SO_4, the solvent was evaporated. The crude product was purified by column chromatography (DCM, then DCM/EtOAc 95/5) and a brown oil was recovered (2.89 g, ^{1}H NMR (300.13 MHz, $CDCl_3$): 90-95% dialdehyde, 5-10% trialdehyde estimated). $POCl_3$ (44.8 mL, 479.5 mmol, 50 eq.) was added portionwise at 0 °C to anhydrous DMF (36.4 mL, 49 eq.). After 1h30 stirring, the intermediary product (2.89 g, 1 eq.) was quickly additioned. The temperature was immediately shifted to 95 °C, and the reaction mixture was stirred for 2h. After extractions and purification like before, **1a** was obtained as a yellow solid (1.20 g, 41%). M.p. 233-235 °C; ^{1}H NMR (300.13 MHz, $CDCl_3$): δ=9.94 (s, 3H), 7.84 and 7.25 ppm (AA'XX', *J*=8.5 Hz, 12H).

*Tris(4-ethenylphenyl)amine (**1b**)*

Air was removed from a solution of **1a** (400 mg, 1.21 mmol, 1.00 eq.) and $MePPh_3^+$, I^- (3.93 g, 9.72 mmol, 8.00 eq.) in anhydrous THF (9.1 mL, 93 eq.). Then, NaH (291 mg, 12.15 mmol, 10.00 eq.) was added and the reaction mixture was stirred at room temperature for 24h. The excess of NaH was destroyed with ice at 0 °C. After addition of water, extractions with DCM, and drying over Na_2SO_4, the solvents were evaporated under reduced pressure. The crude product was purified by column chromatography (heptane/DCM, 40/60) and **1b** was obtained a pale-yellow solid (370 mg, 94%). ^{1}H NMR (300.13 MHz, $CDCl_3$): δ=7.35 and 7.09 (AA'XX', *J*=8.7 Hz, 12 H), 6.72 (dd, *J*=17.6 Hz, *J*=10.9 Hz, 3H), 5.70 (dd, *J*=17.6 Hz, *J*=0.7 Hz, 3H), 5.22 ppm (dd, *J*=10.9 Hz, *J*=0.7 Hz, 3H).

*Tris(4-iodophenyl)amine (**2**)*

Air was removed from a solution of triphenylamine (4.04 g, 16.47 mmol, 1.00 eq.) and acetic acid (60 mL) by blowing argon for 10 min. Then, KI (5.45 g, 32.83 mmol, 2.00 eq.) was added, followed by HIO_4 (3.50 g, 15.35 mmol, 0.93 eq.). The reaction mixture was heated at 85 °C for 14h. After evaporation of acetic acid, the solid was dissolved in DCM and consecutively washed with $Na_2S_2O_3$ and $NaHCO_3$. After drying over Na_2SO_4, the solvent was evaporated. Pure compound **2** was obtained after recrystallization from CH_3CN and filtration, as a brown solid (6.47 g, 65%). ^{1}H NMR (300.13 MHz, $CDCl_3$): δ=7.53 and 6.81 ppm (AA'XX', *J*=8.8 Hz, 12H); ^{13}C NMR (75.47 MHz, $CDCl_3$): δ 146.8, 138.6, 126.2, 86.7 ppm.

*3-[(4-Bromophenyl)thio]propanol (**3**)*

Air was removed from a solution of NaH (4.68 g, 60% in mineral oil, 117 mmol, 2.21 eq.) in anhydrous DMF (31.7 mL). Then, *p*-bromothiophenol (10 g, 52.9 mmol, 1.00 eq.) in anhydrous DMF (10.7 mL) was added dropwise to the solution *via* a dropping funnel at 0 °C (1h). After cooling to room temperature, 3-bromopropanol was added. The reaction mixture was stirred overnight. After addition of water, extractions with EtOAc and drying over Na_2SO_4, the solvents were evaporated. The crude product was then purified by column chromatography (heptane/EtOAc, 70/30) to afford product **3** (8.83 g, 68%) as a pale-yellow oil. ^{1}H NMR (300.13 MHz, $CDCl_3$): δ=7.40 (d, *J*=8.4 Hz, 2H), 7.21 (d, *J*=8.4 Hz, 2H), 3.57 (q, *J*=5.6 Hz, 2H), 3.03 (t, *J*=7.1 Hz, 2H), 1.88 ppm (m, 2H).

*3-[(4-Bromophenyl)sulfonyl]propanol (**4**)*

Air was removed from a solution of **3** (8.83 g, 35.73 mmol, 1.00 eq.) in DCM (93 mL, 40 eq.). Then, *m*-CPBA (70-75%, 20.87 g, 84.67 mmol, 2.37 eq.) was added portionwise. The reaction mixture was stirred for 15h, and then neutralized with 50 mL of 5M $NaOH_{aq.}$ solution at 0 °C. After addition of water, extractions with DCM, and drying over $MgSO_4$, the solvent was evaporated. The crude product was purified by column chromatography (heptane/EtOAc, 50/50) to afford sulfone **4** (7.92 g, 79%) as a white solid. ^{1}H NMR (300.13 MHz, $CDCl_3$): δ=7.76 and 7.72 (AA'XX', *J*=8.7 Hz, 4H), 3.77 (t, *J*=5.9 Hz, 2H), 3.23 (t, *J*=7.8 Hz, 2H), 2.01 (m, 2H), 1.71 ppm (bs, 1H).

*p-Vinylbenzaldehyde (**5**)*

Air was removed from a solution of K_2CO_3 (7.73 g, 55.92 mmol, 1.25 eq.) and $MePPh_3^+$, Br^- (17.58 g, 49.21 mmol, 1.10 eq.) in anhydrous THF (65 mL, 18 eq.) by blowing argon for 20

min. Then, terephtalaldehyde (6.00 g, 44.73 mmol, 1.00 eq.) was added, and the reaction mixture was heated at 80 °C for 20h. After filtration through Celite S® with heptane, the solvent was evaporated. The residue was filtrated (heptane/EtOAc 90/10) and the solvent was evaporated. The crude product was purified by column chromatography (pentane, then pentane/EtOAc, 98/2 to 90/10) and **5** was obtained as a yellow oil (3.60 g, 61%). ^{1}H NMR (300.13 MHz, $CDCl_3$): δ=9.99 (s, 1H), 7.84 (d, *J*=8.3 Hz, 2H), 7.55 d, *J*=8.3 Hz, 2H), 6.77 (dd, *J*=17.6 Hz, *J*=10.9 Hz, 1H), 5.90 (d, *J*=17.6 Hz, 1H), 5.43 ppm (d, *J*=10.9 Hz, 1H).

*4-[(1E)-2-{4-[(3-Hydroxypropyl)sulfonyl]phenyl}ethenyl]benzaldehyde (**6**)*

Air was removed from a solution of **4** (800 mg, 2.87 mmol, 1.00 eq.) and **5** (549 mg, 4.16 mmol, 1.45 eq.) in anhydrous DMF (13.1 mL, 60 eq.) by blowing argon for 30 min. Then, $Pd(OAc)_2$ (32.2 mg, 0.14 mmol, 0.05 eq.), PPh_3 (75.2 mg, 0.29 mmol, 0.10 eq.) and *n*-Bu_4NBr (924 mg, 2.87 mmol, 1.00 eq.) were added. The reaction mixture was heated at 90 °C for 20h. After addition of water, extractions with EtOAc, and drying over Na_2SO_4, the solvent was evaporated. The crude product was purified by solid deposit (DCM) column chromatography (heptane/EtOAc, 30/70 to 25/75) and **6** was obtained as a white solid (410 mg, 43%). M.p. 152-154 °C; ^{1}H NMR (300.13 MHz, $CDCl_3$): δ=10.05 (s, 1H), 7.95 (m, 4H), 7.73 (m, 4H), 7.29 (d, 2H), 3.79 (q, *J*=5.7 Hz, 2H), 3.29 (m, 2H), 2.04 (m, 2H), 1.61 ppm (t, *J*=5.3 Hz, 1H); ^{13}C NMR (75.47 MHz, $CDCl_3$): δ=191.4, 142.2, 142.0, 138.3, 136.1, 131.3, 130.3, 129.9, 128.7, 127.4, 127.4, 60.6, 53.4, 25.8 ppm; HRMS (ES^+, $CH_3OH/CHCl_2$, 90/10): m/z calcd for $C_{18}H_{18}O_4S$: 353.0818 $[M+Na]^+$; found: 353.0823 ; elemental analysis calcd (%) for $C_{18}H_{18}O_4S$ (330.09): C 65.43, H 5.49, S 9.70; found: C 65.36, H 5.44, S 9.43.

*1-Ethenyl-4-[(1E)-2-{4-[(3-hydroxypropyl)sulfonyl]phenyl}ethenyl]benzene (**7**)*

Air was removed from a solution of **6** (1.40 g, 4.24 mmol, 1.00 eq.) and $MePPh_3^+$, I^- (3.43 g, 8.47 mmol, 2.00 eq.) in anhydrous DCM (90 mL, 333 eq.) by blowing argon for 10 min. Then, *t*-BuOK (1.47 g, 13.14 mmol, 3.10 eq.) was added. The reaction mixture was stirred for 15h. After filtration through Celite S® with DCM, the solvent was evaporated. The crude product was purified by column chromatography (heptane/DCM, 50/50). Fractions containing the product were gathered and purified by solid deposit (DCM) column chromatography (DCM/EtOAc, 95/5 to 75/25) and the eluent was evaporated. Then, the residue was triturated with Et_2O, $OPPh_3$ by-product was removed and **7** was obtained as a pale-yellow solid (185 mg, 13%). M.p. 192-194 °C; ^{1}H NMR (300.13 MHz, $CDCl_3$): δ=7.92 (d, *J*=8.4 Hz, 2H), 7.69 (d, *J*=8.4 Hz, 2H), 7.53 (d, *J*=8.3 Hz, 2H), 7.46 (d, *J*=8.3 Hz, 2H), 7.26 (d, *J*=16.3 Hz, 1H) 7.15 (d,

J=16.3 Hz, 1H), 6.76 (dd, *J*=17.6 Hz, *J*=10.9 Hz, 1H), 5.82 (d, *J*=17.6 Hz, 1H), 5.32 (d, *J*=10.9 Hz, 1H), 3.79 (q, *J*=5.7 Hz, 2H), 3.27 (m, 2H), 2.04 (m, 2H), 1.61 ppm (t, *J*=5.3 Hz, 1H); ^{13}C NMR (75.47 MHz, $CDCl_3$): δ=142.9, 138.0, 137.3, 136.3, 135.8, 132.3, 128.5, 127.2, 127.0, 126.7, 126.4, 114.5, 60.6, 53.4, 25.8 ppm; HRMS (ES^+, $CH_3OH/CHCl_2$, 90/10): m/z calcd for $C_{19}H_{20}O_3S$: 351.10254 $[M+Na]^+$; found: 351.1024; elemental analysis calcd (%) for $C_{19}H_{20}O_3S$ (328.11): C 69.49, H 6.14, S 9.76; found: C 68.86, H 5.74, S 9.85.

*Tris{4-[(1E)-2-{4-[(3-hydroxypropyl)sulfonyl]phenyl}ethenyl]phenyl}amine (**8**)*

Air was removed from a solution of **1b** (400 mg, 1.24 mmol, 1.00 eq.) and **4** (1.21 g, 4.328 mmol, 3.50 eq.) in anhydrous DMF (11.5 mL, 120 eq.) and Et_3N (0.7 mL, 4.95 mmol, 4.00 eq.) by blowing argon for 20 min. Then, $Pd(OAc)_2$ (41.6 mg, 0.19 mmol, 0.15 eq.) and (*o*-tol)$_3$P (113 mg, 0.37 mmol, 0.30 eq.) were added. The reaction mixture was heated at 100 °C for 4h. After filtration through Celite S® with DCM, addition of water, extractions with DCM, and drying over $MgSO_4$, the solvents were evaporated. The crude product was purified by solid deposit (DCM) column chromatography (EtOAc/EtOH/Et_3N, 96/3/1 to 87/12/1) to afford fluorophore **8** as an orange solid (349 mg, 31%). M.p. 146-148 °C; ^{1}H NMR (300.13 MHz, $(CD_3)_2CO$): δ=7.90 (d, *J*=8.6 Hz, 6H), 7.86 (d, *J*=8.6 Hz, 6H), 7.66 (d, *J*=8.6 Hz, 6H), 7.51 (d, *J*=16.4 Hz, 3H), 7.33 (d, *J*=16.4 Hz, 3H), 7.16 (d, *J*=8.6 Hz, 6H), 3.73 (m, 3H), 3.62 (q, *J*=5.8 Hz, 6H), 3.30 (m, 6H), 1.88 ppm (m, 6H) ; ^{13}C NMR (75.47 MHz, $(CD_3)_2CO$): δ 147.3, 143.0, 138.0, 132.0, 131.7, 128.5, 128.2, 126.8, 125.6, 124.3, 59.5, 52.9, 26.3 ppm; HRMS (ES^+, $CH_3OH/CHCl_2$, 90/10): m/z calcd for $C_{51}H_{51}NO_9S_3$: 940.26182 $[M+Na]^+$; found: 940.2622; elemental analysis calcd (%) for $C_{51}H_{51}NO_9S_3$ (917.27): C 57.39, H 2.57, N 1.49, S 10.21; found: C 57.19, H 2.78, N 1.39, S 10.22.

*Tris{4-[(1E)-2-(4{(1E)-2[4-(3-hydroxypropylsulfonyl)phenyl]ethenyl}phenyl]ethenyl]phenyl}amine (**9**)*

Air was removed from a solution of **2** (67.5 mg, 0.11 mmol, 1.00 eq.), **7** (160 mg, 0.49 mmol, 4.50 eq.) and K_2CO_3 (80.8 mg, 0.58 mmol, 5.40 eq.) in anhydrous DMF (5.0 mL, 596 eq.) by blowing argon for 30 min. Then, $Pd(OAc)_2$ (3.6 mg, 0.02 mmol, 0.15 eq.), PPh_3 (8.5 mg, 0.03 mmol, 0.30 eq.) and *n*-Bu_4NBr (157 mg, 0.49 mmol, 4.50 eq.) were added. The reaction mixture was heated at 90 °C for 16h. After solvent evaporation, the crude product was purified by solid deposit (DCM/EtOH) column chromatography (DCM/EtOH, 99/1 to 85/15). Fractions containing the product were gathered and purified by solid deposit (THF) column chromatography (petroleum ether/THF, 30/70 to 23/77) and the solvents were evaporated.

Then, BHT from THF was removed by recrystallization (pentane/Et_2O, then pentane/EtOH), to afford fluorophore **9** as a red solid (35.0 mg, 26%). M.p. 179-181 °C; ^{1}H NMR (300.13 MHz, THF-d_8): δ= 7.87 (d, *J*=8.5 Hz, 6H), 7.76 (d, *J*=8.5 Hz, 6H), 7.57 (m, 12H), 7.51 (d, *J*=8.5 Hz, 6H), 7.40 (d, *J*=16.3 Hz, 3H), 7.29 (d, *J*=16.3 Hz, 3H), 7.24 (d, *J*=16.3 Hz, 3H), 7.13 (d, *J*=16.3 Hz, 3H), 7.11 (d, *J*=8.5 Hz, 6H), 3.68 (t, *J*=5.2 Hz, 3H), 3.52 (q, *J*=5.8 Hz, 6H), 3.18 (m, 6H), 1.81 ppm (m, 6H); ^{13}C NMR (75.47 MHz, THF-d_8): δ=147.9, 143.7, 139.7, 139.1, 136.9, 133.6, 132.8, 129.5, 129.3, 128.5, 128.2, 127.8, 127.7, 127.6, 127.4, 125.2, 60.6, 54.1, 27.4 ppm; HRMS (MALDI, DCTB): m/z calcd for $C_{75}H_{69}NO_9S_3$: 1223.4129 [$M^{+\cdot}$]; found: 1223.412.

Photophysical studies of synthesized fluorophores

Solvatochromism studies

All photophysical measurements were performed with freshly prepared air-equilibrated solutions of THF, DMSO, EtOH, DMF or DCM (HPLC grade) at room temperature (20 °C). The fluorophore samples used to prepare the solutions were freshly recrystallized or thoroughly washed with cooled ether/pentane prior to the measurements to remove any organic impurity. UV–Vis absorption spectra (Jasco V-770) and fully corrected excitation and emission spectra (Jasco FP-8300) were obtained on dilute solutions (ca. 10^{-6} M) with an optical density at $\lambda_{exc.} \leq$ 0.1. The fluorescence quantum yield of each compound was calculated using the integral of the fully corrected emission spectra relative to that of a standard, quinine bisulfate (QBS, H_2SO_4 0.5 M, Φ_{QBS} = 0.546).[26-27]

Fluorescence lifetime measurements

Steady-state fluorescence studies were performed in dilute air-equilibrated THF solutions in quartz cells of 1 cm path length (ca. 1×10^{-6} M, optical density < 0.1) at room temperature (20 °C) using an Edinburgh Instruments FLS920 fluorimeter (Xe lamp) in time-correlated single-photon counting mode in order to determine fluorescence lifetime τ of the two synthesized fluorophores.

Bibliography

1. Caminade, A.-M.; Zibarov, A.; Cueto Diaz, E.; Hameau, A.; Klausen, M.; Moineau-Chane Ching, K., et al., Fluorescent phosphorus dendrimers excited by two photons: synthesis, two-photon absorption properties and biological uses. *Beilstein Journal of Organic Chemistry* **2019,** *15*, 2287-2303.

2. Li, G.; Wang, S.; Yang, S.; Liu, G.; Hao, P.; Zheng, Y., et al., Synthesis, Photophysical Properties and Two-Photon Absorption Study of Tetraazachrysene-based N-Heteroacenes. *Chemistry – An Asian Journal* **2019,** *14* (10), 1807-1813.

3. An, J. M.; Kim, S. H.; Kim, D., Recent advances in two-photon absorbing probes based on a functionalized dipolar naphthalene platform. *Organic & Biomolecular Chemistry* **2020,** *18* (23), 4288-4297.

4. Feng, W.; Liu, K.; Zang, J.; Xu, J.; Peng, H.; Ding, L., et al., Resonance-Enhanced Two-Photon Absorption and Optical Power Limiting Properties of Three-Dimensional Perylene Bisimide Derivatives. *The Journal of Physical Chemistry B* **2021,** *125* (41), 11540-11547.

5. Pascal, S.; David, S.; Andraud, C.; Maury, O., Near-infrared dyes for two-photon absorption in the short-wavelength infrared: strategies towards optical power limiting. *Chemical Society Reviews* **2021,** *50* (11), 6613-6658.

6. Wu, L.; Liu, J.; Li, P.; Tang, B.; James, T. D., Two-photon small-molecule fluorescence-based agents for sensing, imaging, and therapy within biological systems. *Chemical Society Reviews* **2021,** *50* (2), 702-734.

7. Rouxel, C.; Charlot, M.; Mir, Y.; Frochot, C.; Mongin, O.; Blanchard-Desce, M., Banana-shaped biphotonic quadrupolar chromophores: from fluorophores to biphotonic photosensitizers. *New Journal of Chemistry* **2011,** *35* (9), 1771.

8. Hu, L.; Zhang, G.; Liu, Y.; Guo, T.; Shao, L.; Ying, L., Efficient dendrimers based on naphthalene indenofluorene for two-photon fluorescent imaging in living cells and tissues. *Journal of Materials Chemistry C* **2020,** *8* (6), 2160-2170.

9. Cvejn, D.; Michail, E.; Polyzos, I.; Almonasy, N.; Pytela, O.; Klikar, M., et al., Modulation of (non)linear optical properties in tripodal molecules by variation of the peripheral cyano acceptor moieties and the π-spacer. *Journal of Materials Chemistry C* **2015,** *3* (28), 7345-7355.

10. Katan, C.; Terenziani, F.; Mongin, O.; Werts, M. H. V.; Porrès, L.; Pons, T., et al., Effects of (Multi)branching of Dipolar Chromophores on Photophysical Properties and Two-Photon Absorption. *The Journal of Physical Chemistry A* **2005,** *109* (13), 3024-3037.

11. Xu, L.; Lin, W.; Huang, B.; Zhang, J.; Long, X.; Zhang, W., et al., The design strategies and applications for organic multi-branched two-photon absorption chromophores with novel cores and branches: a recent review. *Journal of Materials Chemistry C* **2021,** *9* (5), 1520-1536.

12. Le Droumaguet, C.; Sourdon, A.; Genin, E.; Mongin, O.; Blanchard-Desce, M., Two-Photon Polarity Probes Built from Octupolar Fluorophores: Synthesis, Structure-Properties Relationships, and Use in Cellular Imaging. *Chemistry - An Asian Journal* **2013,** *8* (12), 2984-3001.

13. Mizoroki, T.; Mori, K.; Ozaki, A., Arylation of Olefin with Aryl Iodide Catalyzed by Palladium. *Bulletin of the Chemical Society of Japan* **1971,** *44* (2), 581-581.

14. Heck, R. F.; Nolley, J. P., Palladium-catalyzed vinylic hydrogen substitution reactions with aryl, benzyl, and styryl halides. *The Journal of Organic Chemistry* **1972,** *37* (14), 2320-2322.

15. Julia, M.; Duteil, M., Condensation of aromatic halides with olefins catalyzed by palladium(0). *Bulletin de la Société Chimique de France* **1973**, 2790.

16. Mallegol, T.; Gmouh, S.; Meziane, M. A. A.; Blanchard-Desce, M.; Mongin, O., Practical and Efficient Synthesis of Tris(4-formylphenyl)amine, a Key Building Block in Materials Chemistry. *Synthesis* **2005,** *2005* (11), 1771-1774.

17. Khanasa, T.; Jantasing, N.; Morada, S.; Leesakul, N.; Tarsang, R.; Namuangruk, S., et al., Synthesis and Characterization of 2D-D-π-A-Type Organic Dyes Bearing Bis(3,6-di-tert-butylcarbazol-9-ylphenyl)aniline as Donor Moiety for Dye-Sensitized Solar Cells. *European Journal of Organic Chemistry* **2013,** *2013* (13), 2608-2620.

18. Semple, G.; Santora, V. J.; Smith, J. M.; Covel, J. A.; Hayashi, R.; Gallardo, C., et al., Identification of biaryl sulfone derivatives as antagonists of the histamine H3 receptor: Discovery of (R)-1-(2-(4′-(3-methoxypropylsulfonyl)biphenyl-4-yl)ethyl)-2-methylpyrrolidine (APD916). *Bioorganic & Medicinal Chemistry Letters* **2012,** *22* (1), 71-75.

19. Greenhalgh, M. D.; Frank, D. J.; Thomas, S. P., Iron-Catalysed Chemo-, Regio-, and Stereoselective Hydrosilylation of Alkenes and Alkynes using a Bench-Stable Iron(II) Pre-Catalyst. *Advanced Synthesis & Catalysis* **2014,** *356* (2-3), 584-590.

20. Jeffery, T., On the efficiency of tetraalkylammonium salts in Heck type reactions. *Tetrahedron* **1996,** *52* (30), 10113-10130.

21. Fleming, I.; Williams, D. H., *Spectroscopic methods in organic chemistry*. Springer: **1966**.

22. Katan, C.; Charlot, M.; Mongin, O.; Le Droumaguet, C.; Jouikov, V.; Terenziani, F., et al., Simultaneous Control of Emission Localization and Two-Photon Absorption Efficiency in Dissymmetrical Chromophores. *The Journal of Physical Chemistry B* **2010,** *114* (9), 3152-3169.

23. Gautam, P.; Wang, Y.; Zhang, G.; Sun, H.; Chan, J. M. W., Using the Negative Hyperconjugation Effect of Pentafluorosulfanyl Acceptors to Enhance Two-Photon Absorption in Push–Pull Chromophores. *Chemistry of Materials* **2018,** *30* (20), 7055-7066.

24. Tian, Y.-P.; Li, L.; Zhang, J.-Z.; Yang, J.-X.; Zhou, H.-P.; Wu, J.-Y., et al., Investigations and facile synthesis of a series of novel multi-functional two-photon absorption materials. *Journal of Materials Chemistry* **2007,** *17* (34), 3646.

25. Chung, S.-J.; Kim, K.-S.; Lin, T.-C.; He, G. S.; Swiatkiewicz, J.; Prasad, P. N., Cooperative Enhancement of Two-Photon Absorption in Multi-branched Structures. *The Journal of Physical Chemistry B* **1999,** *103* (49), 10741-10745.

26. Crosby, G. A.; Demas, J. N., Measurement of photoluminescence quantum yields. Review. *The Journal of Physical Chemistry* **1971,** *75* (8), 991-1024.

27. Eaton, D. F., Reference materials for fluorescence measurement. *Pure and Applied Chemistry* **1988,** *60* (7), 1107-1114.

CHAPTER 4: Fluorophore-porphyrin PMO nanoparticles, antibiotic loading studies and FRET evaluation

1. Introduction

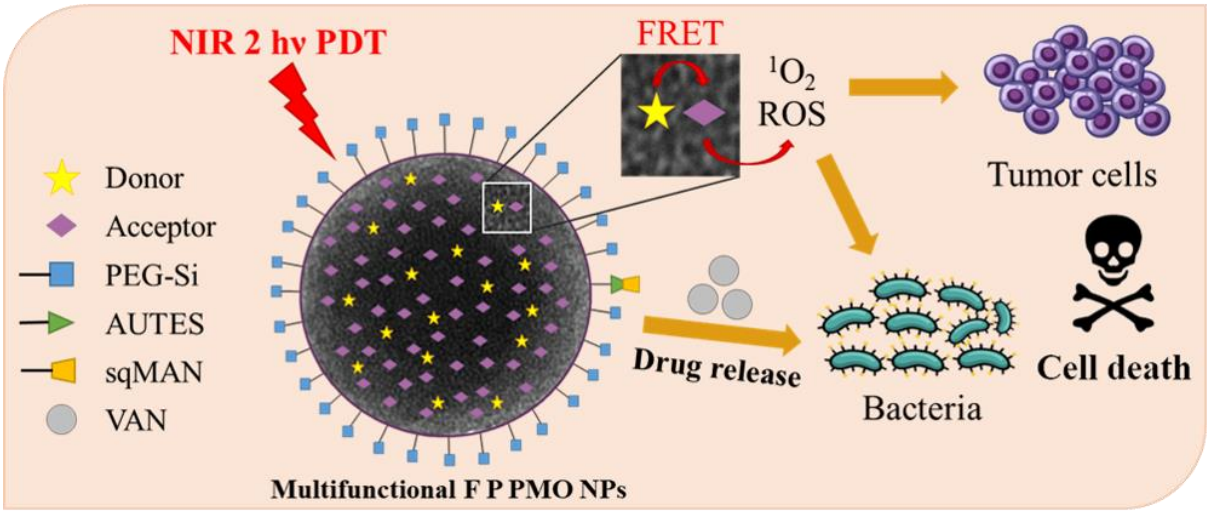

Figure 1: Graphical abstract.

There is a vital need for more advanced anticancer and antibacterial strategies, especially to face acquired resistance issues conjointly with antimicrobial resistance (AMR) that is currently marking the end of the antibiotic era.[1-2]

Two-photon excitation photodynamic therapy (TPE-PDT) is an emerging approach to treat a broad range of solid tumors and infection-associated diseases with three-dimensional resolution and increased penetration depth (> 2 cm) in living tissues compared to UV-visible light. Two-photon photosensitizing probes with high capacity to generate ROS in the NIR region are necessary to efficiently eradicate the targets while reducing the side effects by diminishing the laser irradiation power. However, hyper-conjugated two-photon organic chromophores are generally limited by their poor biocompatibility and dispersion in biological media, and they are not selective for tumors.[3-4] Consequently, third generation PS-based materials have started to be developed to provide solutions to the issues encountered with first-class and second-class chromophores. In that respect, liposomes, dendrimers and nanoparticles have been largely studied as biocompatible platforms where active elements (PSs, drugs, biomolecules, imaging agents, etc.) are entrapped, grafted onto the surface or even integrated in the framework during synthesis.[5-9]

PMO nanoparticles are noteworthy materials for biomedical applications. With their hybrid structure, they can simultaneously integrate hydrophobic and hydrophilic fractions to build functional complex systems that can specifically reach the targeted cells or tissues. Moreover,

their porous framework facilitates interactions with biological environments, ROS diffusion for PDT and biomolecule transport. Mesoporous organosilica nanostructures hold great potential for external stimuli-triggered controlled delivery by the action of pH,[10] temperature,[11] light,[12] or by redox reaction with glutathione reduced form (GSH), a natural tripeptide present in high rates in bacteria environment and in cancer cells.[13]

In this chapter, the development of two-photon responsive fluorophore-porphyrin periodic mesoporous organosilica (F P PMO) NPs and biodegradable analogs (F P BPMO) is described. A highly TPA-active fluorophore (F, introduced in chapter 3) and a porphyrin photosensitizer (P) were integrated in sol-gel synthesis as a potential FRET couple for enhanced TPE-PDT and fluorescence tracking. The photophysical properties of the prepared materials were studied before and after covalent integration of F and P moieties in nanoparticles. Different formulations of organoalkoxysilane precursors were tested, as well as surface functionalization, to prepare multifunctional materials with suitable morphology, size and stability. In particular, the use of a polysulfide-based reactant was explored to enhance NPs biodegradation properties in biological environment.[14] The loading of the well-known vancomycin hydrochloride (VAN) antibiotic was also studied. The potential of PMO NPs for redox-triggered drug release was evaluated by biodegradability simulation and release kinetic studies. Next, the therapeutic potential of the prepared F P (B)PMO nanoparticles for antitumor and antibacterial TPE-PDT, antibiotic delivery, and combination of antibiotherapy and TPE-PDT will be discussed in chapter 5.

2. Results and discussion

2.1 Design of multifunctional fluorophore-porphyrin biodegradable PMO nanoparticles

2.1.1 Preparation of sol-gel precursors

The main objective of this work is to build PMO nanoparticles with enhanced TPE-PDT performances resulting from efficient donor-acceptor FRET couples. To achieve this goal, we proposed to include two-photon chromophores with high potency directly in the PMO framework. Hence, three-branched two-photon fluorophore (F) designed beforehand, and commercial 5,10,15,20-tetrakis(4-aminophenyl)porphyrin (P), possessing two central acidic protons, were respectively chosen as donor and acceptor moieties. Porphyrin P was already employed in PMO nanoparticles as an active two-photon PS against MCF-7 cancer cells.[15] Prior to the sol-gel process leading to the formation of organosilica nanoparticles, the two

chromophores were silylated by condensation with isocyanatopropyltriethoxysilane (ICPTES) in the presence of triethylamine, which was adapted from previously reported procedures.[16-18] Hydroxyl-terminated F was trisilylated by formation of carbamate groups (F-Si), and porphyrin-derivative P was tetrasilylated, forming urea characteristic linkage (P-Si, **Figure 2**).

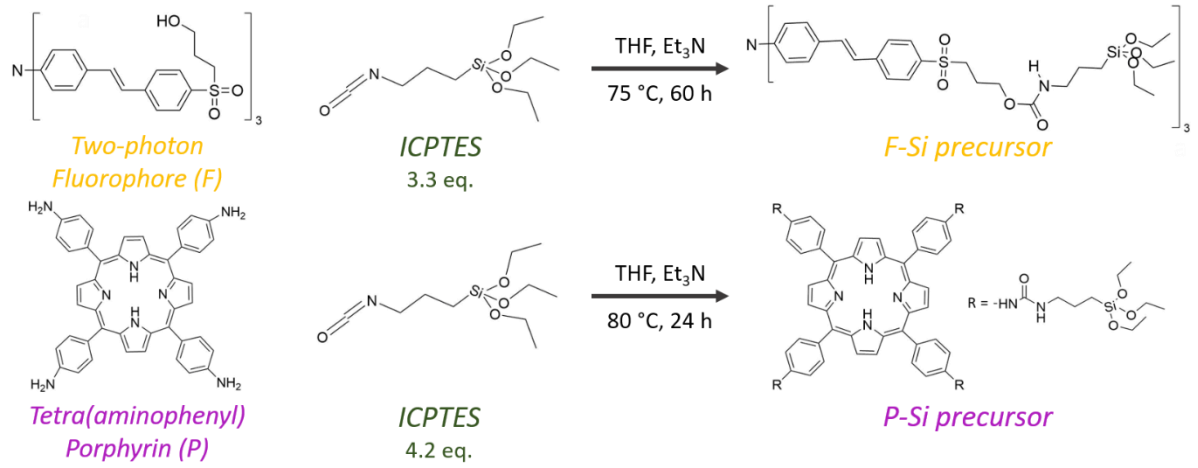

Figure 2: Silylation of two-photon chromophores for further integration in sol-gel synthesis. Fluorophore F was trisilylated and porphyrin P was tetrasilylated with a slight excess of isocyanatopropyltriethoxysilane (ICPTES).

Silylation success of F-Si and P-Si precursors was confirmed by ^{1}H NMR spectroscopy (**Figures 3 and 4**). After reaction of F with ICPTES, a signal corresponding to the carbamate proton (H_9, relative $^{1}H \approx 3$) appeared at $\delta = 6.26$ ppm, showing the formation of F-Si. Similarly, the formation of four urea functions was revealed by the appearance of a signal at $\delta = 6.40$ ppm (H_5, relative $^{1}H \approx 4$) designing the urea ^{1}H close to silyl chain.

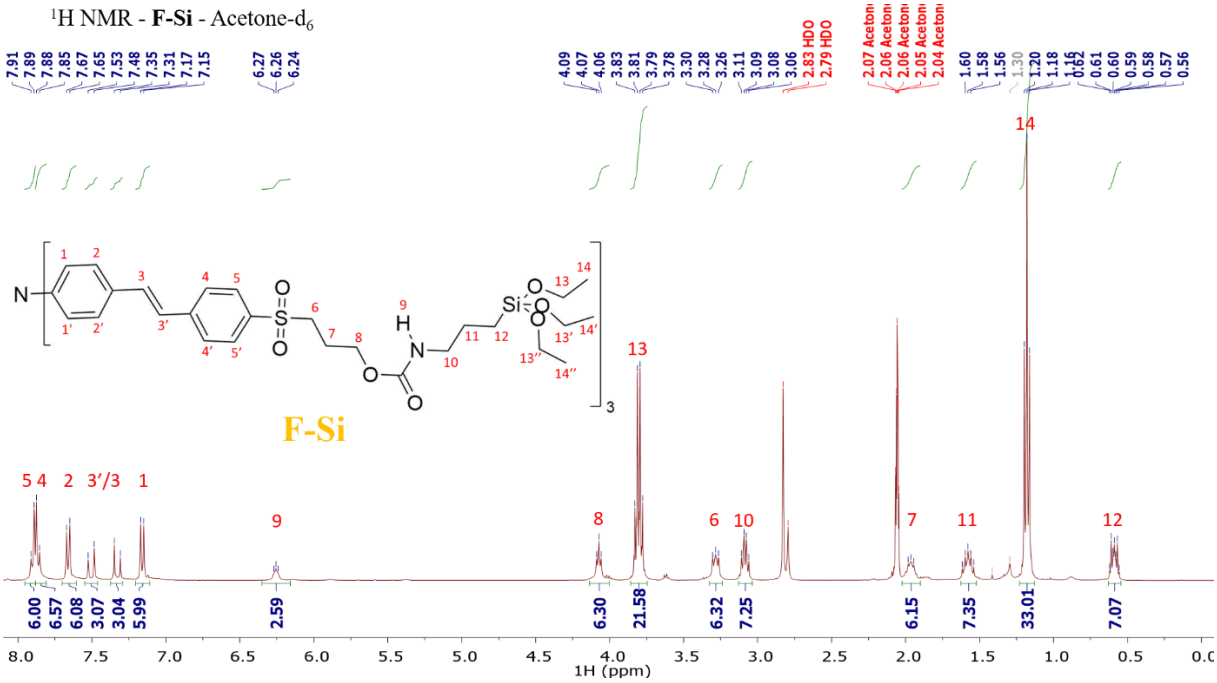

Figure 3: 1H NMR spectrum of F-Si in deuterated acetone.

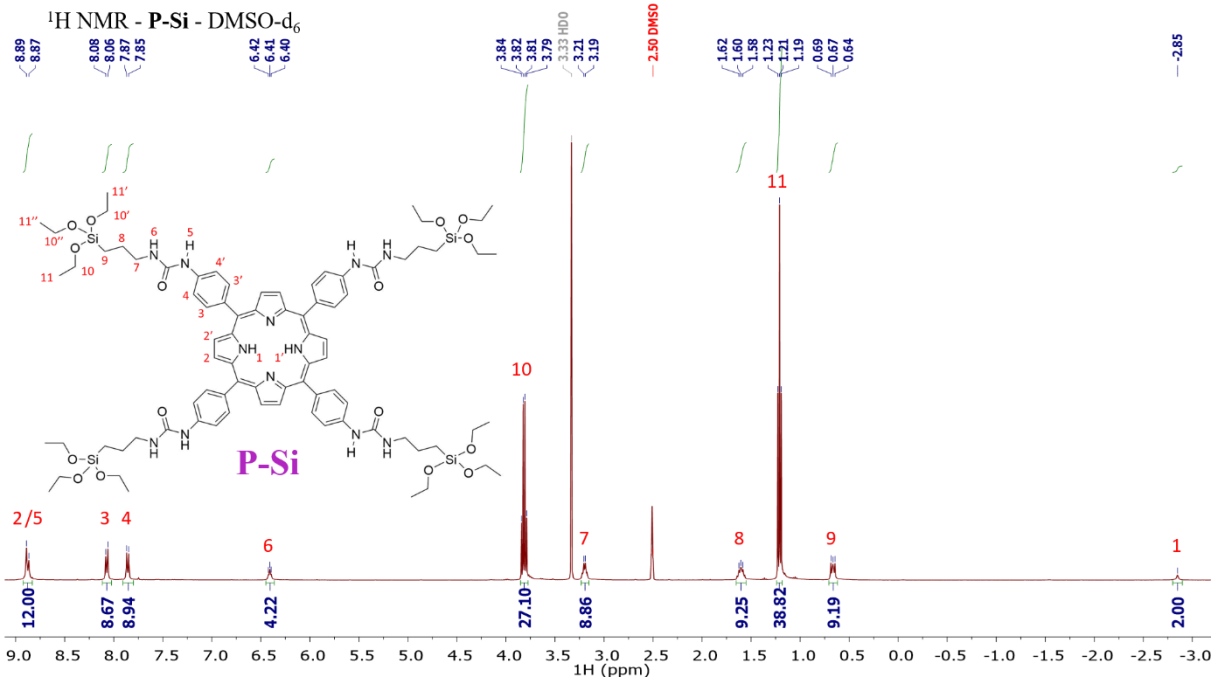

Figure 4: ^{1}H NMR spectrum of P-Si in deuterated DMSO.

To reach the best FRET efficiency (Φ_{ET}), the spectral overlap between the emission spectrum of the donor (D) and the excitation spectrum of the acceptor (A) should be as high as possible. Furthermore, D should exhibit a high fluorescence quantum yield ($\Phi_{f,\,D}$) in the absence of A, which was proven by the photophysical studies in chapter 3, whereas A should have good absorption properties. As demonstrated by fluorescence measurements (**Figure 5**), F-Si/P-Si pair possesses a potential spectral match between the large emission band of the fluorophore ($\lambda_{em.,\ max}$ = 548 nm) and porphyrin Q bands (notably Q4 and Q3 at 519 and 557 nm, respectively).

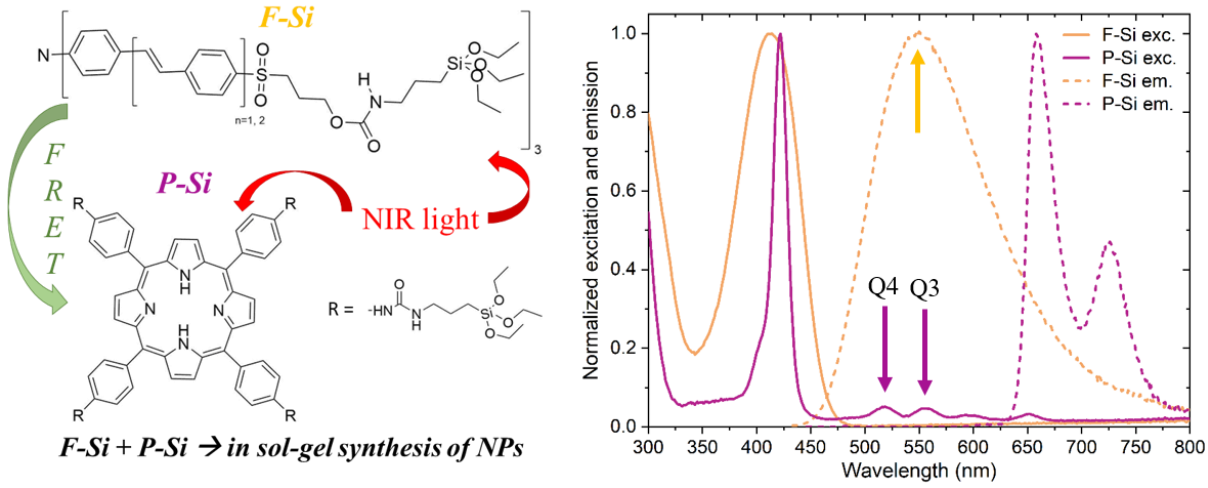

Figure 5: FRET strategy and associated excitation and emission spectra. F-Si and P-Si were excited at their maximum absorbance wavelength determined by UV-visible spectroscopy in EtOH ($\lambda_{exc.,\ F\text{-}Si}$ = 413 nm; $\lambda_{exc.,\ P\text{-}Si}$ = 422 nm).

According to the optical characterization, the use of F and P for FRET-enhanced TPE-PDT could be envisaged. Their integration in the framework of PMO NPs would be beneficial to increase their dispersion and stability in water. Prior to this, preliminary sol-gel synthesis with different experimental protocols was performed to ensure that the materials formed were nanoparticles, with appropriate porosity, morphology and colloidal stability.

2.1.2 Preliminary synthesis of tetrasulfide-based biodegradable PMO nanoparticles

Sol-gel synthesis of PMO NPs is generally performed in the presence of surfactant micelles around which nuclei grow to build porous nanoparticles with well-defined morphology and texture. In our study, the synthesis was based on a modified Stöber process with CTAB cationic surfactant as template in basic conditions using sodium hydroxide. Three symmetrical organoalkoxysilane precursors, with generic chemical formula $(EtO)_3$-Si-R-Si-$(OEt)_3$, were tested in different combinations. It is important to have in mind that the organic bridging group, R, can drastically influence the diameter of the formed pores, the porous volume, as well as NPs morphology and size.[19] Thus, experimentations were focused on the use of 1,2-bis(triethoxysilyl)ethane (E) or 1,2-bis(triethoxysilyl)ethene (ENE), mixed or not with a small amount of biodegradable bis[3-(triethoxysilyl)propyl]tetrasulfide (4S), which possesses easily breakable bonds. Higher specific surface areas can be reached by using E, while ENE could bring local conjugation and enhance electron/hole transfer improving ROS diffusion and generation. Both precursors can provide long-range ordering of the formed mesoporous structure.[19]

Several PMO synthesis, adapted from reported procedures, involving ethylene or methylene bridge on one hand,[20-23] or ethenylene bridge on the other hand,[24-26] were tested. Only one experimental protocol was finally selected for each type (E or ENE).[23, 26] Both processes were performed in soft conditions at 80 °C. For the preparation of ENE-based NPs, racemic β-citronellol was co-added with CTAB as a co-structure-directing agent to control NPs morphologies and pore features *via* the decrease of micellar surface free energy.[27]

With the objective to build biodegradable objects, E or ENE precursor was premixed with 4S in different molar ratios (100:0, 90:10, 80:20, 70:30) to find the highest ratio that could be integrated without provoking the collapse of the NPs (**Figure 6**).

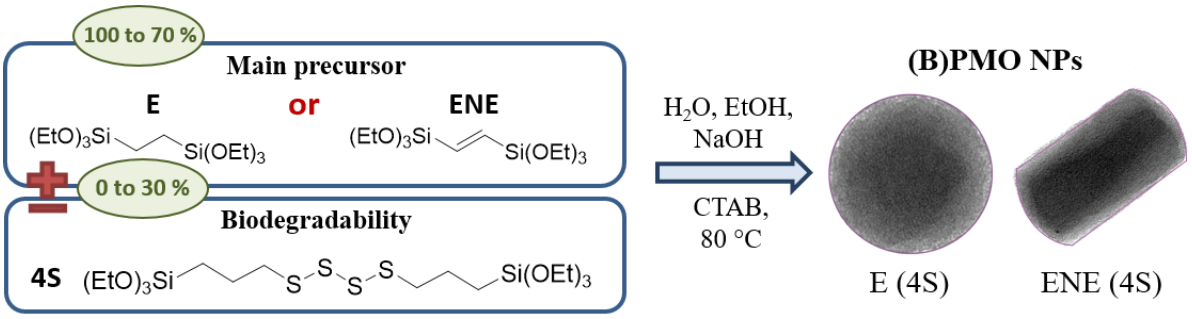

Figure 6: Synthesis conditions of E (4S) and ENE (4S) (B)PMO NPs.

Indeed, 4S can decrease the framework stability even before suspension in GSH-rich environment. A 4S molar ratio of 30% led to collapsed organosilica and not to NP, so this ratio was discarded. The morphology and texture of the obtained nanoparticles was characterized by DLS measurements, TEM imaging and nitrogen sorption measurements (**Table 1**). Ethylene-based NPs displayed good size monodispersity (PDI ≤ 0.20), with decreasing hydrodynamic diameters for superior amounts of 4S, according to DLS measurements (**Figure 7a**).

TEM images revealed the formation of nanospheres with still well-defined shapes up to 20% of 4S, with diameters ranging from 256 ± 32 to 162 ± 26 to 113 ± 19 nm (**Figure 8a to c**). In contrast, ethenylene-based NPs displayed rod-like shape with no significant difference in length and width values (about 300 x 160 nm) with increasing 4S rate (**Figure 8d to f**). This effect was also visible on hydrodynamic diameters, according to DLS measurements (**Figure 7b**).

Table 1: Main characterization data of E (4S) and ENE (4S) (B)PMO NPs. [a] z average hydrodynamic diameter in ethanol, n = 3 independent experiments. PDI ≤ 0.20 indicates good size monodispersity. [b] Average diameters of n ≥ 100 counts determined on TEM images. [c, d, e] SSA: Specific Surface Area, d_p: pore diameter, V_p: pore volume. SSA was calculated by Brunauer-Emmett-Teller (BET) method; pore diameters (most/lowest abundant) and volumes were obtained from the desorption branch of nitrogen sorption isotherm curves and calculated by Barrett–Joyner–Halenda (BJH) theory with only mesopores (1.7-60 nm) taken into consideration.

PMO NPs	DLS[a] (nm)	PDI	TEM[b] (nm)	S content (wt.%)	SSA[c] ($m^2\ g^{-1}$)	d_p[d] (nm)	V_p[e] ($cm^3\ g^{-1}$)
E	353 ± 27	0.20 ± 0.03	256 ± 32	0.08 ± 0.11	1808	3.1	1.62
E:4S 90:10	274 ± 10	0.20 ± 0.11	162 ± 26	4.13 ± 0.06	834	2.2/3.8	0.87
E:4S 80:20	189 ± 3	0.12 ± 0.08	113 ± 19	7.96 ± 0.21	680	2.2/3.8	0.84
ENE	412 ± 44	0.48 ± 0.05	319 ± 49 (l) 157 ± 49 (w)	0.00 ± 0.00	883	2.7	0.64
ENE:4S 90:10	325 ± 7	0.28 ± 0.03	277 ± 62 (l) 147 ± 35 (w)	4.50 ± 0.03	914	2.4	0.74
ENE:4S 80:20	410 ± 15	0.28 ± 0.10	315 ± 75 (l) 171 ± 40 (w)	7.92 ± 0.11	776	2.1	0.53

The integration of 4S was confirmed by microanalysis of sulphur atom, with proportional atom percentage and similar values between E and ENE-based NPs. The rod-like morphology is

attributed to rigid ethenylene groups creating linear arrangement, while 4S is more flexible and does not disturb enough ENE linear growth.

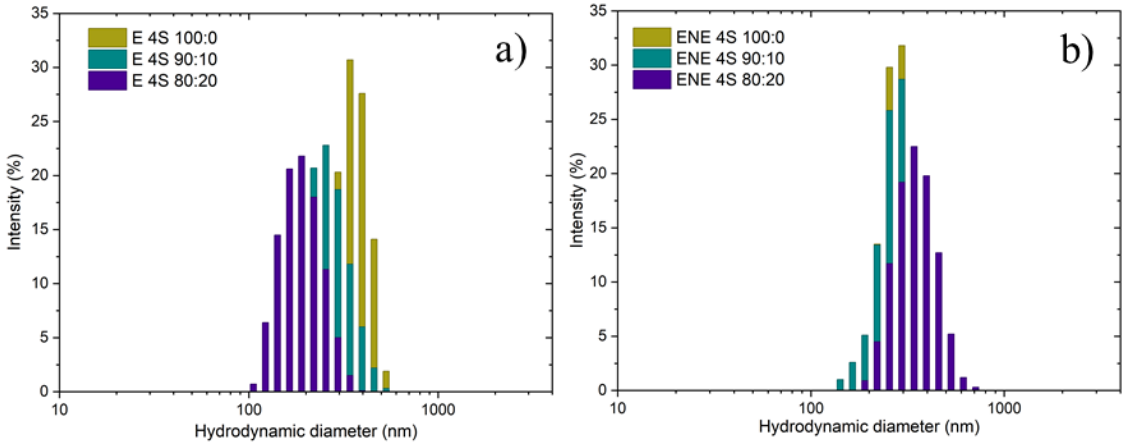

Figure 7: Hydrodynamic diameters of (a) E-based and (b) ENE-based (B)PMO NPs with different ratios in 4S biodegradable precursor.

Moreover, textural properties (specific surface area (SSA), pore diameter and porous volume) were screened by nitrogen sorption measurements on samples previously degassed under reduced pressure. N_2 adsorption-desorption isotherm curves revealed type-IV profile with a step from 0.3 to 0.5 P/P_0, characteristic of mesoporous solids (**Figure 9**).

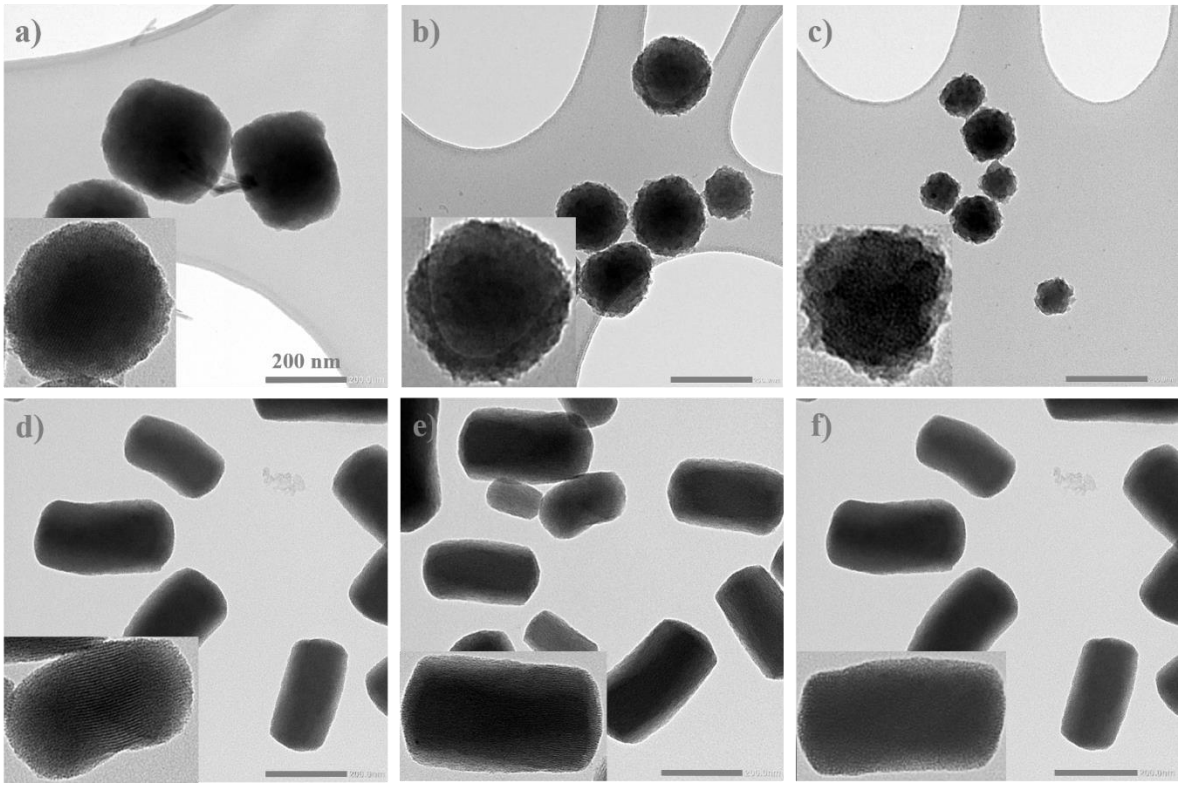

Figure 8: TEM imaging of synthesized (B)PMO NPs. Comparison of (a) E PMO with (b) E:4S 90:10 BPMO and (c) E:4S 80:20 BPMO NPs ; comparison of (d) ENE PMO with (e) ENE:4S 90:10 BPMO and (f) ENE:4S 80:20 BPMO NPs. Scale bar: 200 nm.

For E-based NPs, the thin and regular hysteresis loop is characteristic of cylindrical pores. Using Brunauer-Emmett-Teller (BET) method,[28] a high SSA value of 1808 m^2 g^{-1} was calculated for E PMO NPs, which is typical of the sol-gel conditions that were employed. The addition of 4S led to a strong reduction in accessible surface, with respectively 834 and 680 m^2 g^{-1} in the presence of 10% and 20% 4S. In **Figure 9**, the great nitrogen filling at 0.4 P/P_0 on E PMO BET isotherm curve illustrates well their high SSA, contrary to E:4S 80:20 BPMO. Furthermore, 4S-based E PMO displayed smaller pore diameters (3.1 nm *vs.* 2.2 nm most abundant) as measured on desorption branches by Barrett-Joyner-Halenda (BJH) method.

Similarly for ENE-based PMO, addition of 4S generated smaller pore diameters, from 2.7 to 2.1 nm, respectively for ENE PMO and ENE:4S 80:20 BPMO NPs. Nonetheless, the SSA remained pretty constant with values between 776 and 914 m^2 g^{-1}. The absence of hysteresis loop on ENE-based NPs suggests monodisperse cylindrical pores with no roughness.

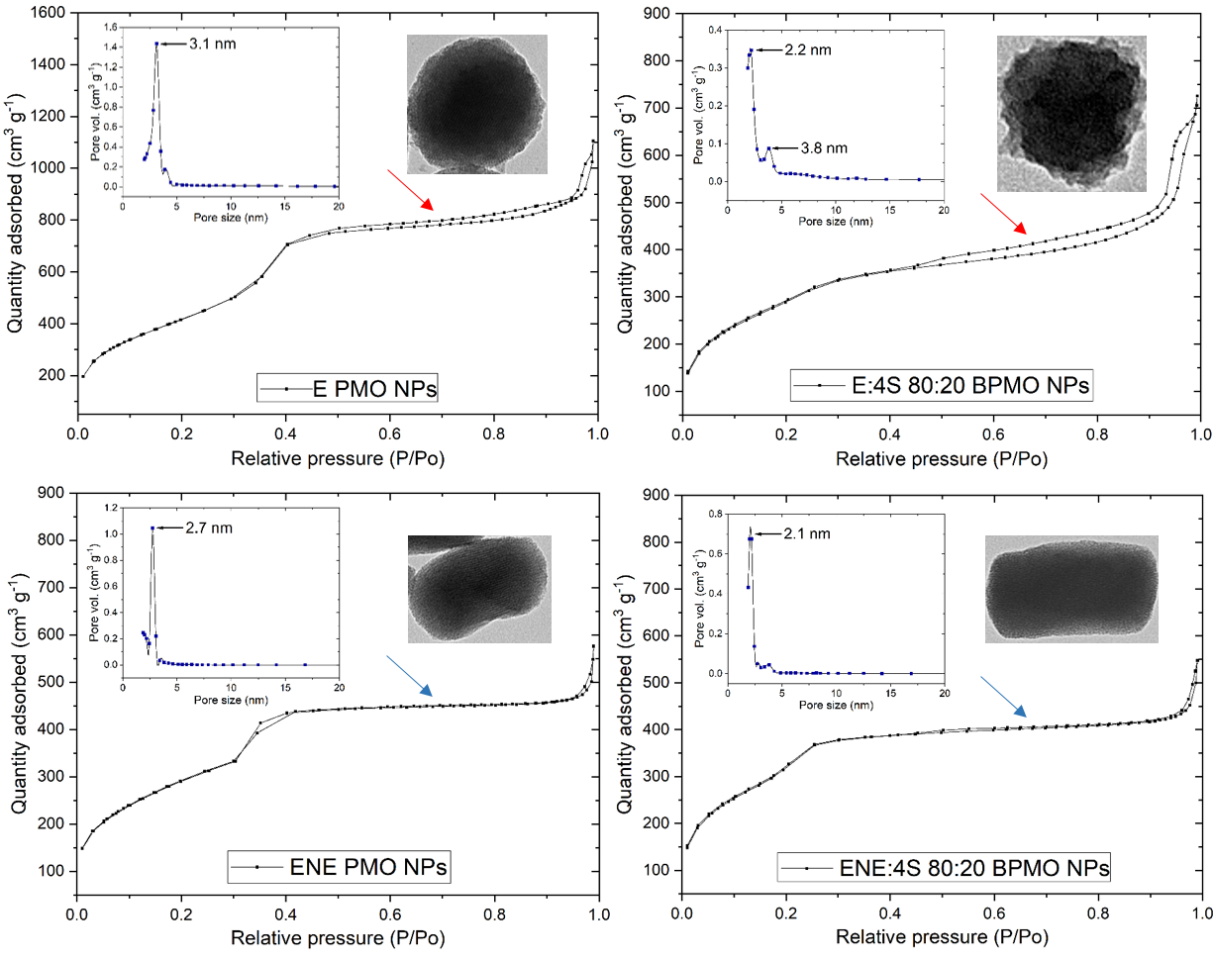

Figure 9: N_2 sorption type-IV isotherm curves and pore distribution profiles of E (4S) and ENE (4S) (B)PMO NPs. Pore distribution were calculated from the desorption branch of isotherms. Red arrows from E indicate a thin hysteresis loop and blue arrows from ENE indicate no hysteresis.

As a conclusion, such NPs with good colloidal stability in ethanol, high surface area and well-defined porosities could be suitable platforms facilitating drug encapsulation or ROS diffusion in the pore walls. For the following step, we chose 20% 4S molar ratio rather than 10% as the corresponding NPs demonstrated satisfying structural and textural properties.

2.1.3 Synthesis and characterization of fluorophore-porphyrin biodegradable PMO nanoparticles

Following preliminary sol-gel optimization, four types of F P PMO nanoparticles were synthesized. Two of them are abbreviated as E 4S F P and ENE 4S F P, are composed of biodegradable tetrasulfide bonds, and the two others, E F P and ENE F P, only contain E or ENE along with the two-photon chromophores (**Figure 10**). Due to the reduced dispersion of F-Si and P-Si in water, all the precursors were premixed in a small volume of absolute ethanol with a 1:0.045:0.005 constant molar ratio ((E or ENE) ± 4S:P-Si:F-Si), right before addition in the sol-gel medium.

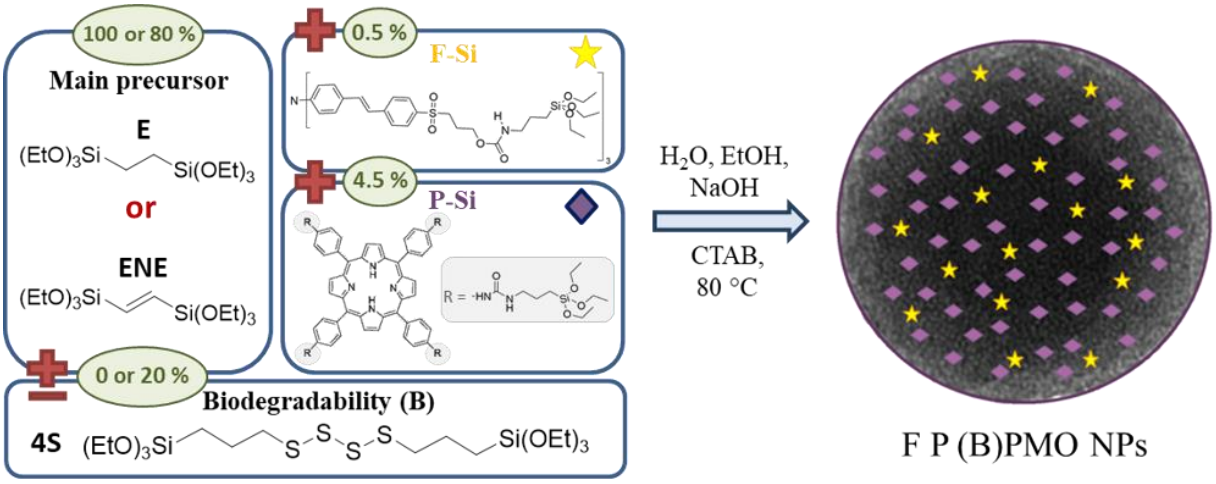

Figure 10: Synthesis conditions of F P (B)PMO NPs.

To confirm whether or not fluorophore F and porphyrin P moieties were integrated in the three-dimensional PMO framework, ^{13}C chemical shifts were screened by solid NMR spectroscopy of ENE F P and ENE 4S FP NPs (**Figure 11**). The most intense carbon chemical shift observed at 145.9 ppm is attributed to sp^2 C=C linkers from ENE precursor.[29-30] Shifts from 150 to 110 ppm are attributed to aromatic carbons and other arylenes from F and P, and the signal at 157.6 ppm is assigned to C=O groups in carbamate and urea groups.[31]

Comparison of alkyl chains between ENE 4S F P and ENE F P (< 50 ppm) clearly evidence the integration of 4S with peaks from R-S-C_A-C_B-C_C-Si-R' environment at 41.0, 23.0 and 11.2 ppm, for C_A, C_B and C_C, respectively. For ENE F P, since there is no 4S in the reaction mixture, the

signals at 43.3, 23.8 and 10.3 ppm can be attributed to the carbons from F-Si and P-Si between Si atoms and carbamate or urea groups.

Altogether, these results indicate the presence of both F, P and 4S within the NPs.

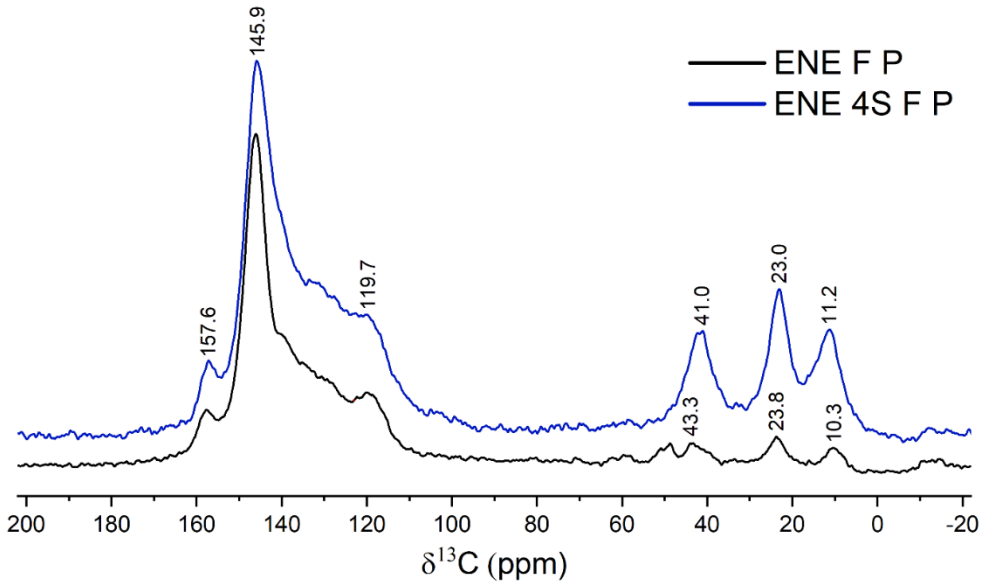

Figure 11: ^{13}C cross-polarization MAS solid-state NMR spectra of (a) ENE F P PMO and (b) ENE 4S F P BPMO NPs.

With respect to the presence of fluorophore in NPs structure, STEM-EDX mapping was performed as F is the only element possessing sulfur atoms. Resulting images of E F P PMO NPs displayed little concentration of S atoms, attributable to F moieties, compared to E 4S F P PMO NPs were S rate was considerably higher (**Figure 12**).

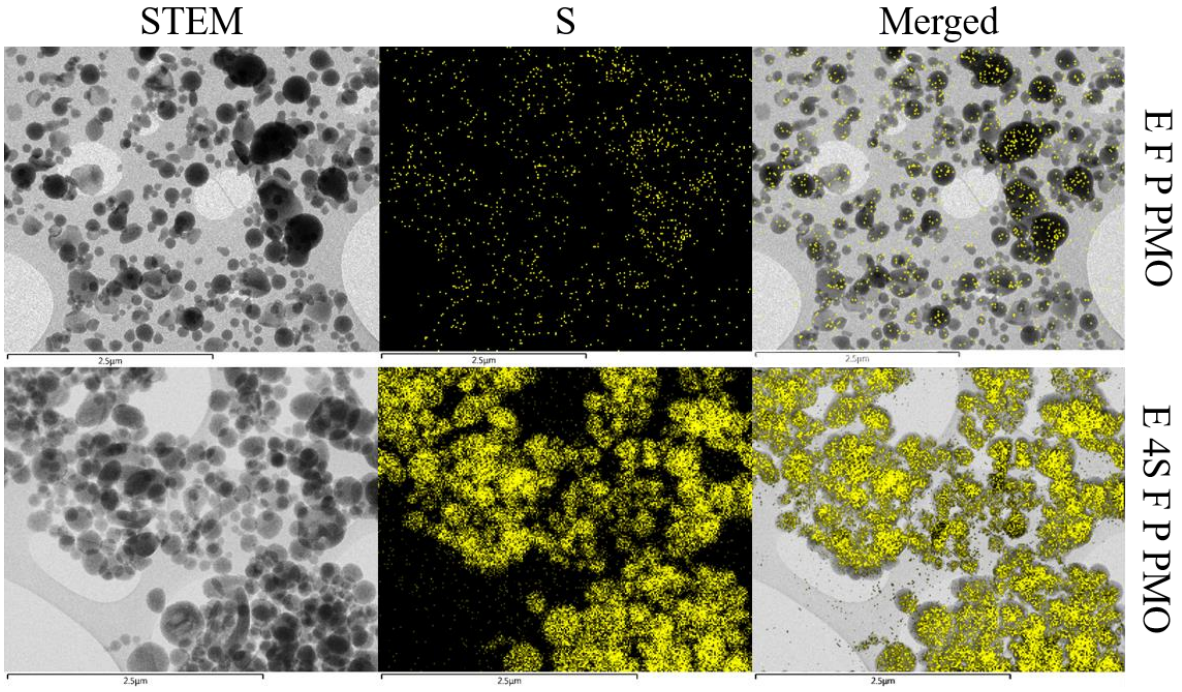

Figure 12: STEM-EDX mapping of E F P PMO and E 4S F P BPMO NPs. Merged images reveal the presence of S in the different NPs. Scale bar: 2.5 µm.

The integration of small fractions of F-Si and P-Si caused significant changes on NPs structure and morphology, with still good characteristics (**Table 2**).

Table 2: Main characterization data of E (4S) F P and ENE (4S) F P (B)PMO NPs. [a] z average hydrodynamic diameter in ethanol, n = 3 independent experiments. [b] Average diameters of n ≥ 100 counts determined on TEM images. [c, d, e] SSA: Specific Surface Area, d_p: pore diameter, V_p: pore volume. SSA was calculated by Brunauer-Emmett-Teller (BET) method; pore diameters (most/lowest abundant) and volumes were obtained from the desorption branch of nitrogen sorption isotherm curves and calculated by Barrett–Joyner–Halenda (BJH) theory with only mesopores (1.7-60 nm) taken into consideration.

F P PMO NPs	DLS[a] (nm)	PDI	TEM[b] (nm)	SSA[c] ($m^2\ g^{-1}$)	d_p[d] (nm)	V_p[e] ($cm^3\ g^{-1}$)
E	492 ± 8	0.34 ± 0.06	142 ± 48	875	2.7	0.66
E 4S 80:20	388 ± 5	0.24 ± 0.02	163 ± 75	500	1.9/3.8	0.64
ENE	524 ± 18	0.30 ± 0.10	153 ± 61	856	2.7/3.8	0.74
ENE 4S 80:20	616 ± 11	0.30 ± 0.03	158 ± 60	699	3.8	0.66

The hydrodynamic diameters and PDI values of E-based F P PMO NPs increased to 492 ± 8 nm (PDI = 0.34 ± 0.06) and 388 ± 5 nm (PDI = 0.24 ± 0.02), for E F P and E 4S F P, respectively. The size polydispersity was also confirmed by TEM imaging. Compared to 100% ethylene PMO (**Figure 13a**), E F P and E 4S F P NPs are clearly more polydisperse with average size of 142 ± 48 and 163 ± 75 nm, respectively (**Figure 13b and c**).

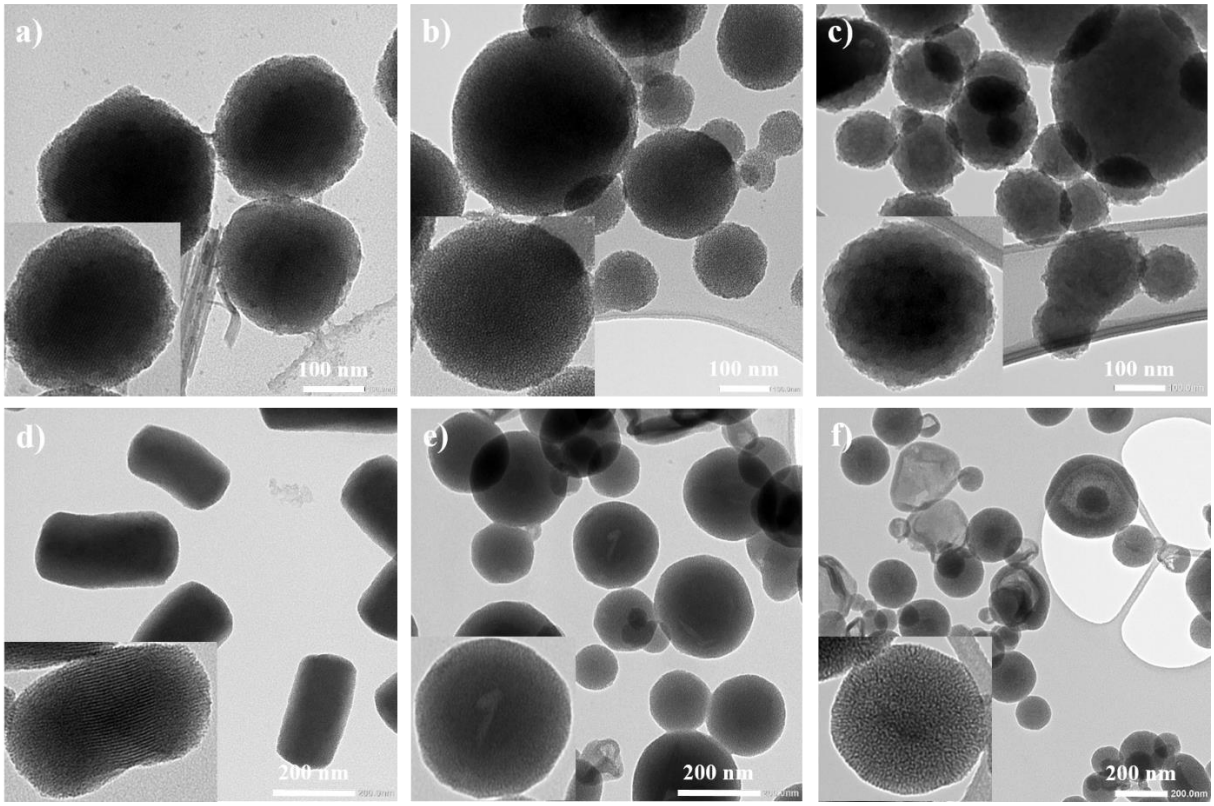

Figure 13: TEM imaging of synthesized F P (B)PMO NPs. Comparison of (a) E PMO with (b) E F P PMO and (c) E 4S F P BPMO NPs. Scale bar: 100 nm; comparison of (d) ENE PMO with (e) ENE F P PMO and (f) ENE 4S F P BPMO NPs. Scale bar: 200 nm.

The morphology of ENE-based F P PMO nanoparticles changed from rod-like (**Figure 13d**) to spherical (**Figure 13e and f**). They showed similar average diameters as E-based structures, with respectively 153 ± 61 and 158 ± 60 nm for ENE F P and ENE 4S FP NPs.

This difference in morphology was attributed to steric hindrance effect of silylated porphyrin and fluorophore precursors that should have affected ENE linear growth, favoring stabilization through a spherical shape that minimizes surface energy.

F P PMO NPs textural properties were determined by N_2 sorption measurements. They showed good Brunauer-Emmett-Teller (BET) SSAs ranging from 500 to 875 $m^2 g^{-1}$, with lower values obtained for 4S-based NPs. Sorption profiles revealed type-IV isotherm profiles for all NPs, indicating the presence of a mesostructure (**Figure 14**). The regular distance between adsorption and desorption branches at $P/P_0 > 0.4$ (type H1 hysteresis) indicates a narrow mesopore size distribution.[32]

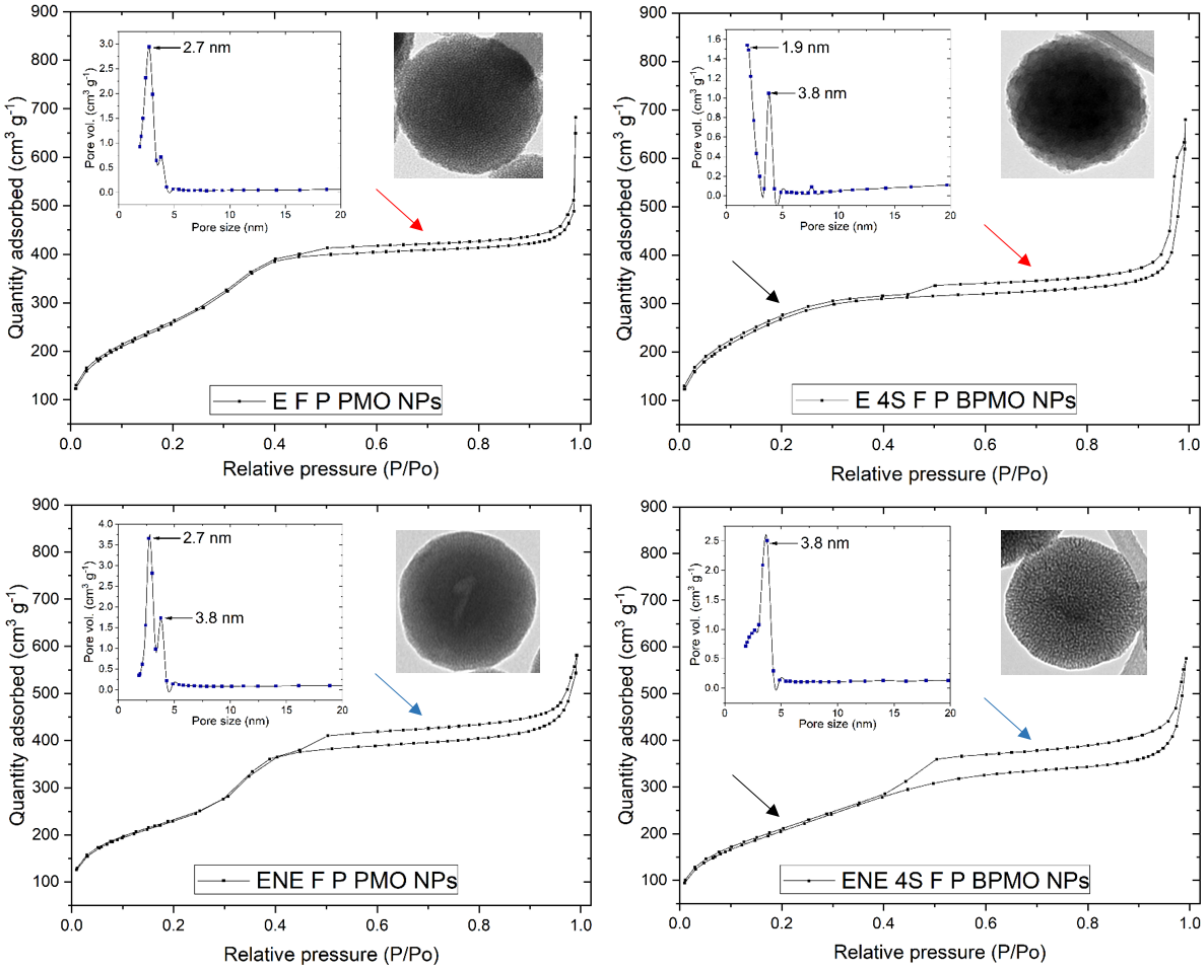

Figure 14: N_2 sorption type-IV isotherm curves and pore distribution profiles of F P (B)PMO NPs. Pore distribution were calculated from the desorption branch of isotherms. Black arrows indicates a slight opening corresponding to the presence of small mesopores (≈ 2 nm); red arrows from E and blue arrows from ENE indicate a regular hysteresis loop.

Moreover, the sharp nitrogen desorption between 0.4 and 0.5 P/P_0 for ENE 4S F P PMO NPs pore structure organization is suggesting cavitation-like phenomenon or at least a slight inner pore enlargement. Furthermore, the presence of 4S could be associated with the generation of small mesopores (≈ 2 nm, hysteresis at low pressures) in the structures and more generally pore size polydistribution (increase of 3.8 nm pores rate).

Altogether, these studies confirm the great structural ordering of the newly synthesized fluorophore-porphyrin PMO nanoparticles.

2.1.4 Functionalization strategy to target cancer cells and bacteria

As in chapter 2, functionalization of NPs using sqMAN derivative was chosen to improve selectivity towards lectins that are overexpressed at the surface of cancer cells, in order to increase NPs cellular uptake and PDT efficiency.[33-34] Among various α-D-mannosides, sqMAN showed higher affinity level towards bacterial FimH adhesin present on the external membrane of most *E. coli* strains.[35] Superior attachment level of mannoside onto carbohydrate selective proteins also demonstrated inhibition growth effect upon planktonic *E. coli*. In this study, sqMAN grafting rate was strongly reduced compared to the previous study of ND@PMO NPs to avoid interparticle and intraparticle aggregation issues that limited NPs targeting capacity.

The main issue associated with organosilica NPs is the adhesion of proteins and blood platelets to their surface. Attachment of hydrophilic PEG grafts onto F P PMO NPs surface is conventionally used to render them less sensitive to recognition by the immune system.[36-37] In fact, PEG inhibits non-specific and specific protein interaction, reducing the reaction of macrophages and other immune cells, thus increasing the circulation half-life of the nanoplatforms.[38]

Hence, (PEG/AUTES)-grafted and (PEG/AUTES@sqMAN)-grafted PMO were prepared with a 25:1 (n:n) ratio between PEG-Si and AUTES (**Figure 15**).

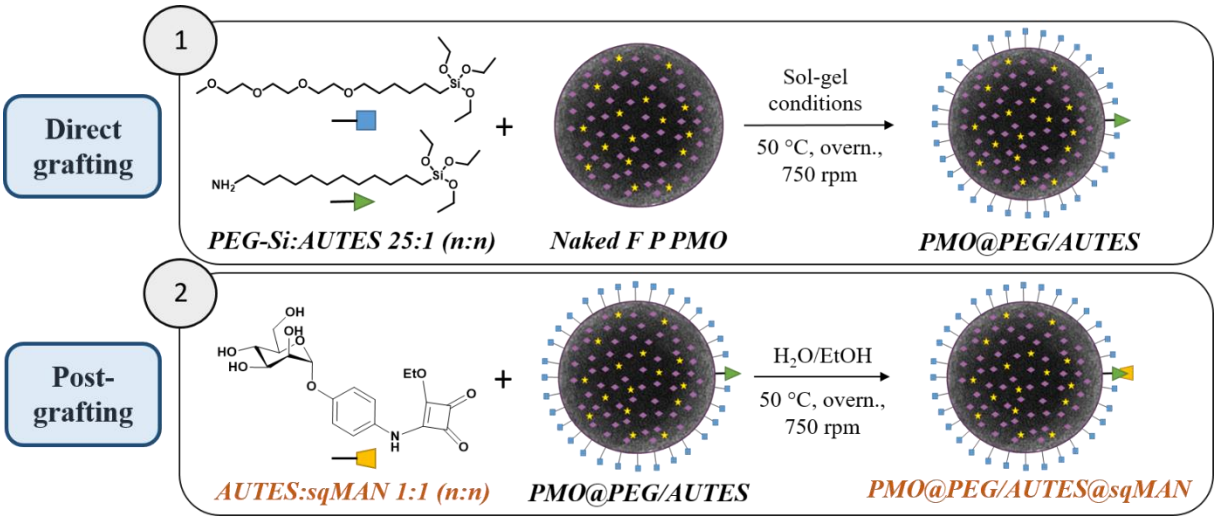

Figure 15: Functionalization conditions on F P PMO NPs. PEG-Si, AUTES and sqMAN were introduced in two steps with a 1:0.22:0.009:0.009 (n:n) relative theoretical ratio compared to nanoparticle synthesis precursors.

AUTES grafting efficiency was evaluated with fluorescamine (FA), which is a commercially available fluorescent probe routinely used for the detection of primary amines and the analysis of amino acid and proteins for biochemistry applications.[39] Such reaction with AUTES primary amine convert FA into a strongly fluorescent chromophore (**Figure 16a**), allowing to perform titration via a standard range. With low AUTES amount introduced in the reaction mixture, this technique would be useful as it enables detection up to picomole levels.[40] Four standards of pyrrolinone derivative, formed by FA:AUTES 1:1 (v:v) mixtures, were analysed by fluorescence spectroscopy and showed a linear behavior, as revealed by the square of linear correlation coefficient $R^2 > 0.99$ (**Figure 16b and c**).

Homogeneous AUTES grafting concentrations were calculated from measured fluorescence intensities at $\lambda_{em.}$ = 482 nm, with values between 2.0 and 2.7 µg per milligram of bare NPs (**Table 3**). Considering the 25:1 (n:n) PEG-Si:AUTES ratio introduced in the sol-gel medium, PEG grafting concentrations were estimated to be between 57.7 and 76.6 µg mg^{-1}. Next, for sqMAN grafting, the necessary amount to substitute all amine functions (1:1 (n:n)) was estimated with respect to functionalized NP@PEG/AUTES (formula in **Experimental Section**). The two grafting steps were confirmed with zeta potential measurements.

Starting from -38 ± 2 mV for bare E F P PMO NPs, the surface charge increased to -3 ± 1 mV after amine and PEG functionalization, and then, the zeta potential was found to be -29 ± 1 mV after sqMAN reaction, characteristic of full amine coverage.[41]

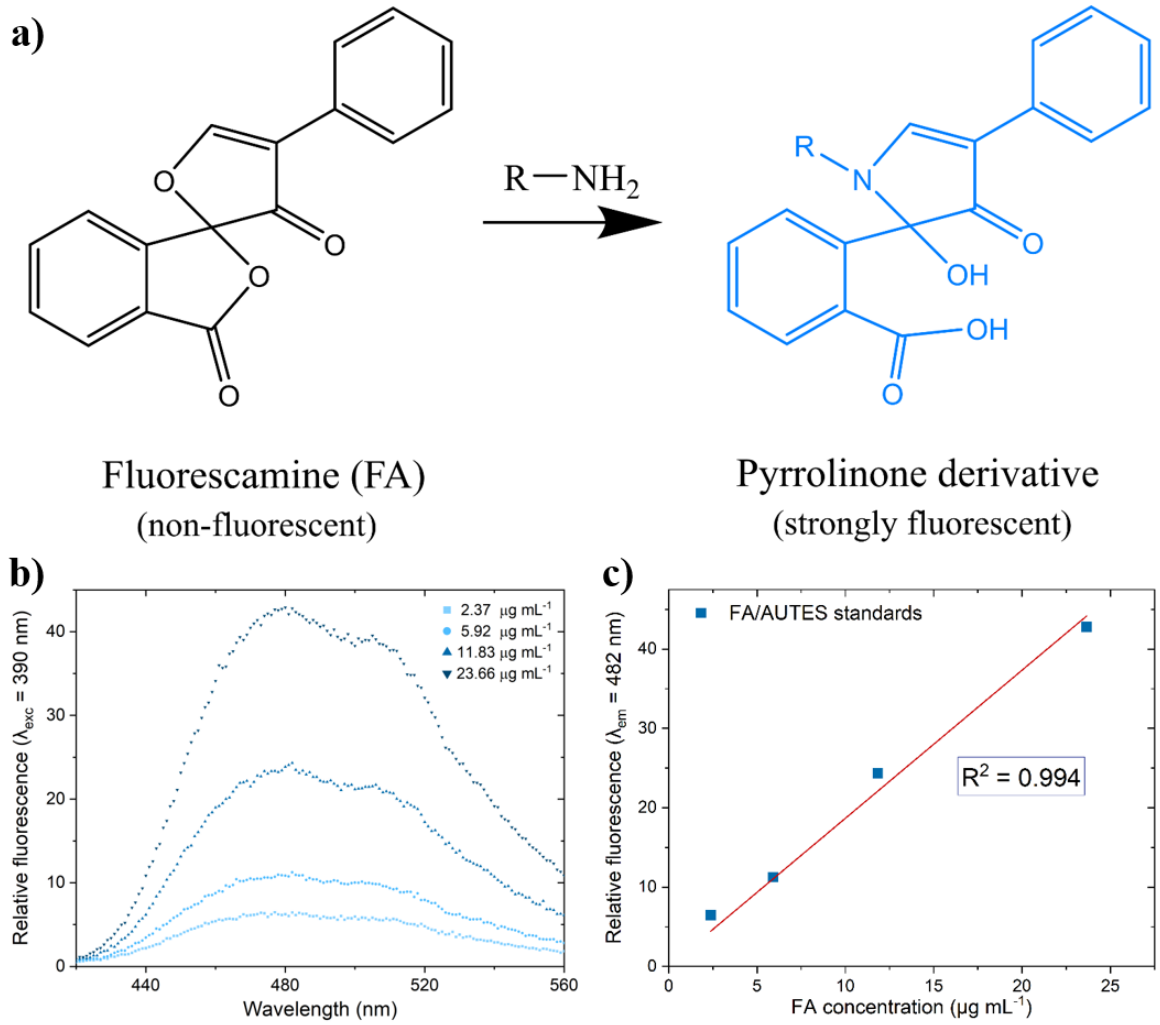

Figure 16: Primary amine assays for AUTES titration using fluorescamine reagent. (a) Formation of fluorescent pyrrolinone by reaction between non-fluorescent FA and AUTES; (b) Fluorescence emission spectra of n = 4 standards (FA:AUTES mixtures, converted into pyrrolinone) and (c) the corresponding standard curve with linear correlation at 482 nm.

Thus, the efficiency of naked, (PEG/AUTES)-functionalized and (PEG/AUTES@sqMAN)-grafted PMO NPs will be compared in following TPE-PDT experiments.

Table 3: Determination of grafting quantities. [a] Calculated AUTES concentration from pyrrolinone fluorescence measurements using linear correlation curve from n = 4 standards. [b] Calculated AUTES grafting amounts *vs.* naked NPs. [c] Estimated PEG-Si grafting amount *vs.* naked NPs. [d] Estimated sqMAN amount *vs.* (PEG/AUTES)-grafted NPs required to further functionalize NPs with a AUTES:sqMAN 1:1 (n:n) ratio. [e] Estimated sqMAN grafting amount *vs.* naked NPs.

PMO NPs	AUTES calcd.[a] (µg mL^{-1})	AUTES[b] (µg mg^{-1})	PEG[c] (µg mg^{-1})	sqMAN *vs.* NP@ PEG/AUTES[d] (µg mg^{-1})	sqMAN[e] (µg mg^{-1})
E F P	2.2	2.4	68.2	2.6	2.8
E 4S F P	2.5	2.7	76.6	2.9	3.2
ENE F P	2.3	2.5	72.2	2.8	3.0
ENE 4S F P	1.9	2.0	57.7	2.2	2.3

2.2 Vancomycin loading and nanoparticles biodegradability

2.2.1 Generalities about vancomycin

The use of porous silica nanoparticles has been extensively described for drug encapsulation.[42-43] Compared to inorganic MSN, hybrid organic-inorganic PMO NPs could provide higher DLC and drug release content (DRC) of antibiotics with plural hydrophilicity features for the treatment of polymicrobial infections that requires combination therapy with different antimicrobial scopes of action.

The studies presented in this section are preliminary assays. Vancomycin hydrochloride (VAN), a FDA-approved glycopeptide antibiotic (**Figure 17a**) was selected as a model drug to study the capacity of loading and release in F P PMO and F P BPMO nanostructures. VAN is well-known for its antibacterial efficiency against most gram-positive bacteria, especially methicillin-resistant *S. aureus* constituting one of the most important current threats regarding AMR-related infections.[44-45]

Loading of VAN in PMO NPs could happen either by encapsulation in the pores or by covalent attachment onto NPs surface. As earlier measured, pore size distributions could fit with the molecular dimensions of VAN (**Figure 17b**). VAN exhibits amino, hydroxyl, carboxyl and chloride groups, which are potential anchoring sites *via* physical interactions and hydrogen bonds (**Figure 17c**).[46] The protonation constants at 7.75 and 8.89 respectively reflect the acid-base character of primary and secondary amine groups.[47] In particular, ammonium forms under acidic conditions could provide favorable interaction with negatively-charged NPs for loading VAN^{+}.[48]

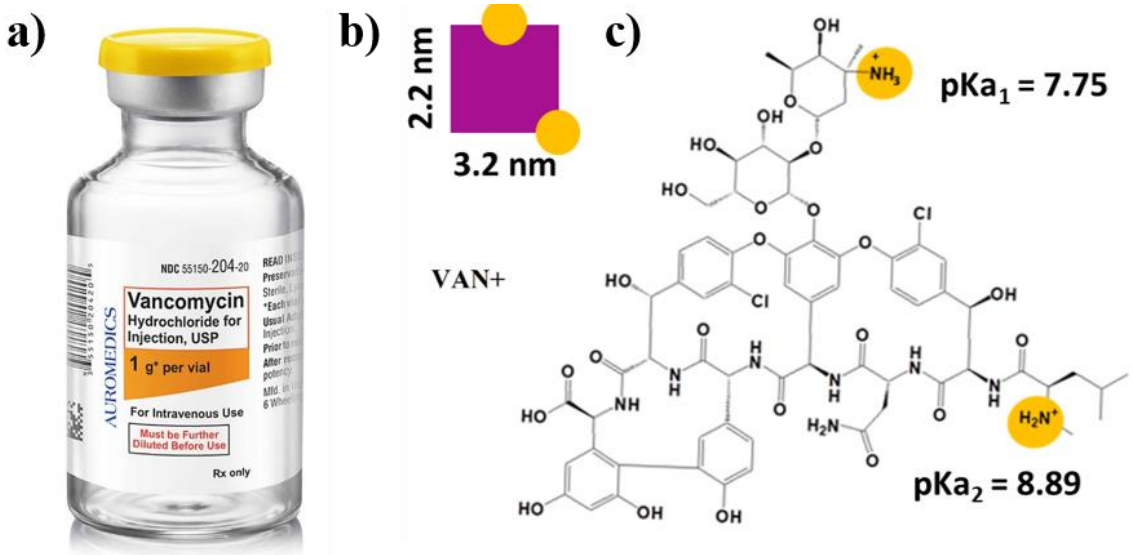

Figure 17: Vancomycin general information. (a) Example of commercial bottle; (b) Molecular dimensions; (c) Developed chemical formula represented under acid form. Adapted from Ural *et al.* (2021).[48]

2.2.2 Antibiotic loading

For VAN loading, pH adjustment strategy was chosen to achieve desired drug concentrations.

First of all, the influence of pH was observed on the surface charge of NPs. With increasing acidity (pH decreasing from 8 to 5), zeta potential values of E F P and ENE F P PMO NPs were switched from z ≈ - 20 mV to more neutral local charge (**Figure 18a**). For 4S-based analogues, zeta potential was found to be stable in the tested range, with z ≈ - 30 mV. This effect could be assigned to a shift of the isoelectric point leading to the deprotonation of P moieties central amino groups (PH_2^{2+}) connected to 4S hydrophobicity in comparison with E and ENE sol-gel precursors.

Loading experiments were conducted by dispersing VAN and dried F P PMO NPs in water. After testing different concentrations for both compounds, the selected conditions were [VAN] = [NPs] = 10 mg mL^{-1}. The use of a low water volume maximized the reaction because VAN is a hydrophilic moiety, which tends to partition into aqueous phase.[49]

Addition of small aliquots of NaOH or HCl solution allowed to tune pH to either 5, 6 or 7. After 24 h stirring, the prepared mixtures were neutralized to stop the loading reaction. Three consecutive washing steps (centrifugation and quick sonication) allowed to remove all the unloaded drug. DLCs were obtained *via* quantification of free VAN in washing supernatants by a UV-visible detector at $\lambda_{abs.,\ max}$ = 280 nm (**Figure 18b**). The linear plot from the six VAN standards (10 to 300 µg mL^{-1}) showed a very high correlation level with R^2 = 0.99992.

DLC values (mean of two replica) were ranging from 2.2 to 20.1 wt%, meaning that 0.022 to 0.201 mg were loaded per mg of NPs. VAN entrapment efficiency, which corresponds to the drug fraction effectively encapsulated, was almost equal to DLC, as initial NPs and VAN amounts were equal (data not shown). These results suggest a clear trend for good payloads at pH 5, where samples showed about 15-18 wt% drug loading (**Figure 18c**). In particular, E 4S F P and ENE 4S F P organosilica nanoparticles showed homogeneous DLC in comparison with E F P and ENE F P for which an important slump is observed for pH = 6 or pH = 7. These results are in line with the low variations in zeta potential value observed for different pH in the case of 4S-based PMO NPs.

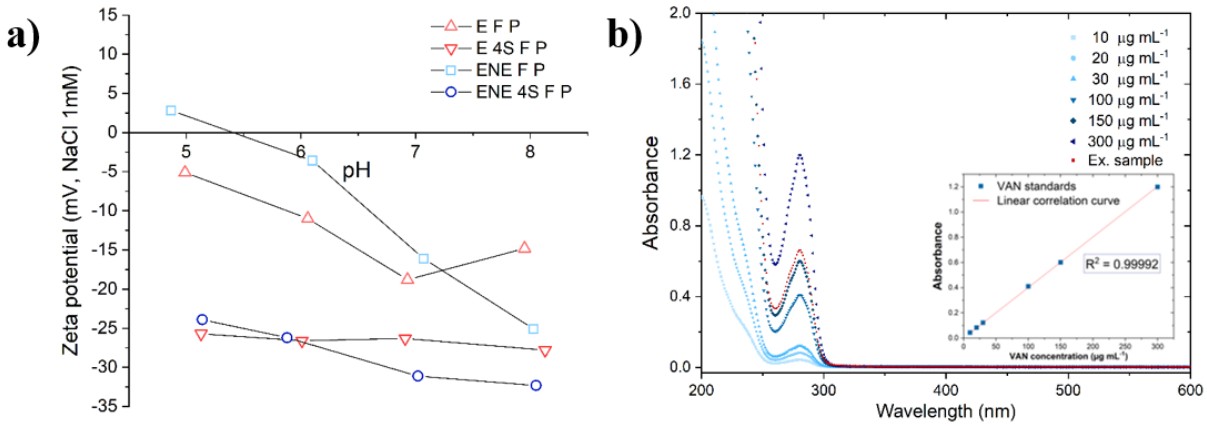

c)

Sample	pH	DLC mean	Std dev.
E F P	5.0	16.9	
	6.0	2.2	0.6
	7.0	2.7	2.7
E 4S F P	5.0	16.8	0.8
	6.0	14.9	2.8
	7.0	12.4	6.8
ENE F P	5.0	18.0	2.4
	6.0	11.2	3.2
	7.0	9.6	2.8
ENE 4S F P	5.0	15.1	0.0
	6.0	20.1	4.5
	7.0	14.2	0.7

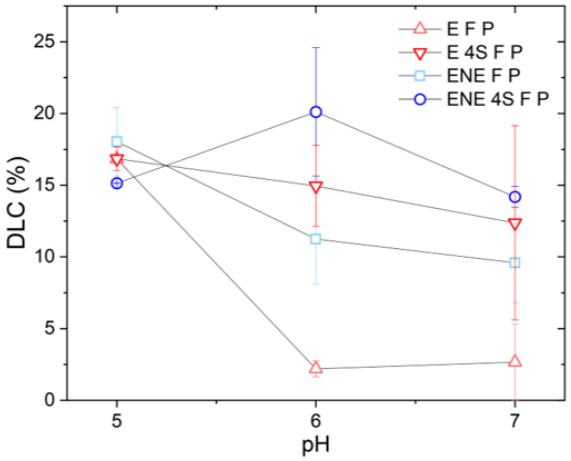

Figure 18: Vancomycin loading studies. (a) Zeta potential measurements of F P (B)PMO NPs as a function of pH; (b) UV-visible absorbance spectra of n = 6 standards (VAN in water) and one example of sample analysis (in red), standard curve (inner graph) with linear correlation at 280 nm; (c) DLC profiles of F P (B)PMO NPs (table and graph) as a function of pH.

As a conclusion, the different PMO NPs presented in this study showed high loading capacity in a pH-controlled manner, especially for NPs synthesized without 4S precursor. No particular relationship with pore and SSA features of organosilica NPs was found, but further studies would be of great interest.

VAN-loaded F P (B)PMO samples with equivalent DLC (≈ 16 wt%) were chosen for proper comparison of antibacterial efficiency against planktonic bacteria.

2.2.3 Biodegradability simulation and release kinetics

By redox process, glutathione reductase can convert R-S-S-S-S-R bridges into reduced R-S-SH thiols. GSH concentration is much higher in tumor cells and in bacterial environment compared to healthy tissues. Thus, drug or biomolecule release can be selectively triggered in such conditions.

Biodegradability simulation assays were performed by suspending unloaded BPMO NPs in physiological medium (PBS 10 mM, pH = 7.4) with the presence of mercaptoethanol (ME, 10 mM), a short thiol commonly employed to mimic a GSH-rich medium.[23] As visible on TEM images (**Figure 19**), ENE 4S F P NPs were eroded after three days contact with ME, displaying enlarged cavities. This effect was even more pronounced after seven days, and already detectable after 24 h. On the other hand, E-based BPMO NPs clearly showed biodegradation ability with substantial decomposition of the porous structures over time. Accordingly, for both NPs, small PMO fragments with a size range of 10-20 nm were also observed on TEM grids.

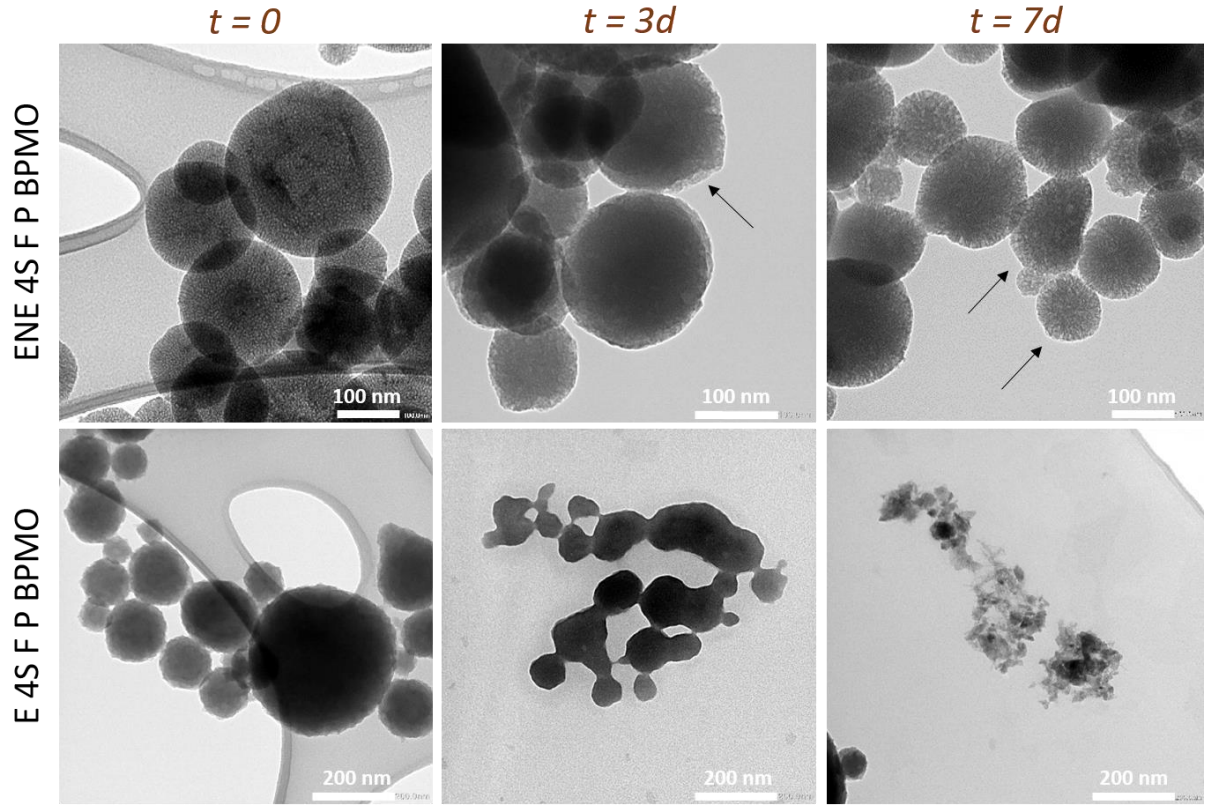

Figure 19: Biodegradability studies in simulated GSH-rich biological environment. TEM imaging of ENE 4S F P (top) and E 4S F P (down) biodegradable PMO NPs after slight stirring in PBS/GSH medium for different times; erosion (black arrows) and fragmentation (E-based NPs) increases over time; d: days.

Furthermore, VAN release in bacterial environment was simulated by stirring VAN-loaded NPs suspensions in GSH-rich PBS medium (10 mM) or in the absence of GSH (PBS only). DRCs from NPs were compared at different time points by semi-quantification using UV-visible titration of VAN in either PBS or PBS/GSH solution. For 4S-based nanoparticles, DRC increases quickly in the presence of GSH (t = 4h) and then seem stable over longer durations. In contrast, DRC is much reduced in the absence of thiol, which is suggesting an enhanced release of VAN *via* GSH-triggered nanoparticle degradation (**Figure 20).**

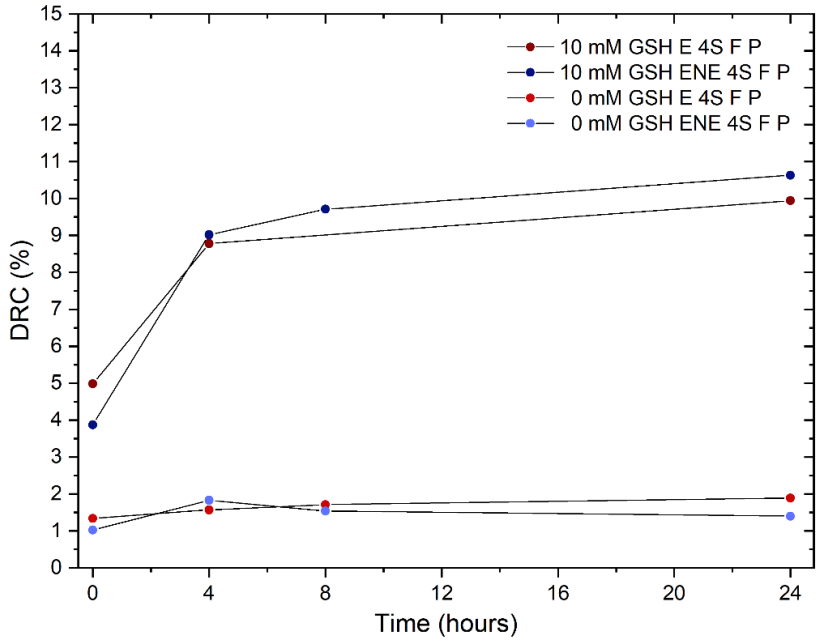

Figure 20: Vancomycin kinetic release studies in the presence (10 mM) or absence (0 mM) of GSH. Separated aliquots were stirred in PBS solution (10 mM) with or without GSH for different time durations.

In conclusion, fluorophore-porphyrin (B)PMO NPs were successfully loaded with vancomycin after optimization of buffer media. In addition, kinetic studies in simulated biological environment revealed the better aptitude of 4S-based NPs for antibiotic release.

2.3 Photophysical studies

Besides structural characterizations (Section 2.1), the photophysical properties of F P PMO NPs were studied to confirm F and P chromophores incorporation within NPs. Then, their FRET efficiencies were quantified by fluorescence measurements in the presence or absence of F and P. All samples were excited in EtOH at 413 nm, the maximum absorption wavelength of F-Si.

2.3.1 Comparison of nanoparticles and silylated chromophores

After sol-gel synthesis, NPs display a broad fluorescence emission band, with a maximum at 544 nm, which is in line with F-Si fluorescence profile with a maximum emission at 548 nm (**Figure 21**). Compared to P-Si, a small bathochromic shift and a broadening of the two porphyrin emission bands was observed with F P PMO NPs due to the formation of J aggregates and π-stacking of the macrocycles in PMO frameworks.[15] Lower fluorescence intensities from F moieties compared to P bands are explained by the 9:1 (n:n) ratio employed *ab initio* between P-Si and F-Si.

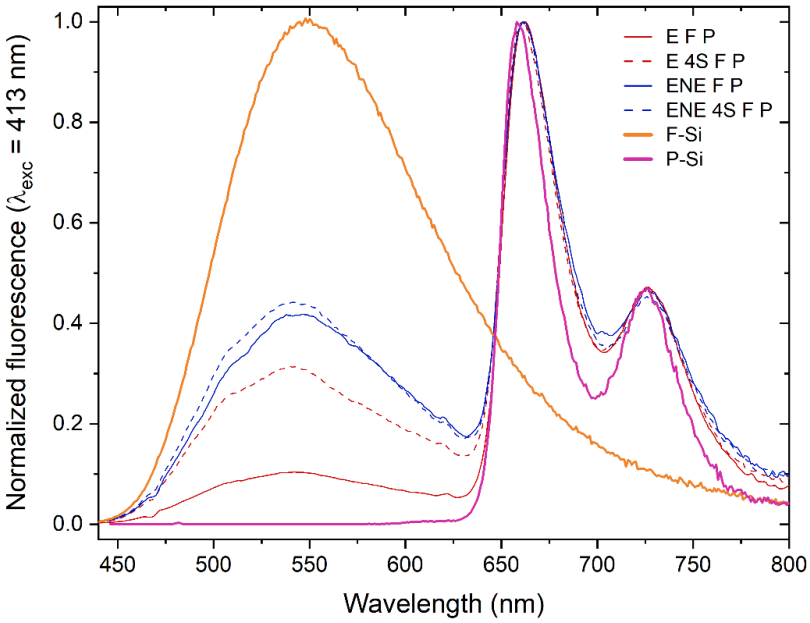

Figure 21: Emission spectra of F P PMO NPs compared to silylated chromophores.

To go further and evaluate the capacity of FRET from F energy donors (D) to P energy acceptors (A), a quantification method was established by comparison of F P PMO NPs with similar NPs prepared without fluorophore (denoted as A) or porphyrin (denoted as D). FRET studies were separated in two categories of NPs (E or ENE-based) to focus on 4S impact on the photophysical properties.

2.3.2 FRET in ethylene-based nanoparticles

Energy transfer from F to P moieties was assessed by comparison of emission profiles of F PMO (D), P PMO (A) and F P PMO (D-A) NPs measured at the same mass concentrations in EtOH (44 µg mL^{-1}). As F-Si and P-Si molar concentrations are the same in all studied PMO materials, the number of absorbed photons by F is also the same, which is mandatory to properly compare I_D and $I_{D\text{-}A}$ fluorescence intensities. As P PMO NPs are not emissive in F emission range (440-625 nm), the decrease of F fluorescence can be studied to assess FRET efficiencies (Φ_{ET}).

For E PMO family (**Figure 22a**), the decrease of donor fluorescence intensity at 544 nm or in the 440-625 nm range leads to 95% FRET efficiency in both cases (comparison of E F and E F P). It is also observed that acceptor fluorescence intensity concomitantly increases in the 650-800 nm range, but this effect is limited for several reasons. Firstly, P absorbs much more than F at the excitation wavelength. As a result, P PMO NPs already display a good level of fluorescence emission. Secondly, $\Phi_{f,\,F}$ is noticeably higher than $\Phi_{f,\,P}$. Finally, one crucial aspect

to consider is that most of the transferred energy serves to boost ROS production quantum yield of P moieties.

Similarly for E 4S BPMO family (**Figure 22b**), based on E 4S F P fluorescence decrease in F emission range (formula in **Experimental Section**), the FRET efficiency was estimated to be 90%. By comparing E 4S P and E 4S F P NPs, porphyrin fluorescence is enhanced. Thus, for this second family, the resonance energy transfer was also evidenced.

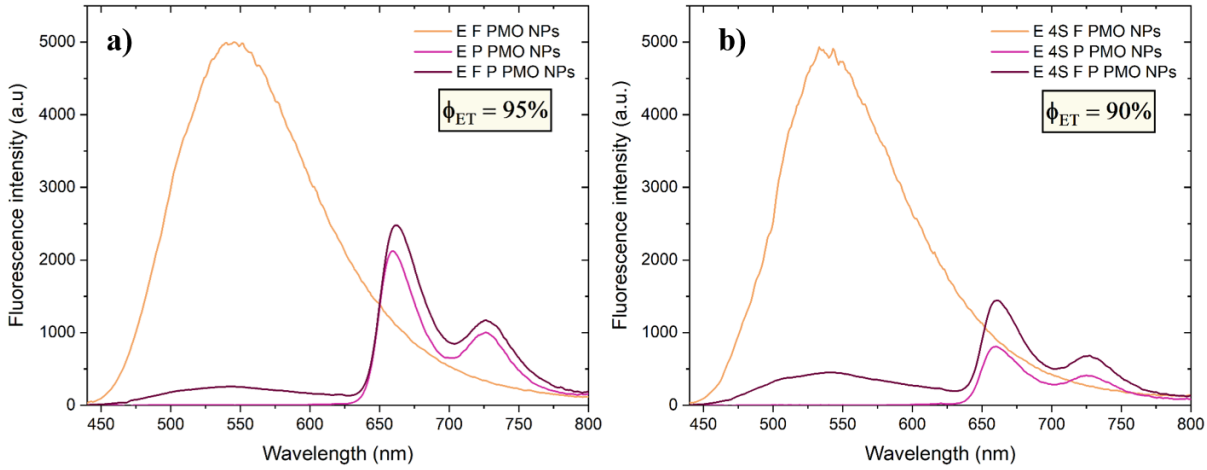

Figure 22: Fluorescence emission spectra and associated FRET efficiencies of (a) E F P PMO NPs and (b) E 4S F P BPMO NPs. F fluorescence is quenched by P *via* energy transfer, and P emission is increased.

Moreover, the impact of a tetrasulfide-based framework was studied. The analogy of E and E 4S NPs reveals that 4S inhibits porphyrin fluorescence, while an effect on F fluorescence emission is noticeable but less important (**Figure 23**).

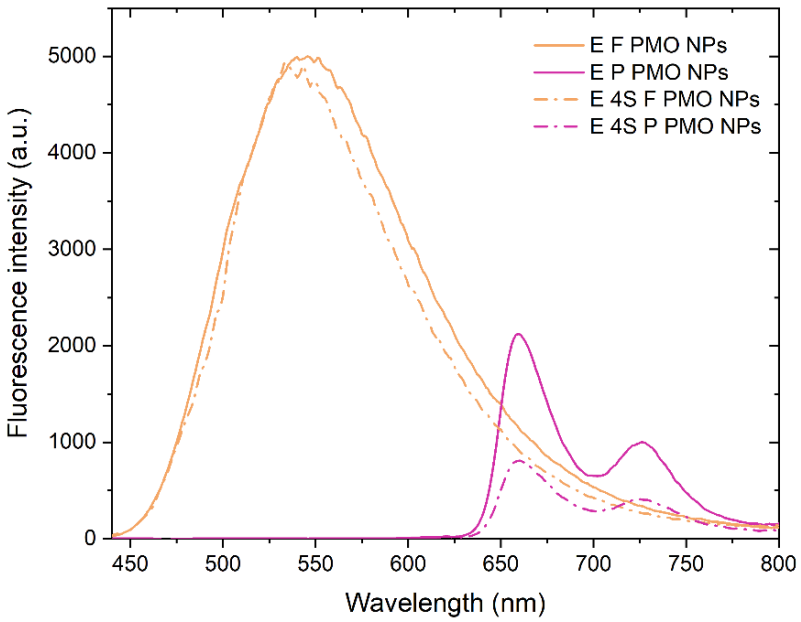

Figure 23: Influence of 4S to fluorescence spectra profiles of ethylene-based PMO NPs.

2.3.3 FRET in ethenylene-based nanoparticles

As for ethylene-based NPs, the potential for efficient energy transfer from F to P was studied in ethenylene-based PMO families. Qualitatively, porphyrin seems to be less fluorescent (650-800 nm range) for these NPs.

For ENE PMO NPs, the partial quenching of donor F allowed estimating a lower FRET efficiency of 73% (**Figure 24a**). This diminution is accompanied by concomitant increase of P fluorescence.

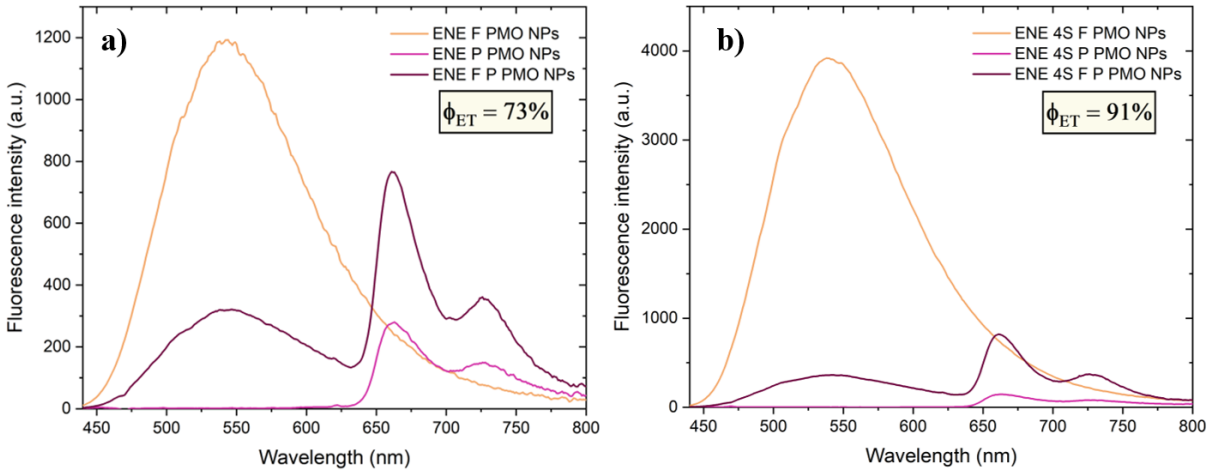

Figure 24: Fluorescence emission spectra and associated FRET efficiencies of (a) ENE F P PMO NPs and (b) ENE 4S F P BPMO NPs. F fluorescence is quenched by P *via* energy transfer, and P emission is increased.

The low fluorescence intensity of ENE F PMO NPs, thus the reduced Φ_{ET} value, can be ascribed to a unique difference in morphology observed by TEM imaging. In fact, sol-gel synthesis with ENE and F produced rod-like shaped NPs (**Figure 24b**). With mean length of 321 ± 53 nm and mean width of 202 ± 29 nm, they look like ENE NPs presented in **Figure 8**, but with lower length-to-width ratio (2.03 for ENE *vs.* 1.59 for ENE F) probably due to F addition. For all other NPs, nanospheres were obtained (**Figure 25b and c**). Thus, in this special case, we hypothesize that the fluorophore integration capacity is lowered in ENE rigid structure, whereas is ENE 4S F, tetrasulfide contributes to F-Si precursors insertion.

For ENE 4S BPMO family, a 91% FRET efficiency was obtained from the decrease of D fluorescence intensity (**Figure 24b**). The concomitant increase of acceptor P fluorescence is more pronounced than for E 4S PMO NPs.

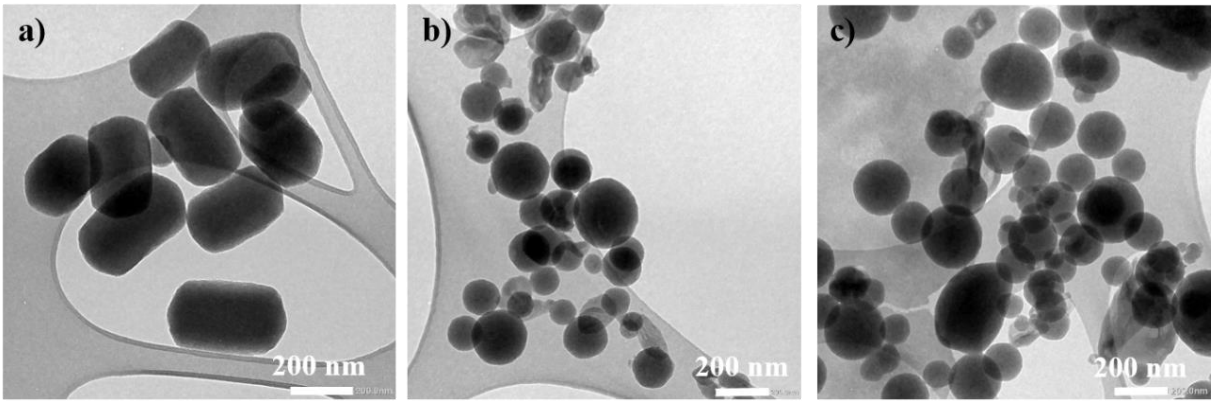

Figure 25: TEM imaging of (a) ENE F, (b) ENE P and (c) ENE F P PMO NPs. Compared to ENE 4S F PMO NPs, the absence of 4S precursor results in the production of nanorods, just as ENE PMO NPs.

Beside ethenylene NPs, superior donor fluorescence of 4S-based ENE NPs (**Figure 26**) is more likely attributable to the limited fluorescence of ENE F due to morphology difference.

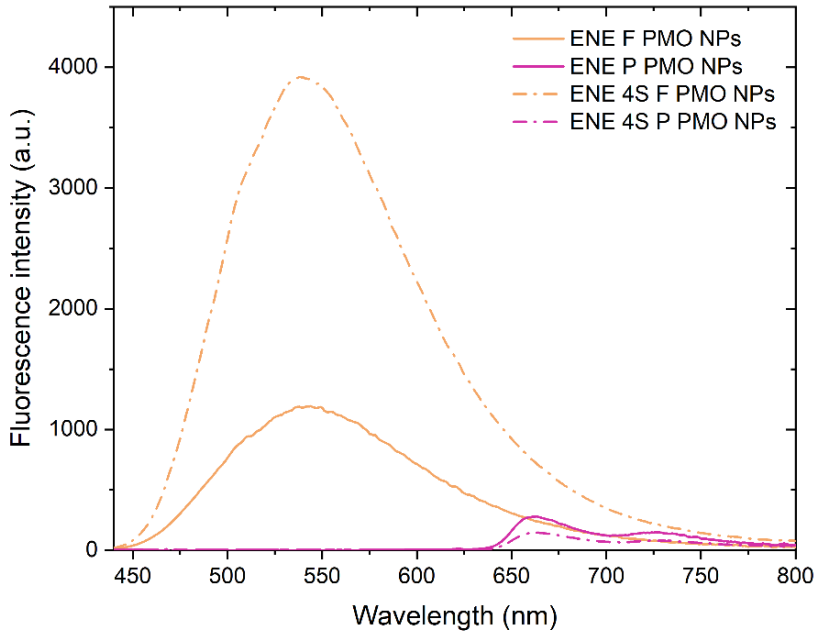

Figure 26: Influence of 4S to fluorescence spectra profiles of ethenylene-based PMO NPs.

To summarize the photophysical studies, both E-based and ENE-based NPs displayed a FRET behavior with or without biodegradable tetrasulfide linker. High Φ_{ET} were deducted from the comparison of the donor emission in F and F P NPs, suggesting good potency for PDT.

3. Conclusions and perspectives

Spherical organosilica nanoparticles with well-defined pores of 2 to 4 nm were prepared by simple routes using different mixtures of organoalkoxysilane precursors. The nanoparticles showed satisfying morphology, structure and particle size for biological applications. On one hand, the loading of vancomycin hydrochloride antibiotic was found to be pH-dependent with more accuracy in acidic conditions. Biodegradability studies of tetrasulfide-based NPs showed redox-triggered structure collapse in models of glutathione-rich environment. This is of high importance to improve drug release and biological clearance.

On the other hand, fluorescence measurements of fluorophore-porphyrin PMO NPs suggested high levels of FRET efficiency from fluorophore to porphyrin moieties within the hybrid frameworks.

As a whole, the design strategies of mixed PMO nanoparticles allowed obtaining suitable materials for both two-photon excitation PDT and antibiotic delivery. In line with prior drug loading, drug release simulation and photophysical characterizations, the potential of F P PMO NPs will be studied *in vitro* in the next chapter.

It is important to note that some research is ongoing to characterize the photophysical properties of both chromophores and nanoparticles by two-photon excitation, notably to compare the materials TPA cross-sections and singlet oxygen quantum yields. This work was not possible earlier due to technical reasons.

4. Experimental section

Materials

Unless otherwise specified, ACS reagent grade starting materials and solvents were used as received from commercial suppliers without further purification.

ASTM type I ultrapure water (resistivity = 18.2 MΩ cm) from an Elga PURELAB® Flex purification system (Veolia Water Technologies, Saint-Maurice, France) was used in all experiments. Tris{4-[(1E)-2-{4-[(3-hydroxypropyl)sulfonyl]phenyl}ethenyl]phenyl}amine (F) was synthesized according to chapter 3 protocols. p-[N-(2-Ethoxy-3,4-dioxocyclobut-1-enyl)amino]phenyl-α-D-mannopyranoside (sqMAN) was synthesized following Sperling *et al.* protocol.[35] 1,2-Bis(triethoxysilyl)ethane (E, 96%), bis[3-(triethoxysilyl)propyl]tetrasulfide (4S, ≥ 90%), 3-(isocyanatopropyl)triethoxysilane (ICPTES, 95%), cetyltrimethylammonium bromide (CTAB, > 98%), sodium hydroxide pellets (NaOH, ≥ 98%), ammonium nitrate (NH_4NO_3, > 98%), phosphate buffer solution (PBS, 1 M, pH 7.4), vancomycin hydrochloride (VAN, ref. 94747, ≥ 85%), 2-mercaptoethanol (ME, > 99%), glutathione (GSH), ethyl acetate, hexane (≥ 97%), $CDCl_3$ (99.9 atom% D), dimethylsulfoxide-d_6 (99.9 atom% D), acetone-d_6 (99.9 atom% D), Whatman® qualitative filter paper, Grade 6 (3 µm) and Fluoropore® PTFE membrane filters (0.22 µm) were purchased from Merck (Saint-Quentin-Fallavier, France). β-Citronellol (95%), fluorescamine, dimethylsulfoxide (DMSO, 99.7 %) hydrochloric acid (HCl, ≥ 37%), methanol (≥ 99.9%), tetrahydrofuran (THF, 99.5 %, extra dry over molecular sieves), boric acid and triethylamine (Et_3N, > 99%) were purchased from Thermo Fisher Scientific (Illkirch-Graffenstaden, France). 1,2-Bis(triethoxysilyl)ethylene (ENE, 95%, 80% trans-isomer) was obtained from abcr GmbH (Karlsruhe, Germany). Absolute ethanol (EtOH) and ethanol (96%) were obtained from Carlo Erba Reagents (Cornaredo, MI, Italy). 5,10,15,20-Tetrakis(4-aminophenyl)porphyrin (P, ≥ 98%) was obtained from PorphyChem (Dijon, France). (6-{2-[2-(2-Methoxy-ethoxy) ethoxy]ethoxy}hexyl)triethoxysilane (PEG-Si, > 98%) and 11-aminoundecyltriethoxysilane (AUTES, > 97%) were purchased from Sikemia (Montpellier, France). Sodium chloride (NaCl) was obtained from VWR (Radnor, PA, USA).

Characterization

Samples for TEM measurements were deposited from suspensions on Cu Formvar/C holey grids and allowed to dry before observation. The main transmission electron microscopy (TEM) images were acquired using a JEOL 1200 EXII (Tokyo, Japan) operated at 120 kV. The quantification of the nanoparticles diameters was performed with the Image*J* software with at

least 100 counts. The elemental mapping was recorded in STEM mode with an Oxford Instruments XMaxN 100 TLE (100 mm^2, windows less) EDX detector with a JEOL 2200 FS (FEG) Transmission Electron Microscope operated at 200 kV with a Gatan UltraScan 4000 (4k x 4k) CCD camera. CHNS elemental analyses were performed on a Elementar Vario Micro Cube (Langensenbold, Germany).

Hydrodynamic diameter and zeta potential measurements were recorded on Malvern NanoSeries (Malvern, UK) Zetasizer NanoZS (model ZEN3600) in a DTS1060C Zetacell (for the zeta potential) at 25 °C, with an equilibration time of 60 s and with automatic measurement, and data were treated by Zetasizer software using a Smoluchowski model.

N_2 adsorption and desorption were measured at 77 K using a Micromeritics TriStar (Norcross, GA, USA) device (V6.06 A). Prior to the sorption experiment, the samples were dried under vacuum at 80 °C for 8 h. The specific surface area (SSA) were obtained from Brunauer-Emmett-Teller (BET) method. Pore size distributions were obtained from the desorption branch of the nitrogen isotherm using the Barrett–Joyner–Halenda (BJH) equation.

Solid-state NMR spectra were acquired on a 300 MHz Varian VNMRS300 spectrometer (Les Ulis, France) equipped with a "wide-bore" magnet at 7.05 T, using a Varian T3 MAS (Magic Angle Spinning) probe with 3.2 mm ZrO_2 rotors. ^{13}C NMR spectra in cross polarization-MAS mode have been acquired with a recycle delay of 3 s and a contact time of 1 ms. A sample of adamantane has been used as a secondary reference (left peak at 38.5 ppm). The samples spun at a spinning speed of 12 kHz, the width of the spectral window is 50 kHz and the line broadening is 50 Hz.

The grafting ratio of amine functions on nanoparticles surface was calculated from fluorescence spectra with a Safas Xenius XM fluorimeter microplate reader (Monaco, Monaco). Antibiotic drug loading contents (DLCs) in water were determined by UV-visible absorption spectroscopy with a Jasco V-770 spectrophotometer (Mary's Court Easton, MD, USA) using quartz cells of 1 cm path length.

^1H NMR spectra were obtained with a Bruker Avance 400 MHz NMR spectrometer (Billerica, MA, USA) equipped with a BBSO probe.

Photophysical properties were obtained in absolute ethanol by performing UV-visible absorption spectroscopy with a Jasco V-770 spectrophotometer and fluorescence spectroscopy at room temperature (25 °C) with a Jasco FP-8300 fluorimeter (Mary's Court Easton, MD, USA) and a Edinburgh Instruments FLS920 fluorimeter (Edinburgh, UK) in photon-counting mode, using quartz cells of 1 cm path length.

Preparation of PMO and F P PMO nanoparticles

Synthesis of F-Si by trisilylation of the two-photon responsive fluorophore (F)

Air was removed from a solution of fluorophore F (100 mg, 109 µmol, 1.00 eq.) and isocyanatopropyltriethoxysilane (85 µL, 343 µmol, 3.15 eq.) in anhydrous THF (553 µL, 6.82 mmol) and Et_3N (11 µL, 109 µmol, 1.00 eq.) in a sealed tube. The reaction mixture was heated at 75 °C for 24 h. After resolubilization in anhydrous THF, the solvent was evaporated and a dark orange powder was obtained (F-Si, 155 mg, 86%). ^{1}H NMR (400 MHz, Acetone-d_6): δ=7.90 (d, *J*= 8.7 Hz, 6H), 7.87 (d, *J*= 8.7 Hz, 6H), 7.66 (d, *J*=8.7 Hz, 6H), 7.51 (d, *J*=16.4 Hz, 3H), 7.33 (d, *J*=16.4 Hz, 3H), 7.16 (d, *J*=8.7 Hz, 6H), 6.26 (t, *J*=6.4 Hz, 3H), 4.07 (t, *J*=6.3 Hz, 6H), 3.80 (q, *J*=7.0 Hz, 18H), 3.28 (m, 6H), 3.08 (q, *J*=6.6 Hz, 6H), 1.96 (m, 6H), 1.58 (m, 6H), 1.18 (t, *J*=7.0 Hz, 27H), 0.59 ppm (m, 6H); HRMS (ES$^+$, CH_3OH/CH_2Cl_2, 90/10): m/z calcd for $C_{81}H_{114}N_4O_{21}S_3Si_3$: 1681.63378 $[M+Na]^+$; found: 1681.6334.

Synthesis of P-Si by tetrasilylation of the commercial porphyrin (P)

Air was removed from porphyrin P (1.00 g, 1.48 mmol, 1.00 eq.) in a 100 mL two-neck round bottom flask. Then, anhydrous THF (14.8 mL, 182 mmol) and Et_3N (207 µL, 1.48 mol, 1.00 eq.) were added, followed by isocyanatopropyltriethoxysilane (1.54 mL, 6.24 mmol, 4.21 eq.). The reaction mixture was heated at 80 °C for 24 h. After resolubilization in ethyl acetate, the solvent was evaporated. Next, the crude product was washed on 0.22 µm polytetrafluoroethylene membrane with ethyl acetate, and recrystallized in hexane using an ice bath. This step was performed four consecutive times. After drying under vacuum, a purple powder was obtained (1.83 g, 74%). ^{1}H NMR (400 MHz, DMSO-d_6): δ=8.89 (s, 8H), 8.87 (s, 4H), 8.07 (d, *J*=8.5 Hz, 8H), 7.86 (d, *J*=8.5 Hz, 8H), 6.41 (t, 4H), 3.80 (q, *J*=7.0 Hz, 24H), 3.20 (m, 8H), 1.59 (m, 8H), 1.21 (t, *J*=7.0 Hz, 36H), 0.67 (m, 8H), -2.85 ppm (s, 2H). HRMS (ES$^+$, CH_3CN/CH_2Cl_2, 90/10): m/z calcd for $C_{84}H_{118}N_{12}O_{16}Si_4$: 1663.7944 $[M+H]^+$; found: 1663.79.

Synthesis of E PMO and E 4S BPMO NPs

A mixture of CTAB (250 mg, 0.69 mmol), ultrapure water (65 mL), and sodium hydroxide (NaOH (2 M), 437 µL) was stirred at 80 °C for 50 min at 750 rpm in a 250 mL round bottom flask. Then, a mixture of 1,2-bis(triethoxysilyl)ethane and bis[3-triethoxysilyl)propyl]tetrasulfide (100:0, 90:10 or 80:20 (n:n), total 0.90 mmol) in 1 mL of absolute ethanol was introduced in the reaction. The condensation process was conducted for 2 h. Then, the solution was cooled to room temperature while stirring; fractions were gathered in propylene tubes and collected by centrifugation for 15 min at 20k rpm. Subsequently, the still

surfactant-filled particles were solvent-extracted three times with ammonium nitrate solution (6 g L^{-1} ethanol) in order to remove the CTAB template, and washed three times with ethanol, water and ethanol. Each extraction and washing involved 20 min sonication at 40 °C and centrifugation for 10 min at 20k rpm. The nanoparticles were finally redispersed in ethanol and dried for a few hours under vacuum at room temperature.

Synthesis of ENE PMO and ENE 4S BPMO NPs

A mixture of CTAB (50 mg, 0.14 mmol) and ultrapure water (30 mL) was stirred at 80 °C in a 100 mL round bottom flask until CTAB complete dissolution. Next, β-citronellol (19 µL, 105 µmol) and sodium hydroxide (NaOH (2 M), 160 µL) were added and the solution was stirred at 80 °C for 30 min at 1000 rpm. Then, a mixture of 1,2-bis(triethoxysilyl)ethylene and bis[3-(triethoxysilyl)propyl]tetrasulfide (100:0, 90:10 or 80:20 (n:n), total 0.65 mmol) in 1 mL of absolute ethanol was introduced in the reaction. The condensation process was conducted for 2 h. Then, the solution was cooled to room temperature while stirring, and a white precipitate was obtained after filtration with a Whatman® qualitative filter paper, Grade 6 (3 µm). The surfactants were extracted with a mixture of methanol (80 mL) and 36 wt% aqueous HCl solution (10 mL) for 24 h while stirring at 750 rpm. Fractions were gathered in propylene tubes and collected by centrifugation for 20 min at 20k rpm and washed 3 times with ethanol, water and ethanol. Each washing involved 20 min sonication at 40 °C and centrifugation for 15 min at 20k rpm. The nanoparticles were finally redispersed in ethanol and dried for a few hours under vacuum at room temperature.

Synthesis of E (4S) F, E (4S) P and E (4S) F P (B)PMO NPs

A mixture of CTAB (250 mg, 0.69 mmol), ultrapure water (65 mL), and sodium hydroxide (NaOH (2 M), 437 µL) was stirred at 80 °C for 50 min at 750 rpm in a 250 mL round bottom flask. Then, a mixture of 1,2-bis(triethoxysilyl)ethane, bis[3-(triethoxysilyl)propyl]tetrasulfide (E:4S, 100:0 or 80:20 (n:n), total 0.90 mmol), silylated fluorophore (F-Si, 7.5 mg, 4.5 µmol) and silylated porphyrin (P-Si, 67.4 mg, 40.5 µmol) in 5 mL of absolute ethanol was introduced in the reaction. The condensation process was conducted for 2 h. Then, the solution was cooled to room temperature while stirring; fractions were gathered in propylene tubes and collected by centrifugation for 20 min at 20k rpm. Subsequently, the still surfactant-filled particles were solvent-extracted three times with ammonium nitrate solution (20 g L^{-1} ethanol) in order to remove the CTAB template, and washed three times with ethanol, water and ethanol. Each extraction and washing involved 20 min sonication at 40 °C and centrifugation for 15 min at 20k rpm. The nanoparticles were finally

redispersed in ethanol and dried for a few hours under vacuum at room temperature. Syntheses without F-Si or without P-Si were also performed (only 1 mL of absolute ethanol was used when there was no porphyrin).

Synthesis of ENE F P PMO and ENE 4S F P BPMO NPs

A mixture of CTAB (50 mg, 0.14 mmol) and ultrapure water (30 mL) was stirred at 80 °C in a 100 mL round bottom flask until CTAB complete dissolution. Next, β-citronellol (19 µL, 105 µmol) and sodium hydroxide (NaOH (2 M), 160 µL) were added and the solution was stirred at 80°C for 30 min at 1000 rpm. Then, a mixture of 1,2-bis(triethoxysilyl)ethylene, bis[3-(triethoxysilyl)propyl]tetrasulfide (ENE:4S, 100:0 or 80:20 (n:n), total 0.65 mmol), silylated fluorophore (F-Si, 5.4 mg, 3.25 µmol) and silylated porphyrin (P-Si, 48.8 mg, 29.3 µmol) in 4 mL of absolute ethanol was introduced in the reaction. The condensation process was conducted for 2 h. Then, the solution was cooled to room temperature while stirring, and a purple precipitate was obtained after filtration with a Whatman® qualitative filter paper, Grade 6 (3 µm). The surfactants were extracted with a mixture of methanol (80 mL) and 36 wt% aqueous HCl solution (10 mL) for 24 h while stirring at 750 rpm. Fractions were gathered in propylene tubes and collected by centrifugation for 20 min at 20k rpm and washed 3 times with ethanol, water and ethanol. Each washing involved 20 min sonication at 40 °C and centrifugation for 15 min at 20k rpm. The nanoparticles were finally redispersed in ethanol and dried for a few hours under vacuum at room temperature. Syntheses without fluorophore or without porphyrin were also performed (only 0.8 mL of absolute ethanol was used when there was no porphyrin).

Direct grafting of PEG-Si and AUTES on ethane-based F P PMO NPs

After 2 h condensation process of E F P or E 4S F P NPs, temperature was decreased to 50 °C. Then, a 25:1 (n:n) mix of PEG-Si (80.7 mg, 196.5 µmol) and 11-aminoundecyltriethoxysilane (2.6 mg, 7.9 µmol) was dissolved in 1 mL of ultrapure water and added to the sol-gel preparation. The reaction was kept under stirring at 750 rpm and 50 °C overnight. Then, the solution was cooled to room temperature while stirring. Some part of the NPs was not treated with ammonium nitrate, and only redispersed in absolute ethanol and stored at +4 °C for further sqMAN grafting step. The other part was extracted and washed according to the previously described protocol.

Direct grafting of PEG-Si and AUTES on ethene-based F P PMO NPs

After 2 h condensation process of ENE F P or ENE 4S F P NPs, temperature was decreased to 50 °C. Then, a 25:1 (n:n) mix of PEG-Si (60.1 mg, 146.2 µmol) and 11-aminoundecyltriethoxysilane (2.0 mg, 5.8 µmol) was dissolved in 1 mL of ultrapure water and

added to the sol-gel preparation. The reaction was kept under stirring at 750 rpm and 50 °C overnight. Then, the solution was cooled to room temperature while stirring, and a purple precipitate was obtained after filtration with a Whatman® qualitative filter paper, Grade 6 (3 µm). Some part of the NPs was not treated with HCl and methanol, and only redispersed in absolute ethanol and stored at +4 °C for further sqMAN grafting step. The other part was extracted and washed according to the previously described protocol.

AUTES titration by fluorescamine primary amine assay and grafting estimation

AUTES (M_w = 333.59 g mol^{-1}, d = 0.895) grafting was quantified by fluorescence using fluorescamine, which is interacting with primary amines. Briefly, a 3:1 (v:v) solution A was prepared by mixing fluorescamine in DMSO (1 mg mL^{-1}) with a buffer borate solution (pH 8.5) prepared from boric acid basified with a 200 mM NaOH aqueous solution. Then, every AUTES standard or F P (B)PMO@PEG/AUTES NPs sample (solution B, in EtOH) was mixed with A in a 1:1 (v:v) ratio. The final AUTES standards concentrations were 2.37, 5.92, 11.83 and 23.66 µg mL^{-1}, and the final NPs samples concentration were 500 µg mL^{-1}. Finally, the grafting amounts were calculated from the fluorescence intensities ($\lambda_{em.,\,max}$ = 482 nm, $\lambda_{exc.}$ = 390 nm, voltage = 645 V) obtained with Safas Xenius XM microplate reader, using a standard curve with linear correlation. PEG-Si (M_w = 410.62 g mol^{-1}) and sqMAN (M_w = 393.33 g mol^{-1}) grafting efficiencies were estimated considering the 25:1 (n:n) PEG:AUTES and 1:1 (n:n) AUTES:sqMAN ratio. Equation (1) was employed to know the necessary amount of sqMAN to put in reaction to reach full coverage of amine functions (*vs.* grafted NPs):

$$m(sqMAN) = \frac{[AUTES]\,Mw\,(sqMAN)}{Mw\,(AUTES)}\,x\,\frac{m\,(NP@PEG/AUTES)}{(1 + [AUTES] + [PEG])} \quad (1),$$

where [AUTES] and [PEG] are the mass concentrations *vs.* bare NPs (in µg mg^{-1}), and m(NP@PEG/AUTES) the amount of grafted NPs (in mg) introduced for sqMAN grafting.

Squarate mannose derivative post-grafting using estimated AUTES amounts

The targeted AUTES:sqMAN ratio for post-grafting of sqMAN was 1:1 (n:n). Briefly, a mixture of F P (B)PMO@PEG/AUTES NPs in EtOH (previously sonicated for 30 min and not extracted in CTAB to avoid grafting in the pore walls) and sqMAN aqueous solution was stirred at 750 rpm and 50 °C overnight in a 50 mL round bottom flask (50:50 (v:v) H_2O:EtOH). The initial amount of mannose was ranging from 2 to 3 µg mg^{-1} F P (B)PMO@PEG/AUTES NPs, depending on AUTES titration results. Then, ENE-based NPs filtration, CTAB extraction and NPs washings were performed according to the previously described protocols, depending on the type of NPs.

Vancomycin loading on F P (B)PMO NPs and stability studies

Impact of pH on nanoparticles surface charge

Dried NPs were redispersed in 1 mM NaCl aqueous solution, yielding a concentration of 200 µg mL^{-1}. After quick sonication, pH values were tuned with NaOH and HCl 20 mM aqueous solutions, using a pH probe, and zeta potential (n = 5) was recorded on the Malvern Zetasizer. For each NPs, pH was first fixed to 5, and then increased to 6, 7 and 8 for the next measurements (tolerance of ± 0.05 pH).

Vancomycin loading by direct pH measurement in VAN+NPs aqueous solutions

VAN+NPs mixtures (20 mg VAN and 20 mg NPs in 2 mL H_2O) were adjusted to pH values equal to 5, 6 or 7 ± 0.05 by adding small aliquots of diluted NaOH or HCl aqueous solutions, and the pH value was tracked by a pH-meter probe. Each sample was divided in two Eppendorf tubes (V ≈ 1 mL, depending on aliquots volumes, with $V_1 = V_2$). Samples were sonicated, vortexed, and then stirred for 24 h with a vertical rotating mixer. Next, each duplicate was reunited and pH neutralized by adding small aliquots of diluted NaOH or HCl aqueous solutions. After that, each sample was again divided in two Eppendorf tubes ($V_{1'} = V_{2'}$) and stirred for 30 min more. VAN-loaded NPs were washed three times by centrifugation (10 min at 13.4k rpm) and redispersion in water (1 min sonication), giving a supernatant (V ≈ 3 mL) containing free VAN for further drug loading content (DLC) determination by UV-visible absorption spectroscopy. After the last centrifugation step, VAN-loaded NPs were neutralized by dispersion in 10 mM PBS aqueous solution (10 mg mL^{-1}) and stored at +4 °C.

Evaluation of DLC by UV-visible spectroscopy of free vancomycin

UV-visible spectra of VAN standards from 10 to 300 µg mL^{-1} (n = 6 standards) in water displayed a high linear correlation at $\lambda_{abs.}$ = 280 nm ($R^2 \geq 0.9998$). Supernatants were diluted by 10 or 20 to reach the concentration range of the standards. After correction of the baseline, DLCs were calculated with the following equation:

$$DLC\ (\%) = \frac{m(ini\ VAN) - m(free\ VAN)}{m(ini\ NPs)} \times 100.$$

Biodegradability simulation studies

F P (B)PMO NPs biodegradation in the presence of mercaptoethanol

Briefly, previously vacuum dried F P PMO or F P BPMO NPs (5 mg) were dispersed in an aqueous medium (5 mL) composed of 10 mM PBS and 10 mM ME (equivalent of GSH).

The suspension was agitated for 7 days, and samples were collected after 1, 3 or 7 days for TEM screening.

VAN-loaded F P (B)PMO NPs kinetic release in the presence of glutathione

VAN-loaded NPs (0.5 mg mL^{-1}) were either suspended in 10 mM PBS medium or in 10 mM PBS/10 mM GSH medium for different contact times. VAN release profiles were then determined after centrifugation (10 min at 13.4k rpm) and titration of free VAN in the suspension supernatant using UV-visible spectroscopy.

Photophysical studies of F-Si, P-Si and F P (B)PMO nanoparticles

Excitation and emission spectra of F-Si and P-Si

UV-visible absorption spectroscopy was performed on F-Si and P-Si dilute solutions (ca. 10^{-6} M) to reach maximum absorbance $A_{max} \approx 0.1$. After that, steady-state fluorescence emission and excitation spectra were recorded on the Edinburgh Instruments FLS920 fluorimeter (Xe lamp) equipped with a dwell time of 0.1 s by exciting at $\lambda_{abs., max}$ (respectively 413 and 422 nm for F-Si and P-Si).

FRET efficiency within different F P (B)PMO nanoparticles

Energy transfer efficiency was evaluated by the fluorescence decrease of the energy donor (D = F) with the following equation:

$$\Phi_{ET} = 1 - \frac{I(DA)}{I(D)},$$

using either the fluorescence intensity of the donor, in the absence (I_D) and in the presence (I_{DA}) of the acceptor (A = P) at the maximum emission wavelength of D, or the area under the corresponding fluorescence bands (results are the same in both cases). Emission spectra were measured on Jasco FP-8300 fluorimeter at $\lambda_{exc.}$ = 413 nm with identical PMO mass concentrations (44 µg mL^{-1}). As F molar ratio in NPs is the same for all studied PMO (0.5% molar ratio), the amount of absorbed photons at 413 nm by F was considered the same.

Bibliography

1. Zugazagoitia, J.; Guedes, C.; Ponce, S.; Ferrer, I.; Molina-Pinelo, S.; Paz-Ares, L., Current Challenges in Cancer Treatment. *Clinical Therapeutics* **2016,** *38* (7), 1551-1566.

2. Mulani, M. S.; Kamble, E. E.; Kumkar, S. N.; Tawre, M. S.; Pardesi, K. R., Emerging Strategies to Combat ESKAPE Pathogens in the Era of Antimicrobial Resistance: A Review. *Frontiers in microbiology* **2019,** *10*.

3. Gan, X. P.; Wang, H. Y.; Lu, L. M.; Li, H.; Wang, K.; Kong, L., et al., Three new water-soluble fluorescent organic nanoparticles with embedded structure: Structure-activity relationship and two-photon bio-imaging application. *Dyes and Pigments* **2018,** *150*, 27-35.

4. Shi, L. M.; Nguyen, C.; Daurat, M.; Richy, N.; Gauthier, C.; Rebecq, E., et al., Encapsulation of Hydrophobic Porphyrins into Biocompatible Nanoparticles: An Easy Way to Benefit of Their Two-Photon Phototherapeutic Effect without Hydrophilic Functionalization. *Cancers* **2022,** *14* (10), 2358.

5. Sercombe, L.; Veerati, T.; Moheimani, F.; Wu, S. Y.; Sood, A. K.; Hua, S., Advances and Challenges of Liposome Assisted Drug Delivery. *Frontiers in Pharmacology* **2015,** *6*, 124133.

6. Sherje, A. P.; Jadhav, M.; Dravyakar, B. R.; Kadam, D., Dendrimers: A versatile nanocarrier for drug delivery and targeting. *International Journal of Pharmaceutics* **2018,** *548* (1), 707-720.

7. McNamara, K.; Tofail, S. A. M., Nanoparticles in biomedical applications. *Advances in Physics: X* **2017,** *2* (1), 54-88.

8. T Al-Jamal, W.; Kostarelos, K., Liposome-nanoparticle hybrids for multimodal diagnostic and therapeutic applications. *Nanomedicine* **2007,** *2* (1), 85-98.

9. Caminade, A.-M.; Zibarov, A.; Cueto Diaz, E.; Hameau, A.; Klausen, M.; Moineau-Chane Ching, K., et al., Fluorescent phosphorus dendrimers excited by two photons: synthesis, two-photon absorption properties and biological uses. *Beilstein Journal of Organic Chemistry* **2019,** *15*, 2287-2303.

10. Yang, S.; Fan, J.; Lin, S. T.; Wang, Y. R.; Liu, C., Novel pH-responsive biodegradable organosilica nanoparticles as drug delivery system for cancer therapy. *Colloids and Surfaces A: Physicochemical and Engineering Aspects* **2020,** *585*.

11. Chen, J. J.; Wang, Y. T.; Ma, B. Y.; Guan, L.; Tian, Z. F.; Lin, K. L., et al., Biodegradable hollow mesoporous organosilica-based nanosystems with dual stimuli-responsive drug delivery for efficient tumor inhibition by synergistic chemo- and photothermal therapy. *Applied Materials Today* **2020,** *19*, 100655.

12. Picchetti, P.; DiMarco, B. N.; Travaglini, L.; Zhang, Y.; Ortega-Liebana, M. C.; De Cola, L., Breaking with Light: Stimuli-Responsive Mesoporous Organosilica Particles. *Chemistry of Materials* **2020,** *32* (1), 392-399.

13. Doura, T.; Nishio, T.; Tamanoi, F.; Nakamura, M., Relationship between the glutathione-responsive degradability of thiol-organosilica nanoparticles and the chemical structures. *Journal of Materials Research* **2019,** *34* (7), 1266-1278.

14. Hadipour Moghaddam, S. P.; Saikia, J.; Yazdimamaghani, M.; Ghandehari, H., Redox-Responsive Polysulfide-Based Biodegradable Organosilica Nanoparticles for Delivery of Bioactive Agents. *ACS Applied Materials & Interfaces* **2017,** *9* (25), 21133-21146.

15. Aggad, D.; Mauriello Jimenez, C.; Dib, S.; Croissant, J. G.; Lichon, L.; Laurencin, D., et al., Gemcitabine Delivery and Photodynamic Therapy in Cancer Cells *via* Porphyrin-Ethylene-Based Periodic Mesoporous Organosilica Nanoparticles. *ChemNanoMat* **2018,** *4* (1), 46-51.

16. Gary-Bobo, M.; Mir, Y.; Rouxel, C.; Brevet, D.; Basile, I.; Maynadier, M., et al., Mannose-Functionalized Mesoporous Silica Nanoparticles for Efficient Two-Photon Photodynamic Therapy of Solid Tumors. *Angewandte Chemie International Edition* **2011,** *50* (48), 11425-11429.

17. Lerouge, F.; Cerveau, G.; Corriu, R. J. P.; Stern, C.; Guilard, R., Self-organization of porphyrin units induced by magnetic field during sol–gel polymerization. *Chemical Communications* **2007,** (15), 1553-1555.

18. Biazzotto, J. C.; Sacco, H. C.; Ciuffi, K. J.; Ferreira, A. G.; Serra, O. A.; Iamamoto, Y., Synthesis and properties of urea porphyrinosilica. *Journal of Non-Crystalline Solids* **2000,** *273* (1), 186-192.

19. Guan, B.; Cui, Y.; Ren, Z.; Qiao, Z.-a.; Wang, L.; Liu, Y., et al., Highly ordered periodic mesoporous organosilica nanoparticles with controllable pore structures. *Nanoscale* **2012,** *4* (20), 6588-6596.

20. Vu, B. T.; Shahin, S. A.; Croissant, J.; Fatieiev, Y.; Matsumoto, K.; Le-Hoang Doan, T., et al., Chick chorioallantoic membrane assay as an in vivo model to study the effect of nanoparticle-based anticancer drugs in ovarian cancer. *Scientific Reports* **2018,** *8* (1), 8524.

21. Motealleh, A.; Czieborowski, M.; Philipp, B.; Nowak, S.; Kehr, N. S., Bifunctional Nanomaterials for Enhanced Cell Proliferation and for the Reduction of Bacterial Bioluminescence/Fitness. *Advanced Materials Interfaces* **2020,** *7* (13), 2000086.

22. Motealleh, A.; Kart, D.; Czieborowski, M.; Kehr, N. S., Functional Nanomaterials and 3D-Printable Nanocomposite Hydrogels for Enhanced Cell Proliferation and for the Reduction of Bacterial Biofilm Formation. *ACS Applied Materials & Interfaces* **2021,** *13* (36), 43755-43768.

23. Mai, N. X. D.; Birault, A.; Matsumoto, K.; Ta, H. K. T.; Intasa-Ard, S. G.; Morrison, K., et al., Biodegradable Periodic Mesoporous Organosilica (BPMO) Loaded with Daunorubicin: A Promising Nanoparticle-Based Anticancer Drug. *ChemMedChem* **2020,** *15* (7), 593-599.

24. Urata, C.; Yamada, H.; Wakabayashi, R.; Aoyama, Y.; Hirosawa, S.; Arai, S., et al., Aqueous Colloidal Mesoporous Nanoparticles with Ethenylene-Bridged Silsesquioxane Frameworks. *Journal of the American Chemical Society* **2011,** *133* (21), 8102-8105.

25. Li, H.; Gascó, C.; Delalande, A.; Charnay, C.; Raehm, L.; Midoux, P., et al., Periodic Mesoporous Organosilica Nanoparticles with BOC Group, towards HIFU Responsive Agents. *Molecules* **2020,** *25* (4), 974.

26. Zhang, M.; Li, Y.; Bi, L.; Zhuang, W.; Wang, S.; Chen, Y., et al., Preparation of Helical Mesoporous Ethenylene-silica Nanofibers with Lamellar Mesopores on Their Surface. *Chinese Journal of Chemistry* **2011,** *29* (5), 933-941.

27. Agarwal, V.; Singh, M.; McPherson, G.; John, V.; Bose, A., Microstructure evolution in aqueous solutions of cetyl trimethylammonium bromide (CTAB) and phenol derivatives. *Colloids and Surfaces A: Physicochemical and Engineering Aspects* **2006,** *281* (1), 246-253.

28. Brunauer, S.; Emmett, P. H.; Teller, E., Adsorption of Gases in Multimolecular Layers. *Journal of the American Chemical Society* **1938,** *60* (2), 309-319.

29. Croissant, J.; Cattoën, X.; Man, M. W. C.; Gallud, A.; Raehm, L.; Trens, P., et al., Biodegradable Ethylene-Bis(Propyl)Disulfide-Based Periodic Mesoporous Organosilica Nanorods and Nanospheres for Efficient In-Vitro Drug Delivery. *Advanced Materials* **2014,** *26* (35), 6174-6180.

30. López, M. I.; Esquivel, D.; Jiménez-Sanchidrián, C.; Van Der Voort, P.; Romero-Salguero, F. J., Vulcanized Ethene-PMO: A New Strategy to Create Ultrastable Support Materials and Adsorbents. *The Journal of Physical Chemistry C* **2014,** *118* (31), 17862-17869.

31. Mezghrani, B.; Ali, L. M. A.; Richeter, S.; Durand, J.-O.; Hesemann, P.; Bettache, N., Periodic Mesoporous Ionosilica Nanoparticles for Green Light Photodynamic Therapy and Photochemical Internalization of siRNA. *ACS Applied Materials & Interfaces* **2021,** *13* (25), 29325-29339.

32. Zhou, Z.; Taylor, R. N. K.; Kullmann, S.; Bao, H.; Hartmann, M., Mesoporous Organosilicas With Large Cage-Like Pores for High Efficiency Immobilization of Enzymes. *Advanced Materials* **2011,** *23* (22-23), 2627-2632.

33. Sturge, J.; Wienke, D.; East, L.; Jones, G. E.; Isacke, C. M., GPI-anchored uPAR requires Endo180 for rapid directional sensing during chemotaxis. *Journal of Cell Biology* **2003,** *162* (5), 789-794.

34. Brevet, D.; Gary-Bobo, M.; Raehm, L.; Richeter, S.; Hocine, O.; Amro, K., et al., Mannose-targeted mesoporous silica nanoparticles for photodynamic therapy. *Chemical Communications* **2009,** (12), 1475.

35. Sperling, O.; Fuchs, A.; Lindhorst, T. K., Evaluation of the carbohydrate recognition domain of the bacterial adhesin FimH: design, synthesis and binding properties of mannoside ligands. *Organic & Biomolecular Chemistry* **2006,** *4* (21), 3913.

36. Akbari, A.; Yegani, R.; Pourabbas, B., Synthesis of poly(ethylene glycol) (PEG) grafted silica nanoparticles with a minimum adhesion of proteins *via* one-pot one-step method. *Colloids and Surfaces A: Physicochemical and Engineering Aspects* **2015,** *484*, 206-215.

37. Qie, Y.; Yuan, H.; von Roemeling, C. A.; Chen, Y.; Liu, X.; Shih, K. D., et al., Surface modification of nanoparticles enables selective evasion of phagocytic clearance by distinct macrophage phenotypes. *Scientific Reports* **2016,** *6* (1), 26269.

38. Nag, O. K.; Awasthi, V., Surface Engineering of Liposomes for Stealth Behavior. *Pharmaceutics* **2013,** *5* (4), 542-569.

39. Udenfriend, S.; Stein, S.; Böhlen, P.; Dairman, W.; Leimgruber, W.; Weigele, M., Fluorescamine: A Reagent for Assay of Amino Acids, Peptides, Proteins, and Primary Amines in the Picomole Range. *Science* **1972,** *178* (4063), 871-872.

40. Motoyoshiya, J.; Tomioka, S.; Kobayashi, D.; Fujimoto, T., A new cyano-substituted fluorescamine superior to its original form as a fluorescent probe for amino acid detection. *Tetrahedron Letters* **2018,** *59* (12), 1104-1107.

41. Daurat, M.; Nguyen, C.; Dominguez Gil, S.; Sol, V.; Chaleix, V.; Charnay, C., et al., The mannose 6-phosphate receptor targeted with porphyrin-based periodic mesoporous organosilica nanoparticles for rhabdomyosarcoma theranostics. *Biomaterials Science* **2020,** *8* (13), 3678-3684.

42. Bharti, C.; Gulati, N.; Nagaich, U.; Pal, A., Mesoporous silica nanoparticles in target drug delivery system: A review. *International Journal of Pharmaceutical Investigation* **2015,** *5* (3), 124.

43. Poscher, V.; Salinas, Y., Trends in Degradable Mesoporous Organosilica-Based Nanomaterials for Controlling Drug Delivery: A Mini Review. *Materials* **2020,** *13* (17), 3668.

44. Gounani, Z.; Asadollahi, M. A.; Pedersen, J. N.; Lyngso, J.; Pedersen, J. S.; Arpanaei, A., et al., Mesoporous silica nanoparticles carrying multiple antibiotics provide enhanced synergistic effect and improved biocompatibility. *Colloids and Surfaces B: Biointerfaces* **2019,** *175*, 498-508.

45. Marsot, A.; Boulamery, A.; Bruguerolle, B.; Simon, N., Vancomycin: a review of population pharmacokinetic analyses. *Clinical pharmacokinetics* **2012,** *51* (1), 1-13.

46. Cauda, V.; Onida, B.; Platschek, B.; Mühlstein, L.; Bein, T., Large antibiotic molecule diffusion in confined mesoporous silica with controlled morphology. *Journal of Materials Chemistry* **2008,** *18* (48), 5888-5899.

47. Takács-Novák, K.; Noszál, B.; Tókés-Kövesdi, M.; Szász, G., Acid-base properties and proton-speciation of vancomycin. *International Journal of Pharmaceutics* **1993,** *89* (3), 261-263.

48. Ural, M. S.; Menéndez-Miranda, M.; Salzano, G.; Mathurin, J.; Aybeke, E. N.; Deniset-Besseau, A., et al., Compartmentalized Polymeric Nanoparticles Deliver Vancomycin in a pH-Responsive Manner. *Pharmaceutics* **2021,** *13* (12), 1992.

49. Nader, D.; Yousef, F.; Kavanagh, N.; Ryan, B. K.; Kerrigan, S. W., Targeting Internalized *Staphylococcus aureus* Using Vancomycin-Loaded Nanoparticles to Treat Recurrent Bloodstream Infections. *Antibiotics* **2021,** *10* (5), 581.

CHAPTER 5: Biological studies of fluorophore-porphyrin PMO nanoparticles

1. Introduction

The previously obtained fluorophore-porphyrin PMO NPs could be suitable systems for biological applications due to their biocompatible porous hybrid framework and their two-photon sensitiveness. In particular, the same porphyrin than the one used in this study already demonstrated ROS generation capability when integrated in the synthesis of different PMO nanoparticle frameworks. Mezghrani and coworkers showed significant OPE-PDT effects of P integrated into periodic mesoporous ionosilica nanoparticles using a green light beam at 545 nm towards MDA-MB-231 cancer cells.[1] Aggad *et al.* observed slight TPE-PDT efficiency on MCF-7 cancer cells treated with ethylene-porphyrin PMO nanoparticles when irradiated at 800 nm.[2] In that way, the therapeutic action of F P PMO materials was assessed upon different strategies. On one hand, their internalization in breast cancer cells and their toxicity upon two-photon excitation PDT were studied using confocal microscopy *via* fluorescence imaging. On the other hand, their activity against traditional antibiotic resistant bacteria, either gram-negative or gram-positive, was evaluated by combined or separated antibiotic delivery from NPs and TPE-PDT. First results from biological assays including first evidence of FRET contribution are debated, as well as the future prospects.

2. Results and discussion

2.1 *In vitro* anticancer studies

2.1.1 Fluorophore-based nanoparticles as fluorescence markers

Before testing synthesized fluorophore-porphyrin PMO NPs in antitumor TPE-PDT, highly fluorescent F PMO NPs were tested as potent markers to assess NPs internalization in cancer cells. The preparation of those NPs was achieved by three different sol-gel conditions (**Experimental Section**). Briefly, the syntheses of E 4S F and E 4S F-2 were performed upon fast reaction kinetics for two hours in aqueous medium with respectively low or high water and catalyst contents. E 4S F-3 were obtained after three days' reactions with slower kinetics in water/ethanol medium and using ammonia as catalyst (**Table 1**). In particular, E 4S F-3 NPs with average diameters of 211 ± 2 nm were very monodisperse according to TEM images (**Figure 1**) and the low PDI value of 0.07 ± 0.03.

Table 1: Synthesis conditions and size measurements of different E 4S F BPMO NPs. [a] z average hydrodynamic diameter in ethanol, n = 5 independent experiments. [b] Average diameters of n ≥ 100 counts determined on TEM images. [*] Compared to E 4S F synthesis, sodium hydroxide and water amounts were about two times higher for E 4S F-2, leading to slower kinetics.

BPMO NPs	Ratio E:4S:F (n:n)	Sol-gel kinetics	Catalyst	Medium	DLS[a] (nm)	PDI	TEM[b] (nm)
E 4S F	80:20:0.50	Fast (+)	NaOH	H_2O	383 ± 13	0.16 ± 0.10	171 ± 22
E 4S F-2	80:20:0.50	Fast (-)	NaOH*	H_2O*	275 ± 1	0.23 ± 0.05	143 ± 28
E 4S F-3	90:10:0.66	Slow	NH_4OH	H_2O/EtOH	211 ± 2	0.07 ± 0.03	149 ± 26

Confocal microscopy images of living breast cancer MCF-7 cells treated with 50 µg mL^{-1} of fluorophore-PMO for 24 h are shown in **Figure 1**. The results showed good levels of cell internalization and fluorescence with higher efficiency for E 4S F-2 and E 4S F-3 than for E 4S F. This demonstrates the bio-imaging potential of fluorophore under 820 nm two-photon excitation in the NIR region when the compound is integrated into various PMO frameworks.

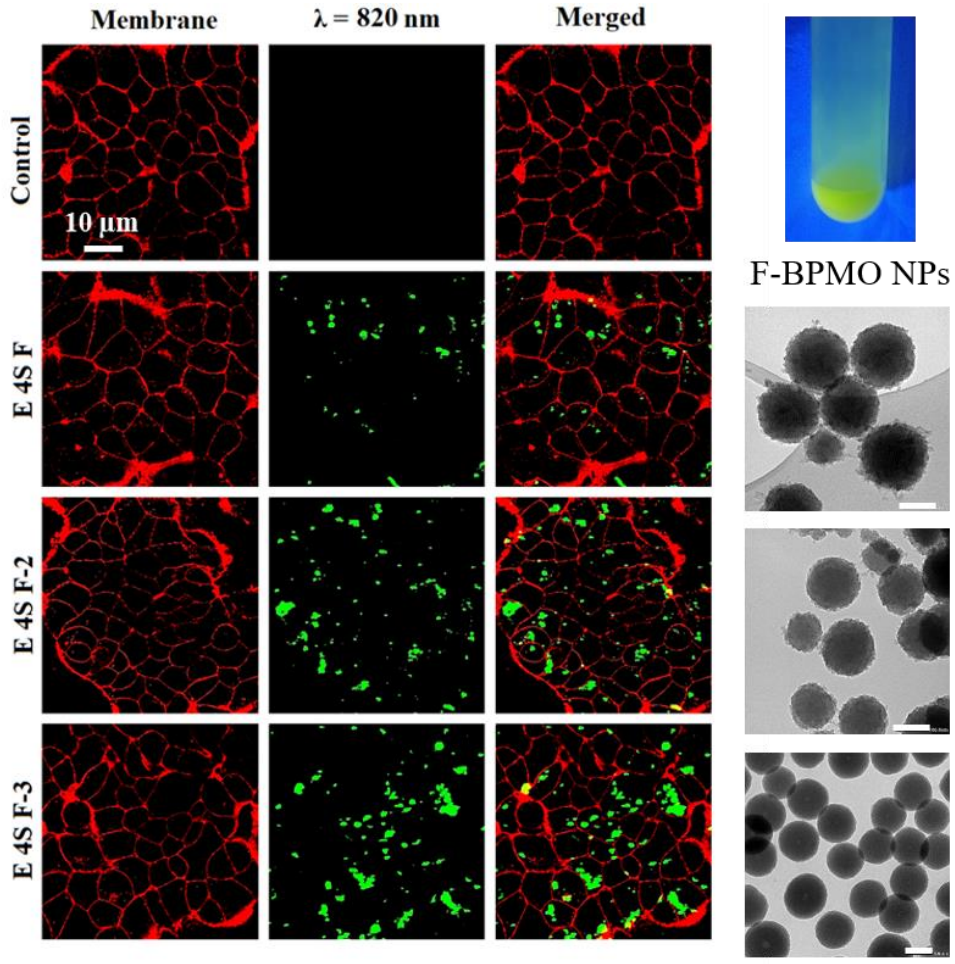

Figure 1: Cell internalization study of different fluorophore-BPMO NPs at 50 µg mL^{-1} using confocal microscopy imaging and associated TEM imaging. MCF-7 cancer cells were stained with Cell Mask™ Orange Plasma Membrane after incubation for 24 h and then visualized at 561 nm (membrane) and 820 nm (F PMO NPs). Images were obtained with Carl Zeiss LSM780 confocal fluorescence microscope using a high magnification (63x/1.4 OIL Plan-Apo). Scale bar (TEM): 100 nm.

Similarly, the internalization of F P PMO NPs in MCF-7 cancer cells was screened by confocal microscopy. After 780 nm NIR excitation, nanoparticles generated high fluorescence intensities in biological media (**Figure 2**). Interestingly, sqMAN-grafted E-based NPs showed higher fluorescence and thus, higher cellular uptake than naked NPs. In contrast, confocal imaging of ENE-based NPs revealed lower fluorescence levels inside cells for sqMAN-functionalized NPs compared to naked ones. For all families, (PEG/AUTES)-grafted NPs displayed an intermediate fluorescence intensity (data not shown). Even if the synthesis and grafting steps were performed with the same initial ratios in reactants, some differences regarding NPs texture and final grafting ratio could explain this result.

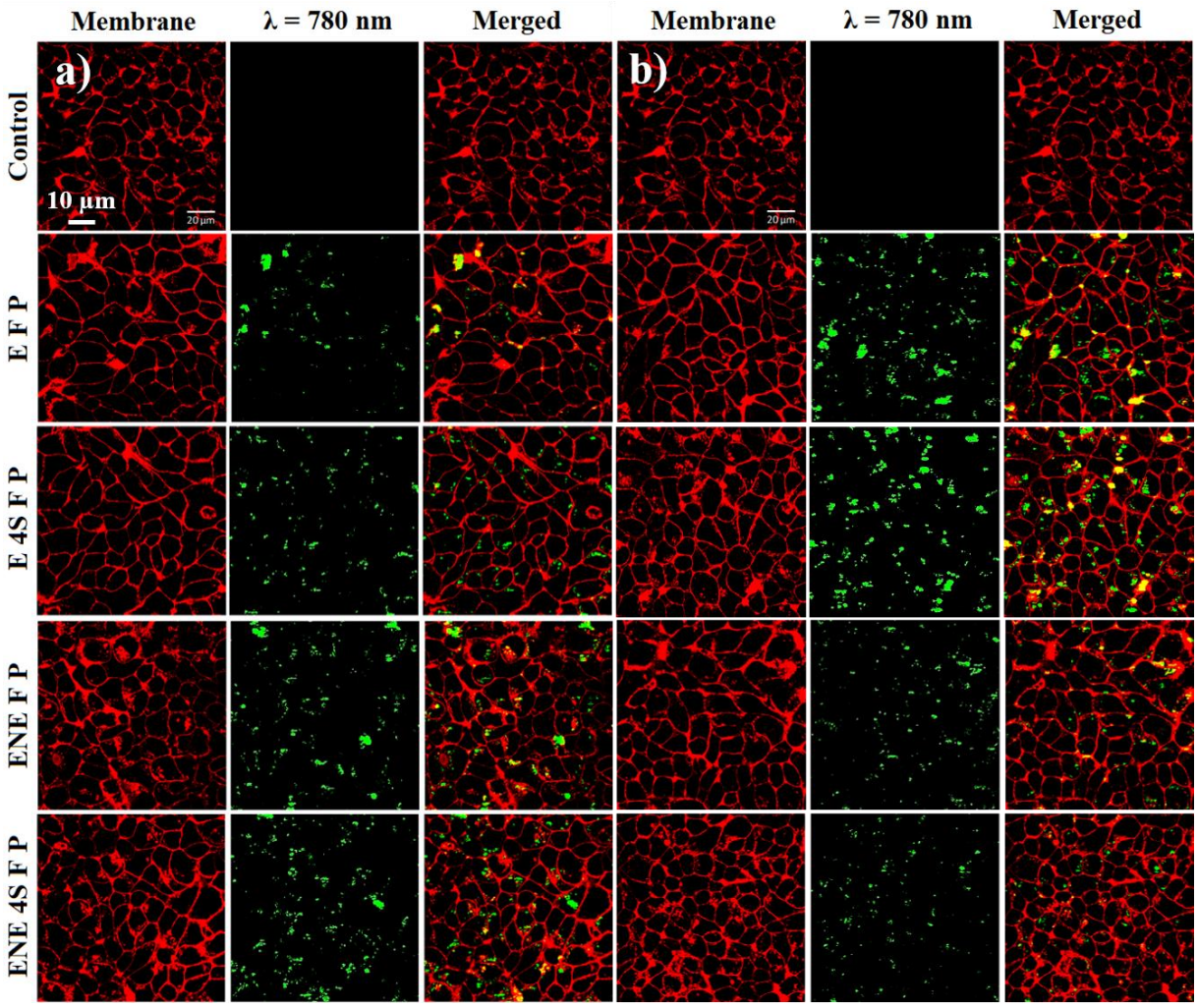

Figure 2: Cell internalization study of different fluorophore-porphyrin-PMO NPs either (a) naked or (b) (PEG/AUTES@sqMAN)-grafted at 50 µg mL^{-1} using confocal microscopy imaging. After incubation for 24 h, MCF-7 cancer cells were stained with Cell Mask™ Orange Plasma Membrane and then visualized at 561 nm (membrane) and 780 nm (F P PMO NPs). Images were obtained with Carl Zeiss LSM780 confocal fluorescence microscope using a high magnification (63x/1.4 OIL Plan-Apo).

To summarize, F PMO and F P PMO NPs with a good *in vitro* internalization levels would be suitable for biolabeling or biotracking to perform light-assisted therapy (for instance,

drug administration for chemotherapy, photoimmunotherapy and PDT). In addition, with the targeting ability of sqMAN (visible in the case of E F P PMO and E 4S FP BPMO NPs), great tumor accumulation of the active materials could be reached.

2.1.2 Efficiency in two-photon excitation PDT

The cell killing efficiencies of the four families of F P PMO (namely E, E 4S, ENE and ENE 4S) were studied *in vitro* upon photodynamic excitation in the NIR region. For each family, naked NPs, PMO@PEG/AUTES NPs and PMO@PEG/AUTES@sqMAN NPs were compared.

Firstly, materials photodynamic activities were evaluated under one-photon excitation at a wavelength of 525 nm, where porphyrin moieties possess great absorption properties *via* the Q4 band, as revealed by previous photophysical studies.[3]

In this case, cell viability was determined by using MTT chromophore to estimate cells survival rates. For those experiments, a routine sample was employed as positive control, while negative control was associated with cancer cell viability in the absence of NPs. OPE-PDT results for irradiation times of 10 min are presented in **Figure 3**. In dark conditions, the viability of MCF-7 cancer cells was always above 80% at 50 µg mL^{-1}, showing the low cytotoxic effect of all nanoparticles. After one-photon excitation, different effects were observed. All ENE 4S F P PMO NPs showed no PDT effect, while a slight killing effect could be attributed to the treatment with ENE F P samples. These inconclusive results cannot be correlated with the cell internalization levels revealed by confocal microscopy imaging. Indeed, while the cell uptake of sqMAN-grafted NPs is lower than (PEG/AUTES)-grafted and naked NPs, the cell viability is remaining constant.

For the E 4S F P family, no effect was visible for naked and (PEG/AUTES)-functionalized nanoparticles. Conversely, the effect of sqMAN targeting is obvious in imaging and in PDT with 44% cell killing. Lastly, the highest efficacies were reached for E F P with respectively 58, 61 and 59% killing efficiencies for naked, (PEG/AUTES)-functionalized and (PEG/AUTES@sqMAN)-functionalized PMO NPs. Surprisingly, the differences in E F P NPs uptake (**Figure 2**) were not in agreement with the homogeneous PDT activities.

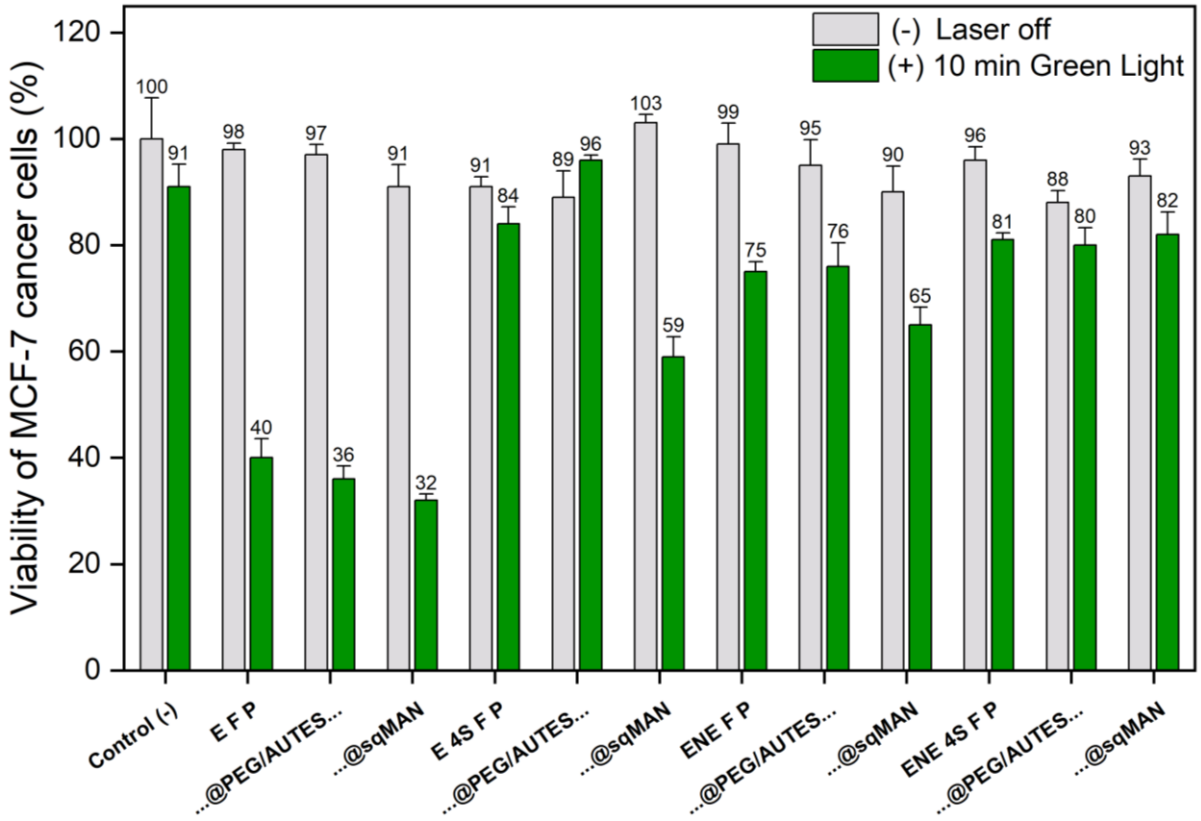

Figure 3: OPE-PDT studies of F P PMO NPs (either naked, functionalized with PEG and AUTES, or further grafted with sqMAN). OPE-triggered MCF-7 cancer cells killing after incubation with NPs at 50 µg mL^{-1} for 24 h and irradiation at 525 nm for 10 min. Lines represent standard deviations of three independent experiments.

Altogether, the variable OPE-PDT efficiency with the four families of NPs is most likely associated with cell uptake efficacy. We also hypothesize that the presence of 4S bridges in the NPs could quench ROS production and diffusion. Indeed, disulfide bonds were previously described as deactivators of $^1O_2$ by physical quenching mechanisms.[4]

In a second time, two-photon excitation PDT studies were then performed at 780 nm to preferentially irradiate fluorophore moieties for optimal FRET efficacy. Living cells nuclei were stained in blue using Hoechst 33342™ and counted on an EVOS™ M5000 imaging system after optimization of photograph parameters (brightness, gain, exposure) to properly distinguish nanoparticles and cellular fragments from living MCF-7 cancer cells.

Contrary to one-photon photodynamic therapy assays, two-photon excitation in the NIR induced high levels of toxicity for the four families of F P PMO NPs at 50 µg mL^{-1}, independently of the functionalization strategy (**Figure 4**). This result originates from the great optical properties of F and P chromophores, and from the crossing by specific electronic excited states due to different selection rules during two-photon irradiation. All the materials were

responsible for 80 to 100% reduction in cancer cell viability, except E 4S F P nanoparticles that caused between 42 and 56% cell death.

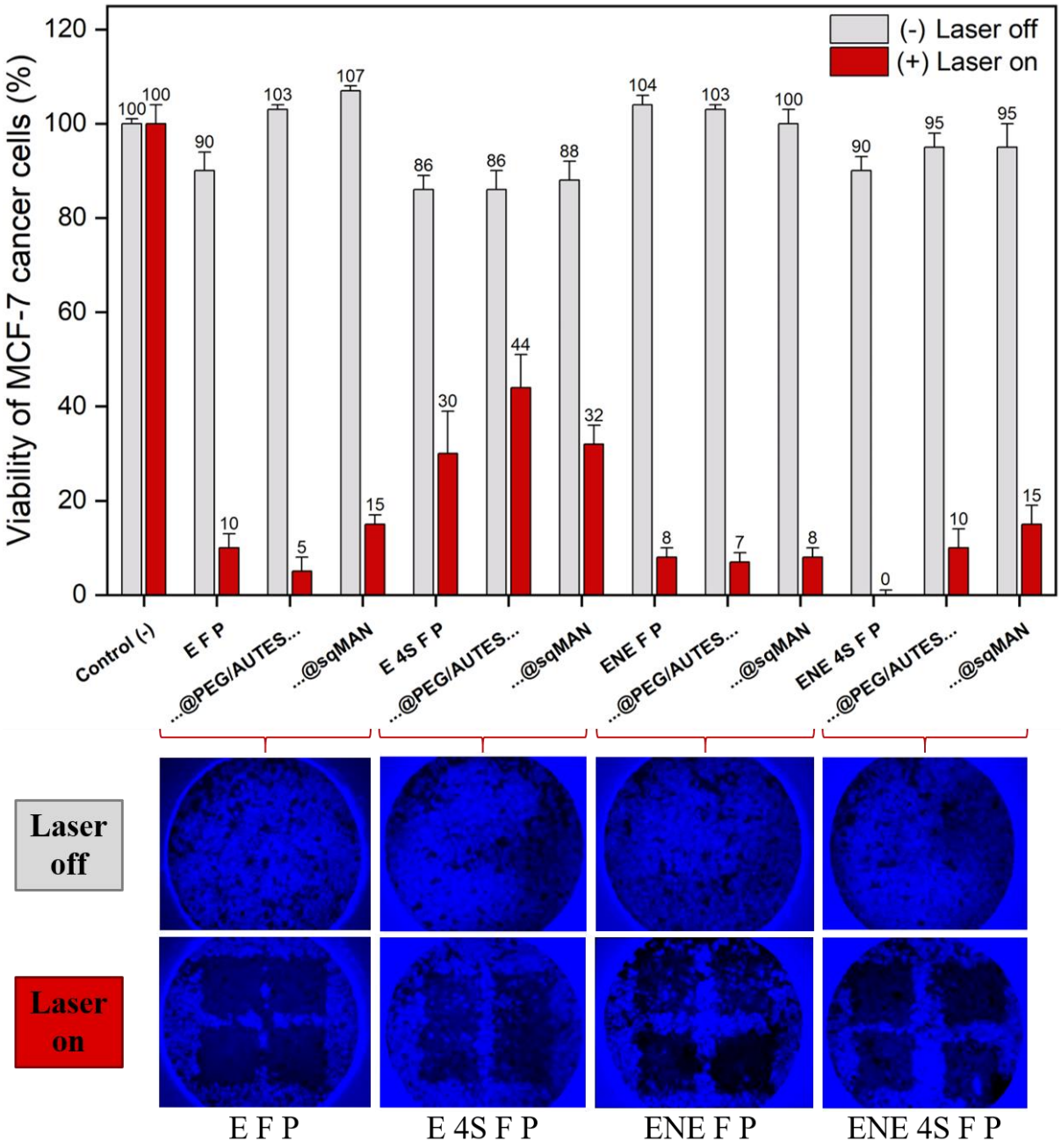

Figure 4: TPE-PDT studies of F P PMO NPs (either naked, functionalized with PEG and AUTES, or further grafted with sqMAN). TPE-triggered MCF-7 cancer cells killing after incubation with NPs at 50 µg mL^{-1} for 24 h and irradiation at 780 nm (3 x 1.26 s). Lines represent standard deviations of six or eight independent experiments. Images represent examples of wells (3.3 x 3.3 mm) used for living cell counting with MCF-7 nuclei staining by Blue Hoechst 33342™, either after no treatment (laser off) or after two-photon irradiation (laser on). Dark clusters correspond to nanoparticles aggregates.

In short, F P PMO NPs exhibited great two-photon photosensitizing capacity for anticancer PDT. To assess whether or not the surface functionalization of the materials could affect TPE-PDT efficacy *in vitro*, further TPE-PDT experiments would be suitable. For

instance, lower NPs doses could better evidence the contribution of sqMAN for cell targeting. In parallel to that, increasing mannoside grafting ratio could lead to enhanced endocytosis, thus improving therapeutic capability.

The high phototoxicity levels upon TPE-PDT suggest good FRET efficiency in biological conditions, from two-photon excited fluorophores to porphyrins. Research is ongoing to confirm the advantage of the FRET strategy for treating cancer cells with either F PMO NPs (theoretical negative control), F P PMO NPs or P PMO NPs, the latter being theoretically less efficient. ROS and $^1O_2$ generation assays using flow cytometry in a specific buffer might also be adequate to evidence materials difference in terms of photodynamic activity.

Next, after having experimented these different ways, we believe that *in vivo* studies should be performed with one or two samples among the best sqMAN-grafted NPs candidates.

2.2 *In vitro* antibacterial studies

During the last two decades, several epidemiological reports alerted of tremendous increases of bacterial resistance to all known classes of conventional antibiotics, especially in hospitals.[5] This is the reason why some alternative therapies in combination with new approaches for antibiotic design and delivery must be further explored to reach superior eradication levels with reduced acquired resistance issues. Among others, the antibacterial PDT (aPDT) using PS-based materials with high ROS generation efficiency, three-dimensional resolution and affinity to bacteria, appears as a good strategy. In our study, fluorophore-porphyrin PMO NPs were employed for both antibiotic delivery and TPE-aPDT, concluding on the potential of individual and combined therapy.

2.2.1 Vancomycin-based antibiotherapy

The antimicrobial activity of vancomycin hydrochloride (VAN) glycopeptide was assessed either under its free form or previously loaded in F P (B)PMO nanoparticles, and bacteria were cultured in Mueller-Hinton broth (MHB) rich environment for bacteria growth.

i. Bactericidal character of the free drug

First, the antibacterial activity of VAN was explored against *E. coli* K-12 LG1655 and *S. aureus* ATCC 43300™ in Mueller-Hinton broth (MHB). The minimum inhibitory concentration (MIC) of VAN is 47.5 ± 4.4 µg mL^{-1} against *E. coli* strain (**Figure 5a**). In

comparison, the MIC of VAN against tested *S. aureus* is significantly lower at 0.45 ± 0.04 µg mL^{-1} (**Figure 5b)**, in line with conventionally good antibacterial properties of vancomycin against gram-positive bacteria.

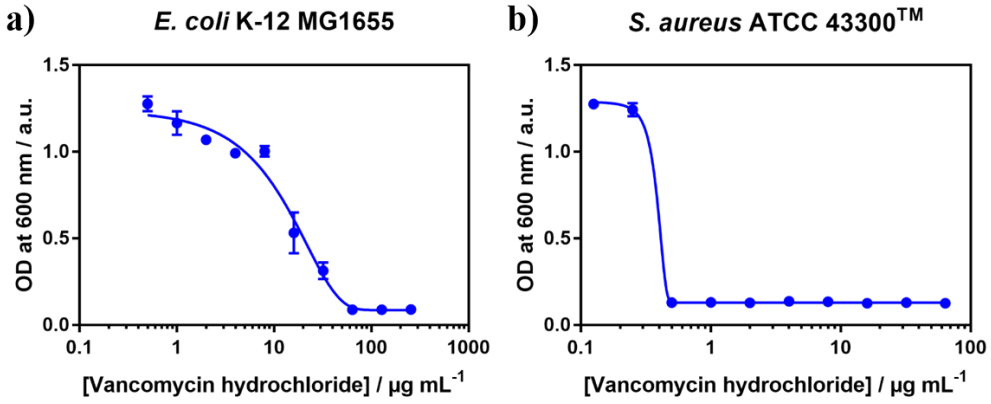

Figure 5: Growth evolution of (a) *E. coli* K-12 MG1655 and (b) *S. aureus* ATCC 43300™ for different concentrations of VAN. Optical density (OD) at 600 nm (dots); fitted Gompertz function (line).

One explanation of this large difference in inhibition capacity lies in VAN antibacterial mode of action. VAN inhibits cell-wall synthesis by binding to D-Ala-D-Ala termini of peptidoglycan moieties at the cell surface and cell division septa in gram-positive strains or in the periplasm of gram-negative ones.[6-7] As a result, the peptide is generally poorly effective against gram-negative bacteria as it cannot cross the outer membrane barrier.[8]

ii. Antibacterial activity from VAN-loaded NPs

To define the bactericidal character of VAN and VAN-loaded F P PMO NPs, the minimum inhibitory concentration (MIC) and minimum bactericidal concentration (MBC) were calculated. The MIC is an indicative value of the bacteriostatic activity and the MBC is an indicative value of the bactericidal activity of the antibiotic. The results summarized in **Table 2** show the superior MBC and MIC values when VAN is loaded in NPs.

Table 2: MIC *vs.* MBC values of VAN and VAN-loaded (B)PMO NPs tested against *E. coli* K-12 MG1655 and *S. aureus* ATCC 43300™. DLC: Drug Loading Content.

		E. coli K-12 MG1655		*S. aureus* ATCC 43300™	
Formulations	**DLC (%)**	**MIC (µg mL^{-1})**	**MBC (µg mL^{-1})**	**MIC (µg mL^{-1})**	**MBC (µg mL^{-1})**
VAN	/	47.5 ± 4.4	128	0.45 ± 0.04	2
VAN-loaded E F P	16.9	n.d.	> 256	4.10 ± 0.26	> 4
VAN-loaded E 4S F P	16.0	n.d.	256	0.98 ± 0.04	> 4
VAN-loaded ENE F P	15.7	n.d.	256	1.69 ± 0.20	4
VAN-loaded ENE 4S F P	15.1	n.d.	256	0.81 ± 0.18	> 4

After treatment with VAN or VAN-loaded PMO NPs, *E. coli* and *S. aureus* were counted. Control experiments were performed with PMO NPs without VAN and showed no significant bacterial decrease.

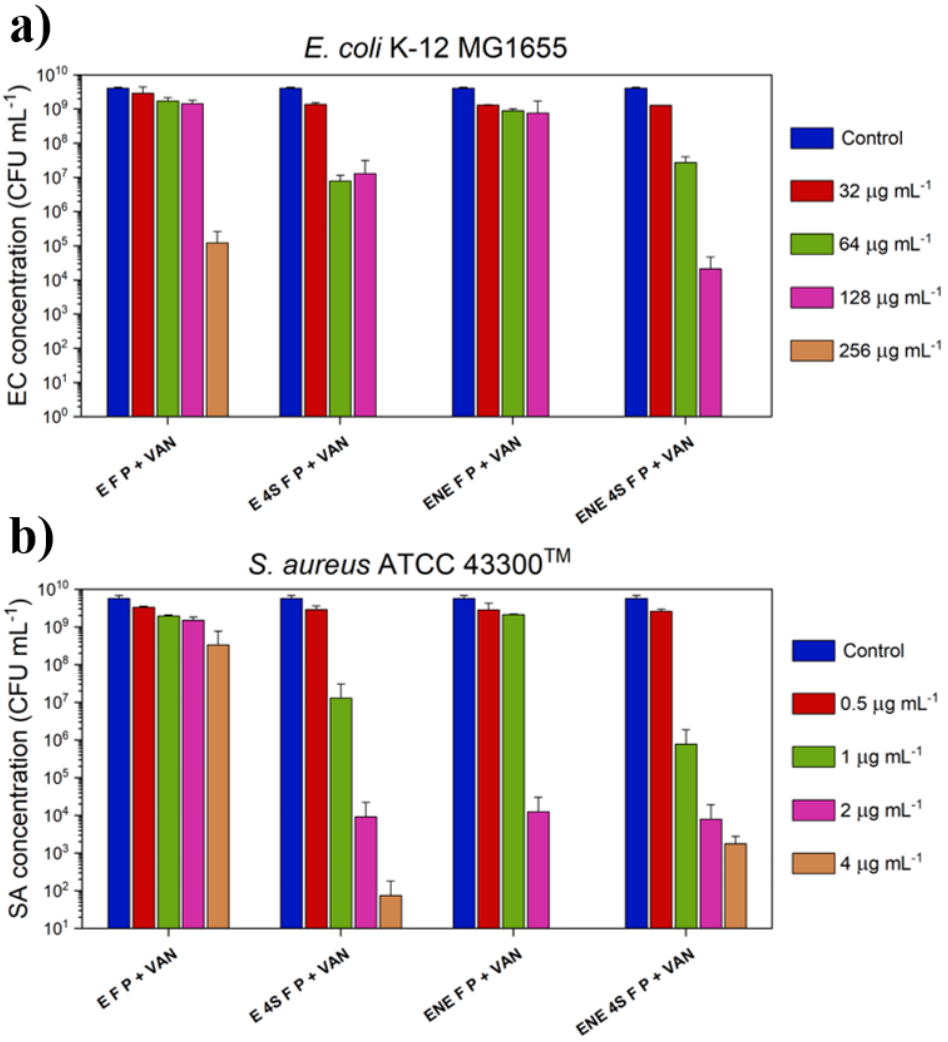

Figure 6: Bacterial viability after 24 h treatment with VAN-loaded PMO NPs against (a) *E. coli* K-12 MG1655 (EC) and (b) *S. aureus* ATCC 43300™ (SA). Survival rates were measured as colony forming units per milliliter (CFU mL^{-1}).

Total bacteria eradication using free VAN was obtained at a MBC of 128 µg mL^{-1} and 2 µg mL^{-1}, respectively for *E. coli* and *S. aureus* (**Table 2**). Treatments with VAN-loaded PMO NPs decreased bacteria growth in a dose-dependent manner. **Figure 6a** shows antibacterial activities on *E. coli*. When VAN-loaded PMO NPs were incubated at a concentration of 256 µg mL^{-1} in VAN, a 4.5-log reduction in colony forming unit per milliliter (CFU mL^{-1}) was measured for E F P NPs, while this same concentration was fond to be the MBC in the case of E 4S F P, ENE F P and ENE 4S F P samples, causing total bacteria eradication. 4S-type PMO NPs are more active than PMO NPs without tetrasulfide structure with already 2 to 3-log reduction at 64 µg mL^{-1}. This efficiency can be associated to GSH-triggered S-S-S-S breaking

by reduction reaction which contributes to nanoparticle fragmentation and facilitates drug liberation.

In **Figure 6b**, antibacterial activities on *S. aureus* were observed while VAN-loaded PMO NPs were incubated at a concentration of 4 µg mL^{-1} in VAN with a 1.2-log, 7.9-log and 6.4-log reduction in CFU mL^{-1} for E F P, E 4S F P and ENE 4S F P, respectively; while total eradication was observed for ENE F P (**Figure 7**). Again, antibacterial activities of ENE 4S F P and E F P BPMO NPs are similar and seem more active than PMO NPs without tetrasulfide bridges in their structure. These results are in line with calculated MIC values (**Table 2**).

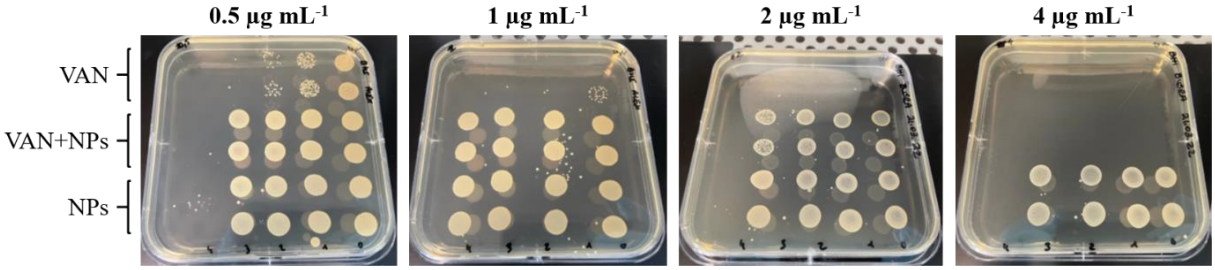

Figure 7: Photographs of *S. aureus* ATCC 43300™ colonies survival in the presence of different concentrations in ENE F P PMO NPs (3.2 to 25.5 µg mL^{-1}) and vancomycin hydrochloride (0.5 to 4 µg mL^{-1}, relatively to DLCs).

As a conclusion, the assessment of bacterial viability suggested that part of loaded VAN is released from the different NPs, with a tendency for higher drug release in the case of biodegradable PMO NPs containing tetrasulfide bridges. Nonetheless, the antibacterial activity of tested VAN-loaded NPs seems limited by drug release and this individual therapy is certainly not strong enough to meet current exigency. Hence, aPDT was performed on F P PMO NPs and VAN-loaded F P PMO NPs.

2.2.2 Antibacterial photodynamic therapy

After antibiotherapy experiments on *E. coli* and *S. aureus* colonies, two-photon excitation aPDT assays were performed in PBS medium at 780 nm and 10 min after incubation with F P PMO NPs (either functionalized or not) or VAN-loaded F P PMO NPs at 200 µg mL^{-1}. No significant toxicity was visible below this concentration. Dark incubations with or without NPs were used as negative controls.

i. Efficiency in two-photon excitation PDT

Before testing all NPs, preliminary optimization of the TPE-aPDT experiments was achieved on one sample (ENE 4S F P) and one strain (*E. coli*). Firstly, the unfocused light beam

was applied on each well for 90 s with varying laser power value, from 0.75 to 1.77 W (**Figure 8a**). High bactericidal activity was observed down to 1.50 W, an activity loss was observed at 1.25 W and below. Then, we tried to extend the laser irradiation time when fixing the laser power value at 1W, but no significant enhancement was observed up to 120 s (**Figure 8b**). Next, switching to 1.50 W, shorter irradiation times did not show a bactericidal effect like in the case of 90 s excitation, with a loss of activity for 60 s or below (**Figure 8c**). It is worth mentioning that in all experiments, no toxicity was observed in the absence of light (control laser off + NPs), demonstrating the biocompatibility of the NPs in these conditions.

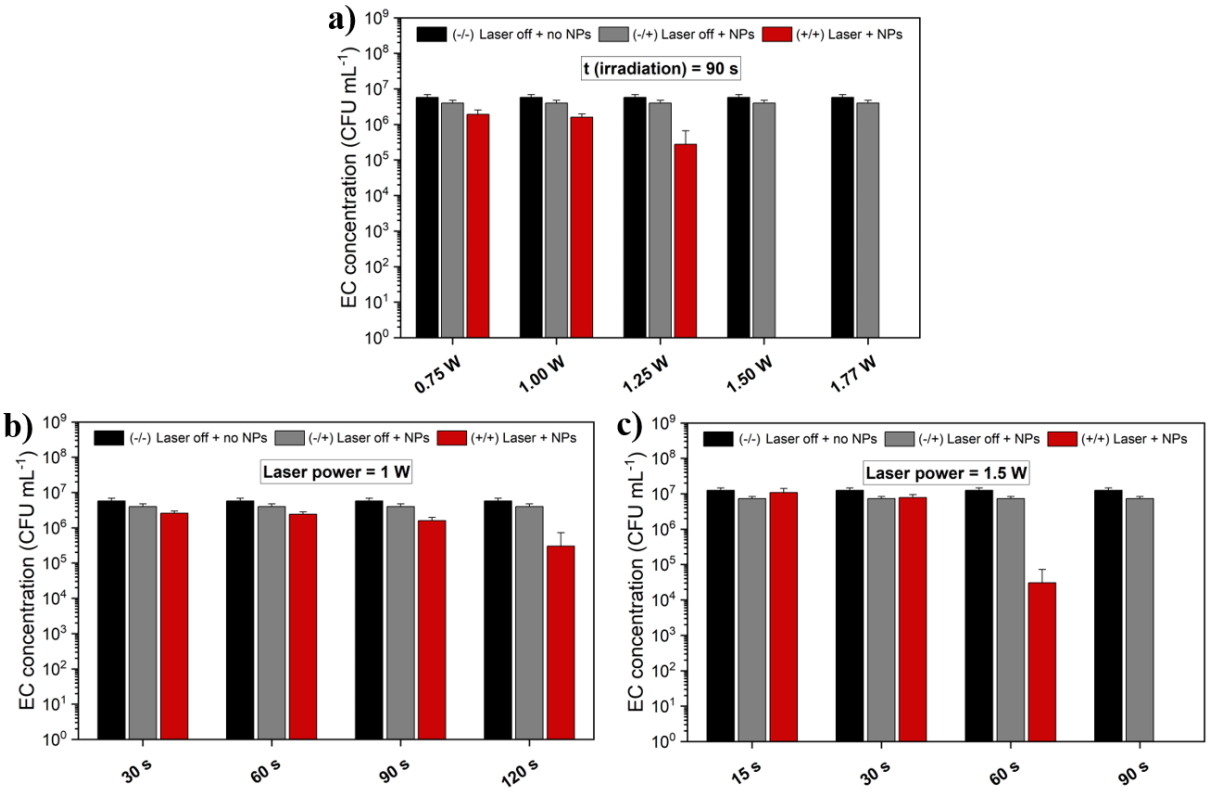

Figure 8: Optimization of antibacterial TPE-PDT experimental conditions against *E. coli* K-12 MG1655 (EC) using ENE 4S F P PMO NPs. A 780 nm unfocused laser beam was applied with either varying (a) laser power value (irradiation time = 90 s), (b) irradiation time (decreased laser power = 1.00 W), or (c) irradiation time (increased laser power = 1.50 W). Survival was measured 6 h after irradiation by plate counting method.

Following these preliminary assays, a laser power value of 1.77 W (maximum of the laser) and an exposure time of 90 s were chosen to ensure efficient treatment, representing about 20 J cm^{-2}.

The different F P PMO NPs were thus incubated with *E. coli* K-12 MG1655 at an initial concentration of either 10^7 or 10^8 CFU mL^{-1} and their efficiency upon TPE-PDT was assessed. As revealed by the control experiments, laser irradiation without NPs did not cause damages to the bacteria colonies (**Figures 9 and 10**).

Ethylene-tetrasulfide nanoparticles showed full eradication of *E. coli* colonies, independently of VAN loading or surface grafting (**Figure 9b**). In contrast, TPE-aPDT with ethylene-based nanoparticles revealed some influence of functionalization. For a bacteria concentration of 10^7 CFU mL^{-1} *ab initio*, a 2.2-log and 1.7-log reduction in CFU mL^{-1} were respectively observed for naked E F P and VAN-loaded E F P PMO NPs, while functionalized NPs caused the full death of *E. coli* populations. Starting with higher bacteria concentration, a similar behavior was observed, with a 2.3-log, 2.4-log and 3.2-log reduction in CFU mL^{-1} for naked, VAN-loaded and (PEG/AUTES)-grafted E F P PMO NPs, respectively (**Figure 9a**). Using E F P PMO@PEG/AUTES nanoparticles grafted with sqMAN led to total eradication. Addition of sqMAN having the capacity to specifically anchor onto *E. coli* FimH lectins is also assumed to mediate bacterial adhesion to host cells by inhibiting their interaction.[9-10] Thus, the aPDT efficiency was certainly enhanced by the targeting property of the systems improving ROS diffusion in the close environment of bacteria, and it is supposed that sqMAN grafts operated as inhibitors for type 1 fimbriae-mediated bacterial adhesion.

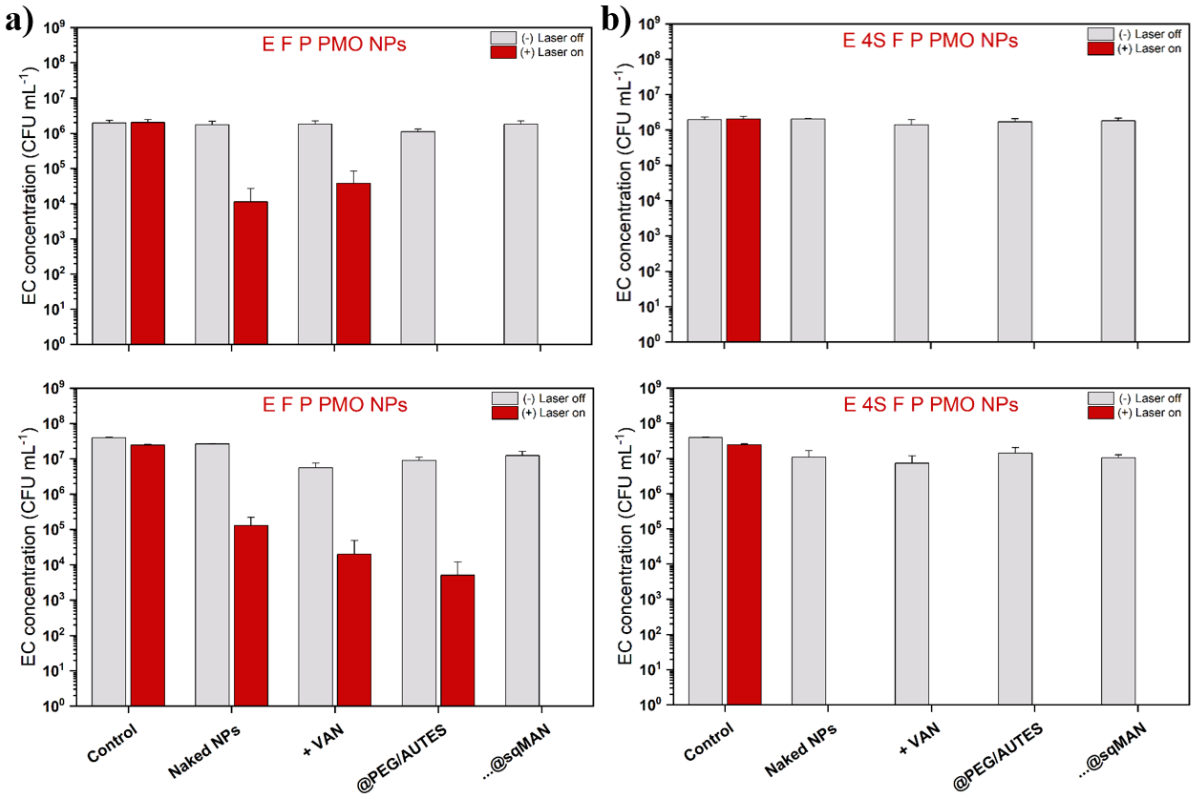

Figure 9: TPE-aPDT activity against *E. coli* K-12 MG1655 (EC) using (a) E F P or (b) E 4S F P PMO NPs at an initial bacteria concentration of 10^7 CFU mL^{-1} (top) or 10^8 CFU mL^{-1} (bottom). A 780 nm unfocused laser beam was applied for 90 s at 1.77 W and survival was measured 6 h after irradiation by plate counting method. For every F P PMO family, either naked, VAN-loaded, (PEG/AUTES)-grafted or (PEG/AUTES@sqMAN)-grafted NPs were tested.

TPE-PDT assays were also performed with ethenylene-based nanoparticles on *E. coli* colonies (**Figure 10**). All ENE F P and ENE 4S F P samples induced full eradication for both concentrations in bacteria. Moreover, slight antibacterial effects from 0.3 to 1.3-log reduction in CFU mL^{-1} were visible in dark conditions with naked NPs loaded with about 15% DLC in VAN, while unloaded NPs showed no toxicity.

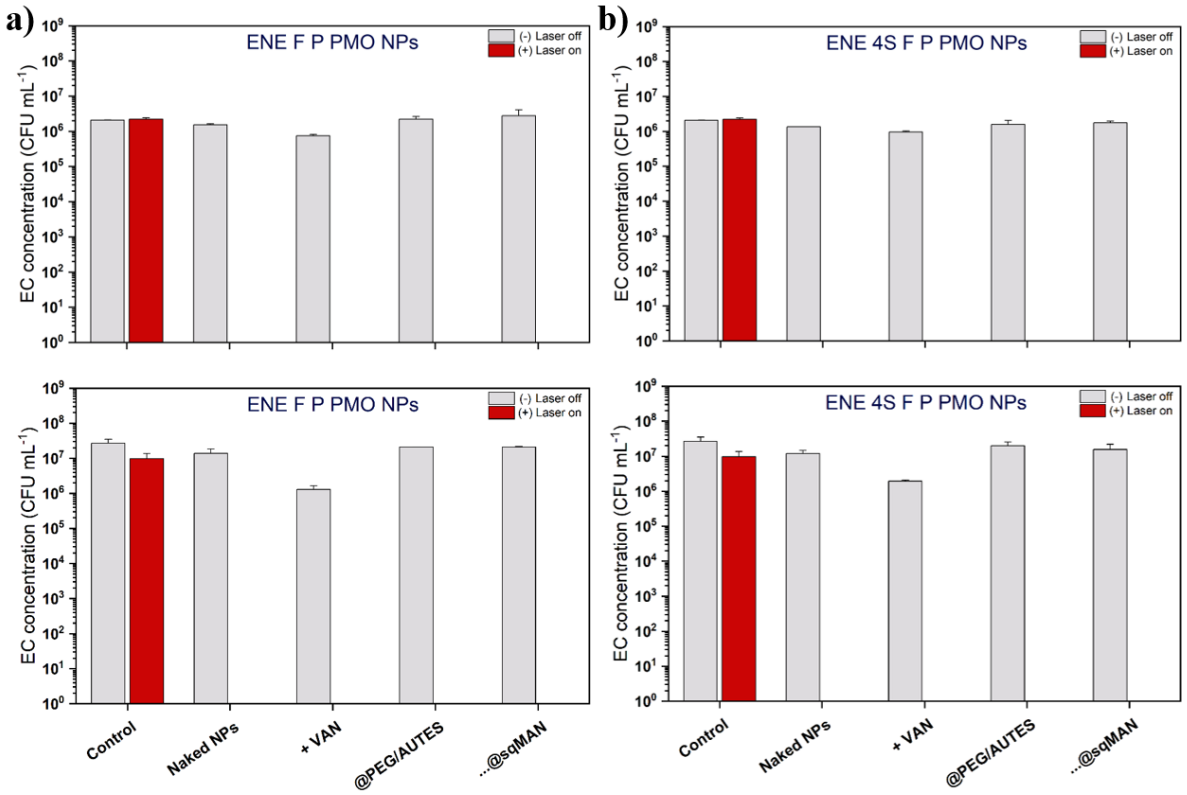

Figure 10: TPE-aPDT activity against *E. coli* K-12 MG1655 (EC) using (a) ENE F P or (b) ENE 4S F P PMO NPs at an initial bacteria concentration of 10^7 CFU mL^{-1} (top) or 10^8 CFU mL^{-1} (bottom). A 780 nm unfocused laser beam was applied for 90 s at 1.77 W and survival was measured 6 h after irradiation by plate counting method. For every F P PMO family, either naked, VAN-loaded, (PEG/AUTES)-grafted or (PEG/AUTES@sqMAN)-grafted NPs were tested.

Regarding combination therapy, the reduced synergy of VAN with aPDT can be attributed to aPDT conditions (i.e. 200 µg mL^{-1} in NPs) where the maximum released concentration of VAN would be around 30 µg mL^{-1} (DLC ≈ 15-17%), which is an insufficient amount to guarantee VAN contribution.

Thus, those results are in line with VAN antibacterial mode of action described in the literature, which is an inhibitory effect against bacteria growth and not a direct killing activity. Indeed, even if vancomycin was used in clinic against gram-positive bacteria, its action is limited on gram-negative bacteria like *E. coli* as it cannot penetrate the outer membrane.[11] This suggests the need for very high DLC to potentially observe synergistic VAN antibiotherapy and aPDT. Other possibilities to explore would be the conjugation of biomolecules to enhance VAN

permeability and the use of other antibiotics with a different mode of action and lowered MIC and MBC values, allowing better synergy with aPDT.[12-13]

ii. *In vitro* FRET demonstration

A first study to assess FRET contribution to TPE-PDT efficiency was performed on EC strain with ENE-4S based NPs (**Figure 11**).

As expected, the sample with only energy donor moieties (ENE 4S F) showed no toxicity upon illumination. ENE 4S P NPs caused an intermediate antibacterial activity with a 4.1-log reduction, while ENE 4S F P sample achieved complete eradication of EC colony. This result is suggesting FRET-enhanced antibacterial TPE-PDT. Some research is ongoing to assess the capacity of other (B)PMO NPs and further work is envisaged to measure ROS generation of acceptor and donor-acceptor structures.

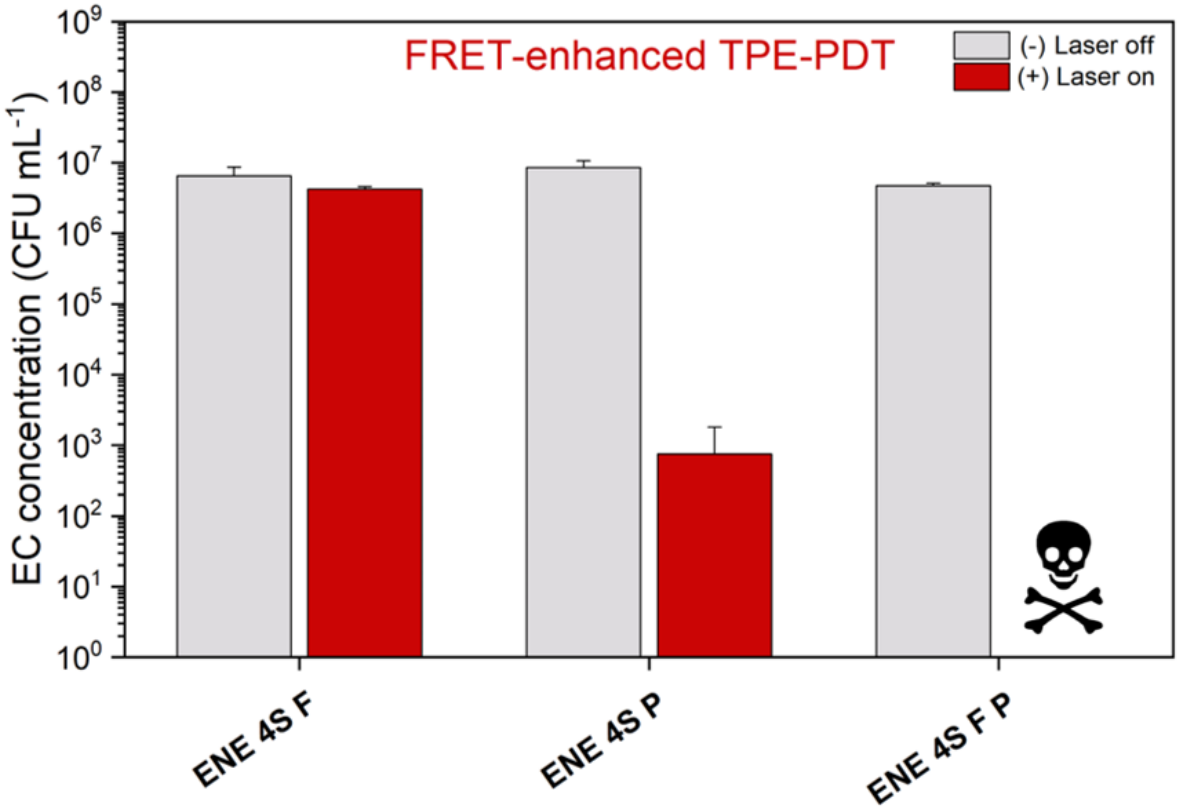

Figure 11: FRET study upon TPE-aPDT against *E. coli* K-12 MG1655 (EC) using ENE 4S F, ENE 4S P or ENE 4S F P BPMO NPs at an initial bacteria concentration of 10^8 CFU mL^{-1}. A 780 nm unfocused laser beam was applied for 90 s at 1.50 W and survival was measured 6 h after irradiation by plate counting method. Only naked NPs were tested.

3. Conclusions and perspectives

To summarize, multifunctional F P PMO NPs were tested *in vitro* and demonstrated high efficiency upon TPE-PDT.

In a first part, fluorophore-based PMO nanoparticles demonstrated effective internalization in MCF-7 breast cancer cells without the need for fluorescence staining. A one-photon excitation treatment with fluorophore-porphyrin organosilica-based nanoparticles caused limited cancer cell death, especially in the case of 4S-based NPs where ROS diffusion could be quenched. As an exception, ethylene-based NPs grafted with sqMAN α-D-mannoside induced high reduction of cancer cells viability, and this effect was in good correlation with the superior uptake of the NPs revealed by confocal imaging.

The changeover to two-photon irradiation dramatically increased the therapeutic potential of the systems *in vitro*, with 80 to 100% reduction in cell viability for E, ENE and ENE 4S-based NPs, either functionalized or naked. For these anticancer studies, next work will consist of studying FRET contribution *in vitro*. Moreover, after optimization of sqMAN-grafting ratio and selection of the best candidate, *in vivo* studies on tumor-bearing zebrafish embryos will be performed to assess the intrinsic cytotoxicity and potential for tumor growth reduction by TPE-PDT.

In a second part, antibacterial assays in MHB revealed the influence of tetrasulfide bridges reduction to better release vancomycin hydrochloride antibiotic. In such glutathione-rich environment, lower minimum inhibitory concentrations were measured against the tested gram-positive *S. aureus* and gram-negative *E. coli* strains.

Antibacterial PDT assays using two-photon excitation demonstrated total eradication of *E. coli* colonies and suggested higher affinity in the presence of sqMAN onto the surface of the NPs. The contribution of FRET was also suggested *in vitro* by TPE-aPDT assay where higher killing efficiency was observed for ENE 4S F P BPMO NPs compared to ENE 4S P BPMO NPs.

The high antibacterial activity of the photodynamic treatment did not allow assessing correctly the synergy with VAN antibiotic release. Thus, further assays are required to conclude on this aspect. Moreover, it would be interesting to test other antibiotics alone or in synergy with two-photon responsive porous organosilica NPs.

Next, ongoing research is focused on TPE-PDT against *S. aureus*. In the long-term perspective, *in vitro* antibacterial studies of biofilm models trying to mimic *in* vivo infection environment should be performed. Indeed, biofilms are considerably more resistant than planktonic bacteria. Furthermore, 65% microbial infections and 80% chronic infections are currently related to biofilm formation, thus, it is a major threat to deal with.[14] Finally, we expect to test our materials as wound healing dressings assisted by TPE-PDT to provide antibacterial activity, tissue repair and eventually help stimulating the immune system on mice models after making voluntarily an excisional wound or provoking a specific skin lesion.[15-16]

4. Experimental section

Part 1: *In vitro* anticancer studies

Materials

Unless otherwise specified, ACS reagent grade starting materials and solvents were used as received from commercial suppliers without further purification.

Deionized water (resistivity = 18.2 MΩ cm) obtained from an Aquadem™ system (Veolia Water Technologies, Saint-Maurice, France) was used in all experiments. 1,2-Bis(triethoxysilyl)ethane (E, 96%), bis[3-(triethoxysilyl)propyl]tetrasulfide (4S, ≥ 90%), cetyltrimethylammonium bromide (CTAB, > 98%), sodium hydroxide pellets (NaOH, ≥ 98%) and ammonium nitrate (NH_4NO_3, > 98%) were purchased from Merck (Saint-Quentin-Fallavier, France). Ammonia (28%), absolute ethanol (EtOH) and ethanol (96%) were obtained from Carlo Erba Reagents (Cornaredo, MI, Italy). Cell Mask™ Orange Plasma Membrane was obtained from Invitrogen (Cergy-Pontoise, France). Glass bottom 8-well tissue culture chambers were purchased from Sarstedt (Marnay, France).

Synthesis of E 4S F BPMO NPs (from chapter 4)

A mixture of CTAB (250 mg, 0.69 mmol), ultrapure water (65 mL), and sodium hydroxide (NaOH (2 M), 437 µL) was stirred at 80 °C for 50 min at 750 rpm in a 250 mL round bottom flask. Then, a mixture of 1,2-bis(triethoxysilyl)ethane, bis[3-(triethoxysilyl)propyl]tetrasulfide (E:4S, 80:20 (n:n), total 0.90 mmol) and silylated fluorophore (F-Si, 7.5 mg, 4.5 µmol) in 1 mL of absolute ethanol was introduced in the reaction. The condensation process was conducted for 2 h. Then, the solution was cooled to room temperature while stirring; fractions were gathered in propylene tubes and collected by centrifugation for 20 min at 20k rpm. Subsequently, the still surfactant-filled particles were solvent-extracted three times with ammonium nitrate solution (20 g L^{-1} ethanol) in order to remove the CTAB template, and washed three times with ethanol, water and ethanol. Each extraction and washing involved 20 min sonication at 40 °C and centrifugation for 15 min at 20k rpm. The nanoparticles were finally redispersed in ethanol and dried for a few hours under vacuum at room temperature.

Synthesis of E 4S F-2 BPMO NPs

A mixture of CTAB (250 mg, 0.69 mmol), ultrapure water (120 mL), and sodium hydroxide (NaOH (2 M), 875 µL) was stirred at 80 °C for 50 min at 750 rpm in a 250 mL round bottom flask. Then, a mixture of 1,2-bis(triethoxysilyl)ethane (E, 267 µL, 0.72 mmol), bis[3-(triethoxysilyl)propyl]tetrasulfide (4S, 89.8 µL, 0.18 mmol) and silylated fluorophore (F-Si, 7.5 mg, 4.5 µmol) in 1 mL absolute ethanol was introduced in the reaction. The condensation process was conducted for 2 h. Then, the solution was cooled to room temperature while stirring. NPs were extracted and washed according to the previously described protocol.

Synthesis of E 4S F-3 BPMO NPs

A mixture of CTAB (242 mg, 0.66 mmol), ultrapure water (45 mL), absolute ethanol (15.5 mL) and ammonia (NH_4OH (2 M), 305 µL) was stirred at room temperature for one hour at 750 rpm in a 250 mL round bottom flask. Then, a mixture of 1,2-bis(triethoxysilyl)ethane (E, 695.3 µL, 1.88 mmol), bis[3-(triethoxysilyl)propyl]tetrasulfide (4S, 89.8 µL, 0.18 mmol) and silylated fluorophore (F-Si, 19.5 mg, 11.8 µmol) in 2 mL absolute ethanol was introduced in the reaction. The condensation process was conducted for 72 h in the dark. NPs were extracted and washed according to the previously described protocol.

Cell line

Human breast adenocarcinoma cell line (MCF-7) was maintained in Dulbecco's Modified Eagle's Medium (DMEM/F12) supplemented with 10% fetal bovine serum (FBS) and 1% penicillin/streptomycin. Cells were allowed to grow in humidified atmosphere at 37°C under 5% CO_2.

Cell internalization study using confocal microscopy

MCF-7 cells were seeded in glass bottom 8-well tissue culture chambers. Twenty-four hours after seeding, cells were treated with 50 µg mL^{-1} of F PMO NPs or F P PMO NPs for 24 h. Untreated cells were considered as a control. Fifteen minutes before the end of incubation, cells were treated with CellMask™ Orange Plasma membrane Stain (Invitrogen, USA) at a final concentration of 5 µg mL^{-1}. Cells were washed two times with culture medium before observation with confocal fluorescence microscope LSM780 (Carl Zeiss, France) at 820 nm and 780 nm, respectively for F PMO NPs and F P PMO NPs (TPEF), and 561 nm for

CellMask™ Orange Plasma membrane stain, using a high magnification (63x/1.4 OIL Plan-Apo).

One-photon excitation photodynamic therapy

MCF-7 cells were seeded in 96-well plates at a density of 3000 cells per well. Cells were allowed to grow for 24 h, and then treated with nanoparticles at 50 µg mL^{-1} for 24 h. Non-treated cells were considered as a control. After incubation, cells were exposed (or not) to green light irradiation at 525 nm for 10 min duration (34 J cm^{-2}). The light beam was focused by a microscope objective lens (4×/0.10). Two days after irradiation, the percentage of cell viability was assessed using MTT assay.

Two-photon excitation photodynamic therapy

MCF-7 cells were seeded in glass bottom 384-well plates and allow to grow for 24 h. Then, cells were incubated with or without 50 µg mL^{-1} of nanoparticles for 24 h. Non-treated cells were considered as a control. After incubation with NPs, cells were maintained in fresh culture medium, and then submitted (or not) to TPE with the LSM980 NLO microscope (Carl Zeiss Microscope). Half of the well was irradiated at 780 nm by three scans of 1.26 s duration in four different areas of the well with a focused laser at a maximum laser power. The laser beam was focused by a microscope objective lens (Carl Zeiss 10×/0.3 EC Plan-Neofluar). The scan size does not allow irradiating more areas without overlapping.

Wells were then incubated for 48 h. Fifteen minutes before the end of incubation, cells were treated with Hoechst 33342™ at a final concentration of 2.5 µg mL^{-1} for a nuclear labelling of living cells. Observation with fluorescence microscope Evos™ M5000 Imaging System (Thermo Fisher Scientific, France) equipped with DAPI filter using 4X magnification gave values for living cells quantification after processing a counting method. This method can be reproduced on all images of a batch in an identical way and served to count the nuclei and to establish a percentage of cell viability according to the following equation:

$$\frac{Number\ of\ nuclei\ in\ the\ well}{Number\ of\ nuclei\ in\ the\ control\ well} \times 100,$$

then, the viability was corrected according to the following formula:

(non irradiated viability – 2 × (non-irradiated viability – irradiated viability)).

Data are mean values standard deviation from six or eight independent experiments (three or four wells by two counting methods on Evos™ M5000).

Part 2: *In vitro* antibacterial studies

Materials

Unless otherwise specified, ACS reagent grade starting materials and solvents were used as received from commercial suppliers without further purification.

ASTM type I ultrapure water (resistivity = 18.2 MΩ.cm) from an Arium® Comfort I water purification system (Sartorius, Dourdan, France) was used in all bacteriological experiments. Phosphate buffer solution (PBS, 1x, 100 mM, pH 7.4) and vancomycin hydrochloride (VAN, ref. 94747, ≥ 85%) were purchased from Merck (Saint-Quentin-Fallavier, France).

The different F P PMO NPs and VAN-loaded F P PMO NPs were prepared according to chapter 4 protocols. Antibiotic drug loading contents (DLCs) in water were determined by UV-visible absorption spectroscopy with a Jasco V-770 spectrophotometer (Mary's Court Easton, MD, USA) using quartz cells of 1 cm path length.

Bacteria strains

Escherichia coli strain K-12 MG1655 (*E. coli* (EC), gram-negative) and *Staphylococcus aureus* strain ATCC 43300™ (*S. aureus* (SA), gram-positive) were used. To prepare the inoculum, -80 °C glycerol stocks were streaked out on Luria-Bertani (LB) and Brain Heart Infusion (BHI) agar plates (Becton Dickinson France SAS Difco™, France), respectively. *E. coli* and *S. aureus* were grown on nutrient agar for 24 h. Bacteria were cultured in Mueller–Hinton broth (MHB) (Becton Dickinson France SAS Difco™, France) under aerobic conditions at 35 °C and 200 rpm to reach exponential growth phase (OD_{600} = 0.5-1) in an orbital shaker incubator (211DS Laboratory incubator, Labnet). The concentrations were routinely estimated by spectrophotometric turbidity measurement at 600 nm on a spectrophotometer (GeneQuant Pro, Amersham Biosciences®) and by colony-forming unit (CFU) counts on LB or BHI agar plates.

Determination of minimum inhibition concentration (MIC)

MICs were determined in alignment with CLSI guidelines. The bacterial pre-cultures were diluted in MHB broth (10^6 CFU mL^{-1}). To perform the minimum inhibition concentration (MIC) assays, 50 µL of different concentrations of vancomycin, nanoparticles (NPs) alone and vancomycin-loaded NPs were prepared by serial dilution in MHB into 96-well microplates. 50

µL of the bacterial suspension was then added into wells, resulting in 5×10^5 CFU mL^{-1}. The as-prepared bacterial suspensions were incubated at 35 °C with shaking (300 rpm) for 24 h in a VICTOR® Nivo™ Plate Reader (Perkin Elmer, France). The optical density (OD_{600}) was determined every hour. The lowest concentration (highest dilution) required to stop the bacterial growth was determined as the MIC value. MIC values (Mean ± standard deviation, n = 3) were calculated with nonlinear regression method published by Lambert and Pearson[17] using GraphPad Prism (7.05) software.

Determination of minimum biocidal concentration (MBC)

The minimum bactericidal concentration (MBC) was obtained after the MIC determination of VAN, NPs alone and VAN-loaded NPs aliquots from the wells which showed no visible bacterial growth when seeded on LB or BHI agar plates and incubated for 24 h at 35 °C. When the bacterial population is killed (absence of bacteria) at the lowest concentration, it is termed as MBC endpoint.

Two-photon excitation-photodynamic therapy (TPE-PDT)

Two-photon excitation-photodynamic therapy (TPE-PDT) was performed on bacterial solutions in sterile 384-well glass bottom black plates #1.5H from IBL (Gerasdorf, Austria). Wells size was 3.3 x 3.3 mm. To perform *in vitro* TPE-PDT assays, 20 µL of different concentrations of VAN, NPs alone and VAN-loaded NPs diluted in PBS (1x, pH 7.4) were added to 20 µL of the bacterial suspension in PBS (1x, pH 7.4), resulting in 1.0 $x10^7$ or 1.0 x 10^8 CFU mL^{-1}, and incubated for 10 min at room temperature. Wells were irradiated at 780 nm using Chameleon Discovery NX – tunable femtosecond laser (Coherent) operating at 80 MHz without focalization during 90 s at the maximum power (Spot size $1/e^2$ diameter = 2 mm, polarization = 24°, laser input power = 1.77 W). Then, survival rates were determined after 6 h incubation at 35 °C by plate counting method.

Bibliography

1. Mezghrani, B.; Ali, L. M. A.; Richeter, S.; Durand, J.-O.; Hesemann, P.; Bettache, N., Periodic Mesoporous Ionosilica Nanoparticles for Green Light Photodynamic Therapy and Photochemical Internalization of siRNA. *ACS Applied Materials & Interfaces* **2021,** *13* (25), 29325-29339.

2. Aggad, D.; Mauriello Jimenez, C.; Dib, S.; Croissant, J. G.; Lichon, L.; Laurencin, D., et al., Gemcitabine Delivery and Photodynamic Therapy in Cancer Cells *via* Porphyrin-Ethylene-Based Periodic Mesoporous Organosilica Nanoparticles. *ChemNanoMat* **2018,** *4* (1), 46-51.

3. Huang, C.-W.; Yuan Chiu, K.; Cheng, S.-H., Novel spectral and electrochemical characteristics of triphenylamine-bound zinc porphyrins and their intramolecular energy and electron transfer. *Dalton Transactions* **2005,** (14), 2417.

4. Clennan, E. L.; Wang, D.; Clifton, C.; Chen, M. F., Geometry-Dependent Quenching of Singlet Oxygen by Dialkyl Disulfides. *Journal of the American Chemical Society* **1997,** *119* (38), 9081-9082.

5. Maisch, T.; Hackbarth, S.; Regensburger, J.; Felgenträger, A.; Bäumler, W.; Landthaler, M., et al., Photodynamic inactivation of multi-resistant bacteria (PIB) - a new approach to treat superficial infections in the 21st century. *Journal der Deutschen Dermatologischen Gesellschaft = Journal of the German Society of Dermatology : JDDG* **2011,** *9* (5), 360-6.

6. Walsh, C. T.; Fisher, S. L.; Park, I. S.; Prahalad, M.; Wu, Z., Bacterial resistance to vancomycin: five genes and one missing hydrogen bond tell the story. *Chemistry & Biology* **1996,** *3* (1), 21-8.

7. Reynolds, P. E., Structure, biochemistry and mechanism of action of glycopeptide antibiotics. *European journal of clinical microbiology & infectious diseases : official publication of the European Society of Clinical Microbiology* **1989,** *8* (11), 943-50.

8. Nikaido, H., Outer membrane barrier as a mechanism of antimicrobial resistance. *Antimicrobial agents and chemotherapy* **1989,** *33* (11), 1831-6.

9. Berglund, J.; Knight, S. D. In *Structural Basis for Bacterial Adhesion in the Urinary Tract*, Glycobiology and Medicine, Boston, MA, 2003; Axford, J. S., Ed. Springer US: Boston, MA, 2003; pp 33-52.

10. Bavington, C.; Page, C., Stopping bacterial adhesion: a novel approach to treating infections. *Respiration; international review of thoracic diseases* **2005,** *72* (4), 335-44.

11. Levine, D. P., Vancomycin: a history. *Clinical Infectious Diseases* **2006,** *42*, S5-S12.

12. Antonoplis, A.; Zang, X.; Wegner, T.; Wender, P. A.; Cegelski, L., Vancomycin–Arginine Conjugate Inhibits Growth of Carbapenem-Resistant *E. coli* and Targets Cell-Wall Synthesis. *ACS Chemical Biology* **2019,** *14* (9), 2065-2070.

13. Meretoudi, A.; Banti, C. N.; Siafarika, P.; Kalampounias, A. G.; Hadjikakou, S. K., Tetracycline Water Soluble Formulations with Enhanced Antimicrobial Activity. *Antibiotics* **2020,** *9* (12), 845.

14. Jamal, M.; Ahmad, W.; Andleeb, S.; Jalil, F.; Imran, M.; Nawaz, M. A., et al., Bacterial biofilm and associated infections. *Journal of the Chinese Medical Association* **2018,** *81* (1), 7-11.

15. Li, L.; Yang, Y.; Yang, Z.; Zheng, M.; Luo, G.; He, W., et al., Effects of ALA-PDT on the macrophages in wound healing and its related mechanisms in vivo and in vitro. *Photodiagnosis and Photodynamic Therapy* **2022,** *38*, 102816.

16. Oyama, J.; Fernandes Herculano Ramos-Milaré, Á. C.; Lopes Lera-Nonose, D. S. S.; Nesi-Reis, V.; Galhardo Demarchi, I.; Alessi Aristides, S. M., et al., Photodynamic therapy in wound healing in vivo: a systematic review. *Photodiagnosis and Photodynamic Therapy* **2020,** *30*, 101682.

17. Lambert, R. J.; Pearson, J., Susceptibility testing: accurate and reproducible minimum inhibitory concentration (MIC) and non-inhibitory concentration (NIC) values. *Journal of Applied Microbiology* **2000,** *88* (5), 784-90.

GENERAL CONCLUSIONS AND OUTLOOKS

The constant need of more efficient theranostics impels to give birth to advanced technologies. In particular, nanomaterials have shown their efficiency in many bioapplications and nanomedicine.

In this project, we focused on mesoporous organosilica nanoparticles, which already proved to be biocompatible in several biological studies, including the preclinical stage. With their versatile internal framework, external surface and pore features, multifunctional nanosystems can be readily designed for virtually any application. Among emerging treatments, photodynamic therapy proved its efficacy against solid and superficial tumors. Switching from one-photon laser excitation to two-photon excitation allows for deeper penetration into tissues and a larger scope of action of this non-invasive technique. Thus, a summary of the main characteristics of the different synthesized nanoparticles is presented in **Table 1**.

Table 1: Characteristics of the synthesized nanoparticles having the greatest potential.

NP Sample	Main Results
ND@ENE PMO @PEG/AUTES	➢ $d_{NP} \approx 140 \pm 80$ nm, reduced size polydispersity via ultrasonication; ➢ On MDA-MB-231 breast cancer cells: biocompatibility, good endocytosis, intrinsic fluorescence and intermediate cell killing efficiency under TPE (46% with FND100 and 36% with DND30).
E (or ENE) F P PMO (@PEG/AUTES) (@sqMAN)	➢ $d_{NP} \approx 150 \pm 60$ nm; ➢ Efficiency for FRET from F to P, enhancing ROS generation by P; ➢ DLC (vancomycin hydrochloride) ≈ 16%, with good release capacity on gram-positive *S. aureus* and gram-negative *E. coli* strains; ➢ Complete eradication of gram-negative *E. coli* by TPE-PDT and impact of mannoside grafting (targeting and/or growth inhibition).
a) Non 4S-based	➢ On MCF-7 breast cancer cells: biocompatibility, intermediate cell killing efficiency by OPE-PDT and high cell killing efficiency by TPE-PDT.
b) 4S-based	➢ Controlled biodegradability by redox reaction with glutathione; ➢ On MCF-7 breast cancer cells: biocompatibility, high cell killing efficiency by TPE-PDT.
E 4S F PMO	➢ $d_{NP} \approx 155 \pm 25$ nm, enhanced monodispersity without P; ➢ Good endocytosis and high intrinsic fluorescence level in MCF-7 breast cancer cells, with potential for bioimaging.

In 2016, the two-photon responsiveness of ND@PMO core-shell nanoparticles for TPE-PDT was firstly reported by Mauriello-Jimenez and coworkers. As my first experimental research focus, nanodiamonds with either small or large particle size and possessing excellent optical properties were successfully embedded in different PMO matrices during sol-gel condensation under ultrasonication. This process promoted a better repartition of the carbon-based cores which naturally tend to aggregate.

Then, *in vitro* studies on MDA-MB-231 breast cancer cells allowed demonstrating the biocompatibility of the ethenylene-based core-shell nanosystems compared to the nanodiamonds alone. Indeed, excellent internalization was revealed by the intrinsic fluorescence of the multifunctional materials and significant killing efficiencies upon two-photon irradiation were observed for both small and large ND@ENE@PEG/AUTES nanoparticles.

In perspective, these nanosystems could be employed for TPE-PDT applications, for instance in combination with drug delivery. Moreover, further experimental synthesis work could be valuable to encapsulate nanodiamonds by different synthetic routes. A larger catalogue of nanodiamonds presenting different particle size and structure composition could be interesting to assess in TPE-PDT to unveil the structure-performance relationship of the gems under two-photon excitation.

In a second part, my research work was focused on the organic synthesis of new two-photon fluorophores with excellent photophysical properties for bio-imaging and FRET-enhanced TPE-PDT was envisaged. After several synthesis and purification steps, the three-branched chromophores F and F2 possessing a triphenylamine core and highly-conjugated branches were obtained pure and isolated, as controlled by elemental analysis, mass spectrometry and liquid nuclear magnetic resonance spectroscopy.

One-photon photophysical characterization revealed a solvatochromic dependency of the chromophores, whose emission spectra were red-shifted with increasing solvent polarity, also influenced by solubility. F2 chromophore possessing one more styrene unit (on each branch) than F showed a bathochromic shift in both absorption and emission. Moreover, high fluorescence quantum yields were measured for both compounds. Hence, our goal was to translate these chromophores presenting excellent optical properties into PMO nanoparticles to increase their dispersion in polar medium, hence, in biological environment.

To go further with this, the two-photon absorption cross-section and two-photon fluorescence quantum yields of the chromophores would need to be evaluated in order to compare their

potential with other compounds from the literature with similar structure. In addition, given the poor F2 overall synthesis yield, further optimization of the key synthesis steps could be worth for future exploitation of this new fluorophore.

Thus, the use of a donor-acceptor FRET pair in nanoparticles composed of two-photon fluorophore F and tetra(aminophenyl)porphyrin P was intended to assess whether the porphyrin could generate more ROS under two-photon excitation. Structural and photophysical characterization confirmed that the silylated precursors were successfully integrated in the three-dimensional framework of different families of PMO nanoparticles, either ethylene or ethenylene-based, in the presence or not of tetrasulfide bridges. Transmission electronic microscopy and dynamic light scanning experiments respectively showed an average nanoparticle size of 150 nm and good colloidal stability in ethanol for the different F P PMO families. The materials presented high specific surface areas (> 500 m^2 g^{-1}) and satisfactory pore sizes and volumes for post-grafting strategies and drug delivery as revealed by N_2 sorption experiments.

Thus, the drug loading and release capacity associated with the nanosystems were assessed for vancomycin hydrochloride antibiotic in the context of performing combination therapy with TPE-PDT. The best drug loading contents ($DLC_{VAN} \approx 160$ µg mg^{-1} NPs) were obtained in slight acidic medium. Thereafter, nanoparticles containing tetrasulfide bonds demonstrated biodegradation capacity, as revealed on the transmission electronic microscopy images with fragmentation and erosion signs. Release studies in glutathione-rich environment showed the correlation between nanoparticles biodegradation and vancomycin redox-triggered delivery.

In the same time, a method was developed to estimate the FRET potential of F/P pair in nanoparticles by comparing PMO nanoparticles with only energy donors, only energy acceptors, or both elements. This revealed high extinction of fluorophore fluorescence for the benefit of porphyrin fluorescence emission and ROS generation efficiency.

Similarly to the molecular chromophores, the two-photon photophysical properties of F P PMO nanomaterials would be interesting to study, notably to evaluate the differences between F PMO, P PMO and F P PMO in terms of absorption and emission from both the donor and the acceptor moieties. ROS generation measurements in biological environment could also provide additional information regarding the photoactivity of the materials.

Finally, the therapeutic performances of ethylene and ethenylene-based PMO nanoparticles were assessed by preliminary *in vitro* studies against cancer cells and bacteria.

F PMO and F P PMO nanoparticles exhibited excellent fluorescence and internalization levels in MCF-7 breast cancer cells, demonstrating their potential for theranostics. One-photon photodynamic therapy assays revealed opposite killing efficiencies on MCF-7 cancer cells. Indeed, tetrasulfide-based biodegradable PMO nanoparticles were not phototoxic, while PMO nanoparticles containing no tetrasulfide bonds could significantly reduce the cancer cell viability. In contrast, TPE-PDT experiments resulted in considerably high reduction in MCF-7 cancer cell viability survival independently of the PMO structure (E, E 4S, ENE or ENE 4S as the most abundant organic moieties).

Vancomycin release in bacterial environment was demonstrated and proved to be slightly more efficient against gram-positive *S. aureus* with tetrasulfide-based biodegradable PMO nanoparticles. Following this, TPE-PDT studies showed full eradication of *E. coli* colonies with bare nanoparticles, Vancomycin-loaded nanoparticles and also (PEG/AUTES@sqMAN)-functionalized nanoparticles. In particular, the presence of the mannose derivative on the surface of E F P PMO nanoparticles enhanced the therapeutic efficiency, which was associated with the targeting feature of this mannoside for *E. coli* FimH lectins. FRET efficiency for TPE-PDT was also evidenced. Indeed, F P-based nanoparticles caused higher mortality than nanoparticles possessing only P moieties.

Next, given the high *in vitro* phototoxicity of the nanoparticles, *in vivo* experiments will be performed to study the theranostic performances of the different TPE-responsive PMO nanoparticles. On one hand, we plan to conduct TPE-PDT anticancer studies on zebrafish embryo models, whose transparency will allow performing fluorescence tracking of the nanoparticles. On the other hand, antibiofilm activity will be assessed to go one step further into the antibacterial resistance issue. Moreover, we expect to study wound repair and infection healing on mice models.

As a whole, this project allowed developing innovative PMO-based multifunctional nanoplatforms with high potential for TPE-PDT applications and antibiotic delivery. Several techniques were used to highlight the structure-property relationships of the molecular moieties and the final materials. In particular, the newly-synthesized two-photon responsive fluorophores and associated PMO nanoparticles hold great potential from their optical features, as highlighted upon fluorescence imaging and FRET-enhanced TPE-PDT assays.

ANNEXES

Review paper

In the context of the pandemic situation, we published a review article untitled “Nanodiamonds for bioapplications, recent developments” compiling the late studies employing nanodiamonds as passive or active agents in the biomedical field. This work gives an overview of their various properties and, thus, their numerous advantages for being used in future strategies in nanomedicine.

Journal of Materials Chemistry B

ROYAL SOCIETY OF CHEMISTRY

REVIEW

View Article Online
View Journal

Published on 06 November 2020. Downloaded by University of Montpellier on 11/6/2020 4:15:11 PM.

Check for updates

Cite this: DOI: 10.1039/d0tb02221g

Nanodiamonds for bioapplications, recent developments

Nicolas Bondon, *[ab] Laurence Raehm,[a] Clarence Charnay,[a] Rabah Boukherroub[c] and Jean-Olivier Durand[a]

The world of biomedical research is in constant evolution, requiring more and more conditions and norms through pre-clinic and clinic studies. Nanodiamonds (NDs) with exceptional optical, thermal and mechanical properties emerged on the global scientific scene and recently gained more attention in biomedicine and bioanalysis fields. Many problematics have been deliberated to better understand their *in vitro* and *in vivo* efficiency and compatibility. Light was shed on their synthesis, modification and purification steps, as well as particle size and surface properties in order to find the most suitable operating conditions. In this review, we present the latest advances of NDs use in bioapplications. A large variety of subjects including anticancer and antimicrobial systems, wound healing and tissue engineering management tools, but also bioimaging and labeling probes are tackled. The key information resulting from these recent works were evidenced to make an overview of the potential features of NDs, with a special look on emerging therapeutic and diagnosis combinations.

Received 14th September 2020,
Accepted 2nd November 2020

DOI: 10.1039/d0tb02221g

rsc.li/materials-b

1. Introduction

Bioapplications need many prerequisites to be safe and efficient. The use of nanoparticles (NPs) has gained more and more attention due to their small size and high surface to volume ratio, but there are many concerns about their harmfulness for the living. Among NPs, nanodiamonds compatibility in living organisms, from administration to clearance, is intensely watched. According to several *in vivo* studies, NDs are well-tolerated and non-toxic.[1] Moreover, in the midst of carbon-based nanomaterials, NDs seem to be the most biocompatible species of their family. This fundamental property is associated with high specific surface area, inert carbon core with various impurities and defects and tunable surface chemistry. Other characteristics of ND-based materials, such as surface zeta potential, tissue penetration, dispersibility and accessibility,

[a] *Institut Charles Gerhardt Montpellier, UMR 5253, CNRS-UM-ENSCM, Université de Montpellier, Place Eugène Bataillon 34095, Montpellier cedex 05, France. E-mail: nicolas.bondon@umontpellier.fr*
[b] *Laboratoire Cogitamus, France*
[c] *Univ. Lille, CNRS, Centrale Lille, Univ. Polytechnique Hauts-de-France, UMR 8520, IEMN, F-59000 Lille, France*



Nicolas Bondon

Nicolas Bondon graduated from Amiens University (France) in 2019 with his master's degree (MSc) in Materials Chemistry and Sustainability. Currently, he is a PhD candidate in the Department of Molecular Engineering and Nano-Objects at Institute Charles Gerhardt Montpellier, in France. His research focuses on developing fluorophores and periodic mesoporous organosilica-based nanomaterials with two-photon capability for bioimaging and photodynamic therapy around antibacterial applications.



Laurence Raehm

Dr Laurence Raehm is associate professor at the University of Montpellier, France. She got her PhD in Strasbourg, France, in 1999 under the supervision of Jean-Pierre Sauvage and Jean-Marc Kern for studies on molecular machines. She spent two years as a postdoctoral researcher in the group of J. K. M. Sanders in Cambridge, UK. Her current research interests involve the use of silica-based nanoparticles for applications in imaging and therapy.

Published on 06 November 2020. Downloaded by University of Montpellier on 11/6/2020 4:15:11 PM.

can be modulated for optimal use in biological media.[2] Therefore, biological parameters such as aggregation, metabolism, internalization and toxicity can be controlled, providing better risk-benefit ratio towards therapeutic and bioimaging systems.[3]

NDs are classified into different categories depending on their bare size and synthesis process. Detonation nanodiamonds (DNDs) basically exhibit monodisperse size close to 5 nm.[1,4,5] They are manufactured by shocks with trinitrotoluene-like explosives and hexogen, where graphite is converted in tiny little gems in a bottom-up approach, prior to purification and washing phases.[6] Fluorescent nanodiamonds (FNDs) with wider size distribution than DNDs, are principally shaped from expensive high pressure and high temperature (HPHT) diamond and grinding procedure, which confer them very stable defects. Their intrinsic fluorescence, originating from nitrogen-vacancy (N-V) color centers, and their good biostability render them ideal for tracking and imaging upon light excitation.[7] Nano-sized diamonds can also be obtained by chemical vapor deposition or pulsed laser ablation in liquids, but these processes are less common and expensive.[8–10]

Before their use in formulations for bioapplications, NDs are purified to selectively remove impurities (non-diamond carbons, metals, oxides and other particles) to control their surface chemistry. The restrictive aggregation effect of bare NDs, which is one frequently discussed issue, can be solved by different strategies governed by physical principles or chemical modifications. The former gathers milling, sonic disintegration, and annealing techniques, while the latter refers to surface modification by oxygenated functions or small molecules to bring stability to the final materials.[3]

DNDs are commonly chosen in anticancer drug delivery systems owing to their low cost, chemical inertia and ability to overcome multidrug resistance.[11] In addition, their high specific surface area and small monodisperse size allow higher release rates and good therapeutic *in vivo* efficacy *via* targeting molecules such as polymers, peptides and liposomes.[1,5,6] They show good relevancy as topical antineoplastic drug delivery transporters, cancer stem cells eradication enhancers and chemoresistance suppressors.[3] Their alterable surface and biocompatibility render them suitable drug carriers protecting against protein adhesion and immune responses, leading to longer circulation time in the body and better selectivity for the tumor sites.[1]



Clarence Charnay

Clarence Charnay obtained his PhD from the University of Montpellier, France, in 1999. After working as a researcher at the Paul Pascal Research Center (Bordeaux, France) with Dr V. Schmitt and at Montpellier with Professor J. M. Devoisselle on drug encapsulation into porous nanoparticles, he joined the Halas Nanophotonics group (Rice University, Texas, USA) and studied the design of new plasmonic nanostructures with professor Naomi Halas. His is now Maître de Conferences (Assistant professor) at the University Montpellier since 2002 and has research interests in nanoparticle science and colloids for drug delivery and nanomedicine applications.



Rabah Boukherroub

Dr Rabah Boukherroub received a PhD in chemistry from the University Paul Sabatier in Toulouse, France. He is currently a CNRS research director and a group leader at the Institute of Electronics, Microelectronics and Nanotechnology (IEMN), University of Lille, France. He is Associate Editor for ACS Applied Materials & Interfaces. He is also a guest Professor, China University of Petroleum, Qingdao, China. His research interests are in the area of functional materials, surface chemistry, and photophysics of semiconductor/metal nanostructures with emphasis on biosensors, photocatalysis, and nanomedicine. He is a co-author of 600+ research publications and wrote 38 book chapters in subjects related to nanotechnology, materials chemistry, and biosensors. He has 12 patents or patents pending.



Jean-Olivier Durand

Dr Jean-Olivier Durand graduated from the Ecole Nationale Supérieure de Chimie de Paris in 1990 and obtained his PhD in organic chemistry with Prof. J. P. Genêt in 1993. He spent a 20 month post-doctoral position with Prof. W. Oppolzer at the University of Geneva (Switzerland). After two other post-doctoral studies in Rennes (Prof. Le Corre) and Paris (Dr M. Larchevêque), he was appointed as a CNRS researcher in 1996 at the Laboratoire de Chimie Moléculaire et Organisation du Solide, Institut Charles Gerhardt Montpellier and is now research director at CNRS since 2012. He is co-founder of Start-Up NanoMedSyn. His research interests include the development of mesoporous nanoparticles (silica and silicon-based) for theranostic applications, photodynamic therapy and drug delivery. He particularly studied two-photon light-triggered systems. He is co-author of 121 publications and 14 patents.

This journal is © The Royal Society of Chemistry 2020

Published on 06 November 2020. Downloaded by University of Montpellier on 11/6/2020 4:15:11 PM.

NDs have been adapted for use with several drugs, demonstrating positive input and lower side effects. For instance, studies of materials loaded with doxorubicin (DOX) displayed interesting tumor growth inhibition, prolonged release in the cytoplasm or increased drug uptake in cancer cells nucleus.[3,12,13] These fluorescent gems can also be beneficial in photodynamic therapy (PDT), generally associated with active photosensitizers whose activity relies on phosphorescence phenomenon. By non-radiative intersystem crossing, these materials can generate reactive oxygen species (ROS) by electron or energy transfer during electronic transitions from excited to ground states.[14] Additionally, there is potential in photothermal therapy (PTT), by which light is converted into heat to wipe out malignant cells.[5]

Otherwise, NDs have considerable potential as bioimaging probes due to their fluorescence properties, generally associated to ND intrinsic impurities (N-V and silica-vacancy color centers). Among the different ranges, FNDs, generally bigger in size than DNDs, can be fluorescent markers to monitor uptake efficiency, uptake pathways, and intracellular behavior.[15] Fluorescence imaging is usually facing two issues: autofluorescence of tissues and light absorption by biomolecules in UV-vis domain, leading to photobleaching and poor brightness level. Intrinsic stable defects fluorescence of NDs is ideal for biotracking, as it displays high lifetime (20–30 ns) contrary to biomolecules autofluorescence that is usually of 1–4 ns, providing high contrast imaging.[6] Interestingly, ND N-V centers are emitting from 600 to 800 nm. In these conditions, there is no intense photon absorption by body biomolecules, thus, no signal perturbation.[5] Autofluorescence photobleaching and bad penetration in the tissues are avoided in near-infrared (NIR) conditions.

Furthermore, covalent and non-covalent attachment of emitting fluorophores enhances imaging quality.[15] Great fluorescence can be achieved by the use of fluorophores, such as fluorescein, Hoechst blue, rare-earth (RE) elements and quantum dots (QDs), but it has been reported that FNDs possess the advantage to show better biocompatibility.[7] Hence, two strategies are considered for their use in bioimaging and labeling: NDs carrying chromophores for a synergistic action or NDs as a unique fluorescence source. Unfortunately, FNDs bioapplications are limited due to their big size compared to classic fluorescent molecules (<20 nm).[1] The use of detonated NDs would be a good alternative as they have better biocompatibility and versatility, but this will require the enhancement of intrinsic N-V distribution and quantity.

NDs have proven their effectiveness for a wide range of diagnosis techniques. In photoacoustic microscopy, the great optical absorbance of NDs can render them suitable CAs to enhance signals' sensitivity.[15] This parameter is also a crucial requirement to perform magnetic resonance imaging (MRI) and a controlled creation of paramagnetic N-V defects could make them outstanding contrast agents (CAs) for MRI based on T_1 relaxation time. Additionally, they can also be used as carriers to enhance the biocompatibility of classic T_1 based CAs.[16] Owing to their optical properties, NDs are naturally good probes for Raman imaging in NIR II domain as they display a strong peak at 1332 cm^{-1}, which is far from living cells' signals (2800–3200 cm^{-1}), allowing an easy monitoring without signal perturbation. Moreover, as Raman spectroscopy made great progress for 4D temporal and spatial resolution and 3D imaging, ND-based materials could enable the access to further information by internalizing into the cells.[5] ND-Based systems could also be well-suited to answer the challenges related to emerging bioimaging techniques. Super-resolution imaging such as stimulated emission depletion (STED) microscopy can be performed with red or green fluorescent NDs, demonstrating impressive resolution of about 10 nm. In STED optical analyses, there is a need for high photostability that could be mastered by FNDs as they can be internalized in living cells.[16,17] NDs use in correlative light-electron microscopy is also a very stimulating challenge for the coming years as electronic and fluorescence properties, coming from defects and surface functionalization, can be combined.[16] More recently, hyperpolarized MRI using dynamic nuclear polarization has emerged as a promising technique even if it presents some drawbacks like the need for cryogenic temperature and long-time analyses.[18] Irradiation at room temperature of ^{13}C nuclear spins from FNDs led to upraising T_1 signal intensities.[19,20]

There is also a renewed interest for elaborating new strategies against infectious diseases causing chronic inflammation and tissue damage, due to the growing antimicrobial resistance phenomenon, characterized by drug-resistant bacteria.[21–23] Some alternatives to antibiotics have already been tested, and many of them consisting of NPs–polymers composites searching for the best anti-adhesive properties against bacteria and their protective barriers, the so-called biofilms.[24–28] Nanodiamonds are gradually tested as potent efficient tools to fight infections, because they can hold optical transparency, fluorescence behavior, and tunable surfaces.[29–34] Like in the majority of bioapplications, biocompatibility and poor toxicity are compelling prerequisites.[35] Thus, with judicious designs, one can easily imagine both passive and active antibacterial roles for these probes.

Previous *in vitro* studies of different NDs antimicrobial efficacy underlined better killing effects depending on purification process, annealing and functional groups, notably in the case of ND negatively-charged surface. Strains nature is also a major parameter according to discordant conclusions with ND-NH_2 and ND-mannose grafting, probably due to the size, morphology, and above all to the biological composition of the bacteria membranes.[36] A better understanding of microbial damaging mechanisms is urgent, including immune system behavior in facing adhesion and growth processes. For example, culture media composition can influence antimicrobial activities as expressed in recent *in vitro* assays on *E. coli* using two different NDs in Luria–Bertani (LB) or Mueller–Hinton (MH) nutritious medium. The nanomaterials seemed more effective in LB media compared to MH due to a poor Ca^{2+} and Mg^{2+} content, more suitable for the generation of oxidative stress.[37] In another study, carboxylated NDs in LB caused partial membrane disruption and cell death.[38] Moreover, glycan-conjugated NDs borne strong affinity to type I FimH fimbriae from *E. coli* lectins, with good

Published on 06 November 2020. Downloaded by University of Montpellier on 11/6/2020 4:15:11 PM.

ability in restraining metabolic pathways, inducing cell death and potential biofilm destruction.[15,36] Research about infections also require to pay attention to biofilms, as they can reproduce fast and gather, in a complex matrix, huge quantities of microbes. Thus, inhibiting biofilm growth at its early stage is decisive and the properties of antimicrobial agents can make a clear difference to solve this problem.[36]

Nanodiamonds could lead to vast findings in many other medicinal applications. In skin relative diseases, for enhanced transport, delivery and efficacy of drugs, hydrophilicity tuning and high dispersibility of functionalized NDs are appealing factors. Therefore, NDs can reinforce both the quality and the activity of classical composites applied for wound management, tissue engineering and various diseases closely linked to the immune system behavior.[2] These hybrid materials generally include biopolymers such as polyethylene glycol, chitosan and bacterial cellulose, with good chemical structures and properties for wound covering designs and skin pathologies applications.[7] Besides, several drug and gene delivery experiments have been performed by using ND-based formulations promoting faster repair process through a large variety of favorable effects like protection against instability and functionalized surfaces for a better penetration.[2] One recurrent strategy is to enhance growing factors distribution to the wound site.[39]

In this review, we selected the most recent articles where NDs potential is explored in a perspective of medicinal use. We divided our review by application type, from cancer research to bioimaging and biolabeling, covering studies dealing with other diseases. We presented the key information about materials synthesis, modification and preparation, toxicity and safety, but also the main results with or without ND moieties (Table 1). Our goal is to provide a summary of NDs advantages and input, when possible, and to shed light on rising strategies for improved therapeutic balance and upgraded diagnosis.

2. Nanodiamonds in cancer therapy research

One of the biggest topics in current cancer therapy research is building nanomaterials with several features. Whether they have a good ability to enhance chemosensitivity, a prolonged delivery with high stability and selectivity levels or an active role in phototherapy due to their fluorescence, nanodiamonds can be efficient tools in lowering drug side effects and enhancing the theranostic outcome.[3]

In this context, there is still room for improving cellular uptake pathways. Sigaeva's group presented an interesting strategy where 120 nm FNDs were stabilized by dilution in high glucose Dulbecco's Modified Eagle Medium (DMEM) containing 10% of fetal bovine serum (FBS). By testing different methodologies, they demonstrated that internalized FNDs amount in HT-29 colon cancer cells was considerably dependent of the taken direction. Uptake was much more efficient when FNDs were guided to enter by the basolateral side of plasma membrane. Moreover, when FNDs were incorporated from the apical border, impressive internalization rates were obtained on gathered HT-29 cells, but these remarkable results were mainly due to an initial trypsin–ethylenediaminetetraacetic acid (EDTA) treatment step performed until particles were well spread. Trypsin, a well-known enzyme, can improve dispersibility by bound cleavage between cells and can also affect cell surface (composition, surface area, *etc.*) for easier penetration. By both strategies, about 95% of colon carcinoma cells contained FNDs for a concentration of 5 $\mu g\ mL^{-1}$, whereas it was 50% when directed to the apical side without enzymatic treatment.[40] This research is notable for not entailing any FNDs surface functionalization and its results could be taken into account in future theranostic applications.

2.1. Cellular uptake and anticancer drug delivery studies

Like many nanoparticles, nano-sized diamonds can be powerful carriers of antineoplastic drugs, providing higher selectivity towards tumor cells due to their protective capacity. In their report, Yu *et al.* developed a sonication method to encapsulate camptothecin (CPT) anticancer agent in alkyl-amine modified NDs. Three different alkyl-amine molecules were grafted to purified DNDs suspended in water (ND-ori, Fig. 1) through condensation between amine moiety and surface carboxyl functions, using water soluble carbodiimide hydrochloride (WSC) carbodiimide linkage agent in a slightly acidic 2-(*N*-morpholino)-ethanesulfonic acid (MES) buffer. Then, these particles self-assembled while being sonicated. The resulting scaffolds were ideal for CPT transport as they gave high biocompatibility results *in vitro* and *in vivo*, but also huge killing effect compared to classic CPT–polyethylene glycol (PEG)–micelles and CPT–intralipid emulsions. The cell viability fell to 10% on bone osteosarcoma cells (20 $\mu g\ mL^{-1}$ of CPT), while it reached around 50–60% for classic CPT-complexes (at same concentration). Moreover, after implementing HT-29 colorectal adenocarcinoma xenografts in mice, ND-CPT synergy significantly reduced tumor volumes compared to phosphate buffer saline (PBS) control measurements.[41]

Another recurrent issue with pristine or modified nanodiamonds is their spontaneous aggregation and limited dispersion in water. Consequently, the design of composites can render NDs more hydrophilic and provide better compatibility with aqueous media. Recently, ND–polymer drug delivery systems showed good dispersibility, biocompatibility and successful transport of doxorubicin (DOX) in hepatitis G2 (HepG2) liver cancer cells. For this purpose, Long *et al.* functionalized small detonated NDs. Using thiol–ene click reaction with dicumyl peroxide, methyl 3-sulfanyl propanoate radicals were generated. After thiol conjugation onto NDs surface, reaction with hydrazine hydrate led to stable amide functions. In parallel, carbonylated PEG was produced by reaction with 4-carboxybenzaldehyde. Then, PEG and DOX were concomitantly anchored to NDs by hydrazone linkages. *In vitro* assays evidenced a good cellular uptake of the cargos and a pH-dependent DOX release with good results at pH 5.4. MTT assays highlighted the therapeutic efficacy of this strategy, demonstrating a good reduction of viability at high concentrations.

 This journal is © The Royal Society of Chemistry 2020

Published on 06 November 2020. Downloaded by University of Montpellier on 11/6/2020 4:15:11 PM.

Table 1 Recent bioapplications using nanodiamonds and relative information

ND type/purification method/ impurities content/ coating	Global system	Average size (technique)/ others	Biological model	Parameter assessed	Conclusions	Ref.
120 nm HPHT FNDs, liquid and air oxid., imp.: n.a.	FNDs in various media	120 nm (n.a.)	HT-29 colon cancer cells	Cellular uptake rate (among direction and pre-treatment)	5 μg mL^{-1} NDs (from apical side + T–EDTA pre-treatment or from basolateral side (no treatment)): 95% cells contain NDs	40
4–5 nm DNDs, liquid oxid., imp.: n.a.	CPT@ND-SPs	20–100 nm (DLS), no CPT	Bone osteosarcoma cells	Cell viability	20 μg mL^{-1} system: 90% killing, other CPT-complexes gave up to 50% killing	41
			HT-29 colon tumor xenografts in mice	Tumor volumes	3 mg kg^{-1} CPT in 56 mg kg^{-1} ND-SPs: 16 days after treatment, about 40% tumor size reduction *vs.* PBS control	
2–10 nm DNDs, imp.: n.a., used as-received	ND–PEG–DOX	979.08 ± 55 nm (DLS in water)	HepG2 liver cancer cells	Cell viability	200 μg mL^{-1} free DOX or system (lower DOX rate): about 75% killing effect	42
100 nm ND–PEG powders (previously carboxylated), liquid oxid., imp.: n.a.	ND–PEG–GLY–DOX	293.6 ± 0.8 nm (DLS in water)	HepG2, HeLa, MCF-7 cancer cells	Cell viability	Inhibition of tumor proliferation, high toxicity levels	43 and
			HepG2 tumor xenografts in mice	Body weight	No weight loss after 25 days compared to 20% change with GLY–DOX	44
			MCF-7 cancer cells	Cell tracking and fluorescence	GLY-DOX released 1 h after injection (green fluorescence). Good photostability compared to free GLY-DOX	
20–50 nm ND–PEG, imp.: n.a., used as-received	ND–PEG–DOX	962 ± 140 nm (DLS in PBS)	BxPC3 pancreatic cancer 3D spheroids	Cell viability	60 μg mL^{-1} system (10 μg mL^{-1} DOX): 90% killing (free DOX: about 50%)	45
			6741 pancreatic tumor xenografts in NSG mice	Tumor volumes	After 3 weeks treatments (2 injections per week of 10 mg kg^{-1}): 4 times lower volumes *vs.* free DOX equivalent	
2–8.3 nm HOOC-DNDs and HPHT NDs, thermally annealed, imp.: n.a.	ND–TTA:RE-DOX	100–200 nm (DLS), no DOX	SGC-7901 gastric cancer cells	Cell viability, drug release, fluorescence properties	1 to 16 μg mL^{-1}: similar toxicity than free DOX for equivalent rate. Prolonged and slow release *vs.* free DOX control (for 24 h). Sustainable fluorescence and high stability for cell imaging	46
<10 nm HOOC-DNDs, liquid oxid., imp.: n.a., coating with ADH	ND–ADH–UA, ND–ADH–CUR, ND–ADH–5-FU	Resp. 114.32 nm, 39.85 nm, 81.6 nm (DLS)	MCF-7 and HepG2 cancer cells	Cell viability	Dose dependent cell growth inhibition with all drugs. High anticancer efficacy at 80 μg mL^{-1}	47
<10 nm DNDs, imp.: 0.1% non-carbon, used as-received	HSA-PTX + NDs	n.a.	MDA-MB-231 breast cancer cells	Cell viability	52% killing effect after NDs + PTX release at minor rates than IC_{50} values	48
3–6 nm HOOC-NDs (air oxid.), alkyl-DNDs, H/NH_2-NDs, imp.: <2 wt%, <0.1 wt% ash, <0.02 wt% ash, used as-received	NDs@PDA@ICG	357.57 ± 8.63 nm (DLS)	U-118 MG glioblastoma cells, shaved Kunming mice	Cell viability, photostability Imaging capability	20–40 μg mL^{-1}: 90% killing effect with 808 nm PTT (NDs@PDA: 55%, NDs: 30%, no laser: 10–20%). Good stability after 5 cycles of irradiation. Photostable and intense red fluorescence compared to classic labels. Fluorescence stability 4 h after injection *in vivo*. Ideal paramagnetic behavior for T_1 based MRI	49
2.1 nm DNDs, imp.: n.a., used as-received	ZnPc-NDs–BODIPY	7.5 nm (DLS), deaggregated	MCF-7 breast cancer cells	Cell viability, thermosensitivity	50 μg mL^{-1}: 21.4 ± 5% viability (≈683 nm laser in PDT), no toxicity without laser. System thermally stable at 80 °C	50
2.3 nm DNDs, imp.: n.a., used as-received	ZnPc-NDs	7.2 nm (DLS), deaggregated	MCF-7 breast cancer cells	Cell viability	50 μg mL^{-1}: 28.8 ± 0.02% viability (≈686 nm laser in PDT). More singlet oxygen than CDs and graphene-type QDs	51
4 nm HO-DNDs, imp.: n.a., used as-received	NDs in ethylene and ethenylene-bridged PMO (ND@E, ND@ENE)	Resp. 80–130 nm, 170–190 nm (TEM), no DOX	MCF-7 breast cancer cells	Cell viability	5 μg mL^{-1}: 87% (ND@E) and 71% (ND@ENE) killing effect (results with DOX + 800 nm excitation in PDT)	52
<10 nm DNDs, imp.: n.a., coating with oleic acid	Ce6/ND/PCM	≈101.9 ± 15.6 nm (DLS in water)	KB (HeLa subline) tumor cells, KB cells xenografts in nude mice	Release, cell viability and tumor volumes under 670 nm laser irradiation	0.5 mg mL^{-1}: thermosensitive PCM/NDs for on–off Ce6 release, cell death area enlarged by laser excitation with PDT and PTT synergy. NDs 5 mg kg^{-1} body weight: continuous and strong reduction for 12 days (irradiations at days 0 and 6) *vs.* ND/PCM	53
2–10 nm HO-DNDs, imp.: n.a., used as-received	ND-AIE dye–polymer	118 ± 45.9 nm, (DLS in PBS)	L929 mouse cells	Cell viability, fluorescence properties	120 μg mL^{-1}: 85% viability after 48 h. Good uptake and strong orange fluorescence for cell imaging	54
	HOOC-NDs		Murine skin models	Multimodal imaging		55

Published on 06 November 2020. Downloaded by University of Montpellier on 11/6/2020 4:15:11 PM.

Table 1 (*continued*)

ND type/purification method/ impurities content/ coating	Global system	Average size (technique)/ others	Biological model	Parameter assessed	Conclusions	Ref.
3–10 nm DNDs, 50 and 100 nm HPHT FNDs, liquid oxid., imp.: n.a.		Resp. 258 ± 60 nm, 118 ± 33 nm, 150 ± 25 nm (DLS)			100 nm FNDs globally more suitable. Tissues autofluorescence superior to NDs fluorescence at 800 nm	
5 nm CD-DNDs (surface COOH), liquid oxid., imp.: 0.5 wt%	CD-DNDs	4–5 nm (DLS), deaggregated	MDA-MB-231 breast cancer cells	Fluorescence properties	488 nm argon laser excitation: good fluorescence after internalization	56
			Zebrafish embryos	Biocompatibility	Good compatibility *in vivo* but need to overcome particles clustering tendency	
25 nm HPHT NDs, liquid oxid., imp.: 1.75% non-diamond	Fe_3O_4–ND–PEI–AMOX	350 nm (DLS)	pH 4 citrate buffer solution	Drug release	Prolonged release (180 h) with NDs, lower without (24 h). More drug release rate in acidic conditions and at 37 °C	57 and 58
100 nm HOOC-NDs, air and liquid oxid., imp.: n.a., PA coated	Ag-ND@BSA	120 ± 30 nm (DLS in water)	*E. coli* strain	Cell viability	250 μg mL^{-1} Ag NPs: strong bactericidal effect for 36 days (CC_{50} ≫ 500 μg mL^{-1}). Low toxicity on healthy human cells	59
3–5 nm HOOC-DNDs, imp.: n.a., used as-received	HOOC-DNDs	≈5 nm (DLS), deaggregated	MC3T3-E1 bone cells	Tribological effect	450 μg mL^{-1} NDs: friction minimized and reduced polyethylene surfaces wear	60
			S. aureus or *E. coli* strain	Bacteria growth	31–1000 μg mL^{-1} NDs: reduced *S. aureus* development but no significant effect against *E. coli* development	
4–6 nm DNDs, imp.: n.a., used as-received	PMMA-ND	Average roughness <200 nm (AFM)	*Candida albicans*	Fungi resistance, mechanical properties	0.1–0.5 wt% NDs: reduced viability and biofilm formation *vs.* ZrO NPs and *vs.* control. Higher flexural strength and elastic modulus	61
3–5 nm HOOC-DNDs, thermally annealed, imp.: n.a.	ND-Doped DLC films (deposited on alloy surface)	1626 nm (n.a), interlayer	*E. coli* strain	Bacteria growth	1% w/v NDs: 95% inhibition growth (no NDs: 30%). Involvement of NDs in cell walls damage, thus, in cell death. Prolonged antibacterial activity	62
<10 nm DNDs (surface COOH and OH), imp.: n.a., used as-received	NDs-Loaded PCL fibers scaffolds	350–500 ± 80 nm (SEM), fiber size	Chinese hamster ovarian cells	Biocompatibility, wound management	1–5% w/w ND: biocompatibility increase (hydrophilicity and thermal stability), better proliferation of epithelial cells and moisture control	63
			S. aureus strain	Bacteria growth	5% w/w ND: lower bacteria sticking for greater inhibition growth *vs.* PCL alone	
NDs (surface COOH and OH), imp.: n.a., used as-received	Electrospun NDs-loaded FG scaffolds	n.a.	hASCs	Biocompatibility, tissue engineering	0, 0.5 and 1% w/v NDs: growing biocompatibility and metabolic activity in NDs-loaded FG scaffolds, better proliferation and adhesion of hASCs	64
25 nm HOOC-DNDs, liquid and air oxid., imp.: 0.6 wt%	ND@SiO_2@DEX nanogel	390 nm (DLS)	pH 7.3 buffer solution	Drug delivery	30 wt% DEX maximum loading (<1 wt% for ND@DEX), totally desorbed, in a prolonged manner (26 h)	65
5 nm HOOC-DNDs, air and liquid oxid., imp.: n.a.	ND–ODA/DEX	5.1 ± 2.2 nm (TEM), deaggregated ND–ODA, no DEX	Arthritic mice limbs	Immune system response, bone volume	16 μg mL^{-1}/0.1 μg mL^{-1} ND–ODA/DEX (5 μL injections): reduction of macrophage invasion and tuning of inflammatory response. Lower bone degradation *ex vivo*. Dose-dependent immunomodulatory effects	66
4–5 nm HOOC-DNDs, liquid oxid., imp.: <2 wt%	ND-NH_2-terminated, ND-COOH	n.a.	Human PBMCs	Interactions with immune cells, dispersibility	Good uptake in PBMCs. Very aggregated ND-COOH caused pro-inflammatory responses. ND-NH_2 were more dispersed and more immunocompatible	67

5-FU: 5-fluorouracil; ADH: adipic acid dihydrazide; AIE: aggregation-induced emission; AMOX: amoxicillin; BODIPY: bore-dipyrromethene; BSA: bovine serum albumin; CC_{50}: half-maximal cytotoxic concentration; CD: carbon dot; Ce6: chlorine e6; CPT: camptothecin; CUR: curcumin; DEX: dexamethasone; DLC: diamond-like carbon; DND: detonation nanodiamond; DOX: doxorubicin; FG: fish gelatin; FND: fluorescent nanodiamond; GLY: glycidol; hASC: human adipose-modified mesenchymal stem cell; HepG2: hepatitis G2; HPHT: high pressure high temperature; HSA: human serum albumin; IC_{50}: half-maximal inhibitory concentration; ICG: indocyanine green; imp.: impurities; n.a.: not indicated; MRI: magnetic resonance imaging; ND: nanodiamond; NP: nanoparticle; ODA: octadecylamine; PA: polyarginine; PBMC: peripheral blood mononuclear cell; PBS: phosphate buffer saline; PCL: poly-ε-caprolactone; PCM: phase-change material; PDA: polydopamine; PDT: photodynamic therapy; PEG: polyethylene glycol; PEI: polyethylene imine; PMMA: polymethyl methacrylate; PMO: periodic mesoporous organosilica; PTT: photothermal therapy; PTX: paclitaxel; QD: quantum dot; RE: rare-earth; SP: supraparticle; T–EDTA: trypsin–ethylenediaminetetraacetic acid; TTA: 2-thenoyltrifluoroacetone; UA: usnic acid; ZnPc: zinc-based phthalocyanine-derivative.

This journal is © The Royal Society of Chemistry 2020

Published on 06 November 2020. Downloaded by University of Montpellier on 11/6/2020 4:15:11 PM.

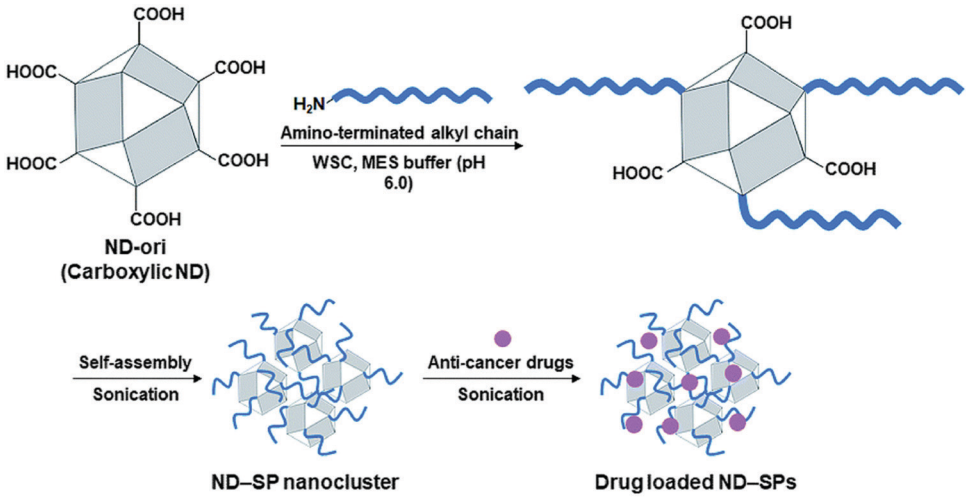

Fig. 1 Synthesis steps of nanodiamond supraparticles loaded with camptothecin from carboxylated detonation NDs. Reproduced from ref. 41 with permission from the Royal Society of Chemistry.

At 200 μg mL^{-1} in free drug, the killing effect was about 75%, similar to the result with DOX loading.[42] This way, dose and relative side effects could be reduced.

Wei's team built a DOX delivery system sensitive to pH-triggered release. At first, a modified polyethylene glycol (H_2N-PEG-COOH) was grafted onto carboxylated nanodiamonds, creating an amide group. Subsequently, a glycidol (GLY)–DOX moiety was attached to the terminal carboxyl function of ND–PEG by ester junction with GLY alcohol, reaching a drug loading of 15 wt%. The material structure was well-suited to prevent drug leakage. Tests in PBS containing 10% FBS revealed no apparent drug release after 50 h.[44] Therefore, when subjected to acidic lysosomes in cancer cells, controllable and extended release of GLY–DOX was detectable by fluorescence intensity measurements, surely arising from ester cleavage. This off–on system was also applied *in vitro* on HepG2, HeLa and MCF-7 cancer cell lines. High survival rates obtained by MTT assays showed satisfactory biocompatibility of ND and ND–PEG nanoparticles. In contrast, when DOX was liberated from ND–PEG–GLY–DOX, cell viability was very low, indicating good tumor proliferation inhibition. Besides, the platform could affect other processes such as migration, apoptosis and cell cycle. Noteworthy, mice body weights were relatively stable, while a serious weight loss occurred with only GLY–DOX. In conclusion, this rich study provided an efficient design for actuable drug transport and drug liberation, and associated monitoring.[44]

Some research about selectivity competence for pancreatic ductal adenocarcinoma was conducted recently.[45] NDs with different surface terminations were loaded with DOX and tested against this rare cancer. Among ND-NH_2, ND-COOH and ND–PEG, the latter conferred the best catch and release ability toward DOX. Up to 75% of drug was complexed by adsorption on NDs surface for an initial weight ratio of 5 : 1 ND–PEG : DOX. In different media, the release efficiency was inversely proportional to the pH value, and best ratios were obtained in acidic environment (≈95% at pH 2). *In vivo* imaging systems with fluorescence snapshots on NSG mice, as well as *ex vivo* biodistribution analyses revealed a remarkable accumulation of DOX in the tumors, 48 h post-injection, indicating a good cellular uptake. This led to lower tumor sizes – after treating the animals for 3 weeks – compared to the free drug. Interesting cytotoxicity of ND–PEG–DOX incorporated in BxPC3 PDAC cancer cells (3D spheroids) was also visible, while ND–PEG without loaded drug were non-toxic. After 96 h exposure, almost all cells were eradicated.[45] Altogether, these systems seem to be efficient for drug delivery purposes, as they promote good biocompatibility and extended drug release.

Nanodiamond fluorescence wavelength is sometimes too short for drug labeling and cell tracking. Qin *et al.* fabricated an innovative material for both therapy and diagnosis purposes using RE-based complexes with nanodiamonds to enhance optical properties. Several steps were necessary to build these materials. In a first part, NDs surfaces were purified by thermal annealing, carboxylated and then partially acylated using $SOCl_2$. To follow, 2-thenoyltrifluoroacetone (TTA) and NDs were silylated with 3-isocyanatopropyltriethoxysilane and 3-aminopropyltriethoxysilane, respectively. Finally, ND-Si and TTA-Si were mixed in presence of europium and gadolinium RE to obtain highly stable biolabelling and drug delivery systems (Fig. 2). These ND-based particles were loaded with up to 37.5 wt% in DOX for an initial feeding of 60 wt%.[46] Drug adsorption was typically between DOX NH_3^+ groups and –CO containing groups from NDs surface. When incorporated in 96-well plates containing gastric cancer cells, they showed anticancer activity equivalent to unentrapped DOX, but with significant prolonged release certainly originating from ND-Si moiety stability.

Garg *et al.* investigated the combination of ND covalently bound to curcumin, usnic acid or 5-fluorouracil after several functionalization steps. After an initial purification of bare nanodiamond powder in ND-COOH, NDs surface was modified with 1-ethyl-3-(3-dimethylaminopropyl)carbodiimide hydrochloride and *N*-hydroxysuccinimide to activate carboxyl function

Published on 06 November 2020. Downloaded by University of Montpellier on 11/6/2020 4:15:11 PM.

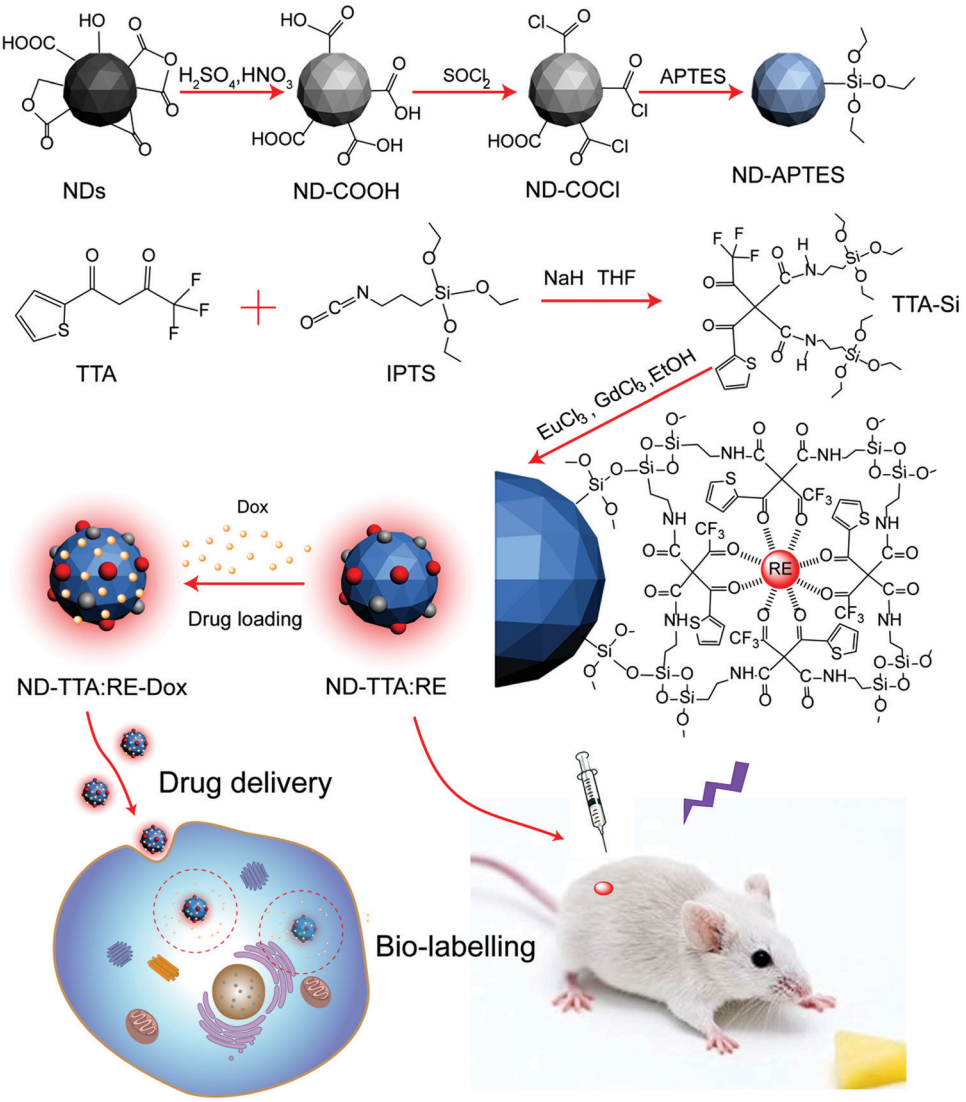

Fig. 2 Schematic view of ND functionalization with thionyl chloride and alkoxysilanes, ultimately for rare-earth immobilization and drug loading for theranostic application. Reprinted from ref. 46, Copyright 2018, with permission from Elsevier.

reactivity for carbodiimide conjugation with adipic acid dihydrazide (ADH). Lastly, one of the three above-mentioned drugs was conjugated by substitution with the terminal hydrazide, reaching about 90% loading (Fig. 3). Tests in PBS with free drugs indicated their almost total release in 3 h, whereas the conjugates showed prolonged drug liberation for 96 h, due to the hydrophilic properties of nanodiamonds.[47] With increasing acidic conditions, greater amounts were freed from NDs. Sulforhodamine B trials evaluation of the cytotoxicity on human MCF-7 and HepG2 cancer cell lines revealed a dose-dependent growth inhibition for all ND–drug couples and antitumor drugs. Tumor killing effect was related to drug internalization in nucleus after escaping from intracellular lysosomes, leading to an inhibition of DNA production. These conjugates could be further investigated for applications in targeted cancer treatment as strong therapeutic efficacy was achieved at relatively low concentrations (80 μg mL^{-1}).[47]

Tumor therapy can be very limited by interactions occurring between drugs and biomolecules from our blood, such as human serum albumin (HSA), the most profuse protein.

Hekmat *et al.* recently presented a study where they admixed nanodiamonds, paclitaxel (PTX) chemotherapeutic agent and HSA in tris(hydroxymethyl)aminomethane buffer. Zeta potential, DLS, and several analytical methods highlighted a complexation of PTX + NDs with the above-mentioned protein. For example, steady-state spectroscopy revealed a fluorescence-quenching phenomenon of tryptophan intrinsic fluorophore moiety of HSA. In presence of PTX, NDs or PTX + NDs, fluorescence emission intensity was weakened, and a blue shift occurred. One answer could be that tryptophan surface was clustered by specific interactions with the molecules, inhibiting the fluorescence properties. Hence, HSA-PTX solutions with NDs were prepared to further examine their bioactivity and therapeutic potential. Drug release studies over time indicated a good

 This journal is © The Royal Society of Chemistry 2020

Published on 06 November 2020. Downloaded by University of Montpellier on 11/6/2020 4:15:11 PM.

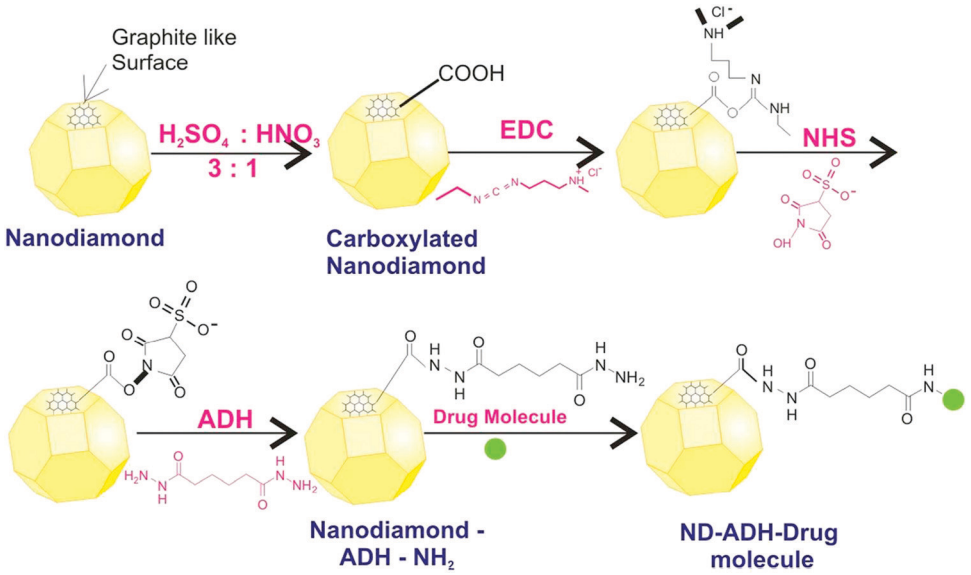

Fig. 3 Synthesis of ND–drug conjugate by activation of surface carboxyls groups for carbodiimide conjugation using adipic acid dihydrazide. One anticancer drug among curcumin, usnic acid and 5-fluorouracil was then loaded. Adapted from ref. 47, Copyright 2019, with permission from Elsevier.

stability of HSA-PTX + NDs systems in the bloodstream. Indeed, only 35% of PTX + NDs were released in physiological media after 48 h, while the results in pH 4.7 media were about 85%. These results among others suggested a preferential targeting of tumor sites, with a better affinity for acidic lysosomes in cells, which might be ascribed to enhanced permeability and retention (EPR) effects as albumin specifically bind to Gp60 (glycoprotein of 60 kDa) and secreted protein acidic and rich in cysteine (SPARC) receptors that are expressed by endothelial cancer cells.[48,68] Once this mixture was integrated *in vitro*, an important reduction of MDA-MB-231 human breast cancer cells multiplication was achieved, contrasting with bare NDs and free drug influence. Moreover, at minor NDs and PTX concentrations *versus* established half-maximal inhibitory concentration (IC_{50}) values for these cell lines, the cell viability largely dropped, providing a synergistic effect of the two materials. This could be correlated with HSA higher binding force in buffers containing PTX + NDs than with PTX or NDs alone.[48] For this reason, it is believed that these systems could furnish good benefit-risk balance in future *in vivo* inquiries.

2.2. Photothermal and photodynamic therapies against cancer

In addition to chemotherapy and radiotherapy, some new techniques presenting limited undesirable effects are emerging to fight cancer. This is the case of photothermal therapy, based on light conversion into heat, and photodynamic therapy, inducing a production of reactive oxygen species. These two phenomena can lead to cells' damaging or even their destruction. By combining a light source (laser, LED, *etc.*) with a photosensitizing agent, high toxicity levels can be reached. Moreover, for a better treatment efficacy, just like in many therapies, the addition of targeting moieties and the use of biodegradable systems are much exploited.[3,69]

Maziukiewicz *et al.* examined the synergistic photothermal and photochemical effects of NDs coated with indocyanine green (ICG) fluorophore and biomimetic polydopamine (PDA). The synthesis protocol started with dopamine hydrochloride applied on top of sonicated NDs exhibiting different surface functionalities (1: –COOH; 2: –alkyl; 3: –H and $–NH_2$) in a tris(hydroxymethyl)aminomethane buffer. After polymerization process of dopamine in ambient conditions for 24 h, ICG was added in the suspension and the mixture reacted in dark conditions for another 24 h. The authors conjectured a π–π bonding between aromatic cycles from PDA and ICG. According to their calculations of photothermal conversion ability, this strategy brought a notable increase of temperature with NDs@PDA (36.5%) and NDs@PDA@ICG (44.5%) compared to the three ND groups (<10%). Referring to its absorption profile, ICG exhibits a maximum absorbance in the NIR region (≈800 nm, Fig. 4), indicating good photophysical properties

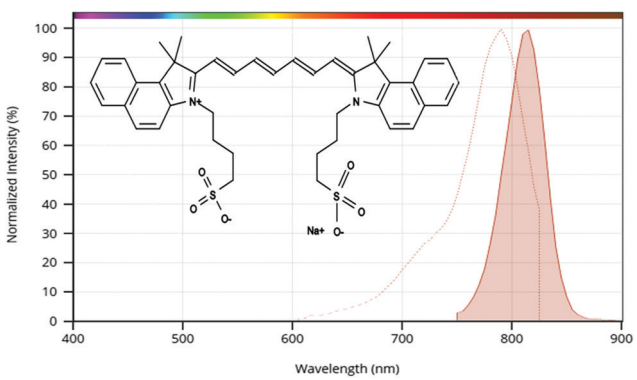

Fig. 4 Chemical structure of indocyanine green (ICG, CAS 3599-32-4) dye. Typical representation of ICG absorbance (dotted lines, maximum close to 800 nm) and emission (filled area, maximum close to 810 nm) spectra. Copyright © 2019 AAT Bioquest, Inc.

Published on 06 November 2020. Downloaded by University of Montpellier on 11/6/2020 4:15:11 PM.

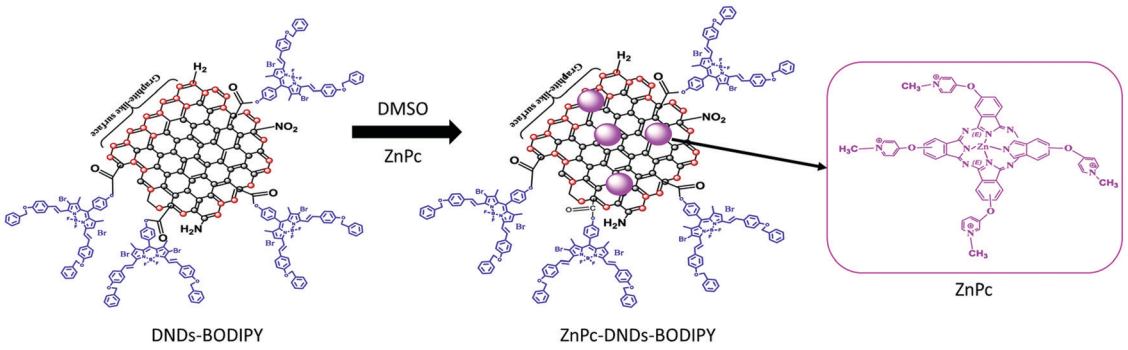

Fig. 5 Conjugation of zinc phthalocyanine derivative to DNDs–BODIPY systems *via* π–π stacking. Adapted from ref. 50, Copyright 2019, with permission from Elsevier.

for theranostics and low autofluorescence photobleaching in biological environments upon irradiation. This maximum was also found on the ICG-based core–shells. Hence, WST-1 assays *in vitro* demonstrated that, after irradiating NDs@PDA@ICG at 808 nm, glioblastoma cell viability completely dropped (10%), in comparison with dark samples (no laser, 80–90%), NDs@PDA (45%) and simple NDs (70%).[49] These results unveiled the suitable properties of these systems for PTT, but only above a certain concentration (20 or 40 μg mL^{-1}), depending on experimental conditions, cell nature and analytical techniques. Notably, core–shell NDs@PDA and NDs@PDA@ICG still had good stability after 5 on–off cycles of irradiation, confirming their good photothermal stability and also ICG high photostability due to strong interactions with PDA. As stated by the authors, their use for repeatable therapy could be an appealing option.[49]

In the experiments of Matshitse's group, three photosensitizers (*i.e.* DNDs, 3,5-di-*p*-benzyloxystyryl borondipyrromethene (BODIPY) chromophore and a zinc-based phthalocyanine-derivative (ZnPc)) were combined to assess their potential in PDT. The halogenated BODIPY dye was covalently attached to DNDs carboxyl functions *via* an esterification reaction. 2,9,16,23-Tetrakis[4-(*N*-methylpyridyloxy)]-phthalocyanine was basically adsorbed onto NDs surface *via* π stacking due to the presence of sp^2 graphite-like composition (Fig. 5). Triplet and singlet quantum yields assessment (in DMSO or in water with 1% v/v DMSO) showed higher scores when all elements were associated contrary to separated tests. Notably, the singlet quantum values were much higher since singlet oxygen is generated from triplet state, whose quantum yield improved. This could be also attributed to a synergistic effect of the photosensitizers, which provide more enhanced non-radiative transitions than radiative fluorescence. As a result, on MCF-7 breast cancer cells, highest PDT efficiency was obtained by gathering the three constituents, lowering the viability down to 21.4 ± 5% with the most concentrated sample at 50 μg mL^{-1}.[50] The authors claimed that positive zeta potentials of the structures could facilitate their anchoring and uptake in tumor cells.[50] Moreover, there was no relative toxicity in dark conditions (98.6 ± 3% viability), reinforcing the biocompatibility of these particles before PDT. Hence, this study highlighted the collaborative effects of photosensitive molecules with DNDs present in the core position due to the great linking potential of their surface.

In another work, Matshitse *et al.* associated the same metallophthalocyanine with other carbon-based nanomaterials (*i.e.* CDs and graphene-type QDs), but without BODIPY. As stated in their report, conjugation with NDs induced slightly more singlet oxygen species production than the other materials. In MCF-7 breast cancer cells, there was no dark toxicity of DNDs and ZnPc-NDs. However, excitation of ND–phthalocyanine for PDT evidenced up to 71.2% killing at 50 μg mL^{-1}, which was close to other carbon–phthalocyanine materials data.[51]

Regarding the photophysical assets, both surface charge and surface composition (specific functional groups and high wt% graphene-like sp^2) seem essential to build suitable PDT agents with nanodiamond.

Our teams recently developed a new strategy for drug delivery purposes. 4 nm hydroxylated nanodiamonds (NDs-OH) were encapsulated in periodic mesoporous organosilica (PMO) by a simple process. Ethenylene and ethylene-based PMO networks were both prepared, NDs being localized inside PMO nanoparticles. ND@PMO were tested *in vitro* by two-photon excitation PDT on MCF-7 cell line cultured in DMEM (see global protocol in Fig. 6). The photosensitizing capability of ND@PMO was proved by two-photon fluorescence imaging, using a confocal microscope, to evidence good ROS generation and cellular uptake. By irradiating at 800 nm and incubating for 20 h, at best 39% killing effect was observed. Adding doxorubicin led to enhanced results than bare ND@PMO with notably 57% cellular eradication. The developed systems were pH-actuable in lysosomal conditions as a fast and great release of DOX occurred right after adding 0.2 mol L^{-1} HCl in ultrapure water. Finally, when combining drug activity with PDT, up to 87% cancer cell death was reached at only 5 μg mL^{-1} in nanoparticles, promoting a good collaboration of both elements.[52]

Similar to PMO, phase-change material (PCM) nanoparticles have been investigated as a matrix containing DNDs (<10 nm) and chlorin e6 (Ce6) photosensitizer. Organic PCM made of lauric acid ($T_{melting}$ = 43.8 °C) reacted with NDs and Ce6 in a dichloromethane media containing sodium lauryl sulfate surfactant. By laser irradiation, an accurate on–off release of Ce6 from Ce6/ND/PCM platform was mediated by the thermosensitive

 This journal is © The Royal Society of Chemistry 2020

Published on 06 November 2020. Downloaded by University of Montpellier on 11/6/2020 4:15:11 PM.

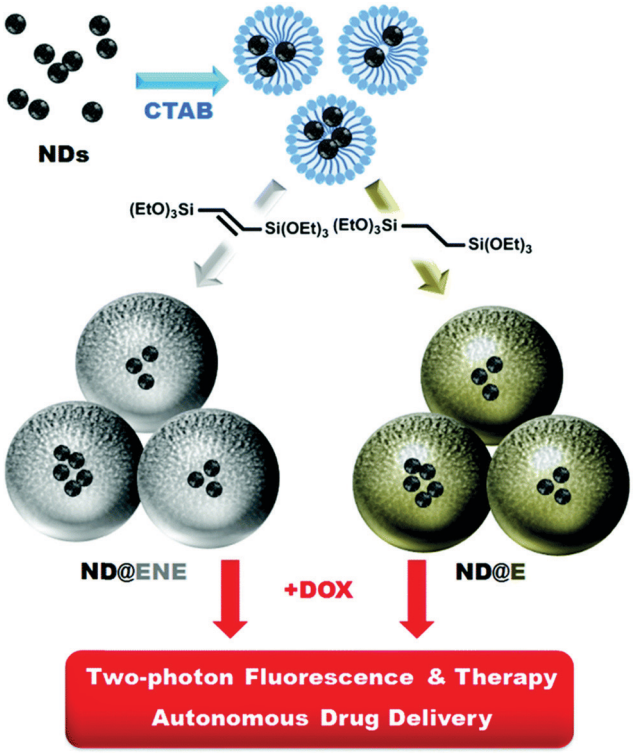

Fig. 6 Sol–gel synthesis of ND@ENE and ND@E, respectively from 1,2-bis(triethoxysilyl)ethene and 1,2-bis(triethoxysilyl)ethane, for two-photon fluorescence imaging, photodynamic therapy and doxorubicin delivery against MCF-7 breast cancer cells. Reproduced from ref. 52 with permission from the Royal Society of Chemistry.

properties of DNDs. Even if solutions average temperature was below PCM melting point, Ce6 was released from the matrix as NDs locally generated heat. Besides, ROS generation was enhanced while increasing the time of exposure. A synergistic result of singlet oxygen species and heat production led to interesting therapeutic effect in KB cells, a subline of HeLa cells (Fig. 7). The cell death area was enhanced by this PDT and PTT combination. *In vivo* assays in nude mice displayed continuous tumor size reduction for twelve days, after 4 min irradiations at day 0 and day 6. It was evidenced that Ce6 and DND particles were still present in sufficient quantities at the tumor site 10 days after intratumoral injection, suggesting a prospective capacity for unique or repeated laser exposure. Noteworthy, no specific conjugation was necessary to build these efficient nanodiamond-based structures that could be good systems for combined PDT and PTT, which harbor many unexplored strategies.[53]

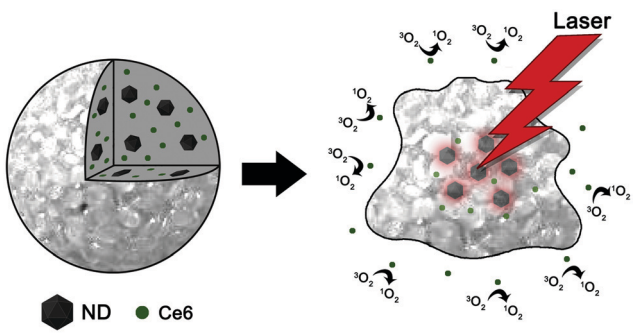

Fig. 7 Lauric acid-based phase change-material spheres incorporated with detonation nanodiamonds (DNDs) and chlorin e6 (Ce6) nanophotosensitizers. Ce6 release was induced by laser irradiation and DNDs local heat generation, respectively participating in singlet oxygen production for photodynamic therapy and tumor cells ablation by photothermal therapy. Reprinted from ref. 53, Copyright 2018, with permission from Elsevier.

In summary, due to their good optical properties and high loading capacities, nanodiamonds are increasingly implemented in new anticancer drug delivery and combined therapies projects (for instance phototherapy and medication delivery) where they can play a large variety of roles.

3. Nanodiamonds for bioimaging and labeling

In the last decades, the vast majority of biological studies using nanodiamonds and applied to bioimaging and labeling operations have been performed using FNDs. Having satisfactory photophysical properties to examine biological samples, and more generally a good contrast level, is obviously important in the election of the best probes, but other features have been identified to improve the feasibility and the quality of the measurements. In this section, recent applications main conclusions will be discussed.

Besides the fabrication of efficient doxorubicin delivery platforms (ND–PEG–GLY–DOX, presented in Section 2), Wei *et al.* created promising drug labels to follow their behavior in cells. Indeed, when entering in acidic intracellular lysosomes, the ester bound connecting ND–PEG and GLY–DOX moieties was cleaved. This induced not only the release of the drug in the tumor cells, but also synchronous fluorescence of GLY–DOX fractions. They were released about one hour after injection according to green fluorescence appearance. After 16 h, fluorescence was still bright, proving that such platforms could be used for long-term cell tracking, contrary to free GLY–DOX. Confocal microscopy imaging allowed confirming GLY–DOX course in time from lysosomes to nucleus, passing by the cytoplasm.[44] For instance, GLY–DOX fluorescence was overlapped with MCF-7 nuclei stained with Hoechst 33258 blue dye. This study, like many others before, suggests an obvious potential of ND-based materials for theranostics. Here, nanodiamonds were essentially acting as carriers as they displayed protection against degradation, low toxicity and better selectivity toward healthy tissues thanks to EPR effect.[44]

ND@PDA@ICG core–shells presented as photothermal agents in Section 2 were a good example of great imaging probes due to their good optical properties. Analyses of polydopamine and photostable indocyanine green, combined with nanodiamonds, revealed multiple assets for high resolution and prolonged fluorescence microscopy to illustrate the efficacy and selectivity of NIR irradiation treatment with the particles towards glioma cancer cells.[49]

Dong *et al.* described recently the synthesis and characterization of fluorescent polymer-grafted nanodiamonds.

Published on 06 November 2020. Downloaded by University of Montpellier on 11/6/2020 4:15:11 PM.

Prepared by a simple synthetic route, the designed composites held great promises for bioapplications, both in drug delivery and imaging. Hydroxylated DNDs were modified with tosyl chloride. Then, 2-ethyl-2-oxazoline ring-opening reaction with tosyl led to chain polymerization. At the same time, 3-(10-hexadecyl-10*H*-phenothiazin-3-yl)-2-(4-hydroxyphenyl)acrylonitrile specific dye was functionalized onto NDs surface by nucleophilic substitution (Fig. 8). This conjugated compound exhibited strong and stable orange fluorescence, following aggregation-induced emission aspect.[70] As demonstrated by CCK-8 assays in L929 mouse cells, the particles were non-toxic at higher concentrations (120 μg mL^{-1}, 85% viability after 48 h) than classical cell imaging agents. This great biostability was connected to polymer chains hydrophilicity, which was also responsible for the considerable systems dispersibility in water. In addition, confocal laser scanning microscopy showed good uptake in L929 cells with a large distribution in the cytoplasm. Thus, these particles could be adapted to serve as theranostic platforms, for instance with an active drug release or in PDT.[54]

Nanodiamonds fluorescence properties are in some cases not enough for selected applications. The innovative material fabricated by Qin *et al.* for therapy and diagnosis using RE-based complexes had enhanced optical properties. The coordination compounds exhibited an intense and remarkably extended red fluorescence (613 nm under UV excitation at 365 nm, best intensity reached after 0.68 ms) compared to other well-known biomarkers. Moreover, the *in vivo* imaging in shaved Kunming mice demonstrated a good fluorescence stability even 4 h after subcutaneous injection. Additionally, these ND-based complexes held excellent paramagnetic properties from Gd^{3+}, making these complexes potent CAs for T_1 weighted MRI.[46] An optimal combination of dual-modal imaging capacities should be very interesting for further bioapplications studies such as targeted theranostic.

In order to perform skin tissues imaging and sensing, together with active materials for wound healing or skin diseases, nanodiamonds might be of great interest due to their small size and good biocompatibility. In this context, Perevedentseva *et al.* evaluated the skin penetration capability of different carboxylated NDs in a murine skin model by the combined power of three optical and spectroscopic techniques. To do this, DNDs (3 to 10 nm) or FNDs (50 or 100 nm) were purified and carboxylated in acidic conditions. Then, they were added in neutralized aqueous PBS suspensions at a concentration of 1 mg mL^{-1} and incubated for 24 h in different environments with mice skin pieces. All the applied NDs were able to cross the skin barrier and penetrate the different layers of the epidermis, but the relative penetration mechanisms and the ultimate re-distribution are still requiring further investigations. FNDs of 100 nm seem to be well-suited specimens for multimodal imaging, notably as contrast agents for optical coherence tomography.[55] In addition, the good dispersion of NDs within the tissues suggested that they could be applied for transcutaneous delivery with targeting species for selective treatment. Nonetheless, fluorescence lifetime imaging with two-photon excitation at 800 nm highlighted that the NIR fluorescence of NDs was masked by tissues' autofluorescence, which was brighter and longer. This question will certainly be investigated in next studies.

Nunn's team described innovative and affordable carbon dot (CD) decorated primary DND particles (CD-DNDs). These particles were obtained after several physicochemical treatments of polydisperse NDs, in order to have 5 nm isolated NPs in the colloids.[56] They showed comparable photoluminescence intensities to the 20 nm reference NDs possessing N-V color centers, one key defect responsible for diamond fluorescence. Laser excitation was performed at 532 nm, which is a well-suited wavelength for ND N-V defects, but not much adapted for CD whose optimal excitation range is in UV-blue, underlining the presumption that CD-DNDs held striking potential. *In vitro* assays with MDA-MB-231 breast cancer cells (Fig. 9) confirmed the ability for bioimaging applications as the confocal microscopy images displayed good fluorescence after cellular uptake, with different levels of NPs aggregation.[56] Moreover, CD-DNDs exhibited good biocompatibility in zebrafish during the development of embryos. Nonetheless, the clustering effect

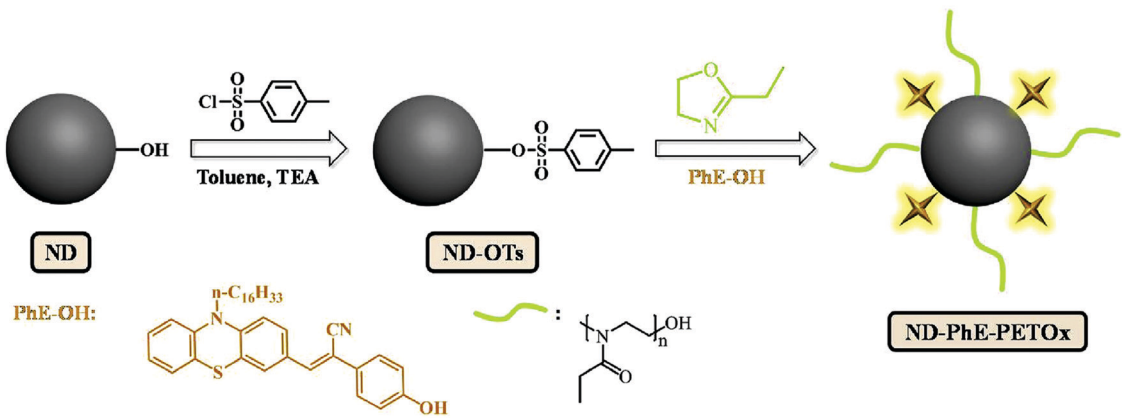

Fig. 8 Representation of hydroxylated NDs surface modification with tosyl chloride, acrylonitrile derivative and specific dye (3-(10-hexadecyl-10*H*-phenothiazin-3-yl)-2-(4-hydroxyphenyl)acrylonitrile: PhE-OH) for bioimaging through fluorescence attributes. Reprinted from ref. 54, Copyright 2020, with permission from Elsevier.

 This journal is © The Royal Society of Chemistry 2020

Published on 06 November 2020. Downloaded by University of Montpellier on 11/6/2020 4:15:11 PM.

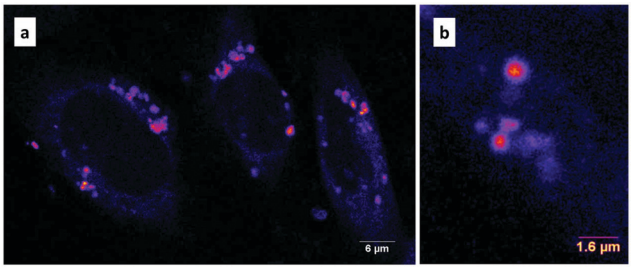

Fig. 9 Visualization of 5 nm CD-DNDs groups into MDA-MB-231 breast cancer cells excited at 488 nm by argon laser irradiation. (a) Lower magnification level. (b) Higher magnification level. Original colors modified by the authors. Reproduced with permission from ref. 56, Copyright 2018 IOP Publishing Ltd.

of the particles will surely need the grafting of chemical functions to apply these NPs in the biomedical field. For instance, examining questions of clearance and accumulation in various organs and blood streams would be relevant. These last years, due to its high resolution, electronic microscopy has been much employed in combination with optical imaging to better understand the living. To this extent, CD-DNDs could perfectly match with correlative light-electron microscopy imaging.[18]

Recent experiments described a few more interesting characteristics of materials composed of nanodiamonds: low toxicity in normal tissues, good protection against degradation, along with sufficient biocompatibility and dispersibility, and high selectivity levels to target molecules and to bypass natural barriers like skin layers.[44,49,54,55] To answer the current challenges, more attention should be given to the use of NDs in multimodal imaging and emerging technologies by tapping their multiple intrinsic defects and versatile surface properties.[56] In this respect, chemical modification and purification protocols seem fundamental to design efficient bioactive systems.

4. Nanodiamonds for fighting antibacterial infections

The use of nanodiamonds against antimicrobial infections using classic antibiotic, protein and carbohydrate delivery has already proven its worth even though there is still a lot of progress to make such as developing new strategies considering release specifications.

Rouhani and Singh evaluated the potential of polyethylene imine (PEI)-grafted Fe_3O_4 and ND hybrid platforms. Three different methodologies were elaborated to associate the polymer and the NPs, before amoxicillin (AMOX) loading by covalent bonding with PEI. First, neither AMOX nor NDs attachment was visible by previously mixing ND–PEI and Fe_3O_4–PEI particles (Fig. 10a). Then, another protocol with ND loading on Fe_3O_4–PEI prior to PEI loading showed high particle diameters (Fig. 10b). Finally, a third approach consisting in the preparation of ND–Fe_3O_4 stable particles by mixing for 24 h, collecting with a magnet, and then, loading NPs with PEI, was adopted (Fig. 10c). Their conclusions highlighted the

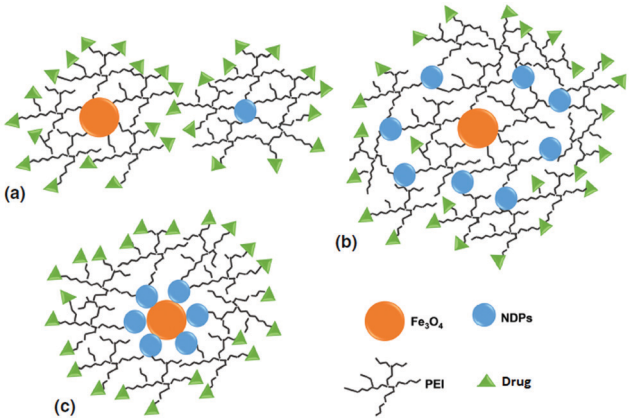

Fig. 10 Three different synthesis strategies of magnetite and ND particles with PEI for amoxicillin transport. (a) Fe_3O_4–PEI and ND–PEI mixture. (b) ND loaded in Fe_3O_4–PEI particles. (c) PEI loaded in ND–Fe_3O_4 particles. Adapted from ref. 58.

good suitability of the last system as it offered a continuous liberation of AMOX (cumulatively, 77% at 37 °C) in acidic conditions for 180 h. In the contrary, other protocols, including experiments without any ND, showed effective drug delivery for 24 h only, and more agglomeration occurred, leading to an inconstant release.[58] Interaction of ND particles with hydrophobic molecules seem to be influencing their release from multicomponent platforms.

Just as drug release, cytotoxicity level and biodegradability are important parameters in the light of the cures for bacteria eradication. Chang *et al.* studied the role of NDs decorating silver nanoparticles (Ag NPs) as the former can be highly biocompatible and the latter is a well-known natural antibiotic. The main target of this study is to design a useful technique to face common issues encountered with high doses of nano-sized Ag regarding antimicrobial resistance, namely cytotoxicity and aggregation. First, Ag NPs were capped with citrate through chemical reduction using $AgNO_3$, reaching a size of 17 ± 6 nm. Then, the Ag NPs were bound to polyarginine (PA)-coated NDs, thanks to the reaction between carboxylate functions of NDs with amine moieties on PA. At the end, BSA serum albumin (BSA) was coated onto the nanoparticles, forming Ag–ND@BSA nanoplatforms of 120 ± 30 nm, able to interact with classical bacteria (1–2 µm). Optical densities and adenosine triphosphate production level tests on *E. coli* strains confirmed this statement. Compared to the control data, Ag–ND@BSA demonstrated considerable bactericidal activities all along 36 days experiments at 250 µg mL^{-1}, which was far below the estimated half-maximal cytotoxic concentration (CC_{50}) value. In addition, ROS levels and cell viability assays were both in agreement with a low toxic response of the nanoparticles on various human cells, even at 500 µg mL^{-1} and after three days of analyses.[59] Compared to previous studies with similar efficacy, the main outcomes with ND and BSA were that antibiotic doses were decreased, given the high selectivity for *E. coli*.

Even more interestingly, recent studies described NDs direct action against microbes by different strategies.[60,61] In artificial

Published on 06 November 2020. Downloaded by University of Montpellier on 11/6/2020 4:15:11 PM.

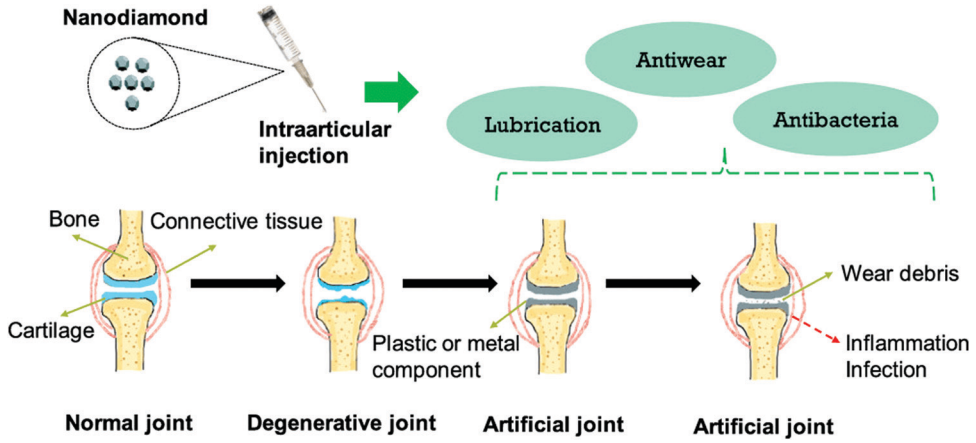

Fig. 11 Multifunctional features of nanodiamonds injected in artificial joints. Reprinted with permission from ref. 60. Copyright 2019 American Chemical Society.

joints and implants, poor material mechanical properties and infectious risks are frequent drawbacks. In their work, Shirani *et al.* assessed the bactericidal and tribological effects of DNDs in titanium (Ti)–polyethylene artificial joints interfaces to reduce inflammation and infection issues (Fig. 11). Raman and energy-dispersive spectroscopy analyses of sliding contact areas between Ti ball and polymer surface demonstrated that NDs were mostly present inside the wear track, which corroborated with low friction and wear coefficients. Considering these good mechanical properties of NDs, enlarged lifetime for such implants and better safety for the patients could be reached. Moreover, highly concentrated solutions of NDs in presence of BSA were non-toxic on MC3T3-E1 bone cells, contrasting with 10 to 20% of viable cells with bare NDs. Following this, the antibacterial effectiveness of BSA-stabilized NDs was almost inexistent while aggregated NDs greatly impacted *S. aureus* growth, by surface carboxyl moiety interaction with bacteria peptidoglycan layer. Unexpectedly, there was no bactericidal effect on *E. coli* strains.[60] This result could be related to the cell wall composition (*E. coli* has a phospholipidic external membrane that *S. aureus* does not have) or could originate from too close surface potential values of diamond and *E. coli* negatively charged surfaces. Zeta potential of bacteria is an important parameter to consider in cell damaging capabilities and can be tuned by several factors such as high temperature, pH or surfactants.[71,72] For future *in vivo* applications, a compromise between BSA anti-flocculation nature and NDs bacterial disruption ability should be necessary. One can say that NDs low aggregation state is generally characteristic of high viability towards cells. Thus, modifying NDs surface with suitable functional groups and targeting moieties could help to provide superior benefit-risk balance.

Comparably, poly(methyl methacrylate) (PMMA), a well-known material for dental applications, does not exhibit ideal mechanical properties. Consequently, doping the systems with various NPs has been tested and brought a successful contribution. In a late study, DNDs were experimented for this purpose by Mangal's team. Different amounts of nanoparticles (from 0.1 to 0.5 wt%) were incorporated within methyl methacrylate monomeric solution. Then, adding autogenous PMMA resin in the mixture generated autogenous polymerization. Better efficiency was provided by homogenous distribution of the particles in the matrix, which was possible here by simple stirring and ultrasonication steps during production of the hybrid materials. ND–PMMA mechanical properties were assessed by physical measurements, concluding to enhanced flexural strength and elastic modulus compared to references holding ZrO particles or without doping. To go further, antimicrobial properties of ND–PMMA were assessed on *Candida albicans* (renowned fungi for its involvement in many oral infections) and showed better resistance over controls. In addition, ND-based samples demonstrated a significant biofilm growth inhibition on salivary-derived biofilms from human donors without dental problems.[61] Over and above their good mechanical properties, these patterns could be good fungicide agents. Further investigations about their impact on microbial strains would be interesting.

According to previous studies, diamond-like carbon (DLC) coatings are also competent materials against bacteria in addition to their resistance to corrosion phenomena. In a very recent work, DNDs were carboxylated by oxidation during thermal annealing, and then suspended in hexane to form DLC–ND suspension. To enhance Ti_6Al_4V substrate compatibility with ND-doped DLC, a thin film of silane derivative was applied on the alloy before performing plasma-enhanced chemical vapor deposition. During the evaporation process, methane plasma generating hydrogen species stabilized DLC–ND drops covering on Si–H interlayer. The final multilayer materials presented interesting corrosion rates, twice lower than DLC or Ti_6Al_4V alone. Alongside anticorrosive properties, antibacterial activity of these materials was tested on *E. coli* strains. The article pointed out the potential role of agglomerated NDs in damaging cell walls, leading to cell apoptosis. With 1% w/v ratio in ND, coatings induced 95% bacteria growth inhibition after 6 h (Fig. 12), whereas bare DLC films achieved only 30% inhibition. Nevertheless, after 18 h incubation, the ND quantity was apparently not enough to block multiplication of remaining bacteria, as 74% bacteria were still alive in the culture media and extra studies would be needed to know the leeway regarding ND concentrations without being too much toxic for potent bioapplications.[62]

This journal is © The Royal Society of Chemistry 2020

Published on 06 November 2020. Downloaded by University of Montpellier on 11/6/2020 4:15:11 PM.

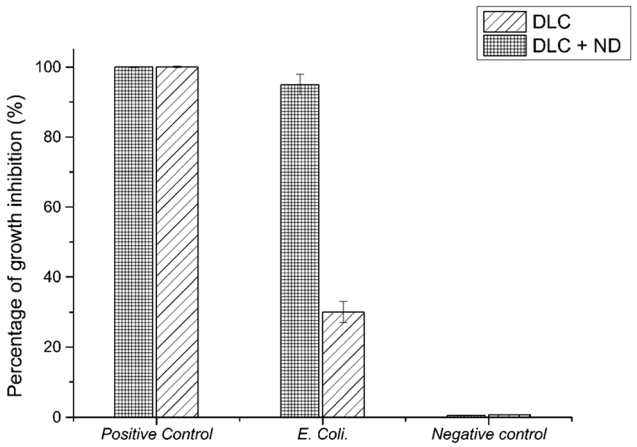

Fig. 12 Antimicrobial capacity of DLC coatings doped or not with 1% w/v NDs and after 6 h incubation with *E. coli* strains. The authors results demonstrated significant growth inhibition with DLC–ND systems compared to streptomycin positive control (15 mg mL^{-1}) and ultrapure water negative control. Reprinted from ref. 62, Copyright 2019, with permission from Elsevier.

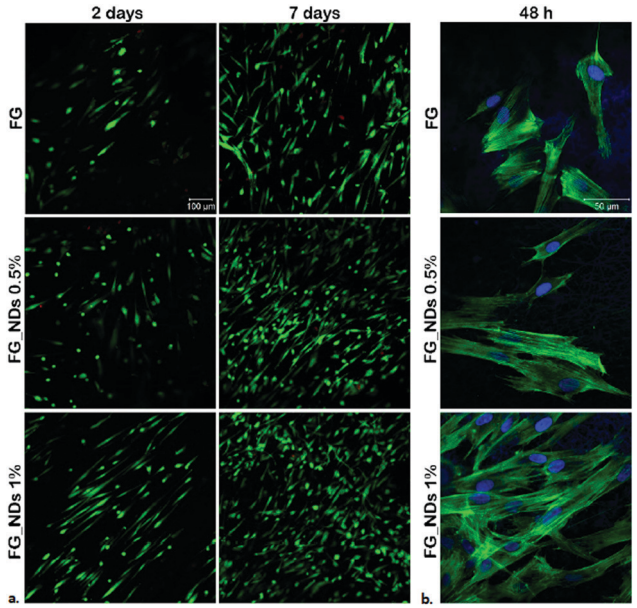

Fig. 13 Confocal imaging of fish gelatin scaffolds with different NDs weight ratios incubated for different times in hASCs. (a) Live/dead assays of hASCs after 2 days and 7 days. Dead cells are represented in red, while cell proliferation is visible in green. (b) F-Actin filaments (green) production by hASCs (nuclei in blue) after 48 h incubation. Adapted from ref. 64 with permission from MDPI.

To sum up, these latest projects demonstrated the reinforcing role of NDs in the treatment of microbial infections, including serious features, especially as an active moiety against pathogen proliferation and biofilm growth.

5. Tissue repairment strategies using nanodiamonds' features

In one recent study, Houshyar and co-workers presented an innovative strategy to improve wound healing quality. DNDs were dispersed in a DMF solution containing poly-ε-caprolactone. Then, the mixture was electrospun under precise conditions to design controlled nanofibers networks. According to their results, DNDs were significantly located at the surface of the fibers, as surface energy increased with increasing DNDs weight concentration from 0 to 5%. This resulted in better capillarity and optimal moisture handling in the tissues due to the presence of several OH polar functions from DNDs, originating from carboxyl and hydroxyl groups. In addition to good viability, better cell proliferation was observed on Chinese hamster ovarian cell models, as higher hydrophilicity allowed better interaction. Thus, these ND-based platforms could promote the multiplication of epithelial cells taking part in internal and external surfaces recovery. At the same time, they displayed great anti-adhesive properties against *S. aureus* cells, typically involved in wound infections issues. Confocal microscopy images revealed that nanocomposites with 5% DNDs significantly inhibited bacterial growth when compared with the polymer alone.[63] To summarize, tunable surfaces and properties of nanodiamonds particles make them very suitable reinforcements in hybrid materials for tissue repair.

Nanodiamonds have recently been combined with biopolymers, stem cells and nanoparticles as potent agents for enhanced tissue reconstruction. Selaru's team fabricated anisotropic fibrous scaffolds of fish gelatin (FG) with a low content of NDs (0%, 0.5% and 1%) and brought them in contact with human adipose-modified mesenchymal stem cells (hASCs) cultures. Gelatin could be a good substrate for cell growth in tissue engineering applications due to its viscoelasticity and rich chemical composition besides the structures tunability brought by electrospinning technology. As shown in Fig. 13a, in presence of aggregated NDs in FG fibers, viability of hASCs increased over time, as cell death occurrence (small red dots) became relatively rare and living cells number boomed (their multiplication is visible in green). Moreover, hASCs behavior changed in terms of adhesion and growth, with a tendency to form groups where NDs were located. In Fig. 13b, hASCs stacks (nuclei represented in blue on the picture) produced more and more F-actin filaments (in green) after 48 h of incubation with scaffolds displaying extended amounts of NDs. These results suggested a much better interaction between fibers and stem cells with 1% of NDs, thus confirming the good biocompatibility of the nanocomposites and enhanced metabolic activity of hASCs. These systems showed very promising outcome and could be further developed in the treatment of harmed tissues or for neuroregeneration.[64]

6. Other challenges around nanodiamonds relevancy

Nanodiamonds interactions with biological environments and their global behavior are still unclear. Their biocompatibility and their relevancy in some specific therapies have been questioned in recent reports. One tremendous example was

Published on 06 November 2020. Downloaded by University of Montpellier on 11/6/2020 4:15:11 PM.

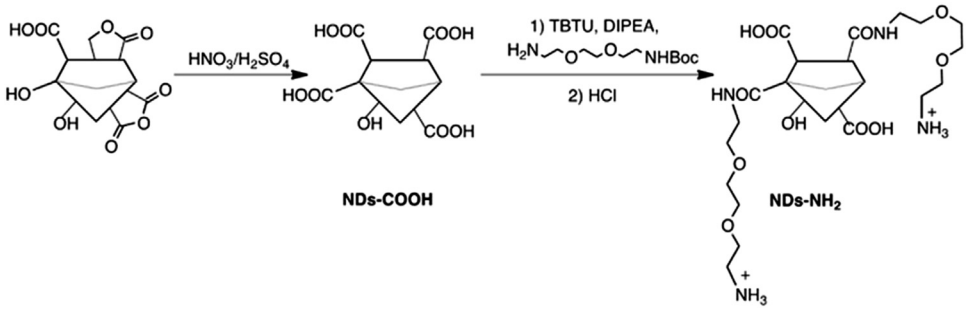

Fig. 14 Sulfonitric acid treatment of 4–5 nm pristine nanodiamond particles to obtain purified NDs-COOH, followed by carboxylate activation using 2-(1*H*-benzotriazole-1-yl)-1,1,3,3-tetramethylaminium tetrafluoroborate (TBTU), *N*,*N*-diisopropylethylamine (DIPEA) and amide formation using *N*-Boc-amino-diethoxyethylamine to obtain NDs-NH_2. Functional groups quantity and structure proportions were arbitrary drawn. Adapted from ref. 67, Copyright 2020, with permission from Elsevier.

about the treatment of glaucoma, where lysozyme-activated desorption of timolol maleate drug encapsulated in ND-based nanogels furnished promising results when deposited into therapeutic contact lenses, demonstrating controlled and prolonged release competency.[15,73] In these systems, NDs acted as mechanical performance enhancer and promoted efficient drug delivery.

Lately, ND-based carriers of dexamethasone (DEX) also showed active release, this time as a potent solution to treat shocks due to DEX great immunomodulatory and anti-inflammatory properties. Unfortunately, this well-known glucocorticoid presents the inconveniency to display low selectivity during its delivery. To answer this, two strategies using 25 nm DNDs were compared: ND@DEX and ND@SiO_2@DEX core–shells with a mesoporous silica interlayer. In the second method, carboxylated NDs were coated by a sol–gel process using tetraethyl orthosilicate. Then, for both protocols, a DEX solution was added to ND or ND@SiO_2 particles in cyclohexane to form the final core–shells. The ones with silica allowed at best 30 wt% loading with a sustainable drug release, while the former transported only a short content (<1 wt%) that was almost totally released in one hour in various buffer solutions.[65] According to the authors, the ND@SiO_2@DEX features could be handy to enhance anaphylactic shocks' treatment, but also in other cures in which DEX is already commercialized.

In another study conducted on dexamethasone medicinal effects, materials containing aggregated diamonds were experimented in the context of rheumatoid arthritis. In more details, octadecylamine (ODA)-grafted NDs were synthesized by chlorination of the carboxylated surface of 5 nm NDs prior to reaction with ODA, and the biggest aggregates were removed by washing and centrifugation processes. Then, dexamethasone was adsorbed onto the particles by a simple condensation reaction protocol overnight. These anti-inflammatory and pro-regenerative probes were studied in human macrophages samples and were incorporated in arthritic mice limbs to get some information about the immunorestrictive power of the materials against collagen type II-induced arthritis. In contrast with control representative, 5 μL injections of solutions containing ND–ODA (15 μg mL^{-1}), DEX (0.1 μg mL^{-1}) or ND–ODA/DEX (respectively 16 μg mL^{-1} and 0.1 μg mL^{-1}) lowered the expression of pro-inflammatory mediators and partially inhibited macrophages invasion in the joints. Therefore, *ex vivo* microcomputed tomography images showed reduced bone degradation with these solutions, but the authors highlighted opposite effects when working at higher ND–ODA concentration (50 μg mL^{-1}), meaning that immune cells modulation and, thus, therapeutic efficacy, are dose-dependent. Further *in vivo* inquiries will probably give more information concerning the pro-regenerative aptitude of these ND-based structures.[66]

In Fusco's group recent report, human peripheral blood mononuclear cells (PBMCs) were chosen as a model to study biomedical scenarios of NDs interaction with the human body. The aim was to assess immune responses toward functionalized NDs by strongly copying an *in vivo* behavior. Carboxylated (NDs-COOH) and amino-functionalized diamonds (NDs-NH_2), prepared as shown in Fig. 14, were compared. Confocal microscopy images revealed their efficient internalization in PBMCs cytoplasm probably due to their glycolic chain targeting capacity. As stated by multiple gene expression and protein analyses, carboxylated NDs induced significant undesirable pro-inflammatory responses. On the contrary, the authors described that amino-terminated NDs were more immunocompatible, which could be related to their better dispersion state.[67] Thereby, grafting antibodies or other targeting molecules onto amino-NDs to further study the behavior of the immune system would be worthwhile to extend the knowledge about many diseases and improve their treatment and diagnosis.[67]

To resume, nanodiamonds are presented as promising agents for tissue regeneration and several diseases when combined with other entities (biopolymers, drugs, nanoparticles) in different arrangements (fibrous scaffolds or multifunctional core–shell). By tuning the metabolism of specific biomolecules and by further exploring immunomodulatory processes, enhanced therapies might be reachable. In parallel, care must be taken in designing materials that do not adversely affect the immune system and the body integrity.

7. Conclusion

Nanodiamonds already exhibited significant action in tens of bioapplications. The latest approaches and associated results summarized in our review indicated the large application scope of these tiny little gems. As highlighted in the most recent

 This journal is © The Royal Society of Chemistry 2020

Published on 06 November 2020. Downloaded by University of Montpellier on 11/6/2020 4:15:11 PM.

works, rightfully tailored NDs display enhanced biocompatibility and their functionalization with targeting molecules and different moieties led to better selectivity to specific body cells, with generally lower toxicity in healthy tissues, better cellular uptake and sustainable release. Thus, their use as drug carriers for better therapeutic balance is no longer to prove. Nonetheless, the use of aggregated NDs as active therapeutic agents will require more studies to figure out biodistribution and elimination concerns.

The great optical properties of NDs make them suitable for bioimaging, sensing, labeling and phototherapies. For this reason, the scientific community experimented them in a large range of disease treatments and analytical technologies, leading to some input from their use. Moreover, the outlined papers demonstrated that fluorescence is not the only noticeable characteristic of NDs for diagnosis and drug delivery tracking. Their intrinsic core defects and external surface properties, as well as their covalent and non-covalent environment are a reservoir of striking potentials for theranostics and multimodal monitoring with their thermal properties for sensing and phototherapy, and their paramagnetic defects for MRI or correlative light-electron microscopy.

Diamond mechanical attributes are also very interesting in artificial joints and implants, providing lubrication and tribological properties. In addition, better antiproliferative effects were evidenced on fungi and bacteria proliferation when materials contained NDs. Similar systems could promptly reduce inflammation and infection symptoms in future wound healing and tissue regeneration applications.

One main recent advancement is the immunomodulatory competency of NDs in the cure of a few diseases and stimulated tissue engineering with human mesenchymal stem cells. Puzzling out the biomechanisms behind those themes will certainly expand the knowledge associated to immune system behavior, and NDs could play a leading role for this purpose.

Consequently, the clinical translation of ND particles is currently a serious challenge for the scientific community as many parameters should be validated: appropriate dispersibility to bypass the biological barriers, right size and concentration for safe elimination and a better knowledge about global pharmacokinetics.[74,75] To elucidate this, reproducible and rigorous procedures should be performed to rightly identify the best ND-based systems able to outpace the clinical standards in terms of safety and efficacy.[3,76,77] In addition, this translation will require costless manufacturing as most ND synthesis pathways are expensive. Empowering this research field could be worthy, viewing the current elaborated studies and the first clinic validation of a ND-based biomaterial.[78]

From all this information and because nanodiamond-based solutions are more and more studied and commercialized for bio-relative applications, nanodiamonds, among all nanomaterials, are frequently affiliated to a golden future.[16,79,80]

Conflicts of interest

There are no conflicts to declare.

References

1 K. J. van der Laan, M. Hasani, T. T. Zheng and R. Schirhagl, *Small*, 2018, **14**, 1703838.
2 R. Namdar and S. Nafisi, *Drug Discovery Today*, 2018, **23**, 1152–1158.
3 M. S. Ali, A. A. Metwally, R. H. Fahmy and R. Osman, *Int. J. Pharm.*, 2019, **558**, 165–176.
4 M. Ozawa, M. Inaguma, M. Takahashi, F. Kataoka, A. Kruger and E. Osawa, *Adv. Mater.*, 2007, **19**, 1201–1206.
5 G. Y. Gao, Q. Y. Guo and J. F. Zhi, *Small*, 2019, **15**, 1902238.
6 G. Reina, L. Zhao, A. Bianco and N. Komatsu, *Angew. Chem., Int. Ed.*, 2019, **58**, 17918.
7 A. Rehman, S. Houshyar and X. Wang, *J. Biomed. Mater. Res., Part A*, 2020, **108**, 906–922.
8 D. Amans, A. C. Chenus, G. Ledoux, C. Dujardin, C. Reynaud, O. Sublemontier, K. Masenelli-Varlot and O. Guillois, *Diamond Relat. Mater.*, 2009, **18**, 177–180.
9 J. E. Butler and A. V. Sumant, *Chem. Vap. Deposition*, 2008, **14**, 145–160.
10 F. Gorrini, M. Cazzanelli, N. Bazzanella, R. Edla, M. Gemmi, V. Cappello, J. David, C. Dorigoni, A. Bifone and A. Miotello, *Sci. Rep.*, 2016, **6**, 35244.
11 N. Panwar, A. M. Soehartono, K. K. Chan, S. Zeng, G. Xu, J. Qu, P. Coquet, K. T. Yong and X. Chen, *Chem. Rev.*, 2019, **119**, 9559–9656.
12 H. Zhu, Y. Wang, A. Hussain, Z. P. Zhang, Y. Y. Shen and S. R. Guo, *J. Mater. Chem. B*, 2017, **5**, 3531–3540.
13 J. S. Xiao, X. P. Duan, Q. Yin, Z. W. Zhang, H. J. Yu and Y. P. Li, *Biomaterials*, 2013, **34**, 9648–9656.
14 Y. Xiong, X. Tian and H.-w. Ai, *Bioconjugate Chem.*, 2019, **30**, 1297–1303.
15 S. Chauhan, N. Jain and U. Nagaich, *J. Pharm. Anal.*, 2020, **10**, 1–12.
16 N. Prabhakar and J. M. Rosenholm, *Curr. Opin. Colloid Interface Sci.*, 2019, **39**, 220–231.
17 Y.-K. Tzeng, O. Faklaris, B.-M. Chang, Y. Kuo, J.-H. Hsu and H.-C. Chang, *Angew. Chem., Int. Ed.*, 2011, **50**, 2262–2265.
18 M. D. Torelli, N. A. Nunn and O. A. Shenderova, *Small*, 2019, **15**, 1902151.
19 R. Fischer, C. O. Bretschneider, P. London, D. Budker, D. Gershoni and L. Frydman, *Phys. Rev. Lett.*, 2013, **111**, 057601.
20 J. P. King, K. H. Jeong, C. C. Vassiliou, C. S. Shin, R. H. Page, C. E. Avalos, H. J. Wang and A. Pines, *Nat. Commun.*, 2015, **6**, 8965.
21 S. M. Schrader, J. Vaubourgeix and C. Nathan, *Sci. Transl. Med.*, 2020, **12**, eaaz6992.
22 M. Ye, Y. Zhao, Y. Wang, N. Yodsanit, R. Xie and S. Gong, *Adv. Funct. Mater.*, 2020, **30**, 2002655.
23 M. Sutradhar, H. J. Raj, P. Trigunait, S. Chhaule, R. Ray, U. Roy, R. Das and A. Ghosh, *J. Evol. Med. Dent. Sci.*, 2020, **9**, 2284–2288.
24 W. Cao, X. Wang, Q. Li, X. Peng, L. Wang, P. Li, Z. Ye and X. Xing, *Mater. Sci. Eng., C*, 2018, **92**, 307–316.
25 B. A. F. de Camargo, D. E. S. Silva, A. N. da Silva, D. L. Campos, T. R. M. Ribeiro, M. J. Mieli, M. B. T. Zanatta,

Published on 06 November 2020. Downloaded by University of Montpellier on 11/6/2020 4:15:11 PM.

P. B. da Silva, F. R. Pavan, C. G. Moreira, F. A. Resende, A. A. Menegario, M. Chorilli, A. V. D. Netto and T. M. Bauab, *Mol. Pharmaceutics*, 2020, **17**, 2287–2298.
26 A. Kumar, S. Gahlyan, R. Thakur, S. Devi and S. Duhan, *J. Nanosci. Nanotechnol.*, 2020, **20**, 4210–4215.
27 Y. C. Yeh, T. H. Huang, S. C. Yang, C. C. Chen and J. Y. Fang, *Front. Chem.*, 2020, **8**, 286.
28 H. Zazo, C. I. Colino and J. M. Lanao, *J. Controlled Release*, 2016, **224**, 86–102.
29 I. P. Chang, K. C. Hwang, J.-a. A. Ho, C.-C. Lin, R. J. R. Hwu and J.-C. Horng, *Langmuir*, 2010, **26**, 3685–3689.
30 O. Faklaris, D. Garrot, V. Joshi, J.-P. Boudou, T. Sauvage, P. Curmi and F. Treussart, *J. Eur. Opt. Soc.-Rapid Publ.*, 2009, **4**, 09035.
31 S. Kühn, C. Hettich, C. Schmitt, J.-P. Poizat and V. Sandoghdar, *J. Microsc.*, 2001, **202**, 2–6.
32 J. H. Li, R. Yu and X. Yang, *Appl. Phys. B: Lasers Opt.*, 2013, **111**, 65–73.
33 P. Reineck, D. W. M. Lau, E. R. Wilson, K. Fox, M. R. Field, C. Deeleepojananan, V. N. Mochalin and B. C. Gibson, *ACS Nano*, 2017, **11**, 10924–10934.
34 H. Yokota, *Biochim. Biophys. Acta, Gen. Subj.*, 2020, **1864**, 129362.
35 K. Turcheniuk and V. N. Mochalin, *Nanotechnology*, 2017, **28**, 252001.
36 S. Szunerits, A. Barras and R. Boukherroub, *Int. J. Environ. Res. Public Health*, 2016, **13**, 413.
37 J. Jira, B. Rezek, V. Kriha, A. Artemenko, I. Matolinova, V. Skakalova, P. Stenclova and A. Kromka, *Nanomaterials*, 2018, **8**, 140.
38 A. Chatterjee, E. Perevedentseva, M. Jani, C. Y. Cheng, Y. S. Ye, P. H. Chung and C. L. Cheng, *J. Biomed. Opt.*, 2015, **20**, 051014.
39 S. Pacelli, F. Acosta, A. R. Chakravarti, S. G. Samanta, J. Whitlow, S. Modaresi, R. P. H. Ahmed, J. Rajasingh and A. Paul, *Acta Biomater.*, 2017, **58**, 479–491.
40 A. Sigaeva, A. Morita, S. R. Hemelaar and R. Schirhagl, *Nanoscale*, 2019, **11**, 17357–17367.
41 Y. Yu, X. Yang, M. Liu, M. Nishikawa, T. Tei and E. Miyako, *Nanoscale Adv.*, 2019, **1**, 3406–3412.
42 W. Long, H. Ouyang, W. M. Wan, W. F. Yan, C. Q. Zhou, H. Y. Huang, M. Y. Liu, X. Y. Zhang, Y. L. Feng and Y. Wei, *Mater. Sci. Eng., C*, 2020, **108**, 110413.
43 Y. Dong, R. X. Cao, Y. Q. Li, Z. Q. Wang, L. Li and L. Tian, *RSC Adv.*, 2015, **5**, 82711–82716.
44 S. G. Wei, L. Li, X. B. Du and Y. Q. Li, *J. Mater. Chem. B*, 2019, **7**, 3390–3402.
45 V. S. Madamsetty, A. Sharma, M. Toma, S. Samaniego, A. Gallud, E. F. Wang, K. Pal, D. Mukhopadhyay and B. Fadeel, *Nanomedicine*, 2019, **18**, 112–121.
46 S. R. Qin, Q. Zhao, Z. G. Cheng, D. X. Zhang, K. K. Zhang, L. X. Su, H. J. Fan, Y. H. Wang and C. X. Shan, *Diamond Relat. Mater.*, 2019, **91**, 173–182.
47 S. Garg, A. Garg, N. K. Sahu and A. K. Yadav, *Diamond Relat. Mater.*, 2019, **94**, 172–185.
48 A. Hekmat, F. Salavati and S. H. Tackallou, *Protein J.*, 2020, 268–283, DOI: 10.1007/s10930-020-09882-4.
49 D. Maziukiewicz, B. F. Grzeskowiak, E. Coy, S. Jurga and R. Mrowczynski, *Biomimetics*, 2019, **4**, 3.
50 R. Matshitse, B. P. Ngoy, M. Managa, J. Mack and T. Nyokong, *Photodiagn. Photodyn. Ther.*, 2019, **26**, 101–110.
51 R. Matshitse, M. Managa and T. Nyokong, *Diamond Relat. Mater.*, 2020, **101**, 107617.
52 C. Mauriello-Jimenez, N. Z. Knezevic, Y. G. Rubio, S. Szunerits, R. Boukherroub, F. Teodorescu, J. G. Croissant, O. Hocine, M. Seric, L. Raehm, V. Stojanovic, D. Aggad, M. Maynadier, M. Garcia, M. Gary-Bobo and J. O. Durand, *J. Mater. Chem. B*, 2016, **4**, 5803–5808.
53 T. K. Ryu, S. W. Baek, R. H. Kang, K. Y. Jeong, D. R. Jun and S. W. Choi, *J. Controlled Release*, 2018, **270**, 237–245.
54 J. D. Dong, R. M. Jiang, H. Y. Huang, J. Y. Chen, J. W. Tian, F. J. Deng, Y. F. Dai, Y. Q. Wen, X. Y. Zhang and Y. Wei, *Mater. Sci. Eng., C*, 2020, **106**, 110297.
55 E. Perevedentseva, N. Ali, A. Karmenyan, I. Skovorodkin, R. Prunskaite-Hyyrylainen, S. Vainio, C. L. Cheng and M. Kinnunen, *Materials*, 2019, **12**, 3762.
56 N. Nunn, M. D'Amora, N. Prabhakar, A. M. Panich, N. Froumin, M. D. Torelli, I. Vlasov, P. Reineck, B. Gibson, J. M. Rosenholm, S. Giordani and O. Shenderova, *Methods Appl. Fluoresc.*, 2018, **6**, 035010.
57 P. Rouhani, N. Govindaraju, J. K. Iyer, R. Kaul, A. Kaul and R. N. Singh, *Mater. Sci. Eng., C*, 2016, **63**, 323–332.
58 P. Rouhani and R. N. Singh, *J. Nanosci. Nanotechnol.*, 2020, **20**, 3957–3970.
59 B. M. Chang, L. Pan, H. H. Lin and H. C. Chang, *Sci. Rep.*, 2019, **9**, 13164.
60 A. Shirani, Q. C. Hu, Y. C. Su, T. Joy, D. H. Zhu and D. Berman, *ACS Appl. Mater. Interfaces*, 2019, **11**, 43500–43508.
61 U. Mangal, J. Y. Kim, J. Y. Seo, J. S. Kwon and S. H. Choi, *Materials*, 2019, **12**, 3438.
62 J. M. Gutierrez, K. Conceicao, V. M. de Andrade, V. J. Trava-Airoldi and G. Capote, *Surf. Coat. Technol.*, 2019, **375**, 395–401.
63 S. Houshyar, G. S. Kumar, A. Rifai, N. Tran, R. Nayak, R. A. Shanks, R. Padhye, K. Fox and A. Bhattacharyya, *Mater. Sci. Eng., C*, 2019, **100**, 378–387.
64 A. Selaru, D. M. Dragusin, E. Olaret, A. Serafim, D. Steinmuller-Nethl, E. Vasile, H. Iovu, I. C. Stancu, M. Costache and S. Dinescu, *Materials*, 2019, **12**, 2933.
65 K. A. Laptinskiy, H. Kettiger, O. A. Shenderova, S. A. Burikov, J. M. Rosenholm and T. A. Dolenko, *Nanodiamond based complexes for prolonged dexamethasone release*, SPIE, 2019.
66 A. Pentecost, M. J. Kim, S. Jeon, Y. J. Ko, I. C. Kwon, Y. Gogotsi, K. Kim and K. L. Spiller, *Regener. Biomater.*, 2019, **6**, 163–174.
67 L. Fusco, E. Avitabile, V. Armuzza, M. Orecchioni, A. Istif, D. Bedognetti, T. Da Ros and L. G. Delogu, *Carbon*, 2020, **160**, 390–404.
68 Y. Gou, Z. L. Zhang, D. Y. Li, L. Zhao, M. L. Cai, Z. W. Sun, Y. P. Li, Y. Zhang, H. Khan, H. B. Sun, T. Wang, H. Liang and F. Yang, *Drug Delivery*, 2018, **25**, 321–329.
69 J. G. Croissant, C. Mauriello-Jimenez, M. Maynadier, X. Cattoen, M. W. C. Man, L. Raehm, O. Mongin, M. Blanchard-Desce, M. Garcia, M. Gary-Bobo, P. Maillard and J. O. Durand, *Chem. Commun.*, 2015, **51**, 12324–12327.

 This journal is © The Royal Society of Chemistry 2020

Published on 06 November 2020. Downloaded by University of Montpellier on 11/6/2020 4:15:11 PM.

70 J. Mei, N. L. C. Leung, R. T. K. Kwok, J. W. Y. Lam and B. Z. Tang, *Chem. Rev.*, 2015, **115**, 11718–11940.
71 E. Kłodzińska, M. Szumski, E. Dziubakiewicz, K. Hrynkiewicz, E. Skwarek, W. Janusz and B. Buszewski, *Electrophoresis*, 2010, **31**, 1590–1596.
72 S. Halder, K. K. Yadav, R. Sarkar, S. Mukherjee, P. Saha, S. Haldar, S. Karmakar and T. Sen, *SpringerPlus*, 2015, **4**, 672.
73 H.-J. Kim, K. Zhang, L. Moore and D. Ho, *ACS Nano*, 2014, **8**, 2998–3005.
74 M. Gu, T. B. Toh, L. Hooi, J. J. Lim, X. Zhang and E. K.-H. Chow, *ACS Appl. Mater. Interfaces*, 2019, **11**, 45427–45441.
75 H. Li, M. Ma, J. Zhang, W. Hou, H. Chen, D. Zeng and Z. Wang, *ACS Appl. Mater. Interfaces*, 2019, **11**, 20341–20349.
76 K. Solarska-Ściuk and H. Kleszczyńska, *Acta Pol. Pharm.*, 2019, **76**, 779–796.
77 V. Vaijayanthimala, D. K. Lee, S. V. Kim, A. Yen, N. Tsai, D. Ho, H. C. Chang and O. Shenderova, *Expert Opin. Drug Delivery*, 2015, **12**, 735–749.
78 D.-K. Lee, T. Kee, Z. Liang, D. Hsiou, D. Miya, B. Wu, E. Osawa, E. K.-H. Chow, E. C. Sung, M. K. Kang and D. Ho, *Proc. Natl. Acad. Sci. U. S. A.*, 2017, **114**, E9445–E9454.
79 O. Shenderova and N. Nunn, in *Nanodiamonds: Advanced Material Analysis, Properties and Applications*, ed. J.-C. Arnault, Elsevier, Amsterdam, Micro and Nano Technologies, 2017, ch. 2, pp. 25–56.
80 J. Whitlow, S. Pacelli and A. Paul, *J. Controlled Release*, 2017, **261**, 62–86.

FRENCH RESUME

La nanomédecine est devenue une branche importante de la thérapie, regroupant les domaines de la biologie, la physique, la chimie et la science des matériaux.[1-2] Possédant au moins une dimension entre 1 et 100 nm, les nanomatériaux sont intéressants pour leur rapport surface-volume élevé et leur capacité à pénétrer facilement dans les cellules et les organites cellulaires. Pour cette raison, ils sont applicables pour le traitement et le diagnostic de nombreuses maladies, tel que le diabète, le cancer et les infections microbiennes.[3]

Parmi les nanoparticules (NPs) de silice, les nanoparticules d'organosilice mésoporeuse (MONs) sont des matériaux prometteurs pour surmonter certains challenges actuels dans le domaine du biomédical. Elles sont préparées par voie sol-gel en phase aqueuse dans un milieu chargé en molécules tensioactives organisées en micelles permettant la co-condensation de précurseurs à base d'alcoxysilanes et de précurseurs à base d'organoalcoxysilanes simples ou pontés. Les matériaux hybrides organique-inorganique synthétisés contiennent des fragments organiques distribués de manière homogène dans les parois des pores, dans les cavités des pores ou dans les deux (**Figure 1**).1 Il est également possible de former des NPs d'organosilice mésoporeuse périodique (PMO) avec une distribution dense et uniforme des parties organiques en utilisant uniquement des précurseurs à base d'organoalcoxysilanes pontés.[4]

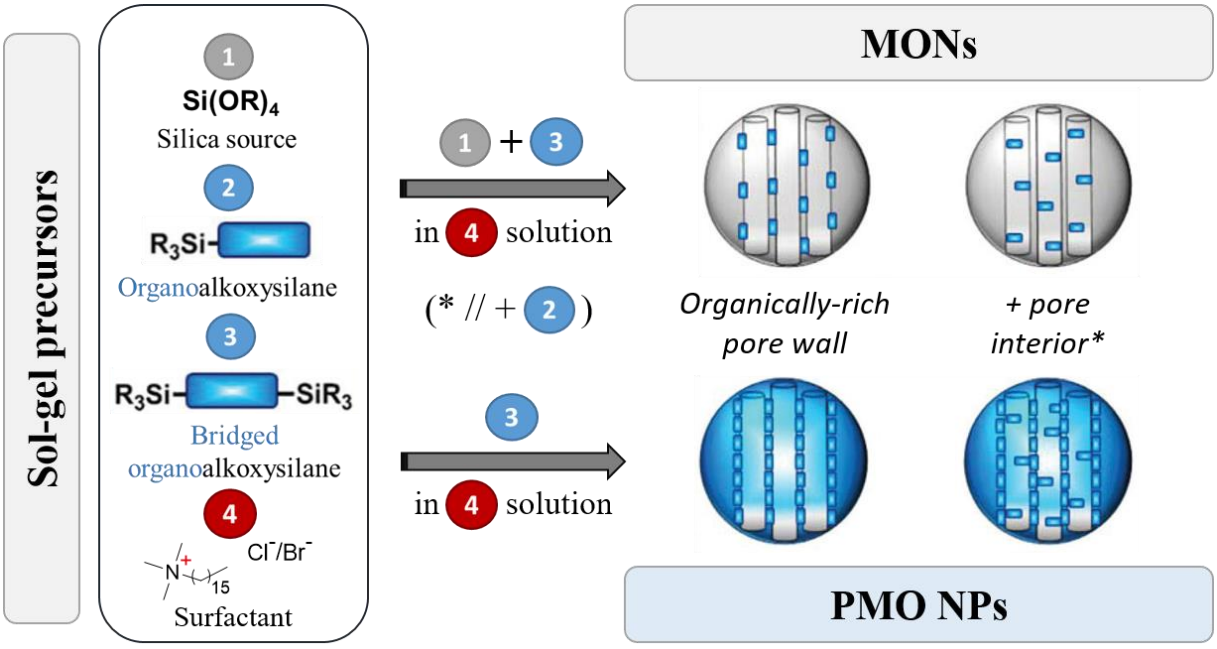

Figure 1 : Conditions de synthèse de nanoparticules à base d'organosilice mésoporeuse et d'organosilice mésoporeuse périodique et structures associées. La surface des nanoparticules peut être fonctionnalisée par greffage direct ou post-greffage par un organoalcoxysilane avant ou après avoir retiré le tensioactif. MONs : nanoparticules d'organosilice mésoporeuse; PMO NPs : nanoparticules d'organosilice mésoporeuse périodique. Adapté de Croissant *et al.* (2016).[5]

Grâce à leur nanostructure poreuse facilement ajustable sous différentes formes, morphologies et tailles, et grâce à leur matrice biocompatible, les NPs MONs et PMO peuvent servir de plateformes multifonctionnelles pour administrer de manière sélective et contrôlée toutes sortes de biomolécules et agents actifs. La grande versatilité de synthèse dont disposent les MONs offre la possibilité de les combiner avec des biomarqueurs, des biocapteurs et des éléments actifs à fort potentiel pour la théranostique, y compris des propriétés magnétiques, des propriétés thermiques ou encore des propriétés de photosensibilisation.

Les nanoparticules à base de PMO possèdent fondamentalement des caractéristiques uniques vis-à-vis des autres types de nanoparticules de silice, que ce soient les NPs de silice mésoporeuse (MSNs) ou les MONs.[6] Premièrement, les NPs PMO partagent les avantages des nanoparticules à base de silice :

- La morphologie, la structure et la taille des pores sont ajustables durant la synthèse pour pouvoir incorporer des médicaments et pour offrir une meilleure accessibilité avec les fonctions actives incorporées dans la matrice d'organosilice, telles que les fragments magnéto-, thermo- et photo-réactifs;
- La biocompatibilité, largement décrite dans la littérature, qui reste toutefois importante à vérifier dans chaque étude biologique;
- Une ingénierie de surface polyvalente grâce aux connaissances étendues des scientifiques dans la synthèse de précurseurs organoalcoxysilanes et dans le domaine de la chimie de surface des matériaux à base de silice.

Deuxièmement, les ponts organiques présents dans les précurseurs offrent un champ d'application potentiellement infini. Comme la synthèse de NPs PMO NPs permet d'atteindre une fraction organique très élevée, les propriétés biologiques et physicochimiques associées sont ainsi enrichies. De plus, ces NPs hybrides peuvent présenter des caractéristiques synergiques, rendant ainsi ces nanomatériaux de sérieux candidats pour améliorer l'efficacité des futurs traitements.

Troisièmement, après leur synthèse, les NPs d'organosilice peuvent être greffées en surface par réactions avec les fonctions silanols (Si-OH). Cela offre ainsi une possibilité supplémentaire de personnaliser les propriétés finales des nanoplateformes en fonction de l'environnement biologique associé à l'application visée (**Figure 2**).

Parmi les différentes caractéristiques requises pour les applications biomédicales, la furtivité vis-à-vis du système immunitaire peut améliorer la stabilité in vivo et la rétention des NPs, assurant ainsi leur protection et celle du « cargo » qu'elles transportent.[7] Pour ce faire, on

procède généralement à un recouvrement de la surface des NPs avec une membrane bio-inspirée, une enveloppe de silice, ou bien une enveloppe à base de polymère tel que le polyéthylène glycol (PEG).[8-13]

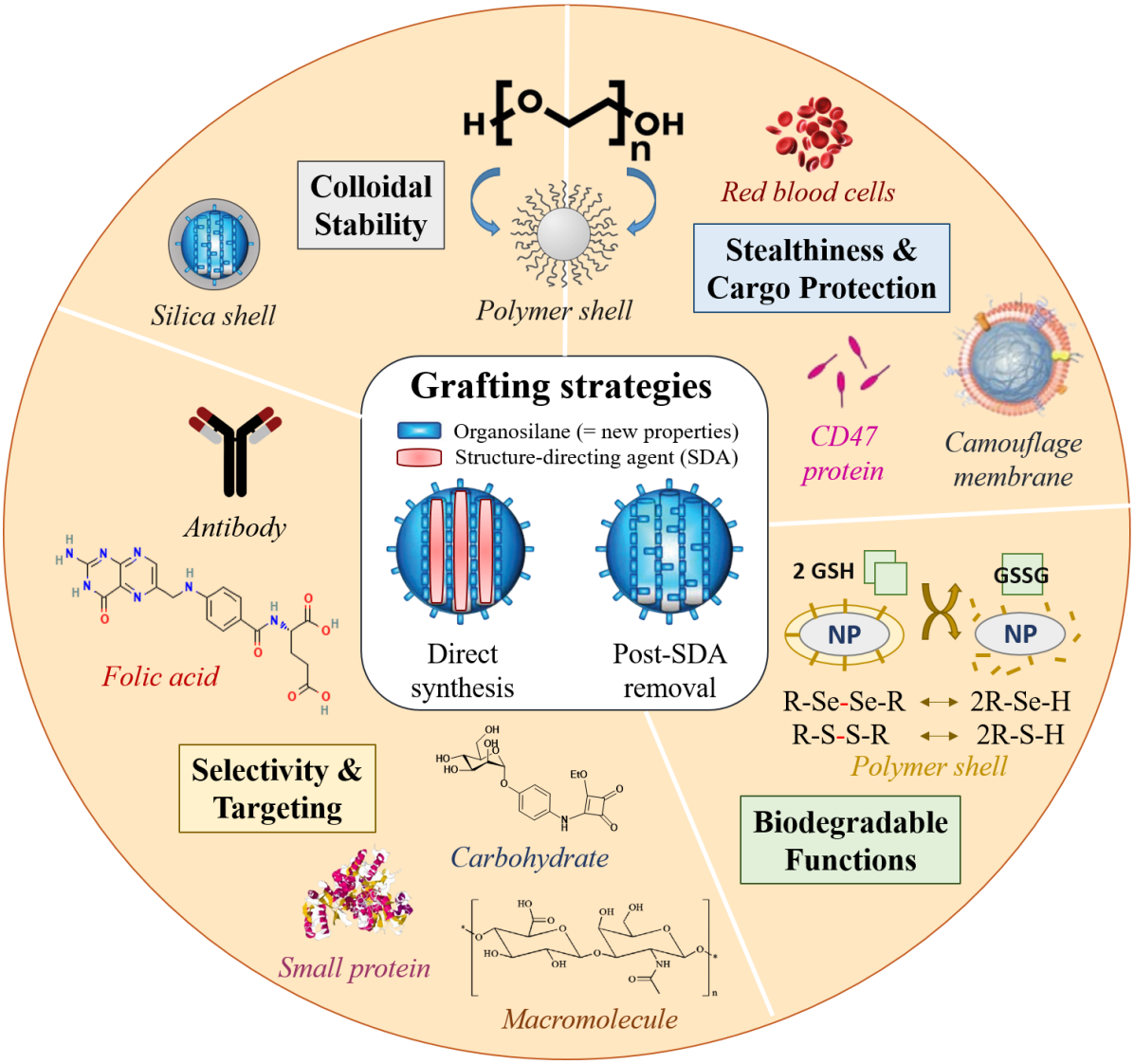

Figure 2 : Fonctionnalisation de surface de différents matériaux et différentes biomolécules, stratégies et avantages pour des applications biomédicales. GSH/GSSG : couple redox de la glutathione; SDA : agent structurant.

En général, les cellules cancéreuses et les microbes surexpriment certaines protéines et biomolécules. Ainsi, les nanomatériaux multifonctionnels sont recouverts de fonctions de ciblage afin d'augmenter la biodistribution et la sélectivité des NPs envers les cellules malades.[14-15]

En outre, la biodégradabilité et le devenir *in vivo* des NPs PMO sont particulièrement importants; d'une part, pour contrôler correctement la délivrance de médicaments et de biomolécules en fonction des besoins (libération complète à haute dose ou libération

prolongée). D'autre part, la fragmentation des NPs permet d'éviter leur accumulation dans les organes, ce qui constitue un défi important à relever pour estimer leur efficacité et leur impact sur la santé.[16] Un bon exemple est la dégradation par réaction redox entre les ponts disulfure d'une matrice PMO et la fonction thiol du glutathion (GSH), un tripeptide naturel présent à des taux plus élevés dans l'environnement proche de nombreuses cellules malades.[17-18]

De nombreuses alternatives aux thérapies conventionnelles sont actuellement en fort développement, notamment la thérapie photodynamique (PDT) qui est approuvée en clinique pour le traitement des tumeurs solides, des pré-cancers et des pathologies non oncologiques.[19] Ce traitement non invasif consiste en l'excitation de molécules ou de matériaux photosensibles par la lumière visible, déclenchant ainsi l'activation de processus photochimiques. Ces derniers engendrent des réactions biologiques spécifiques au niveau des cellules et tissus pour détruire les cellules défectueuses. La thérapie est basée sur l'interaction de trois éléments: une source de lumière, un milieu riche en oxygène et un photosensibilisateur (PS) qui va réagir avec l'oxygène pour générer des espèces réactives de l'oxygène (ROS) hautement cytotoxiques.[20-21]

L'excitation laser classique à un photon ne peut pas pénétrer profondément dans les tissus, et la technique est aussi limitée par des problèmes de photoblanchiment (photodégradation des chromophores). Ainsi, pour exploiter pleinement le potentiel de la PDT, la stratégie d'excitation simultanée de deux photons équivalents de plus faible énergie permet un contrôle plus précis de la zone irradiée, réduisant ainsi les effets secondaires et le risque d'endommagement des tissues le long du trajet du laser. L'utilisation de photosensibilisateurs (PSs) à deux-photons ayant d'excellentes propriétés d'absorption dans le domaine du proche infrarouge permet de réduire la puissance du laser et d'obtenir un niveau de pénétration beaucoup plus élevé.

Les mécanismes de la PDT par excitation à un et deux-photons (OPE et TPE-PDT) sont décrits dans la **Figure 3**.[22-23] Lors de l'irradiation, un PS dans son niveau d'énergie le plus bas (ou état fondamental) ($^1PS_0$) peut être excité vers un état singulet de plus haute énergie (^1PS_n). Cet état excité très instable peut ensuite atteindre son état excité singulet le plus bas ($^1PS_1$) avant de passer par un état excité triplet d'une durée relativement longue ($^3PS_1$) par le biais d'un processus non-radiatif connu sous le nom de conversion intersystème (ISC).[24] L'état triplet excité peut subir différents processus photophysiques et photochimiques impliqués dans la PDT, qui peuvent être classés en trois types (**Figure 3**).[25]

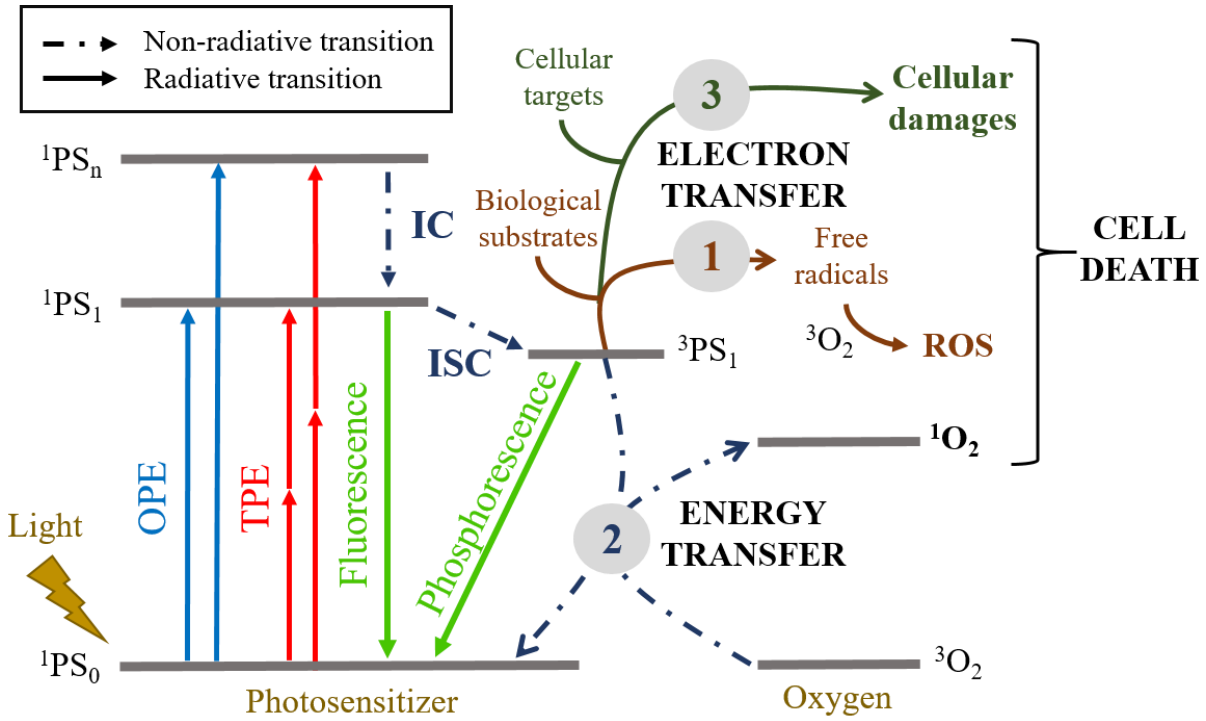

Figure 3 : Diagramme de Jablonski dans le cadre de la thérapie photodynamique (PDT). À partir de son état triplet excité, le photosensibilisateur (PS) peut subir trois types de mécanismes photochimiques pouvant déclencher la mort cellulaire dans le milieu irradié. IC : conversion interne; ISC : conversion intersystème; OPE : excitation à un photon; ROS : espèces réactives de l'oxygène; TPE : excitation à deux-photons. Adapté de Sun *et al.* (2017).[24]

L'avantage de la TPE-PDT réside dans sa résolution tridimensionnelle et sa morbidité réduite à long terme. Ainsi, une liste des orientations futures à entreprendre pourrait être vue comme suit :

- Une stratégie théranostique utilisant la fluorescence des PSs pour le suivi en temps réel des nanoplateformes administrées, ce qui permet de mieux contrôler le traitement;
- Le traitement des maladies qui s'accompagnent de petites lésions dans les organes majeurs;
- Une thérapie secondaire pour guérir les lésions résiduelles dans les tissus après avoir eu recours à la chirurgicale ou à un traitement conventionnel;
- Des systèmes plus efficaces où les PSs sont assemblés avec des matériaux innovants comme les quantum dots, les liposomes et les NPs. Une attention particulière doit être accordée à la reproductibilité de la synthèse de tels composites, ainsi qu'à leur composition et à leur stabilité dans les milieux biologiques.[24]

Ainsi, au cours de ce projet, différentes strategies de synthèse de NPs PMO à base de PSs ont été développées. Leur potentiel thérapeutique a été ensuite testé *in vitro* sur différentes souches de cellules cancéreuses et de bactéries.

La première approche a consisté à développer des nanoparticules cœur-coquille avec des cœurs nanodiamant (ND) qui sont connus pour leurs propriétés mécaniques, thermiques, et optiques. La capacité des NDs à générer des ROS pour la TPE-PDT a récemment été démontrée pour la première fois. En bref, des NDs seuls ou encapsulés dans une matrice de PMO à base d'éthylène ont été irradiés à 800 nm avec un laser femtoseconde pulsé et ont induit une mortalité de 32 ± 6 et 39 ± 10% sur des cellules de cancer du sein MCF-7, respectivement.[26]

Ainsi, dans notre étude, le potentiel thérapeutique de différents NDs hydroxylés (NDs-OH) a été évalué en TPE-PDT avant de les encapsuler dans une matrice PMO par voie sol-gel. Des nanodiamants fluorescents de large diamètre (FND100, 100 représentant la taille moyenne statistique en nm), produits dans des conditions de haute pression et haute température ont été comparés avec des petits nanodiamants produits par détonation de l'hexogène et d'explosifs semblables au trinitrotoluène (DND30 et DND20).

Comme FND100 et DND30 ont démontré une phototoxicité *in vitro* sur cellules de cancer du sein en TPE-PDT, ils ont été sélectionnés pour être encapsulés dans une matrice de PMO afin d'améliorer leur stabilité colloïdale et leur biocompatibilité. En effet, ces nanomatériaux carbonés s'agrègent facilement, et peuvent de ce fait être très toxique pour le corps. La synthèse sol-gel a donc été réalisée sous ultrasonication afin de maximiser la répulsion des NDs durant la formation de la coquille de PMO, coquille composée de ponts éthyléniques (ENE, **Figure 4**).[27-28] Ces ponts peuvent améliorer le transfert de paires électron/trou et ainsi contribuer à la diffusion et à la génération de ROS.[29]

Ainsi, en utilisant le bromure de cétyltriméthylammonium (CTAB) en tant qu'agent structurant, des particules de taille nanométrique ont été formées sous ultrasonication pendant cinq minutes, puis sous agitation pendant 24h (**Figure 4**, 1-2). Ensuite, du polyéthylène glycol silylé à chaîne courte (PEG-Si, M_w = 410,62 g mol-1) et de l'aminoundécyltriéthoxysilane (AUTES, M_w = 333,59 g mol-1) ont été directement conjugués à la surface des NPs dans le milieu réactionnel avec un rapport molaire ENE:PEG-Si:AUTES de 9,6:2:1 (**Figure 4**, 3). Après séparation par centrifugation, le greffage du dérivé de mannose squarate (sqMAN) sur les fonctions amines a été réalisé par substitution nucléophile de type 2 (**Figure 4**, 4).[30] Cet α-D-mannoside possède la capacité de cibler spécifiquement les lectines de certaines cellules cancéreuses et bactéries.[31-32]

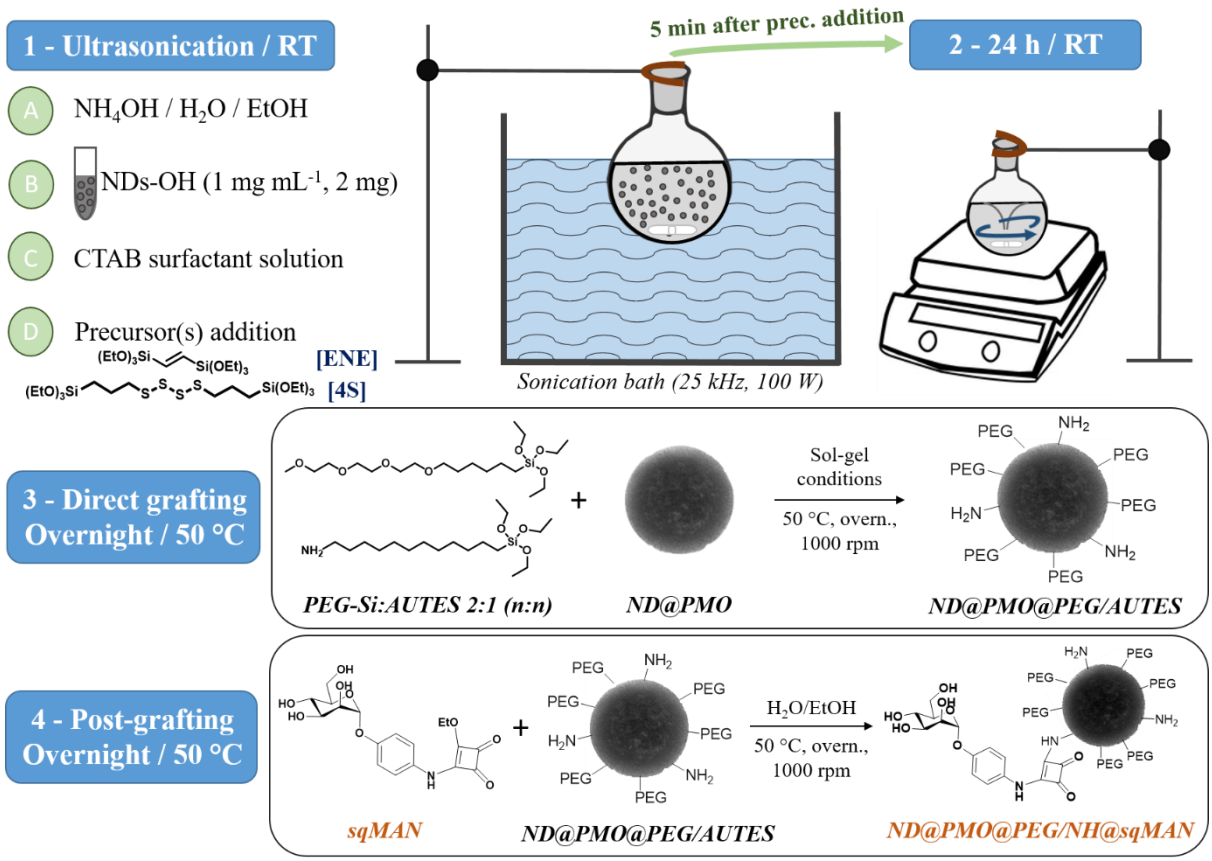

Figure 4 : Etapes de synthèse et de fonctionnalisation de surface de nanoparticules coeur-coquille nanodiamant-PMO (ND@PMO NPs). 4S : matrice constituée de ponts tétrasulfure; AUTES : aminoundecyltriéthoxysilane; CTAB : bromure de cétyltriméthylammonium; ENE : matrice constituée de ponts éthyléniques; PEG(-Si) : polyéthylène glycol (silylé); sqMAN : dérivé de squarate mannose.

Les imageries de microscopie électronique à transmission (MET) ont ainsi confirmé la formation de nanoparticules avec une distribution polydisperse de tailles entre 50 et 200 nm et intégrant pour certaines des NDs (**Figure 5**).

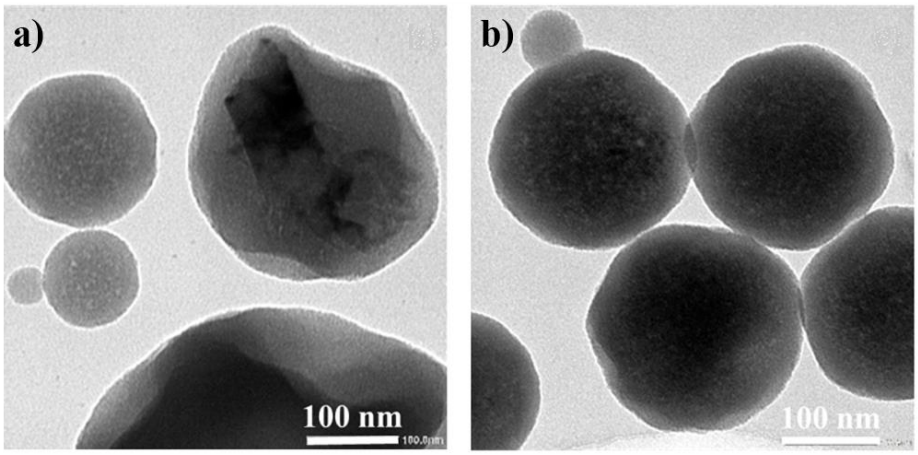

Figure 5 : Imageries de nanoparticules cœur-coquille ND@ENE@PEG/AUTES réalisées au microscope électronique à transmission (MET). (a) Nanoparticules sphériques ou irrégulières contenant de multiple nanodiamants FND100; (b) Nanoparticules sphériques ou irrégulières contenant de multiple nanodiamants DND30. Les nanoparticules PMO < 60 nm ne contiennent pas de nanodiamant.

Finalement, les études d'internalisation *in vitro* réalisées par imagerie confocale ont révélé une internalisation efficace des systèmes cœur-coquille ND@ENE@PEG/AUTES dans les cellules cancéreuses MDA-MB-231. Par ailleurs, les tests biologiques en TPE-PDT ont mis en avant la grande biocompatibilité des NPs (laser off, **Figure 6**) et leur phototoxicité sous irradiation, avec 46 et 36% de mort cellulaire respectivement avec les nanoparticules à base de FND100 et DND30 (laser on, **Figure 6**). En revanche, les NPs modifiées avec du sqMAN étaient moins internalisées et, probablement de ce fait, moins toxiques pour les cellules cancéreuses.

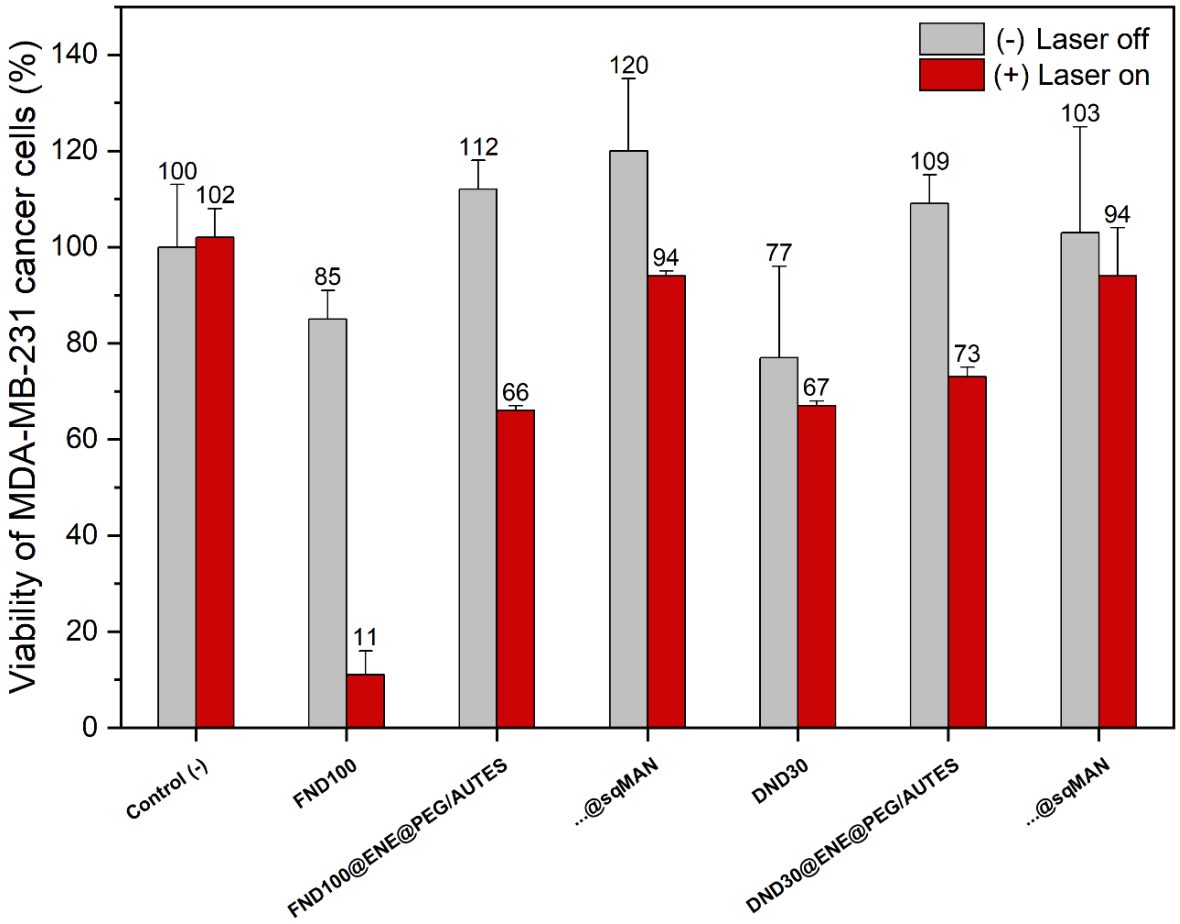

Figure 6 : Études TPE-PDT *in vitro* de survie cellulaire en présence de NPs coeur-coquille ND@ENE@PEG/AUTES et des NDs correspondants. L'éradication de cellules cancéreuses est déclenchée par TPE (cellules cancéreuses épithéliales humaines de la lignée MDA-MB-231) après incubation avec des NPs à 80 µg mL^{-1} pendant 20 h, suivi d'une irradiation à 800 nm (3 x 1,57 s). Les barres d'erreur représentent les écarts-types de trois expériences indépendantes.

La seconde approche de ce projet s'est basée sur la synthèse de fluorophores possédant d'excellentes propriétés d'absorption à deux-photons et de fluorescence, ainsi que sur leur intégration dans la synthèse de NPs PMO.

Dans un premier temps, de nouveaux chromophores organiques à deux-photons ont été préparés par synthèse multi-étapes. Ces molécules hyper-conjuguées et tri-branchées appartenant à la famille des octupoles peuvent être décrites comme des systèmes $D(-\pi-A)_3$.[33] L'absorption à deux-photons (TPA) intrinsèque de ces matériaux résulte de l'ICT du noyau donneur de triphénylamine vers les groupes périphériques à base de sulfone qui sont fortement attracteurs d'électrons. Les groupements phénylène-vinylène conjugués permettent une communication électronique efficace entre les groupes électro-actifs.[34] De plus, la ramification conduit à une amélioration coopérative des propriétés de TPA, en relation avec un couplage excitonique cohérent entre les branches.[35]

Ainsi, deux molécules de structure proche, abrégées en F et F2 et possédant respectivement un ou deux groupements phénylène-vinylène, ont été obtenues. Leurs propriétés photophysiques d'absorption et d'émission ont été ensuite étudiées dans différents solvants (**Figure 7**).

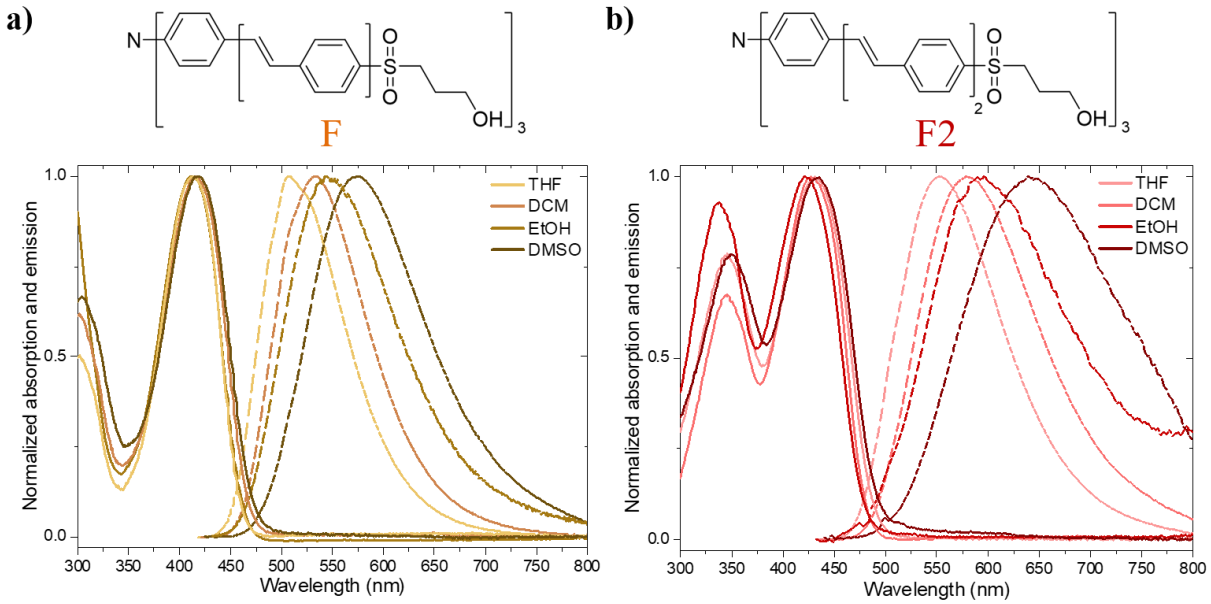

Figure 7 : Structures simplifies, spectres d'absorption (en trait plein) et spectres d'émission (en pointillés) des fluorophores à deux-photons (a) F et (b) F2. Lorsque la polarité du solvant augmente, l'émission est décalée vers le rouge. THF : tétrahydrofurane; DCM : dichlorométhane; EtOH : éthanol absolu; DMSO : diméthylsulfoxyde.

Les résultats démontrent des propriétés de solvatochromie pour F et F2, notamment en émission. En effet, un effet bathochrome de la longueur d'onde maximale d'émission de fluorescence est observé pour une polarité croissante (et une solubilité décroissante). Pour F,

$\lambda_{em.,\ max}$ est décalée de 507 à 575 nm, alors que le maximum d'émission de F2 se voit décalé vers le rouge en passant de 533 à 639 nm (**Figure 7**).

Les fluorophores à deux-photons F et F2 sont de bons candidats pour les bioapplications car ils présentent des propriétés photophysiques appropriées dans le domaine du proche infrarouge et une longueur d'onde d'émission variable en raison du caractère solvatochrome. Egalement, des études précédentes sur des octupoles similaires ont démontré des valeurs de sections efficace élevées en TPA et une fluorescence accrue en milieu biologique. Ces molécules pourraient donc fournir une excellente résolution tridimensionnelle intrinsèque et donc être utilisés en tant que biocapteurs et biomarqueurs, notamment dans des systèmes pour la théranostique.

Grâce aux groupements hydroxyles présents aux extrémités de ses trois branches, les fluorophore F a été modifié par trisilylation pour être utilisé en tant que précurseur organoalcoxysilane dans la synthèse sol-gel de NPs PMO. De façon similaire, la 5,10,15,20-tetrakis(4-aminophenyl)porphyrine (P) a été tétrasilylée par réaction sur ses groupements amine. Cette porphyrine a déjà été intégrée dans une matrice PMO et a démontré des qualités de PS à deux-photons pour la TPE-PDT *in vitro* contre des cellules cancéreuses MCF-7.[36]

Dans notre cas, l'objectif est de concevoir des nanoparticules dans lesquelles les fluorophores intégrés peuvent transférer l'énergie absorbée à deux-photons vers les porphyrines par transfert d'énergie par résonance de type Förster (FRET, **Figure 8**).

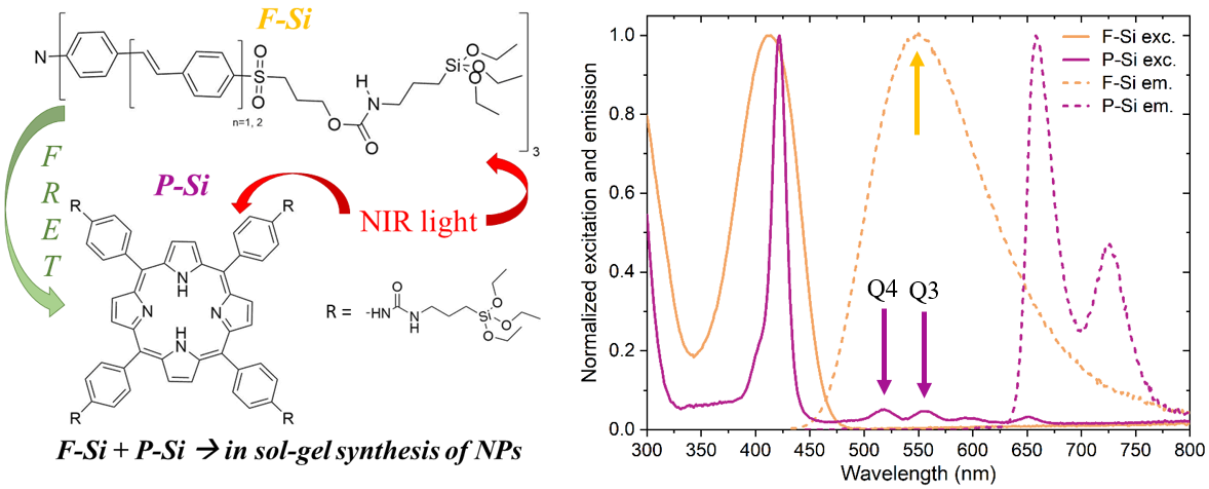

Figure 8 : Principe du transfert d'énergie par résonance de type Förster (FRET) illustré par les spectres d'excitation (en trait plein) et d'émission (en pointillés) des chromophores F et P silylés (F-Si, P-Si). Les composés silylés ont été excités à leur longueur d'onde d'absorption maximale déterminée au préalable par spectroscopie UV-visible ($\lambda_{exc.,\ F\text{-}Si}$ = 413 nm; $\lambda_{exc.,\ P\text{-}Si}$ = 422 nm, solvant : EtOH).

En effet, ce mécanisme photophysique non-radiatif se produit à longues distances (1-10 nm) entre deux chromophores.[37-38] Pour cela, un bon recouvrement spectral entre le spectre d'émission du fluorophore à deux photons hautement fluorescent (le donneur d'énergie, F-Si) et le spectre d'absorption du PS possédant un rendement quantique élevé en ROS (l'accepteur d'énergie, P-Si) est nécessaire pour que le FRET soit exalté.

Comme indiqué dans les spectres de la **Figure 8**, le couple F/P démontre une bonne correspondance spectrale entre la large bande d'émission du fluorophore ($\lambda_{em.,\,max}$ = 548 nm) et les bandes Q de la porphyrine (notamment Q4 et Q3 à 519 et 557 nm, respectivement).

Ainsi, la stratégie globale avec ces NPs F P PMO consiste en l'utilisation du FRET pour améliorer l'efficacité de la TPE-PDT pour éradiquer des métastases ou des colonies bactériennes dans le contexte d'une infection (**Figure 9**). En parallèle à cela, la mésoporosité des nanoparticules ainsi que leur grande surface spécifique sont exploités pour fonctionnaliser la surface avec du PEG et du sqMAN pour une thérapie plus sélective et ciblée. De plus, le chargement et relargage contrôlé d'un antibiotique – dans le cadre de l'étude, la vancomycine (VAN) – est considéré pour promouvoir une thérapie combinée plus efficace.

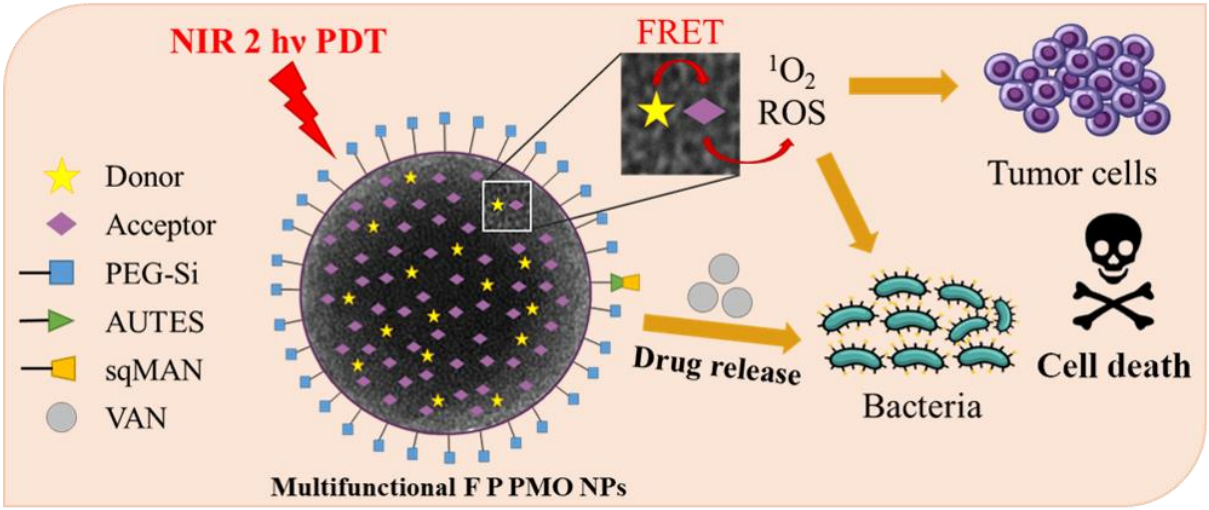

Figure 9 : Schéma synthétique de la stratégie de design de nanoparticules F P PMO pour des traitements anticancéreux ou antibactériens. La stratégie de FRET s'effectue depuis un donneur d'énergie (fluorophore F) vers un accepteur d'énergie (porphyrine P). VAN : vancomycine (antibiotique).

Tout comme pour la synthèse des NPs ND@PMO, les NPs F P PMO ont été préparées en milieu basique avec du CTAB.[39-40] Cette fois, le précurseur organoalcoxysilane principalement utilisé était le 1,2-bis(triéthoxysilyl)éthane (E) ou le 1,2-bis(triéthoxysilyl)éthène (ENE), mélangé ou non avec une petite quantité de bis[3-(triéthoxysilyl)propyl]tétrasulfure (4S) biodégradable, qui possède des ponts tétrasulfure

facilement clivables (**Figure 10a**). Ainsi, quatre types de NPs F P PMO ont été formées (E, E 4S, ENE, ENE 4S).

En utilisant le précurseur E, les nanoparticules peuvent atteindre des surfaces spécifiques plus élevées pour la fonctionnalisation et le greffage, alors que le précurseur ENE peut apporter une conjugaison locale et renforcer le transfert de paires électron/trou, améliorant ainsi la diffusion et la génération de ROS. De plus, les deux précurseurs peuvent fournir une organisation régulière à la structure mésoporeuse formée.[29] Pour les NPs à base d'ENE, le β-citronellol racémique a été ajouté avec le CTAB en tant que co-agent structurant pour contrôler la morphologie et la porosité en diminuant l'énergie libre de surface des micelles.[41] En raison de la dispersion réduite de F-Si et P-Si dans l'eau, tous les précurseurs ont été pré-mélangés dans un petit volume d'éthanol absolu avant addition dans le milieu sol-gel, avec un rapport molaire constant ((E ou ENE) ± 4S):P-Si:F-Si de 1:0,045:0,005 (**Figure 10a**).

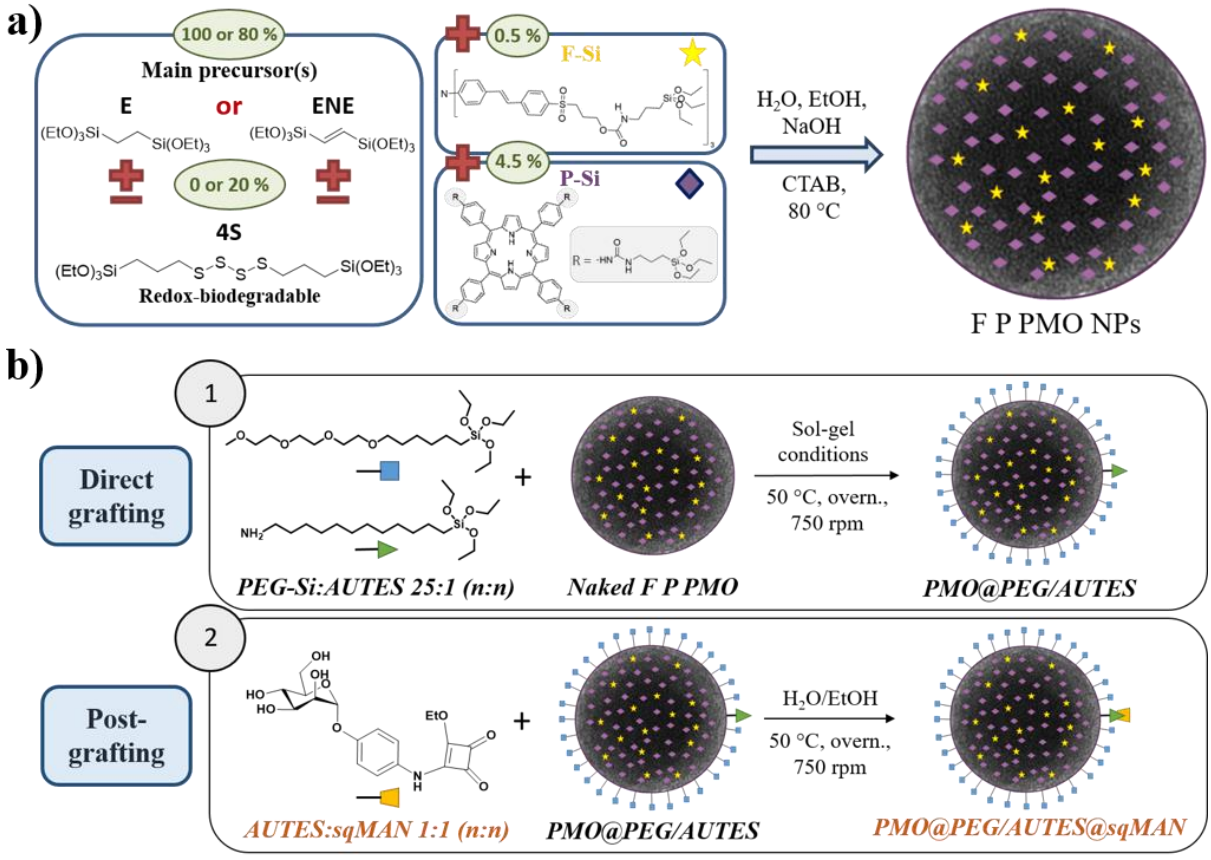

Figure 10 : Design de nanoparticules fluorophore-porphyrine PMO (F P PMO NPs) multifonctionnelles. (a) La matrice principale des nanoparticules est constituée de ponts éthylique (E) ou éthyléniques (ENE), en présence ou non de ponts tétrasulfure (4S) biodégradables (dans ce cas, les NPs sont abrégées en BPMO); (b) Fonctionnalisation de surface en deux étapes.

L'intégration homogène des différents précurseurs a par la suite été démontrée par RMN du solide, par analyse élémentaire du soufre et par caractérisation photophysique. Par rapport à P-Si, un léger décalage bathochrome et un élargissement des deux bandes d'émission des

porphyrines ont été observés avec les NPs F P PMO. Ces changements s'expliquent par la formation d'agrégats J et par l'empilement π des macrocycles une fois intégrés dans la matrice PMO, qui ont pour effet d'améliorer la génération de ROS pour la PDT.[36]

Enfin, les NPs ont été modifiées en surface avec une grande quantité de greffons PEG et une petite quantité d'AUTES@sqMAN pour le ciblage biologique (Figure **10b**) afin de comparer le potentiel des différentes NPs.

Comme observé par les imageries obtenues au MET, les NPs obtenues sont de forme arrondie et de tailles comprises entre 100 et 200 nm. De plus, en fonction des précurseurs utilisés aux côtés de F-Si et P-Si, la morphologie et la porosité semblent changer (**Figure 11**). En effet, pour les NPs E 4S F P PMO, la surface est irrégulière, ce qui semble indiquer la présence de ponts 4S à ce niveau, contrairement aux NPs ENE 4S F P PMO où la surface est beaucoup plus régulière.

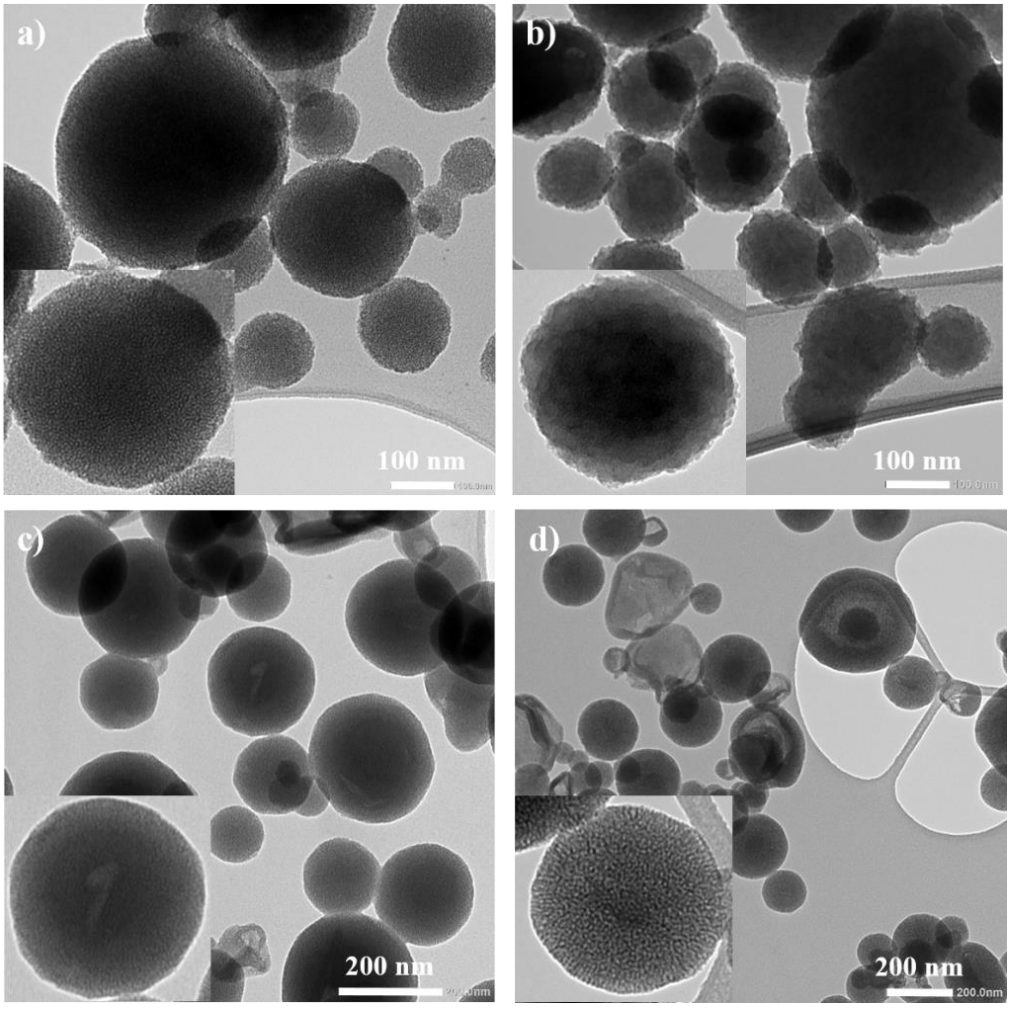

Figure 11 : Imageries de nanoparticules fluorophore-porphyrin PMO (F P PMO NPs) et de nanoparticules biodégradables fluorophore-porphyrin PMO (F P BPMO NPs) réalisées au MET. Nanoparticules (a) E F P PMO et (b) E 4S F P BPMO. Echelle : 100 nm; nanoparticules (c) ENE F P PMO et (d) ENE 4S F P BPMO NPs. Echelle : 200 nm.

Parallèlement à cela, les propriétés de texture et de porosité des NPs ont été étudiées par adsorption-désorption d'azote dans les structures. Les résultats obtenus par la méthode Brunauer-Emmett-Teller ont montré que les surfaces spécifiques des NPs à base de 4S étaient plus faibles (respectivement 500 et 699 m^2 g^{-1} pour E 4S F P et ENE 4S F P, contre 875 et 856 m^2 g^{-1} pour E F P et ENE F P). De plus, des volumes conséquents en mésopores (de 2.7 à 3.8 nm) ont été calculés par la théorie Barrett-Joyner-Halenda à partir de la branche de désorption des isothermes de sorption, démontrant ainsi le potentiel des NPs à encapsuler des médicaments ou biomolécules de petite taille.

Par la suite, des études biologiques *in vitro* ont été réalisées sur des modèles de cellules cancéreuses MCF-7 et de bactéries gram-positives (*Staphylococcus aureus*) et gram-négatives (*Escherichia coli)*. Dans un premier temps, la capacité d'internalisation dans les cellules MCF-7 a été étudiée par microscopie confocale pour les quatre types de F P PMO NPs sous leurs différents environnements de surface (**Figure 12**).

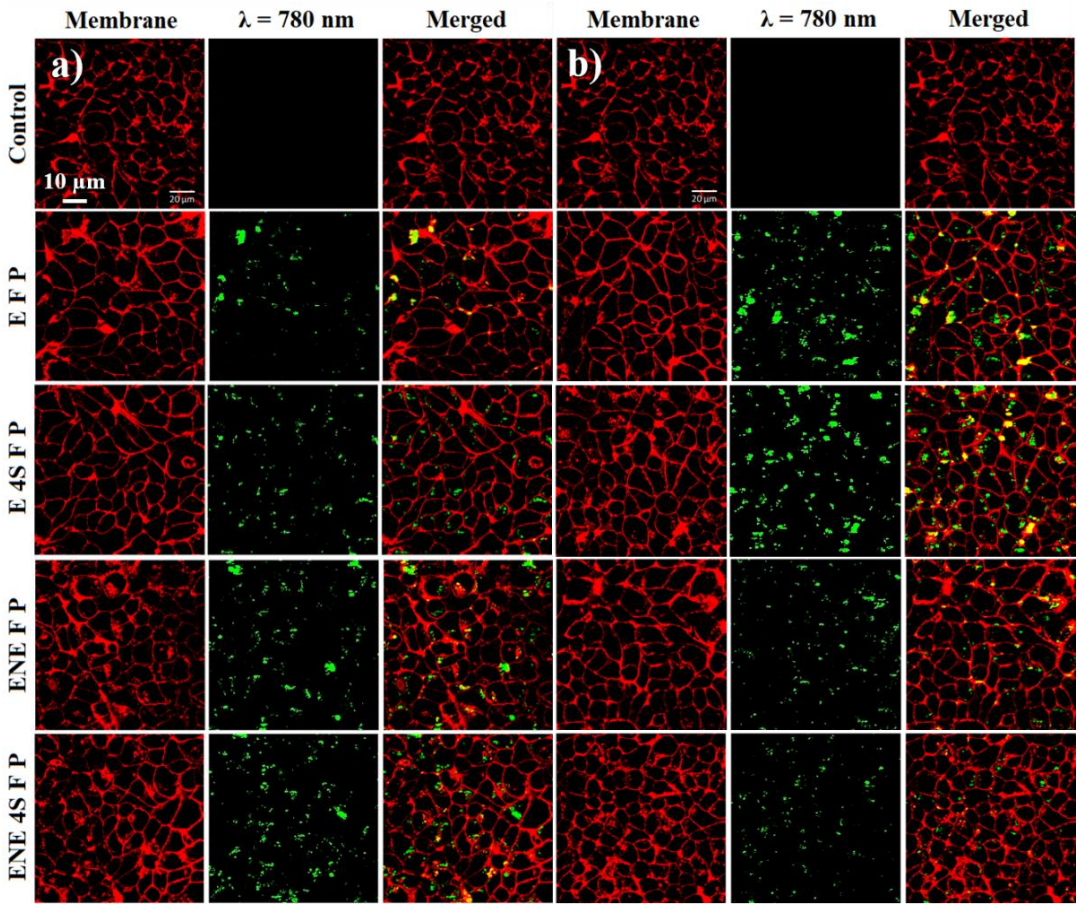

Figure 12 : Imageries de fluorescence représentant l'internalisation cellulaire de différentes F P (B)PMO NPs (50 µg mL^{-1}) (a) nues ou (b) modifiées en surface (PEG/AUTES@sqMAN) réalisées au microscope confocal. Après incubation pendant 24 h, les cellules MCF-7 de cancer du sein ont été marquées au Cell Mask™ Orange Plasma Membrane, puis visualisées à 561 nm (membrane) et 780 nm (F P PMO NPs). Images obtenues au microscope confocal Carl Zeiss LSM780 avec un fort grossissement (63x/1,4 OIL Plan-Apo).

Après une excitation dans le proche infrarouge à 780 nm, les nanoparticules ont généré des intensités de fluorescence élevées dans les milieux biologiques (**Figure 12**). De plus, dans le cas des NPs E et E 4S, les images superposées des cellules ont montré une plus grande fluorescence en présence de sqMAN, ainsi qu'une plus grande absorption cellulaire que les NP nues (en jaune), suggérant un ciblage actif du mannoside. En revanche, l'imagerie confocale des NPs ENE et ENE 4S a révélé des niveaux de fluorescence et d'internalisation plus faibles que pour les NPs E et E 4S. Même si les étapes de synthèse et de greffage ont été réalisées avec les mêmes ratios initiaux de réactifs, certaines différences concernant la texture des NPs et le ratio de greffage final pourraient expliquer ce résultat.

L'activité des NPs F P PMO a ensuite été évaluée en TPE-PDT sur MCF-7 sous irradiation à 780 nm (3 x 1,26 s). Les noyaux des cellules vivantes ont été colorés en bleu à l'aide de Hoechst 33342™ et comptés sur un système d'imagerie EVOS™ M5000 après optimisation des paramètres photographiques (luminosité, gain, exposition) pour distinguer correctement les nanoparticules et les fragments cellulaires (en noir) des cellules cancéreuses MCF-7 vivantes (**Figure 13**).

L'excitation à deux-photons a induit des niveaux élevés de toxicité pour les quatre familles de NPs F P PMO à 50 µg mL^{-1}, indépendamment de la stratégie de fonctionnalisation et du taux d'internalisation observé précédemment. Ce résultat provient des excellentes propriétés optiques des chromophores F et P dans le proche infrarouge, et du passage par des états excités électroniques spécifiques pendant l'irradiation à deux-photons dû à des règles de sélection différentes. Tous les matériaux ont ainsi été responsables d'une réduction de 80 à 100 % de la viabilité des cellules cancéreuses, à l'exception des nanoparticules E 4S F P qui ont provoqué une mort cellulaire de 42 à 56 % (**Figure 13**). Il est aussi important de noter l'excellente biocompatibilité des NPs sans excitation laser.

La grande phototoxicité des NPs suggère une bonne efficacité de FRET en milieu biologique, des fluorophores excités à deux-photons jusqu'aux porphyrines. Des recherches sont en cours pour confirmer l'apport du FRET pour le traitement anticancéreux avec des F PMO NPs (contrôle négatif, non toxique), des F P PMO NPs ou des P PMO NPs, ces dernières étant théoriquement moins efficaces. Des tests de génération de ROS et d'oxygène singulet par cytométrie de flux en milieu tamponné pourraient également s'avérer utiles pour mettre en évidence la différence d'activité photodynamique des nanomatériaux.

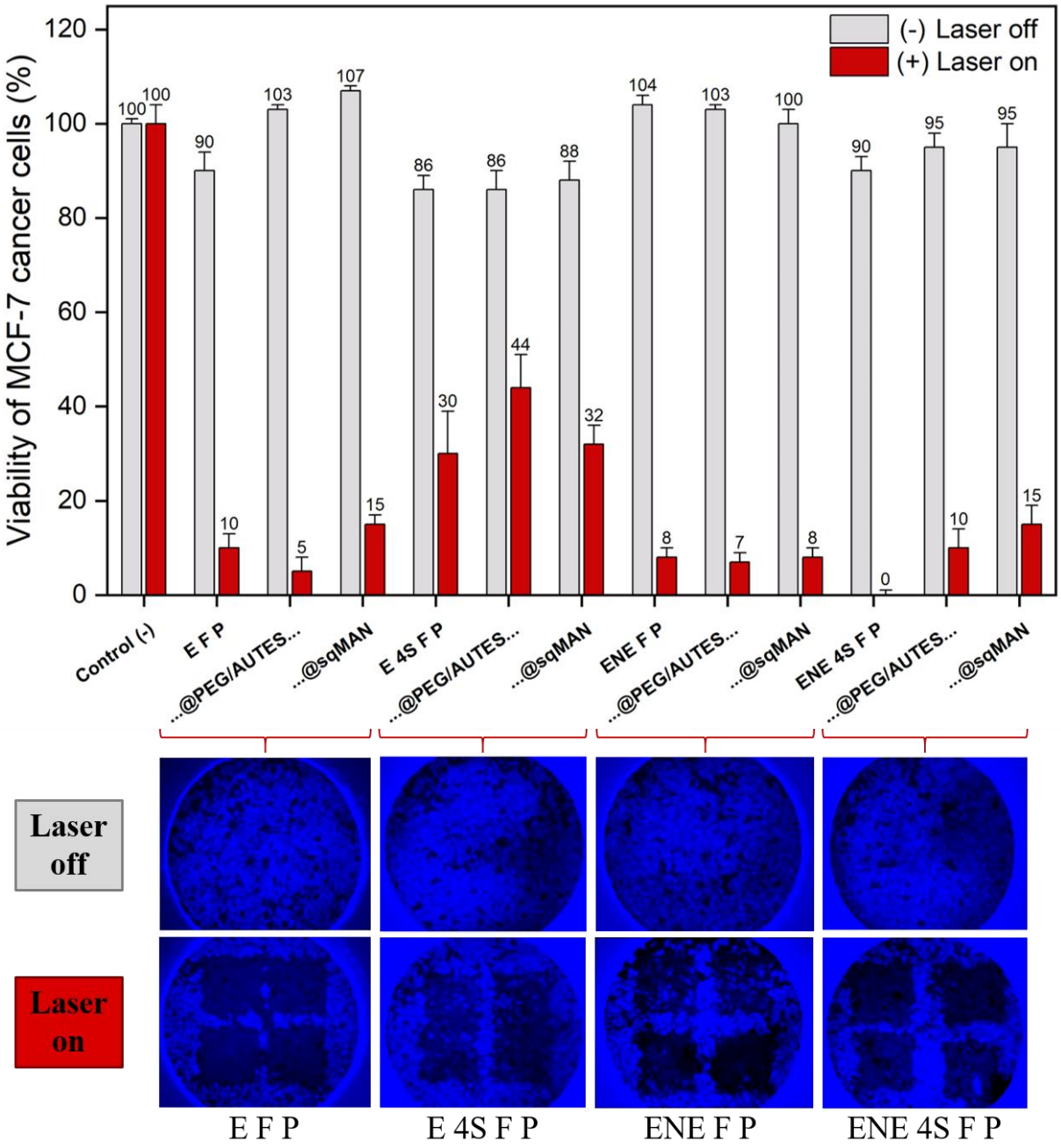

Figure 13 : Études *in vitro* TPE-PDT de survie cellulaire en présence de F P (B)PMO NPs (soit nues, soit fonctionnalisées PEG/AUTES, soit fonctionnalisées PEG/AUTES@sqMAN). L'éradication de cellules cancéreuses est déclenchée par TPE (cellules de cancer du sein de la lignée MCF-7) après incubation avec des NPs (50 µg mL^{-1}) pendant 20 h, suivi d'une irradiation à 780 nm (3 x 1,26 s). Les barres représentent les écarts-types de six ou huit expériences indépendantes. Les images représentent des exemples de puits (3,3 x 3,3 mm) utilisés pour le comptage des cellules vivantes grâce au marquages des noyaux cellulaires avec du Blue Hoechst 33342™, soit après aucun traitement (laser off), soit après irradiation à deux-photons (laser on). Les amas noirs foncés correspondent à des agrégats de nanoparticules.

Après cela, le passage à l'*in vivo* sur un modèle embryonnaire de poisson-zèbre devraient être réalisé en testant le ou les meilleurs candidats de NPs greffées avec du sqMAN.

L'utilisation de nanoparticules de silice mésoporeuse a été largement décrite pour l'encapsulation de médicaments.[42-43] Comparées aux MSNs inorganiques, les NPs PMO organiques-inorganiques pourraient fournir un rendement de chargement (DLC) et un rendement de relargage (DRC) en antibiotique supérieurs, notamment en encapsulant des médicaments aux propriétés d'hydrophilie opposés. Une thérapie combinée aurait pour effet d'améliorer le traitement d'infections polymicrobiennes en employant des agents antimicrobiens agissant de différents façons pour combattre l'infection.[44-45]

Le chlorhydrate de vancomycine (VAN), un antibiotique glycopeptidique approuvé par la Food & Drug Administration (**Figure 14a**) a été choisi comme médicament-test pour étudier la capacité de chargement et de libération dans les nanostructures F P (B)PMO. La VAN est bien connue pour son efficacité antibactérienne contre la plupart des bactéries gram-positives, en particulier les staphylocoques dorés (*S. aureus*) résistants à la méthicilline qui constituent l'une des menaces actuelles les plus alarmantes concernant les infections liées à la résistance microbienne accrue aux antibiotiques.[44-45]

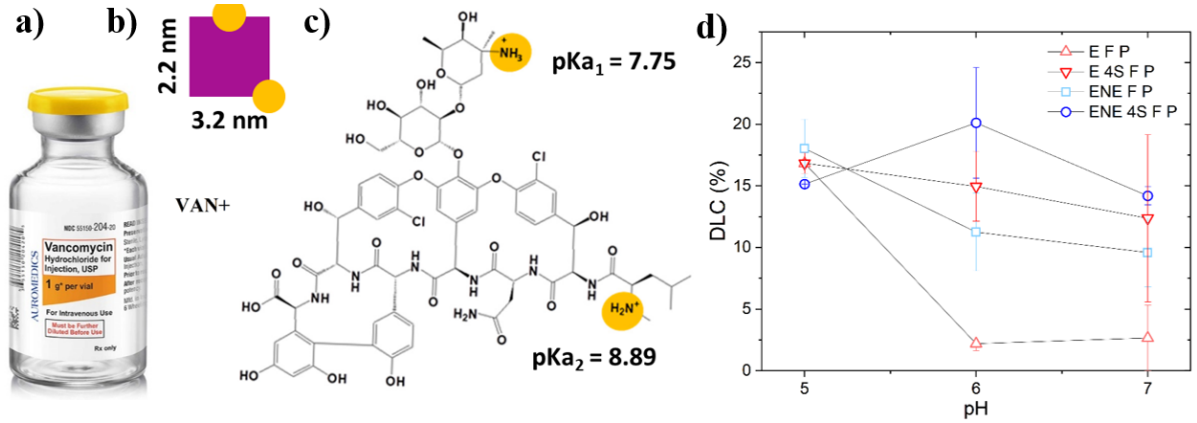

Figure 14 : Informations générales sur la vancomycine (VAN) et rendement de chargement en antibiotique dans les nanoparticules. (a) Exemple de flacon commercial; (b) Dimensions de l'antibiotique; (c) Structure développée sous forme acide (VAN^+); (d) Rendements de chargement en VAN (DLC = mg VAN / mg NPs) pour différentes F P (B)PMO NPs et différent pH. Structure adaptée de Ural *et al.* (2021).[46]

Le chargement en VAN dans les NPs PMO pourrait se faire soit par encapsulation dans les pores, soit à la surface des NPs. Comme cela a été mesuré précédemment, les distributions de taille des pores des NPs F P PMO sont compatibles avec les dimensions moléculaires de la VAN (**Figure 14b**). Des expériences de chargement ont donc été réalisées en dispersant des NPs avec de l'antibiotique. Après avoir testé différentes concentrations pour les deux éléments, les conditions sélectionnées furent les suivantes :

- [VAN] = [NPs] = 10 mg mL^{-1};
- Un pH fixé à 5, 6 ou 7 en utilisant des aliquots de NaOH ou de HCl pour avoir la VAN sous sa forme protonée afin de faciliter les interactions avec les NPs (**Figure 14c**).[47]

Etant donné que la VAN est hydrophile, nous avons décidé de travailler en milieu concentré plutôt qu'en milieu dilué afin de déplacer l'équilibre réactionnel vers un chargement sur les NPs.[48] Les DLCs ont été obtenues via la quantification de la VAN libre dans les surnageants de lavage par spectroscopie UV-visible à $\lambda_{abs., max}$ (VAN) = 280 nm.

Les valeurs de DLC étaient comprises entre 2,2 et 20,1 % en poids, ce qui signifie que 0,022 à 0,201 mg étaient chargés par mg de NPs. Ces résultats suggèrent une bonne efficacité de chargement à pH 5, avec environ 15-18% de VAN par mg de NPs (**Figure 14d**). Ainsi, les échantillons de F P (B)PMO chargés en VAN avec un DLC équivalent (≈ 16 % en masse) ont été choisis pour une comparaison adéquate de l'efficacité antibactérienne contre les bactéries planctoniques (**Tableau 1**). Pour définir le caractère bactéricide de la VAN et des NPs F P PMO chargées en VAN, la concentration minimale inhibitrice (MIC) et la concentration minimale bactéricide (MBC) ont été déterminées *in vitro* sur des colonies de *S. aureus* et *E. coli*. La MIC est une valeur indicative de l'activité bactériostatique et la MBC est une valeur indicative de l'activité bactéricide de l'antibiotique. Les résultats résumés dans le **Tableau 1** montrent que lorsque la VAN est chargée dans les NPs, il faut des concentrations supérieures en VAN pour atteindre la MIC et la MBC, en comparaison avec la VAN directement placée en solution, probablement car tout le médicament n'est pas délivré.

Tableau 1 : Concentration minimale inhibitrice (MIC) et concentration minimale bactéricide (MBC) pour la VAN libre et des (B)PMO NPs chargées en VAN contre des bactéries *E. coli* K-12 MG1655 (gram-négatives) et *S. aureus* ATCC 43300™ (gram-positives).

		E. coli K-12 MG1655		*S. aureus* ATCC 43300™	
Formulations	**DLC (%)**	**MIC (µg mL^{-1})**	**MBC (µg mL^{-1})**	**MIC (µg mL^{-1})**	**MBC (µg mL^{-1})**
VAN	/	47.5 ± 4.4	128	0.45 ± 0.04	2
VAN-loaded E F P	16.9	n.d.	> 256	4.10 ± 0.26	> 4
VAN-loaded E 4S F P	16.0	n.d.	256	0.98 ± 0.04	> 4
VAN-loaded ENE F P	15.7	n.d.	256	1.69 ± 0.20	4
VAN-loaded ENE 4S F P	15.1	n.d.	256	0.81 ± 0.18	> 4

Après ces expériences d'antibiothérapie, des tests aPDT par excitation à deux photons ont été réalisés sur *E. coli* dans un milieu PBS à 780 nm et 10 min après incubation avec des NPs F P (B)PMO (à 200 µg mL^{-1}) fonctionnalisées ou non ou après incubation avec des NPs nues et chargées en VAN. Aucune toxicité n'a été détectée pour des concentrations inférieures ou égales à 200 µg mL^{-1}. Des puits non irradiés de bactéries, avec ou sans NPs, ont servi de contrôles négatifs. Les différentes NPs F P PMO ont donc été incubées avec *E. coli* K-12 MG1655 à une concentration initiale de 10^8 unités formatrices de colonies (CFU) par millilitre, et leur efficacité en TPE-PDT a été évaluée. Comme l'ont révélé les contrôles, l'irradiation laser

sans NPs n'a pas causé de dommages aux colonies de bactéries, tout comme l'incubation avec des NPs sans irradiation (**Figure 15**).

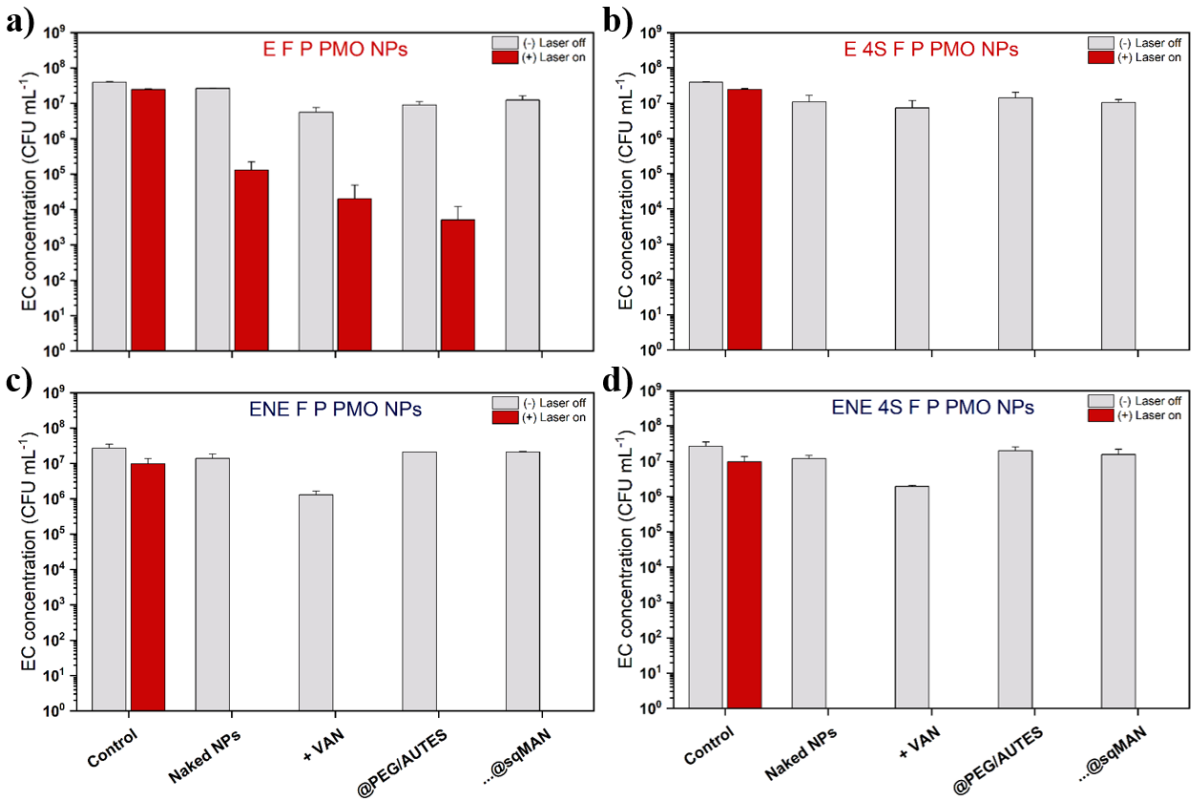

Figure 15 : Etudes TPE-aPDT contre *E. coli* K-12 MG1655 (EC) en présence de différentes F P (B)PMO NPs pour une concentration initiale en bactéries de 10^8 CFU mL^{-1}. (a) E F P, (b) E 4S F P, (c) ENE F P et (d) ENE 4S F P. Un faisceau laser non focalisé (780 nm) a été appliqué pendant 90 s à 1,77 W et la survie a été mesurée 6 h après irradiation par la méthode de comptage sur plaque. Différentes compositions ont été testées chaque famille de nanoparticules (NPs nues, NPs nues + antibiotique, NPs fonctionnalisées PEG/AUTES, soit fonctionnalisées PEG/AUTES@sqMAN). CFU: unités formatrices de colonies.

Les NPs E 4S F P, ENE F P et ENE 4S F P ont montré une éradication complète des colonies, indépendamment de la charge en VAN ou du greffage de surface (**Figure 15b à d**). En revanche, la TPE-PDT avec des nanoparticules E F P a révélé l'influence de la surface. L'utilisation de nanoparticules E F P PMO@PEG/AUTES greffées avec sqMAN a conduit à une éradication totale. En effet, sqMAN est capable de s'ancrer spécifiquement sur les lectines FimH d'*E. coli* et peut également inhiber l'adhésion bactérienne sur de potentielles cellules hôtes. Ainsi, l'efficacité de la TPE-PDT a certainement été renforcée par la propriété de ciblage des systèmes améliorant la diffusion des ROS dans l'environnement proche des bactéries.[49-50]

La contribution de l'antibiotique est légèrement visible sur les essais sans TPE, notamment pour les NPs à base de ponts ENE, où une réduction en viabilité d'environ 1-log a été observée. Toutefois, la synergie des deux traitements est difficile à démontrer à ce stade. Des tests complémentaires sont nécessaires pour avoir une réponse plus rigoureuse sur ce point.

Par ailleurs, l'usage d'autres agents antibactériens comme la tétracycline - dont les valeurs de DLC sont de 2 à 3 log inférieurs à celles de la VAN - est envisagé, afin d'avoir un ratio NP/antibiotique plus adapté.[51]

Le transfert d'énergie des fractions F vers P a été évalué en comparant les profils d'émission des NPs F PMO (donneur), P PMO (accepteur) et F P PMO (donneur-accepteur) mesurés aux mêmes concentrations massiques dans l'éthanol (44 µg mL^{-1}). Comme les concentrations molaires de F-Si et de P-Si initialement intégrées sont les mêmes dans tous les matériaux PMO étudiés, le nombre de photons absorbés par F est également le même, ce qui est obligatoire pour comparer correctement les intensités de fluorescence de F PMO et F P PMO. En outre, comme les P PMO ne sont pas émissives dans la gamme d'émission de F (440-625 nm), la diminution de la fluorescence de F peut être étudiée pour évaluer l'efficacité du FRET (Φ_{ET}). Par exemple, avec la famille ENE 4S BPMO, une efficacité FRET de 91% a été obtenue à partir de la diminution de l'intensité de la fluorescence de F avec l'augmentation concomitante de la fluorescence de l'accepteur P (**Figure 16a**).

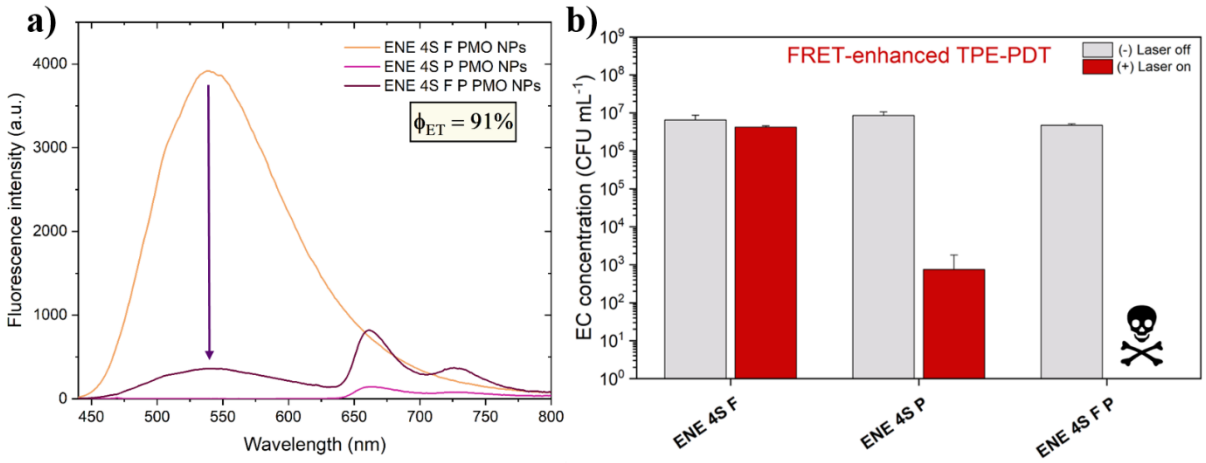

Figure 16 : Principe de FRET démontré et appliqué à la TPE-aPDT pour les ENE 4S F P PMO NPs. (a) Spectres d'émission de fluorescence des nanoparticules ENE 4S F (donneur), ENE 4S P (accepteur) et ENE 4S F P (donneur-accepteur) démontrant le transfert d'énergie de F vers P; (b) Etudes TPE-aPDT contre *E. coli* K-12 MG1655 (EC). Un faisceau laser non focalisé (780 nm) a été appliqué pendant 90 s à 1,50 W et la survie a été mesurée 6 h après irradiation par la méthode de comptage sur plaque. Seulement des nanoparticules nues ont été testées.

Une première étude *in vitro* sur *E. coli* a été réalisée avec le même type de NPs pour ainsi évaluer la contribution du FRET à l'efficacité du TPE-PDT (**Figure 16b**).

Comme prévu, l'échantillon contenant uniquement des parties donneuses d'énergie (ENE 4S F) n'a montré aucune toxicité après excitation. Les NPs ENE 4S P ont provoqué une activité antibactérienne intermédiaire avec une réduction de 4,1 log CFU mL^{-1}, tandis que l'échantillon ENE 4S F P a permis l'éradication complète des colonies. Ce résultat suggère que

la TPE-PDT antibactérienne est bel et bien renforcée par le FRET grâce aux propriétés d'absorption à deux-photons du fluorophore F. Des recherches sont en cours pour évaluer la capacité des autres NPs de (B)PMO et d'autres travaux sont envisagés pour comparer la génération de ROS avec des configurations donneur-accepteur (F P) et accepteur (P).

En perspective, le potentiel en TPE-PDT sera évalué contre *S. aureus*. Des études antibactériennes *in vitro* sur des modèles de biofilms tentant de reproduire l'environnement d'infection *in vivo* devraient être réalisées. En effet, les biofilms sont considérablement plus résistants que les bactéries planctoniques. De plus, 65% des infections microbiennes et 80% des infections chroniques sont actuellement liées à la formation de biofilms, ce qui en fait une menace majeure à traiter.[52] Enfin, nous prévoyons de tester nos matériaux en tant que pansements antibactériens assistés par TPE-PDT permettant de limiter une infection tout en participant à la régénération tissulaire et à la stimulation du système immunitaire. Pour cela, une plaie d'excision ou une lésion cutanée sera volontairement pratiquée sur la souris afin d'évaluer le potentiel thérapeutique des nanomatériaux.[53-54]

Références bibliographiques

1. Alshamrani, M., Broad-Spectrum Theranostics and Biomedical Application of Functionalized Nanomaterials. *Polymers* **2022,** *14* (6), 1221.

2. Wang, X.; Liu, L. H.; Ramström, O.; Yan, M., Engineering nanomaterial surfaces for biomedical applications. *Experimental Biology and Medicine* **2009,** *234* (10), 1128-39.

3. Lim, E. K.; Kim, T.; Paik, S.; Haam, S.; Huh, Y. M.; Lee, K., Nanomaterials for Theranostics: Recent Advances and Future Challenges. *Chemical Reviews* **2015,** *115* (1), 327-394.

4. Nunes, S. C.; Almeida, P.; de Zea Bermudez, V., Ordered Mesoporous Sol–Gel Materials: From Molecular Sieves to Crystal-Like Periodic Mesoporous Organosilicas. In *The Sol-Gel Handbook*, **2015**; 575-604.

5. Croissant, J. G.; Cattoen, X.; Durand, J. O.; Man, M. W. C.; Khashab, N. M., Organosilica hybrid nanomaterials with a high organic content: syntheses and applications of silsesquioxanes. *Nanoscale* **2016,** *8* (48), 19945-19972.

6. Croissant, J. G.; Cattoën, X.; Wong Chi Man, M.; Durand, J.-O.; Khashab, N. M., Syntheses and applications of periodic mesoporous organosilica nanoparticles. *Nanoscale* **2015,** *7* (48), 20318-20334.

7. Butcher, N. J.; Mortimer, G. M.; Minchin, R. F., Unravelling the stealth effect. *Nature Nanotechnology* **2016,** *11* (4), 310-311.

8. Gheibi Hayat, S. M.; Bianconi, V.; Pirro, M.; Sahebkar, A., Stealth functionalization of biomaterials and nanoparticles by CD47 mimicry. *International Journal of Pharmaceutics* **2019,** *569*, 118628.

9. Grenier, P.; Viana, I. M. O.; Lima, E. M.; Bertrand, N., Anti-polyethylene glycol antibodies alter the protein corona deposited on nanoparticles and the physiological pathways regulating their fate in vivo. *Journal of Controlled Release* **2018,** *287*, 121-131.

10. Jin, J.; Bhujwalla, Z. M., Biomimetic Nanoparticles Camouflaged in Cancer Cell Membranes and Their Applications in Cancer Theranostics. *Frontiers in Oncology* **2019,** *9*, 1560.

11. Panja, P.; Das, P.; Mandal, K.; Jana, N. R., Hyperbranched Polyglycerol Grafting on the Surface of Silica-Coated Nanoparticles for High Colloidal Stability and Low Nonspecific Interaction. *ACS Sustainable Chemistry & Engineering* **2017,** *5* (6), 4879-4889.

12. Su, X. D.; Tao, J.; Wang, Q.; Xu, P.; Luo, W.; Dang, M., et al., Controlled PEGylation of periodic mesoporous organosilica nanospheres for improving their stability in physiological solutions. *Chinese Chemical Letters* **2019,** *30* (4), 929-932.

13. Xiang, W.; Liu, X.; Zhang, L.; Liu, C.; Liu, G., Cell membrane-encapsulated nanoparticles for vaccines and immunotherapy. *Particuology* **2022,** *64*, 35-42.

14. Yu, M. K.; Park, J.; Jon, S., Targeting strategies for multifunctional nanoparticles in cancer imaging and therapy. *Theranostics* **2012,** *2* (1), 3-44.

15. Pardhi, D. M.; Şen Karaman, D.; Timonen, J.; Wu, W.; Zhang, Q.; Satija, S., et al., Anti-bacterial activity of inorganic nanomaterials and their antimicrobial peptide conjugates against resistant and non-resistant pathogens. *International Journal of Pharmaceutics* **2020,** *586*, 119531.

16. Ajdary, M.; Moosavi, M. A.; Rahmati, M.; Falahati, M.; Mahboubi, M.; Mandegary, A., et al., Health Concerns of Various Nanoparticles: A Review of Their in Vitro and in Vivo Toxicity. *Nanomaterials* **2018,** *8* (9), 634.

17. Tan, X.; Yang, L.; Huang, Z.; Yu, Y.; Wang, Z.; Zhang, X., Amphiphilic diselenide-containing supramolecular polymers. *Polymer Chemistry* **2015,** *6* (5), 681-685.

18. Chinnathambi, S.; Tamanoi, F., Recent Development to Explore the Use of Biodegradable Periodic Mesoporous Organosilica (BPMO) Nanomaterials for Cancer Therapy. *Pharmaceutics* **2020,** *12* (9), 890.

19. Abrahamse, H.; Michael, H. R., New photosensitizers for photodynamic therapy. *Biochemical Journal* **2016,** *473* (4), 347-364.

20. Wang, S.; Wu, W.; Manghnani, P.; Xu, S.; Wang, Y.; Goh, C. C., et al., Polymerization-Enhanced Two-Photon Photosensitization for Precise Photodynamic Therapy. *ACS Nano* **2019,** *13* (3), 3095-3105.

21. Zheng, Z.; Liu, H.; Zhai, S.; Zhang, H.; Shan, G.; Kwok, R. T. K., et al., Highly efficient singlet oxygen generation, two-photon photodynamic therapy and melanoma ablation by rationally designed mitochondria-specific near-infrared AIEgens. *Chemical Science* **2020,** *11* (9), 2494-2503.

22. Yano, S.; Hirohara, S.; Obata, M.; Hagiya, Y.; Ogura, S.-i.; Ikeda, A., et al., Current states and future views in photodynamic therapy. *Journal of Photochemistry and Photobiology C: Photochemistry Reviews* **2011,** *12* (1), 46-67.

23. Shen, Y. Z.; Shuhendler, A. J.; Ye, D. J.; Xu, J. J.; Chen, H. Y., Two-photon excitation nanoparticles for photodynamic therapy. *Chemical Society Reviews* **2016,** *45* (24), 6725-6741.

24. Sun, Z. Y.; Zhang, L. P.; Wu, F. P.; Zhao, Y. X., Photosensitizers for Two-Photon Excited Photodynamic Therapy. *Advanced Functional Materials* **2017,** *27* (48), 1704079.

25. Horne, T. K.; Cronjé, M. J., Mechanistics and photo-energetics of macrocycles and photodynamic therapy: An overview of aspects to consider for research. *Chemical Biology & Drug Design* **2017,** *89* (2), 221-242.

26. Mauriello Jimenez, C.; Knezevic, N. Z.; Rubio, Y. G.; Szunerits, S.; Boukherroub, R.; Teodorescu, F., et al., Nanodiamond-periodic mesoporous organosilica nanoparticles (PMO) for two-photon photodynamic therapy (PDT) and drug delivery. *Journal of Materials Chemistry B* **2016,** *4* (35), 5803-5808.

27. Bumb, A.; Sarkar, S. K.; Billington, N.; Brechbiel, M. W.; Neuman, K. C., Silica Encapsulation of Fluorescent Nanodiamonds for Colloidal Stability and Facile Surface Functionalization. *Journal of the American Chemical Society* **2013,** *135* (21), 7815-7818.

28. Von Haartman, E.; Jiang, H.; Khomich, A. A.; Zhang, J.; Burikov, S. A.; Dolenko, T. A., et al., Core–shell designs of photoluminescent nanodiamonds with porous silica coatings for bioimaging and drug delivery I: fabrication. *Journal of Materials Chemistry B* **2013,** *1* (18), 2358.

29. Guan, B.; Cui, Y.; Ren, Z.; Qiao, Z.-a.; Wang, L.; Liu, Y., et al., Highly ordered periodic mesoporous organosilica nanoparticles with controllable pore structures. *Nanoscale* **2012,** *4* (20), 6588-6596.

30. Daurat, M.; Nguyen, C.; Dominguez Gil, S.; Sol, V.; Chaleix, V.; Charnay, C., et al., The mannose 6-phosphate receptor targeted with porphyrin-based periodic mesoporous organosilica nanoparticles for rhabdomyosarcoma theranostics. *Biomaterials Science* **2020,** *8* (13), 3678-3684.

31. Zhao, L.; Chen, Y.; Yuan, J.; Chen, M.; Zhang, H.; Li, X., Electrospun Fibrous Mats with Conjugated Tetraphenylethylene and Mannose for Sensitive Turn-On Fluorescent Sensing of Escherichia coli. *ACS Applied Materials & Interfaces* **2015,** *7* (9), 5177-5186.

32. Gary-Bobo, M.; Mir, Y.; Rouxel, C.; Brevet, D.; Basile, I.; Maynadier, M., et al., Mannose-Functionalized Mesoporous Silica Nanoparticles for Efficient Two-Photon Photodynamic Therapy of Solid Tumors. *Angewandte Chemie International Edition* **2011,** *50* (48), 11425-11429.

33. Le Droumaguet, C.; Sourdon, A.; Genin, E.; Mongin, O.; Blanchard-Desce, M., Two-Photon Polarity Probes Built from Octupolar Fluorophores: Synthesis, Structure-Properties Relationships, and Use in Cellular Imaging. *Chemistry - An Asian Journal* **2013,** *8* (12), 2984-3001.

34. Katan, C.; Terenziani, F.; Mongin, O.; Werts, M. H. V.; Porrès, L.; Pons, T., et al., Effects of (Multi)branching of Dipolar Chromophores on Photophysical Properties and Two-Photon Absorption. *The Journal of Physical Chemistry A* **2005,** *109* (13), 3024-3037.

35. Xu, L.; Lin, W.; Huang, B.; Zhang, J.; Long, X.; Zhang, W., et al., The design strategies and applications for organic multi-branched two-photon absorption chromophores with novel cores and branches: a recent review. *Journal of Materials Chemistry C* **2021,** *9* (5), 1520-1536.

36. Aggad, D.; Mauriello Jimenez, C.; Dib, S.; Croissant, J. G.; Lichon, L.; Laurencin, D., et al., Gemcitabine Delivery and Photodynamic Therapy in Cancer Cells *via* Porphyrin-Ethylene-Based Periodic Mesoporous Organosilica Nanoparticles. *ChemNanoMat* **2018,** *4* (1), 46-51.

37. Valeur, B., Resonance Energy Transfer and Its Applications. In *Molecular Fluorescence*, **2001**; 247-272.

38. Förster, T., Zwischenmolekulare Energiewanderung und Fluoreszenz. *Annalen der Physik* **1948,** *437* (1-2), 55-75.

39. Mai, N. X. D.; Birault, A.; Matsumoto, K.; Ta, H. K. T.; Intasa-Ard, S. G.; Morrison, K., et al., Biodegradable Periodic Mesoporous Organosilica (BPMO) Loaded with Daunorubicin: A Promising Nanoparticle-Based Anticancer Drug. *ChemMedChem* **2020,** *15* (7), 593-599.

40. Zhang, M.; Li, Y.; Bi, L.; Zhuang, W.; Wang, S.; Chen, Y., et al., Preparation of Helical Mesoporous Ethenylene-silica Nanofibers with Lamellar Mesopores on Their Surface. *Chinese Journal of Chemistry* **2011,** *29* (5), 933-941.

41. Agarwal, V.; Singh, M.; McPherson, G.; John, V.; Bose, A., Microstructure evolution in aqueous solutions of cetyl trimethylammonium bromide (CTAB) and phenol derivatives. *Colloids and Surfaces A: Physicochemical and Engineering Aspects* **2006,** *281* (1), 246-253.

42. Bharti, C.; Gulati, N.; Nagaich, U.; Pal, A., Mesoporous silica nanoparticles in target drug delivery system: A review. *International Journal of Pharmaceutical Investigation* **2015,** *5* (3), 124.

43. Poscher, V.; Salinas, Y., Trends in Degradable Mesoporous Organosilica-Based Nanomaterials for Controlling Drug Delivery: A Mini Review. *Materials* **2020,** *13* (17), 3668.

44. Gounani, Z.; Asadollahi, M. A.; Pedersen, J. N.; Lyngso, J.; Pedersen, J. S.; Arpanaei, A., et al., Mesoporous silica nanoparticles carrying multiple antibiotics provide enhanced synergistic effect and improved biocompatibility. *Colloids and Surfaces B: Biointerfaces* **2019,** *175*, 498-508.

45. Marsot, A.; Boulamery, A.; Bruguerolle, B.; Simon, N., Vancomycin: a review of population pharmacokinetic analyses. *Clinical pharmacokinetics* **2012,** *51* (1), 1-13.

46. Ural, M. S.; Menéndez-Miranda, M.; Salzano, G.; Mathurin, J.; Aybeke, E. N.; Deniset-Besseau, A., et al., Compartmentalized Polymeric Nanoparticles Deliver Vancomycin in a pH-Responsive Manner. *Pharmaceutics* **2021,** *13* (12), 1992.

47. Cauda, V.; Onida, B.; Platschek, B.; Mühlstein, L.; Bein, T., Large antibiotic molecule diffusion in confined mesoporous silica with controlled morphology. *Journal of Materials Chemistry* **2008,** *18* (48), 5888-5899.

48. Nader, D.; Yousef, F.; Kavanagh, N.; Ryan, B. K.; Kerrigan, S. W., Targeting Internalized *Staphylococcus aureus* Using Vancomycin-Loaded Nanoparticles to Treat Recurrent Bloodstream Infections. *Antibiotics* **2021,** *10* (5), 581.

49. Berglund, J.; Knight, S. D. In *Structural Basis for Bacterial Adhesion in the Urinary Tract*, Glycobiology and Medicine, Boston, MA, 2003; Axford, J. S., Ed. Springer US: Boston, MA, 2003; pp 33-52.

50. Bavington, C.; Page, C., Stopping bacterial adhesion: a novel approach to treating infections. *Respiration; international review of thoracic diseases* **2005,** *72* (4), 335-44.

51. Meretoudi, A.; Banti, C. N.; Siafarika, P.; Kalampounias, A. G.; Hadjikakou, S. K., Tetracycline Water Soluble Formulations with Enhanced Antimicrobial Activity. *Antibiotics* **2020,** *9* (12), 845.

52. Jamal, M.; Ahmad, W.; Andleeb, S.; Jalil, F.; Imran, M.; Nawaz, M. A., et al., Bacterial biofilm and associated infections. *Journal of the Chinese Medical Association* **2018,** *81* (1), 7-11.

53. Li, L.; Yang, Y.; Yang, Z.; Zheng, M.; Luo, G.; He, W., et al., Effects of ALA-PDT on the macrophages in wound healing and its related mechanisms in vivo and in vitro. *Photodiagnosis and Photodynamic Therapy* **2022,** *38*, 102816.

54. Oyama, J.; Fernandes Herculano Ramos-Milaré, Á. C.; Lopes Lera-Nonose, D. S. S.; Nesi-Reis, V.; Galhardo Demarchi, I.; Alessi Aristides, S. M., et al., Photodynamic therapy in wound healing in vivo: a systematic review. *Photodiagnosis and Photodynamic Therapy* **2020,** *30*, 101682.

ABSTRACT

Among the different existing nanomaterials, periodic mesoporous organosilica-based nanoparticles (PMO NPs) hold great promises for nanomedicine due to their biocompatibility and their versatile synthesis, providing the integration of a large variety of bioactive compounds. In combination with current treatments or as an individual strategy, two-photon excitation photodynamic therapy (TPE-PDT) offers a better benefit-risk ratio for the patient thanks to its non-invasive nature and its three-dimensional resolution. Upon laser irradiation, two-photon photosensitizer (PS)-based systems with a high capacity to generate reactive oxygen species (ROS) are required to efficiently eradicate diseased cells.

During this project, various photosensitive moieties were integrated into multifunctional PMO NPs prepared in basic media. As a first strategy, nanodiamond-PMO core-shell NPs have been employed in *in vitro* anticancer TPE-PDT. After encapsulation, these materials containing nanodiamonds showed significant cell uptake and phototoxicity. A second approach consisted in enhancing the ROS generation by fluorescence resonance energy transfer mechanism from an energy donor possessing high absorption capacity to an energy acceptor, namely, the PS. For this purpose, a newly-synthesized octupolar fluorophore have been integrated in the three-dimensional framework of PMO NPs, conjointly with a two-photon porphyrin PS. Photophysical characterization of the materials and TPE-PDT studies showed excellent eradication of either cancer cells and pathogenic bacteria, thus confirming the satisfying energy conversion between the two moieties. Moreover, antibiotic-loaded NPs showed a controlled release of the drug in a bacterial environment with potential for combination therapy.

These active nanoplatforms may have multiple benefits for anticancer and antibacterial therapy, leading to novel formulations that have been capable of performing imaging, TPE-PDT and antibiotic delivery.

Keywords: organosilica-based nanoparticles; photodynamic therapy; fluorophores; photosensitizers; two-photon; antibiotic delivery.

ABSTRACT

Parmi les différents types de nanomatériaux développés à ce jour, les nanoparticules à base d'organosilice mésoporeuse périodique (PMO NPs) sont très prometteuses pour la nanomédecine en raison de leur biocompatibilité et de leur synthèse très polyvalente, permettant l'intégration d'une grande diversité de composés bioactifs. Combinée avec les traitements actuels ou en tant que stratégie unique, la thérapie photodynamique par excitation à deux photons (TPE-PDT) améliore la balance bénéfice/risque pour le patient du fait de son caractère non-invasif et de sa résolution tridimensionnelle. Pour éradiquer efficacement les cellules malades sous irradiation laser, il est nécessaire d'utiliser des systèmes innovants à base de photosensibilisateurs (PSs) à deux photons ayant une grande capacité à générer des espèces réactives de l'oxygène (ROS).

Au cours de ce projet, différents composés photosensibles ont été intégrés dans des PMO NPs multifonctionnelles synthétisées par différentes voies sol-gel en milieu basique. Dans un premier temps, des NPs coeur-coquille de nanodiamant-PMO ont été préparées pour la TPE-PDT anticancéreuse *in vitro*. Après encapsulation, ces systèmes constitués de nanodiamants ont démontré une forte capacité d'internalisation cellulaire et une toxicité importante sous irradiation à deux-photons. Une seconde approche basée sur le transfert d'énergie par résonance de fluorescence a été envisagée pour augmenter la génération de ROS. Ce mécanisme photophysique se produit à partir d'un donneur d'énergie possédant une capacité d'absorption élevée à destination d'un accepteur d'énergie, à savoir le PS. Dans ce but, un fluorophore octupolaire nouvellement synthétisé a été intégré dans la matrice tridimensionnelle de PMO NPs, conjointement avec une porphyrine connue comme PS à deux-photons. La caractérisation photophysique des matériaux et les études TPE-PDT ont démontré une excellente capacité à éradiquer des populations de cellules cancéreuses et de bactéries pathogènes, confirmant ainsi la conversion énergétique optimale entre les deux chromophores. De plus, les NPs chargées en vancomycine - un antibiotique utilisé à grande échelle - ont démontré une libération contrôlée du médicament en milieu bactérien avec un potentiel pour la thérapie combinée à explorer.

Ainsi, ces nouvelles formulations qui ont été capables de réaliser de l'imagerie biologique, de la TPE-PDT et de l'administration d'antibiotique, présentent de multiples avantages dans le domaine de la théranostique pour combattre efficacement le cancer et les infections dans des applications futures.

Mots-clés: nanoparticules à base d'organosilice; thérapie photodynamique; fluorophores; photosensibilisateurs; deux-photons; délivrance d'antibiotique.